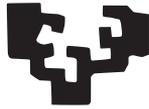eman ta zabal zazu

Universidad
del País Vasco

Euskal Herriko
Unibertsitatea

Study of Geometrical Frustration and Thermal Activation in Arrays of Magnetic Nanostructures

Matteo Pancaldi

– Ph.D. Thesis –

Supervisor: Prof. Paolo Vavassori

2018

CIC nanoGUNE

nanoscience cooperative research center

Resumen

El *magnetismo* es una materia fascinante. Pese a que algunos de los fenómenos relacionados con el tema ya se conocían unos pocos siglos a.C., la aparición de la mecánica cuántica dio explicación a los mecanismos que gobiernan las propiedades magnéticas de la materia. Una vez se conoce el comportamiento de la materia y como este puede ser descrito matemáticamente, es posible fabricar dispositivos que combinan las propiedades de los materiales de forma predeterminada. Esta norma no se cumple únicamente en el magnetismo, si no en la *física* en general, cuyo mayor objetivo es proporcionar conocimiento cuantitativo (y experimentalmente verificado) de la Naturaleza hasta el más profundo nivel.

No obstante, la mecánica cuántica no ha sido el único descubrimiento que ha ayudado al uso práctico del magnetismo. Durante el último siglo muchas de las innovaciones del magnetismo han sido posibles debido al desarrollo de la nanotecnología: la disminución de al menos una de las dimensiones de los dispositivos en una rango de $1 - 1000$ nm causa la aparición de nuevos fenómenos físicos. Por ello, la unión del magnetismo y la nanotecnología dio lugar al campo fundamental del nanomagnetismo [1].

Esta tesis recoge la parte más relevante del trabajo realizado durante mi proyecto de doctorado, el cual comenzó el 6 de febrero del 2014 en el grupo de Nanomagnetismo, como parte del Centro de Investigación Cooperativa de nanoGUNE (Donostia–San Sebastián, España). El título de la tesis ayuda a elaborar un resumen de los temas tratados: *Estudio de la **Frustración Geométrica** y **Activación Térmica** en **Conjuntos de Nanoestructuras Magnéticas***.

Conjuntos de nanoestructuras magnéticas

Esta tesis trata de *nanoescructuras magnéticas*, definidas por la disminución de sus tres dimensiones y formadas por materiales magnéticos. La *condición me-*

soscópica determina la longitud L en el que las dimensiones están confinadas [2]:

$$L \approx \rho_C,$$

donde ρ_C es la longitud característica del fenómeno a considerar. En este caso, la longitud de interés será la que deriva del peso relativo de los términos que componen la energía libre micromagnética: reduciendo el tamaño de las estructuras magnéticas, las paredes de dominio se convierten energéticamente desfavorables, haciendo así que la imanación de las estructuras se organice en un único dominio cuando la dimensión de las mismas llegue a ser menor de la extensión de la pared de dominio (la longitud característica). Para tal fin, las dimensiones consideradas a lo largo de la tesis son inferiores a los 700 nm, y hasta un mínimo de 3 nm de grosor. Otro aspecto relevante a considerar es la importancia de la *forma*. La formación de los dominios en un cuerpo magnético está relacionada con la reducción de la extensión espacial del campo magnético producido por el propio cuerpo. Por tanto, en una nanoestructura de un solo dominio, la mayor contribución a su energía libre es debida a la *energía magnetostática*, que en efecto depende del campo magnético generado por la nanoestructura. Asimismo, el perfil energético está definido por la forma de la nanoestructura: la estabilidad de la imanación que yace paralela al eje mayor de una nanoestructura alargada depende del ratio entre el tamaño de los ejes de la nanoestructura. Escogiendo un material magnéticamente isótropo (p.ej. Permalloy), se obtiene la unidad de base requerida: una nanoestructura que se comporta como una aguja imantada cuya estabilidad con respecto a estímulos magnéticos y temperatura está gobernada por su forma. El último aspecto relevante está relacionado con la palabra *conjuntos*. Cualquier tipo de entidad (desde las personas hasta las nanoestructuras magnéticas) puede ser muy interesante por si misma, aunque propiedades emergentes pueden aparecer como consecuencia de la introducción de *interacciones* entre las unidades básicas[1]. En el caso de las nanoestructuras magnéticas, las interacciones empiezan a ser efectivas cuando las unidades de base se encuentran lo suficientemente cerca como para ser afectadas por el campo magnético producido por nanoestructuras vecinas.

En este marco, el Cap. 1 explica las nociones básicas del magnetismo necesarias para la comprensión de cómo las nanoestructuras magnéticas se ven afectadas por temperatura y campos magnéticos y de cómo interactúan entre si. Uno de los apartados del capítulo está dedicado a la explicación de la interacción de la luz con nanoestructuras metálicas, ya que el Cap. 5 se ha desarrollado a partir

---

[1]De hecho, en un sistema complejo "el todo es más que la simple suma de sus partes".

de este fenómeno. Una vez conocidas las herramientas para describir los sistemas de interés, las nanoestructuras magnéticas deben ser fabricadas y caracterizadas. El capítulo 3 ahonda en la fabricación de nanoestructuras mediante el uso de litografía por haz de electrones y en la caracterización de las mismas mediante medidas de efecto Kerr magneto-óptico. Debido al la importancia de esta última técnica para el desarrollo de mi proyecto doctoral, el Cap. 2 está completamente dedicado a la descripción de los efectos magneto-ópticos en la materia y cómo estos pueden proporcionar información relativa a la imanación de nanoestructuras. Asimismo, el Cap. 3 contiene los principales resultados obtenidos durante una estancia de cuatro meses (Septiembre 2016 – Diciembre 2016) en el grupo de "Ultrafast Dynamics in Condensed Matter" de la Universidad de Estocolmo (Suecia).

Frustración geométrica

Esta tesis contiene resultados inéditos relacionados con nanoestructuras magnéticas en interacción. Un efecto peculiar relacionado con las interacciones es la *frustración*, es decir, la inhabilidad de un sistema físico de minimizar simultáneamente la energía de todas sus interacciones. Debido a la frustración, pueden coexistir configuraciones no triviales que poseen la misma energía. Cuando esto ocurre, el estado fundamental del sistema resulta degenerado, dando origen a propiedades singulares, p.ej. entropía residual a temperatura próxima a cero. Un clásico ejemplo es la disposición de los átomos de hidrogeno en el hielo. Igualmente el mismo comportamiento ha sido descubierto en otros materiales debido a la disposición espacial de los espines atómicos. Estos materiales constituyen la categoría de sistemas de *hielo de espín*. Tanto en el hielo como en el hielo de espín, la frustración está determinada por la disposición geométrica de las unidades de base, de ahí el nombre "frustración *geométrica*". Una desventaja de estos sistemas resulta del hecho que las propiedades característica de la frustración son definidas por el material: una vez se tenga el material con sus propiedades, no hay mucho que se pueda modificar para investigar de manera sistemática la física de la frustración. Sin embargo, en el año 2006 [3], una nueva clase de metamateriales fue creada: sistemas de *hielo de espín artificial*, que son una construcción bidimensional de hielo de espín fabricada mediante litografía por haz de electrones (básicamente un conjunto de nanoestructuras magnéticas en interacción). Para que los sistemas de hielo de espín artificial funcionen debidamente, las nanoestructuras magnéticas que los componen deben comportarse como agujas imantadas, como se ha discutido previamente.

En este marco, el Cap. 4 introduce brevemente el concepto de frustración para posteriormente enfocarse en el desarrollo de los sistemas de hielo de espín artificial. El fin de este capítulo es resumir nuestro intento en describir y simular la evolución temporal de los sistemas de hielo de espín artificial cuando el efecto de la *temperatura* es considerado. De hecho, el calentamiento de los sistemas de hielo de espín artificial es el proceso clave para poder obtener la formación del estado fundamental. Dependiendo de los parámetros que caracterizan el sistema, se podría llegar a conseguir o no el estado fundamental, dado que (i) el material, (ii) la disposición de las nanoestructuras en el conjunto, (iii) la forma de cada nanoestructura y (iv) la temperatura tienen un impacto sobre el proceso. Por tanto, tuvimos en cuenta todos estos factores desarrollando así un esquema de simulación a multi-escala que es capaz de combinar simulaciones micromagnéticas estocásticas (cientos de nanómetros, decenas de microsegundos) con el método de Monte Carlo cinético al fin de considerar el comportamiento del sistema en su totalidad (decenas de micrómetros, cientos de segundos). Los resultados derivados de este método de simulación han sido comparados con datos de la literatura con el fin de verificar la validez de nuestra estrategia. A pesar de no estar directamente relacionado con la frustración, la competición entre interacciones magnetostáticas también puede ser aprovechada para explorar el perfil energético de nanoestructuras magnéticas, mas allá de lo que se podría obtener con el solo uso de campos magnéticos homogéneos. El capítulo 6 recoge todas las simulaciones y evidencias experimentales de cómo una unidad quiral formada por cuatro nanoestructuras alargadas puede inducir la formación de un estado de magnetización energéticamente metaestable e imposible de obtener con una nanoestructura aislada. Por consiguiente, fuimos capaces de inducir de manera reproducible el estado de vórtice magnético en una nanoestructura diseñada para que actúe como una aguja imantada. Este descubrimiento acentúa de manera aún más evidente el papel fundamental que juegan las interacciones magnetostáticas entre nanoestructuras magnéticas.

Activación térmica

Tal y como se ha discutido en el apartado anterior, el calentamiento de los sistemas de hielo de espín artificial es el proceso fundamental a investigar. Además del esquema de simulación de multi-escala descrito en el Cap. 4 y su desarrollo con la finalidad de simular procesos térmicamente activados, nos basamos en el conocimiento de nuestro grupo de investigación en magnetismo y plasmónica para idear una técnica no estándar de calentamiento de sistemas de hielo de espín artificiales: el *calentamiento termoplasmónico* de nanoestructuras magnéticas. La

transferencia de energía de una onda electromagnética a una nanoestructura me-
tálica puede ser muy efectiva cuando se excita de forma resonante la oscilación
colectiva de los electrones libres del metal que constituye la nanoestructura (ex-
citación de un plasmón localizado de superficie), mientras que esta transferencia
puede ser prácticamente interrumpida cuando el sistema electrónico está fuera
de resonancia. Además, a una determinada longitud de onda, la transferencia de
energía puede ser modulada acorde a la dirección de la polarización linear con
respecto a los ejes de la nanoestructura, debido al hecho que la frecuencia de re-
sonancia depende del ratio entre la longitud de los ejes (*calentamiento selectivo*).
Finalmente, utilizando haces de luz es posible controlar el tamaño de la región de
la muestra donde se deposita la energía a través del control del foco del mismo
haz, hasta un diámetro de 1 μm (*calentamiento local*).

En este marco, el Cap. 5 describe el diseño y la fabricación de nanoestruc-
turas magnéticas las cuales pueden ser (i) parte de un sistema de hielo de espín
artificial y (ii) calentadas de manera eficaz a través de la interacción con la luz.
Ambos requerimientos se cumplen trabajando con nanoestructuras alargadas de
multicapa, donde el Permalloy proporciona las propiedades magnéticas y el oro
es un eficaz material plasmónico. Dado que las nanoestructuras son alargadas, es
posible implementar un calentamiento selectivo basado en la dirección de polari-
zación y en la elección de la frecuencia. Tras analizar nanoestructuras aisladas,
nos centramos en averiguar que sucede cuando cuatro nanoestructuras forman
un vértice de un sistema cuadrado de hielo de espín artificial. En particular, las
cuatro nanoestructuras están organizadas en parejas y alineadas acorde a dos
direcciones perpendiculares. Las dos nanoestructuras paralelas a la dirección de
polarización pueden ser calentadas de manera más eficaz respecto a las otras
dos, debido a la selectividad de calentamiento descrita anteriormente. No obs-
tante, también el número de nanoestructuras por unidad de área (proporcional
al coeficiente de recubrimiento superficial) ejerce una influencia sobre la tempe-
ratura que se puede alcanzar. Por lo tanto, deben considerarse varios aspectos a
la hora de aplicar el calentamiento termoplasmónico a los sistemas de hielo de
espín artificial. Para llevar a cabo los experimentos sobre el calentamiento termo-
plasmónico, no solo fue necesaria la fabricación de nanoestructuras alargadas de
multicapa, sino también el desarrollo de un dispositivo de calentamiento que se
pudiese combinar con nuestro equipo de medida de efecto Kerr magneto-óptico.
De esta manera, a través de la medición de la variación del campo coercitivo en
función de la temperatura, fuimos capaces de medir el aumento de temperatu-
ra y correlacionarlo con el ratio entre el tamaño de los ejes y el coeficiente de
recubrimiento superficial.

Summary

Magnetism is a very fascinating topic. Despite some of the phenomena related to it have been known since few centuries BC, only the advent of quantum mechanics shed light on the mechanisms governing the magnetic properties of matter. Once we know *how*² matter behaves and *how* it can be mathematically described, we can build devices which combine various material properties in order to carry out the functions they have been designed to supply. This is not only true for magnetism, but for *physics* in general, whose main goal is to provide quantitative (and experimentally verified) knowledge of Nature, down to the deepest possible level.

However, quantum mechanics has not been the only discovery paving the way for the practical exploitation of magnetism during the last century. A lot of *room* [4] for extending the properties of bulk magnetism has been introduced by *nanotechnology*: the reduction in at least one of the devices' dimensions to (typically) the $1 - 1000$ nm range determines the appearance of new physical phenomena. Therefore, the union of magnetism and nanotechnology gave rise to the fundamental field of *nanomagnetism* [1].

This thesis collects the most relevant part of the work carried out during my Ph.D. project, started on the 6th of February 2014 in the Nanomagnetism group part of the nanoGUNE Cooperative Research Center (Donostia–San Sebastián, Spain). A brief summary of the considered topics (all related to nanomagnetism) can be organized by following the keywords contained in the thesis' title: *Study of Geometrical Frustration and Thermal Activation in Arrays of Magnetic Nanostructures*.

---

²"The next reason that you might think you do not understand what I am telling you is, while I am describing to you *how* Nature works, you won't understand *why* Nature works that way. But you see, nobody understands that. I can't explain why Nature behaves in this peculiar way." R. P. Feynman, *QED – The Strange Theory of Light and Matter* (Princeton University Press, 1985).

Arrays of magnetic nanostructures

All this thesis deals with *magnetic nanostructures*, which are entities characterized by three reduced dimensions and formed by magnetic materials. The length scale L which the dimensions are confined to is dictated by the *mesoscopic condition* [2]

$$L \approx \rho_C,$$

where ρ_C is the characteristic length scale of the involved phenomenon. Here, the length scale of interest is the one which derives from the relative weight of the various terms composing the micromagnetic free energy: by reducing the structure size, the domain walls become energetically too "expensive" and so the magnetization inside a magnetic nanostructure ends up to be organized in a single domain. For this purpose, the considered dimensions through the thesis are all below 700 nm, down to a minimum of 3 nm for the thickness. Another relevant aspect related to confinement is the role of *shape*. The reason leading to the formation of domains in a magnetic body is connected to the reduction of the spatial extent of the stray magnetic field produced by the body itself. Hence, in a single-domain nanostructure, the main contribution to its free energy is given by the so called *magnetostatic energy*, which indeed depends on the magnetic field the nanostructure generates in space. Moreover, it turns out the associated energy landscape is controlled by the nanostructure shape: the stability of the magnetization lying along the major axis of an elongated nanostructure depends on the ratios in between the nanostructure axes. By choosing a material in which the magnetocrystalline anisotropy can be neglected (e.g. Permalloy), we obtain the desired basic units: nanostructures behaving like magnetic needles, whose stability with respect to both an applied magnetic field and temperature is governed by their shape. The last relevant aspect is coded in the *array* keyword. Any kind of entity (from people to magnetic nanostructures) can be extremely interesting by itself, but complex phenomena can appear as a consequence of introducing *interactions* in an array of basic units[3]. In the case of magnetic nanostructures, interactions start to be effective when the basic units are placed close enough to "feel" the stray magnetic field produced by their neighbours.

In this framework, Chap. 1 provides the basic notions on magnetism needed for understanding how magnetic nanostructures behaves under the action of both magnetic fields and temperature and how they can interact. A small section is also devoted to the interaction between light and metallic nanostructures, since this phenomenon will be exploited in Chap. 5. Once the tools for describing the

---

[3]Indeed, a complex system is "more than simply the sum of its parts".

systems of interest are known, the magnetic nanostructures have to be (i) fabricated and (ii) the expected features have to be investigated. Chapter 3 deals with both these tasks: the fabrication of nanostructures by means of electron beam lithography and their characterization through magneto-optical Kerr effect measurements. Since this latter technique has been fundamental for the development of my Ph.D. project, Chap. 2 is completely dedicated to the description of magneto-optical effects in matter and on how they can provide information on the magnetization, to understand what are the right quantities to be measured. Chapter 3 also contains a report on the main results obtained during a four-month research stay (September 2016 – December 2016) in the "Ultrafast Dynamics in Condensed Matter" group at Stockholm University (Sweden).

Geometrical frustration

The original results contained in this thesis are all connected to interacting magnetic nanostructures. A peculiar effect related to interactions is *frustration*, namely the inability of a physical system to simultaneously satisfy (i.e. energetically minimize) all the pairwise interactions within it. This definition means there can be various (non-trivial) configurations of the considered system which are associated to the same energy. When this happens, the system ground state results to be degenerate, leading to the appearance of interesting features, e.g. a finite value for the zero-point entropy. A classical example is given by the proton arrangement in water ice. Moreover, the same behaviour has been found in other condensed matter compounds, in particular regarding the atomic spin arrangement. These materials constitute the class of *spin ice systems*. Both in water ice and in spin ice systems, the frustration is determined by the geometrical arrangement of their building blocks, whence the name "*geometrical* frustration". The drawback of these systems is the fact that the interesting features introduced by frustration are fixed by the material: once you chose the compound, there is not too much you can do for systematically investigate the physics of frustration. However, in 2006 [3], a new class of metamaterials has been introduced: the *artificial spin ice systems*. They are two-dimensional realization of bulk spin ice systems that can be fabricated by electron beam lithography, since they basically are nothing else than arrays of interacting magnetic nanostructures. For artificial spin ice systems to properly work, the involved magnetic nanostructures should behave as magnetic needle, which is what we discussed in the previous section.

In this framework, Chap. 4 briefly introduces frustration and then it focuses on the development of artificial spin ice systems. The purpose of this chapter

is to summarize our efforts in trying to better describe and simulate the time evolution of artificial spin ice systems when *temperature* comes into play. Indeed, the heating of artificial spin ice systems is the key process possibly leading to the ground state formation. Depending on the parameters characterizing both the whole system and its building blocks, the ground state can finally be reached or not, since (i) the material, (ii) the nanostructure arrangement in the array, (iii) the nanostructure shape and (iv) the temperature do have an impact on the process. Hence, we took into account all these factors by designing a multiscale simulation scheme which could be able to combine micromagnetic simulations for the description of the thermal behaviour of magnetic nanostructures (hundreds of nanometers, tens of microseconds) with kinetic Monte Carlo calculations for considering the response of the whole system (tens of micrometers, hundreds of seconds). The results derived form our approach have been compared to data available in literature to check the validity of our arguments. Even if not strictly related to frustration, the competition in between magnetostatic interactions can also be exploited to explore the energy landscape of magnetic nanostructures beyond what achievable by a spatially uniform applied magnetic field. Chapter 6 collects all the simulations and experimental evidences related to how a properly designed chiral square unit formed by four nanostructures can induce the formation of a magnetization state which is energetically stable but impossible to obtain in an isolated nanostructure. Indeed, we were able to reproducibly bring a nanostructure designed to behave as a magnetic needle to a magnetic vortex state. This finding further stresses the essential role of magnetostatic interactions in between magnetic nanostructures.

Thermal activation

As discussed in the previous section, the heating of artificial spin ice systems is the fundamental process to be investigated. Besides the multiscale simulation scheme described in Chap. 4 and developed for simulating thermally activated processes, we also exploited the base knowledge of our research group (i.e. magnetism and plasmonics) for conceiving a non-standard heating technique for artificial spin ice systems: the selective and localized *thermoplasmonic heating* of magnetic nanostructures. The transfer of energy from an electromagnetic wave to a metallic nanostructure can be tremendously effective when the localized surface plasmon resonance is excited, whereas this transfer can be almost turned off when the nanostructure electron system is out of resonance. Moreover, at a fixed incident wavelength, the energy transfer can be modulated according to

the direction of linear polarization with respect to the nanostructure axes, since the resonance frequency depends on the axes aspect ratio (*heating selectivity*). Eventually, a great advantage of working with light beams is the fact that the sample area in which energy is delivered can be controlled by simply focusing or defocusing the beam itself, down to a diameter of 1 μm (*localized heating*).

In this framework, Chap. 5 describes the design and the fabrication of magnetic nanostructures which can be (i) part of an artificial spin ice system and (ii) effectively heated by the interaction with light. Both these requirements can be satisfied by elongated multilayer nanostructures, where Permalloy provides the needed magnetization and gold is a good plasmonic material. Since the nanostructures are elongated, it is possible to implement a certain degree of heating selectivity based on frequency and on the polarization direction. After having analyzed magnetically and optically non-interacting nanostructures, we also considered what happens when four nanostructures meet at a point, forming the vertex of a square artificial spin ice system. In particular, the four nanostructures are arranged (in pairs) along two perpendicular directions, meaning that the two nanostructures parallel to the polarization direction can be heated more efficiently than the other pair, thanks to the above-mentioned heating selectivity. Nonetheless, also the number of nanostructures per unit area (proportional to the filling factor) influences the final temperature, so care as to be taken when trying to apply the thermoplasmonic heating to artificial spin ice systems. The experimental realization of the elongated multilayer nanostructure not only involved their fabrication, but also the development of a thermoplasmonic heating stage to be combined with our magneto-optical Kerr effect setup. Indeed, through the measurement of the coercive field variation as a function of temperature, we have been able to track the temperature increase and to correlate it to both the axes aspect ratio and to the filling factor.

Contents

List of Figures

List of Tables

List of Symbols

Abbreviations

α-Si   Amorphous silicon

AR   Anti-reflection or aspect ratio, depending on the context

ASI   Artificial spin ice

BE   Bottom edge

cCDF   Complementary cumulative distribution function

CW   Continuous-wave

DMM   Dynamical matrix method

DMOKE   Diffracted magneto-optical Kerr effect

DVA   Double-vertex approximation

e-beam   Electron beam

EBL   Electron beam lithography

EM   Edge mode

FDM   Finite-difference method

FWHM   Full width at half maximum

GS   Ground state

kMC   Kinetic Monte Carlo

LLG   Landau–Lifshitz–Gilbert

LSP   Localized surface plasmon

MFM   Magnetic force microscopy

MOKE   Magneto-optical Kerr effect

NIR   Near-infrared

PEM   Photoelastic modulator

PMMA   Polymethyl methacrylate

Py   Permalloy ($Ni_{80}Fe_{20}$ alloy)

QU   Quasi-uniform

SEM   Scanning electron microscopy

sLLG   Stochastic Landau–Lifshitz–Gilbert

SVA   Single-vertex approximation

TE   Top edge

TMM   Transfer matrix method

XMCD   X-ray magnetic circular dichroism

Constants and Variables

ε_0 Permittivity of free space ($\varepsilon_0 = \dfrac{1}{\mu_0 c^2} \approx 8.854 \cdot 10^{-12}$ F $\cdot$ m^{-1})

γ Gyromagnetic ratio ($\approx 1.761 \cdot 10^{11}$ rad $\cdot$ s^{-1} $\cdot$ T^{-1} for an electron spin)

$\hbar$ Reduced Planck constant ($\hbar = \dfrac{h}{2\pi} \approx 1.055 \cdot 10^{-34}$ J $\cdot$ s)

μ_0 Permeability of free space ($4\pi \cdot 10^{-7}$ H $\cdot$ m^{-1})

μ_B Bohr magneton ($\approx 9.274 \cdot 10^{-24}$ A $\cdot$ m^2)

c Speed of light in vacuum (299 792 458 m $\cdot$ s^{-1})

e Electron charge magnitude ($\approx 1.602 \cdot 10^{-19}$ C)

h Planck constant ($\approx 6.626 \cdot 10^{-34}$ J $\cdot$ s)

k_B Boltzmann constant ($\approx 1.381 \cdot 10^{-23}$ J $\cdot$ K^{-1})

m Electron mass ($\approx 9.109 \cdot 10^{-31}$ kg), but also context-dependent mass

α Fine structure constant ($\alpha = \dfrac{e^2}{4\pi\varepsilon_0\hbar c} \approx 1/137.036$) or LLG damping constant, depending on the context

α_p Polarizability

$\boldsymbol{\chi}$ Dielectric susceptibility tensor

$\boldsymbol{\chi}_m$ Magnetic susceptibility tensor

$\boldsymbol{\varepsilon}$ Dielectric permittivity tensor

$\boldsymbol{\mu}$ Magnetic permeability tensor or magnetic moment, depending on the context

$\varepsilon_{F,K}$ Faraday or Kerr ellipticity, respectively

Γ Damping parameter of the considered system

κ Thermal conductivity

$\mathbb{R}, \mathbb{C}$ Real and complex numbers sets, respectively

$\hat{\mathbf{n}}$ Outward-pointing surface normal

$\hat{\mathbf{x}}, \hat{\mathbf{y}}, \hat{\mathbf{z}}$ Unit vectors along the Cartesian axes

$\mathbf{A}$ Vector potential

$\mathbf{B}$ Magnetic induction

$\mathbf{D}$ Electric displacement

$\mathbf{E}$ Electric field

$\mathbf{H}$ Magnetic field

$\mathbf{H}_C$ Coercive field (coercivity)

$\mathbf{I}$ Identity tensor

$\mathbf{J}$ Electric current density (per unit area)

$\mathbf{M}$ Magnetization (magnetic polarization)

$\mathbf{m}$ Vector whose components correspond to the direction cosines of $\mathbf{M}$ (i.e. $\mathbf{m} = \mathbf{M}/\mathrm{M}_S$)

$\mathbf{P}$ Electric polarization

$\mathbf{p}$	Electric dipole moment
$\mathcal{E}$	Energy density (per unit volume)
$\mathcal{H}$	Hamiltonian
$\mathcal{L}$	Lagrangian
$\mathcal{P}$	Power
$\mathcal{Z}$	Partition function
M_R	Remanent magnetization (remanence)
M_S	Saturation magnetization
ω_0	Resonance frequency of the considered system
ω_C	Cyclotron frequency
ω_p	Plasma frequency
ϕ	Scalar potential
$\Re(z), \Im(z)$	Real and imaginary parts of z, respectively
ρ	Electric charge density or mass density (per unit volume), depending on the context
ρ_m	Magnetic charge density (per unit volume)
σ_m	Magnetic charge density (per unit area)
σ_{abs}	Absorption cross section
σ_{ext}	Extinction cross section
σ_{sca}	Scattering cross section
ϑ_C	Critical angle
$\vartheta_{F,K}$	Faraday or Kerr rotation, respectively
A	Exchange stiffness
c_p	Specific heat capacity at constant pressure
D	Exposure dose, i.e. incident charge per unit area in EBL
E	Energy

g_S Spin g-factor

I Intensity

J Exchange constant

l_{ex} Exchange length

n Number of base units (atoms or electrons) per unit volume

Q_h Heat power

q_h Heat power density (per unit volume)

q_m Magnetic charge

R Reflectance

T Temperature or transmittance, depending on the context

T_b Blocking temperature

T_C Curie temperature

Z Atomic number

$\dot{\mathbf{r}}$ Derivative with respect to time: $\dfrac{d\mathbf{r}}{dt}$

$\ddot{\mathbf{r}}$ Second derivative with respect to time: $\dfrac{d^2\mathbf{r}}{dt^2}$

Chapter 1

Magnetism and Plasmonics

All the concepts reported in this thesis can be coarsely classified into the two broad fields appearing in this chapter's name: *magnetism* and *plasmonics*. Magnetism comes into play when the properties of interest have to do with magnetic fields, whereas plasmonics describes the interaction between metals and electric fields. A link between these two worlds is provided by Maxwell equations, in which the constitutive relations define the behaviour of matter when it is perturbed by an electromagnetic field. So, for the study of magnetism and plasmonics in condensed matter systems, the two relevant quantities to be considered are the magnetization $\mathbf{M}$ and the electric polarization $\mathbf{P}$, and the relevant phenomena are well described by the relation occurring between these quantities and the electromagnetic field. The chapter is then devoted to introduce the basic aspects of this relation needed to better understand the rest of the thesis.

1.1 Maxwell equations

The interaction of the electromagnetic field with matter (i.e. an ensemble of atoms) allows us to interpret almost all the phenomena related with the human daily experience and with technological achievements. From a theoretical point of view, so far there are only four *fundamental interactions* which do not appear to be reducible to more basic interactions. The *strong* and the *weak* interactions are of interest only when considering in detail the atomic nuclei and radioactive decay processes. The *gravitational* interaction governs the motion of massive objects and regulates the behaviour of our universe, but it can be neglected for electrons and atoms composing ordinary matter. Despite their fundamental value in terms of a deep knowledge of Nature, none of these interactions can explain

the stability of ordinary matter. For this purpose, the *electromagnetic interaction* has been identified, which describes the (long-range) interaction between electrically charged particles and provides the basis for chemical bondings. Once atoms are stable, they are kept together by electromagnetic forces. However, *electromagnetism* (i.e. the theory describing electromagnetic interactions) has to be considered inside the framework provided by *quantum mechanics* in order to obtain an effective description of reality. So, the ultimate theory of ordinary matter is called *quantum electrodynamics*. Anyway, as far as this thesis is concerned, it is enough to consider two key features part of this theory: *(classical) electrodynamics* and *quantum mechanics*.

Classical electrodynamics is based upon four equations, called *Maxwell equations* [5, 6]:

$$\boldsymbol{\nabla} \cdot \mathbf{D} \; = \; \rho, \tag{1.1a}$$

$$\boldsymbol{\nabla} \cdot \mathbf{B} \; = \; 0, \tag{1.1b}$$

$$\boldsymbol{\nabla} \times \mathbf{E} \; = \; -\frac{\partial \mathbf{B}}{\partial t}, \tag{1.1c}$$

$$\boldsymbol{\nabla} \times \mathbf{H} \; = \; \mathbf{J} \; + \; \frac{\partial \mathbf{D}}{\partial t}, \tag{1.1d}$$

where $\mathbf{D}$ is the *electric displacement*, $\mathbf{B}$ is the *magnetic induction*, $\mathbf{E}$ is the *electric field*, $\mathbf{H}$ is *the magnetic field*, $\mathbf{J}$ is the *electric current density* and ρ is the *electric charge density*. Equations (1.1) consist of a set of coupled first-order partial differential equations relating the various components of electric and magnetic fields. However, it is often convenient to introduce potentials for obtaining a smaller number of second-order equations, while satisfying some of the Maxwell equations identically. In this respect, the magnetic field $\mathbf{B}$ can be defined in terms of a *vector potential* $\mathbf{A}$:

$$\mathbf{B} \; = \; \boldsymbol{\nabla} \times \mathbf{A}, \tag{1.2}$$

whereas both $\mathbf{A}$ and a *scalar potential* ϕ are needed in order to define $\mathbf{E}$:

$$\mathbf{E} \; = \; -\boldsymbol{\nabla}\phi \; - \; \frac{\partial \mathbf{A}}{\partial t}. \tag{1.3}$$

It can be seen that the definitions (1.2) and (1.3) satisfies Eqs. (1.1b) and (1.1c), and so the dynamic behaviour of $\mathbf{A}$ and ϕ is determined by Eqs. (1.1a) and (1.1d), where the source terms are present. To be noted that all the scalar and vector quantities so far introduced are implicitly assumed to be dependent on position

$\mathbf{r}(t)$ and time t.

To allow for a unique determination of the vector fields from a given distribution of electric currents and charges, the Maxwell equations must be supplemented by relations (called *constitutive relations*) describing the behaviour of matter under the influence of the electromagnetic field [6]:

$$\mathbf{D} \;=\; \boldsymbol{\varepsilon}\mathbf{E} \;=\; \varepsilon_0\mathbf{E} \;+\; \mathbf{P}, \tag{1.4a}$$

$$\mathbf{B} \;=\; \boldsymbol{\mu}\mathbf{H} \;=\; \mu_0\left(\mathbf{H} \;+\; \mathbf{M}\right), \tag{1.4b}$$

$$\mathbf{J} \;=\; \boldsymbol{\sigma}\mathbf{E}. \tag{1.4c}$$

The *electric polarization* $\mathbf{P}$ is related to the electric field by means of the *dielectric susceptibility tensor* $\boldsymbol{\chi}$ (i.e. $\mathbf{P} = \varepsilon_0\boldsymbol{\chi}\mathbf{E}$), which allows introducing the *dielectric permittivity tensor* $\boldsymbol{\varepsilon} = \varepsilon_0(\mathbf{I}+\boldsymbol{\chi})$. The *magnetization* $\mathbf{M}$ is related to the magnetic field by means of the *magnetic susceptibility tensor* $\boldsymbol{\chi}_m$ (i.e. $\mathbf{M} = \boldsymbol{\chi}_m\mathbf{H}$), which allows introducing the *magnetic permeability tensor* $\boldsymbol{\mu} = \mu_0(\mathbf{I}+\boldsymbol{\chi}_m)$. The tensor $\boldsymbol{\sigma}$ is the *conductivity tensor*: the susbstances characterized by negligibly small components of $\boldsymbol{\sigma}$ are called *dielctrics*, whereas sizeable components of $\boldsymbol{\sigma}$ identify *semiconductors* and *conductors*. Stated in this form, Eqs. (1.4) express the linear relationship occurring between $\mathbf{D}$ and $\mathbf{E}$, $\mathbf{B}$ and $\mathbf{H}$, $\mathbf{J}$ and $\mathbf{E}$. However, if the fields are exceptionally strong [6, 7], $\mathbf{D}$, $\mathbf{B}$ and $\mathbf{J}$ may have to be supplemented by terms involving components of the field vectors in power higher than the first.

The classical equation of motion for a charged particle is given by the *Lorentz force equation*:

$$\mathbf{F} \;=\; q\left(\mathbf{E} \;+\; \mathbf{v}\times\mathbf{B}\right), \tag{1.5}$$

which expresses the force $\mathbf{F} = m\ddot{\mathbf{r}}$ acting on a point charge q with mass m and velocity $\mathbf{v} = \dot{\mathbf{r}}$ in the presence of an electromagnetic field. Equation (1.5) can be obtained by applying the Euler-Lagrange equations to the following non-relativistic Lagrangian $\mathcal{L}$ [5, 8]:

$$\mathcal{L}(\mathbf{r},\dot{\mathbf{r}}) \;=\; \frac{1}{2}m\dot{\mathbf{r}}^2 \;+\; q\left[\dot{\mathbf{r}}\cdot\mathbf{A}(\mathbf{r},t) - \phi(\mathbf{r},t)\right]. \tag{1.6}$$

The *canonical* momentum derived from this Lagrangian is $\mathbf{p} = m\dot{\mathbf{r}} + q\mathbf{A}(\mathbf{r},t)$, and so the corresponding Hamiltonian $\mathcal{H}$ is given by the Legendre transform of Eq. (1.6) [9]:

$$\mathcal{H}(\mathbf{r},\mathbf{p}) \;=\; \left(\sum_j r_j p_j\right) - \mathcal{L}(\mathbf{r},\dot{\mathbf{r}}) \;=\; \frac{1}{2m}\left[\mathbf{p} - q\mathbf{A}(\mathbf{r},t)\right]^2 \;+\; q\phi(\mathbf{r},t). \tag{1.7}$$
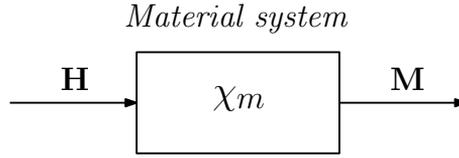
Material system

Figure 1.1: Block diagram outlining the action of a magnetic field **H** on a material system.

1.2   The appearance of magnetism

In condensed matter, *magnetism* can be defined as the property of a given substance to respond to an external magnetic field. Borrowing the schematic in Fig. 1.1 from linear system theory, the magnetic field **H** constitutes the input for the system (the considered material) and the resulting output (the response) is given by the magnetization **M** (i.e. a net magnetic dipole moment per unit volume). As stated by Eq. (1.4b) and detailed in the discussion below it, the corresponding transfer function is represented by the magnetic susceptibility tensor $\boldsymbol{\chi}_m$:

$$\mathbf{M} \;=\; \boldsymbol{\chi}_m \mathbf{H}. \tag{1.8}$$

In case of an isotropic body, $\boldsymbol{\chi}_m$ reduces to a scalar (χ_m) and its value allows classifying the various material into categories [10,11]:

- **diamagnetic materials**, for which $\chi_m < 0$ and $|\chi_m| \ll 1$;

- **paramagnetic** and **antiferromagnetic materials**, for which $\chi_m > 0$ and $|\chi_m| \ll 1$;

- **ferromagnetic** and **ferrimagnetic materials**, for which $\chi_m > 0$ and $|\chi_m| \gg 1$.

Considering ferromagnets (i.e. ferromagnetic materials), the relation between the applied field and the magnetization is no longer well represented by a one-to-one linear correspondence through a constant parameter χ_m, but the specification of a *hysteresis loop* is required, and so χ_m itself becomes a function of **H**. This *irreversible*, *non-linear* response of an infinite ferromagnetic body to an applied magnetic field depends on the structure of the measured specimen and on the past magnetic and thermal history. Moreover, hysteresis leads to the fact that a ferromagnet can show a spontaneous net magnetization (*remanent magnetization* M_R) even in the absence of an applied magnetic field. Whereas M_R depends on the structure of the hysteresis loop, the *saturation magnetization* M_S is an intrinsic property of the material: it represents the maximum magnetization value that

can be reached by applying a high enough magnetic field (a process called *saturation*). However, all the ferromagnetic materials become regular paramagnets at a temperature above the so-called *Curie temperature* T_C and, as such, they have a non-zero net magnetization only in the presence of an external applied field and the linear relation (1.8) is recovered.

The materials considered during the development of the Ph.D. project here presented are all ferromagnetic metals: iron (Fe), cobalt (Co), nickel (Ni) and Permalloy, a $Ni_{80}Fe_{20}$ alloy (Py). The next sections will be devoted to the description of the magnetic properties of such materials. To understand the phenomenon of magnetism one might be tempted to develop a completely classical description, which could be a useful limit of an underlying quantum-mechanical theory. However, it turns out that magnetism is incomprehensible within the framework of an *exact* classical theory based on the behaviour of moving electrons, a framework that has been successfully used to build the Drude model for metals. To inspect this fact, we can write the Hamiltonian (1.7) for a system of N electrons of charge $-e$ and mass m immersed in a magnetic field specified by the vector potential $\mathbf{A}$:

$$\mathcal{H} \; = \; \frac{1}{2m} \sum_{j=1}^{N} \left(\mathbf{p}_j + e\mathbf{A}_j \right)^2 \; + \; V\left(\mathbf{r}_1, \cdots, \mathbf{r}_N \right). \tag{1.9}$$

The potential V represents the interaction potential between the N electrons and $\mathbf{A}_j = \mathbf{A}(\mathbf{r}_j)$. The classical *partition function* $\mathcal{Z}$ is given by

$$\mathcal{Z} \; = \; \int \exp\left(-\beta\mathcal{H} \right) d\mathbf{r}_1 \cdots d\mathbf{r}_N d\mathbf{p}_1 \cdots d\mathbf{p}_N, \tag{1.10}$$

where $\beta = 1/(k_B T)$. It is now important to note that the integration in Eq. (1.10) goes from $-\infty$ to ∞ for all the integration variables. With the substitutions $\boldsymbol{\rho}_j = \mathbf{r}_j$ and $\boldsymbol{\mu}_j = \mathbf{p}_j + e\mathbf{A}_j$ $(\forall j)$, the partition function becomes[1]

$$\mathcal{Z} \; = \; \int \exp\left[-\beta V - \frac{\beta}{2m} \sum_{j=1}^{N} \boldsymbol{\mu}_j^2 \right] d\boldsymbol{\rho}_1 \cdots d\boldsymbol{\rho}_N d\boldsymbol{\mu}_1 \cdots d\boldsymbol{\mu}_N, \tag{1.11}$$

where all the integration limits are still $-\infty$ to ∞. Hence $\mathcal{Z}$ is independent from $\mathbf{A}$ (and so from $\mathbf{H}$), whence the magnetization $\mathbf{M}$, which is thermodynamically

---

[1]In the integration by substitution leading to Eq. (1.11), the following property helps in transforming the differentials:

$$\det \begin{bmatrix} A & 0 \\ C & B \end{bmatrix} \; = \; \det \begin{bmatrix} A & C \\ 0 & B \end{bmatrix} \; = \; \det(A)\det(B),$$

where A, B and C are $n \times n$ matrices.

given by

$$\mathbf{M} \;=\; k_B T \frac{\partial}{\partial \mathbf{H}} \ln \mathcal{Z}, \tag{1.12}$$

vanishes. This result is known as the *Bohr–van Leeuwen theorem* [12,13]: within the framework provided by classical mechanics, a system of moving electrons cannot respond to an applied field $\mathbf{H}$ by developing a net magnetization $\mathbf{M}$, no matter what the actual motion of the electrons is. The limit of a pure classical description can be overcome by the use of quantum-mechanical concepts. For example, classical electrons cannot move in a circular orbit around the atomic nucleus without radiating their energy and collapsing into the center. However, the circular orbits permitted by the *Bohr model* allows having a semi-classical theory of diamagnetism [12], a phenomenon occurring in any material system.

1.2.1   The Dirac Hamiltonian

In any case, a satisfactory theory of magnetism in ferromagnetic metals have to deal with all the prescriptions imposed by quantum mechanics. A complete picture can be obtained through the Dirac Hamiltonian, and then useful information can be extracted by suitable simplifications. The Stern–Gerlach experiment (1921) and its interpretation by Goudsmit and Uhlenbeck (1925) introduced a new intrinsic degree of freedom for the electron, namely the *electron spin* $\mathbf{S}$. This quantity behaves like an angular momentum with quantum number $s = 1/2$ and so its expectation value S_z along the quantization direction (usually identified with the z-axis) can only take the two values $S_z = \pm\hbar/2$. A magnetic moment $\boldsymbol{\mu}_S$ is associated to the electron spin through the relation

$$\boldsymbol{\mu}_S \;=\; -g_S \mu_B \left(\frac{\mathbf{S}}{\hbar} \right), \tag{1.13}$$

where g_S is the *spin g-factor* and $\mu_B = e\hbar/(2m)$ is the *Bohr magneton* (expressing the natural unit for atomic magnetic moments). In this respect, electrons can interact with a magnetic field not only by their motion but also through $\boldsymbol{\mu}_S$.

The behaviour of an electron (massive spin-1/2 particle with $-e$ charge) in the presence of an electromagnetic field $(\mathbf{A}, \phi)$ can be described by the *Dirac Hamiltonian* [14]:

$$\mathcal{H} \;=\; c\boldsymbol{\alpha} \cdot (-i\hbar\boldsymbol{\nabla} + e\mathbf{A}) \;-\; e\phi \;+\; \beta mc^2, \tag{1.14}$$

where

$$\boldsymbol{\alpha} = \begin{bmatrix} 0 & \boldsymbol{\sigma} \\ \boldsymbol{\sigma} & 0 \end{bmatrix}, \qquad \beta = \begin{bmatrix} \mathbf{I} & 0 \\ 0 & -\mathbf{I} \end{bmatrix}, \qquad \mathbf{I} = \begin{bmatrix} 1 & 0 \\ 0 & 1 \end{bmatrix},$$

$$\sigma_1 = \begin{bmatrix} 0 & 1 \\ 1 & 0 \end{bmatrix}, \qquad \sigma_2 = \begin{bmatrix} 0 & -i \\ i & 0 \end{bmatrix}, \qquad \sigma_3 = \begin{bmatrix} 1 & 0 \\ 0 & -1 \end{bmatrix},$$

and $\mathbf{S} = \hbar\boldsymbol{\sigma}/2$, making use of Pauli matrices. The wave functions associated to the Dirac Hamiltonian are *four-component spinors*, since 4×4 are the minimum dimensions for the matrices $\boldsymbol{\alpha}$ and β in order to satisfy all the conditions imposed by Dirac during the derivation of his Hamiltonian [14]. So, four components can accommodate the description of a particle and an antiparticle, each one of spin $1/2$. For low energies (compared with the electron's rest mass), the Dirac Hamiltonian can be expanded in series, where the parameter governing the expansion is $p/(mc)$, and the most relevant terms for this thesis are:

$$\mathcal{H} = \frac{1}{2m}\left(-i\hbar\boldsymbol{\nabla} + e\mathbf{A}\right)^2 - e\phi + \frac{2\mu_B}{\hbar}\mathbf{S}\cdot(\boldsymbol{\nabla}\times\mathbf{A}) + \frac{ie\hbar}{2m^2c^2}\mathbf{S}\cdot(\boldsymbol{\nabla}\phi\times\boldsymbol{\nabla}). \quad (1.15)$$

The first three terms in Eq. (1.15) constitute the *non-relativistic* limit of the Dirac Hamiltonian (called *Pauli Hamiltonian*), whereas the last term gives rise to the *spin-orbit interaction* in case we are considering atomic electrons. To be noted that the non-relativistic limit of the Dirac Hamiltonian already contains the spin operator, whereas the spin-orbit interaction is a relativistic correction to the Pauli Hamiltonian. Moreover, comparing Eq. (1.15) with Eq. (1.13), the Dirac theory predicts that $g_S = 2$, in good agreement with experiments (neglecting small corrections coming from quantum electrodynamics). For a one-electron atom with atomic number Z, $\phi(\mathbf{r}) = Ze/(4\pi\varepsilon_0 r)$ is spherically symmetric and Eq. (1.15) becomes

$$\mathcal{H} = -\frac{\hbar^2}{2m}\nabla^2 - \frac{Ze^2}{4\pi\varepsilon_0 r} + \xi_{SO}(r)\mathbf{S}\cdot\mathbf{L}$$
$$+ \frac{\mu_B}{\hbar}\mathbf{B}\cdot(\mathbf{L}+2\mathbf{S}) + \frac{e^2}{8m}\left(\mathbf{B}\times\mathbf{r}\right)^2, \quad (1.16a)$$

$$\xi_{SO}(r) = \frac{1}{2m^2c^2}\frac{Ze^2}{4\pi\varepsilon_0}\frac{1}{r^3}, \quad (1.16b)$$

where we made use of the fact that $\mathbf{L} = -i\hbar(\mathbf{r}\times\boldsymbol{\nabla})$ is the orbital angular momentum of the electron (with quantum number l) and we considered an applied uniform magnetic field $\mathbf{H} = \mathbf{B}/\mu_0$, for which $\mathbf{A} = (\mathbf{B}\times\mathbf{r})/2$ and $\boldsymbol{\nabla}\cdot\mathbf{A} = 0$ [14].

The spin-orbit interaction term can then be seen as the energy of the spin magnetic moment immersed in the magnetic field produced by the electron's motion around the nucleus. As shown by Eq. (1.16b), the weight of this term increases along with the atomic number Z of the considered element. The expectation value of the first two terms of Eq. (1.16a) (kinetic and Coulomb interaction energies) is

$$E_n \;=\; -\frac{1}{2}mc^2\frac{(Z\alpha)^2}{n^2}, \tag{1.17}$$

where $\alpha \approx 1/137.036$ is the *fine structure constant* and $n = 1, 2, \ldots$ is the *principal quantum number*. The expectation value of the energy splitting ΔE_{SO} determined by the spin-orbit interaction is given by

$$\Delta E_{SO} \;=\; |E_n|\left[\frac{(Z\alpha)^2}{nl\,(l+1)}\right], \tag{1.18}$$

which is valid for $l \neq 0$. Considering a $3d$ orbital for a one-electron atom with $Z = 26$, $\Delta E_{SO}/|E_n| \approx 2 \cdot 10^{-3}$. The term linear in $\mathbf{B}$ in Eq. (1.16a), namely

$$\frac{\mu_B}{\hbar}\mathbf{B} \cdot (\mathbf{L} + 2\mathbf{S})\,, \tag{1.19}$$

is called the *paramagnetic term*, because it induces the alignment of magnetic moments in an external magnetic field (paramagnetism). From this term, it is possible to define the orbital magnetic moment $\boldsymbol{\mu}_L$, as we did in Eq. (1.13) for the spin:

$$\boldsymbol{\mu}_L \;=\; -\mu_B\left(\frac{\mathbf{L}}{\hbar}\right). \tag{1.20}$$

1.2.2   The exchange interaction and the Heisenberg model

By considering isolated one-electron atoms, we are missing a key ingredient: ferromagnetism is a many-body effect. Current theories are the evolution of basic concepts postulated by Weiss in 1906 [15]. He assumed that there was a certain *internal* (or *molecular*) *field* proportional to the net magnetization in ferromagnetic materials which tries to align the neighbouring atomic magnetic moment, stabilizing their parallel orientation against the disordering effect of thermal fluctuations. In fact, ordinary applied magnetic fields are unable to compete against interatomic energies and temperatures of the order of 1 K are sufficient to destroy any order established by the interactions of atomic magnetic moments (for reference, consider that $k_B/\mu_B \approx 1.489$ T $\cdot$ K^{-1}). However, the origin of Weiss molecular field had to wait the advent of quantum mechanics in

order to find a proper interpretation. Once the spin has been identified as the fundamental character in the previous sections, we have to inspect the way this degree of freedom impact the behaviour of an ensemble of atoms constituting an actual material. In order to do so, we will closely follow the argument developed by Skomski [16], summarizing just the main results.

The simplest description is provided by a two-atom system, each one of them possessing one electron. The starting point is the *Pauli principle*, which forbids the double occupancy of a quantum state by *fermions* (i.e. particles with half-integer spin). Since the spin is associated to a quantum number, double occupancy of an orbital is possible for antiparallel spins (antiferromagnetic configuration, ↑↓) but forbidden for parallel spins (ferromagnetic configuration, ↑↑). To realize a parallel spin orientation, one electron must occupy an excited one-electron orbital. The necessary energy comes from the Coulomb interaction

$$V_C(\mathbf{r}, \mathbf{r}') \; = \; \frac{e^2}{4\pi\varepsilon_0 \, |\mathbf{r} - \mathbf{r}'|} \tag{1.21}$$

between two electrons at $\mathbf{r}$ and $\mathbf{r}'$. The Coulomb interaction is spin-independent but larger for electrons in a common orbital (↑↓) than for electrons in different orbitals (↑↑). In other words, the Coulomb interaction favours parallel spin alignment since it competes against an increase in one-electron energy.

Taking into account the Pauli principle for a system composed by two electrons and two atomic sites (L and R), the *exchange constant J* is given by [16]:

$$J \; = \; \frac{E_{\uparrow\downarrow} - E_{\uparrow\uparrow}}{2} \; = \; J_D \; + \; \frac{U}{4} \; - \; \sqrt{t^2 + \frac{U^2}{16}}. \tag{1.22}$$

The energy J can be used to define the *exchange interaction*. This apparently simple expression actually contains a lot of physical insight and it deserves a detailed explanation. The *Bethe-Slater curve* [10,16], which predicts the emergence of ferromagnetism in Fe, Co and Ni in terms of the distance between neighbouring atoms, can be qualitatively fitted by Eq. (1.22). The energies $E_{\uparrow\downarrow}$ and $E_{\uparrow\uparrow}$ represent the energies of the antiferromagnetic and ferromagnetic configurations, respectively: when $J > 0$, a ferromagnetic order is favoured over an antiferromagnetic configuration. Regarding the last equality in Eq. (1.22), U represents the Coulomb integral

$$U \; = \; \iint \Phi_L^*(\mathbf{r})\Phi_L^*(\mathbf{r}')V_C(\mathbf{r}, \mathbf{r}')\Phi_L(\mathbf{r})\Phi_L(\mathbf{r}')dV\,dV' \tag{1.23}$$

and J_D is the direct exchange integral

$$J_D \;=\; \iint \Phi_L^*(\mathbf{r})\Phi_R^*(\mathbf{r}')V_C(\mathbf{r},\mathbf{r}')\Phi_R(\mathbf{r})\Phi_L(\mathbf{r}')dV\,dV'. \qquad (1.24)$$

The Coulomb integral describes the strong repulsion between two electrons in an atom and it is equal to the energy needed to add an electron to an already occupied localized orbital. By comparison, the direct exchange has no classical equivalent. Typical orders of magnitude are a few 0.01 eV for J_D and a few eV for U, so $J_D \ll U$. Finally, t is the *hopping integral* and it is associated to the hopping of an electron from an atom to the neighbouring one thanks to the effect of the kinetic-energy operator. The considered wave functions in the integrals of Eqs. (1.23) and (1.24) are *Wannier functions*, i.e. orthogonal wave functions for a two-electron system which are well localized around a given atom (L or R in this case). In conclusion, the balance between U, J_D and t in Eq. (1.22) determines the ground state of the two-electron system, and the Pauli principle applied to the resulting wave function dictates the spin configuration ($\uparrow\downarrow$ or $\uparrow\uparrow$).

The relative weight of U, J_D and t in Eq. (1.22) allows defining various approximate models. The *Heisenberg model* considers the electrons as localized around the atom it belongs to and, as such, this model works best for well-separated atoms, where the number of electrons per atom is fixed. In terms of Eq. (1.23), the electron localization can be imposed by considering $U \to \infty$ and Eq. (1.22) turns out to be [16]

$$J \;\approx\; J_D\left(1 - \frac{2t^2}{J_D U}\right). \qquad (1.25)$$

This equation can be used to explain the sign of the exchange: the direct exchange J_D is ferromagnetic, but hopping yields an antiferromagnetic contribution. More generally, it is possible to define the Heisenberg model in terms of the *Heisenberg Hamiltonian*:

$$\mathcal{H} \;=\; -\frac{2}{\hbar^2}\sum_{i>j} J_{ij}\mathbf{S}_i \cdot \mathbf{S}_j \;-\; \frac{g_S \mu_B}{\hbar}\sum_i \mathbf{S}_i \cdot \mu_0 \mathbf{H}_i, \qquad (1.26)$$

where the summation includes all the atomic spins and $\mathbf{H}_i$ is the local magnetic field acting on the i-th spin. From a quantum-mechanical point, Eq. (1.26) is an approximation, but the model works surprisingly well for a broad range of materials and phenomena. The exchange constants J_{ij}, which are of the form (1.25), relates any pair of spins (i,j) and, in practice, they are often treated as phenomenological parameters. The most usual assumption is to consider the exchange integral to be effectively different from zero only between nearest-

neighbour atoms, taking a common value $J_{ij} \approx J$ $(\forall i, j)$. Combining statistical mechanics with a mean-field approach [12, 17], J can be related to the Curie temperature T_C:

$$J \;=\; \frac{3}{2pS\,(S+1)}k_B T_C, \tag{1.27}$$

where p is the number of nearest neighbours and S is the total spin quantum number. For body-centered cubic iron, the Curie temperature is 1043 K, $p = 8$ and we can consider $S = 1$ [17], so $J \approx 8.4$ meV. To have an idea of the strength of the exchange interaction, the magnitude of the magnetic induction needed in order to have the same interaction energy with a magnetic moment μ_B is $B = J/\mu_B \approx 146$ T.

1.2.3   The itinerant electron magnetism

Even if the obtained values are of the right order of magnitude for iron, the Heisenberg model is not the most appropriate model for metals. A better description can be obtained by considering the weak-correlation limit (*independent-electron approximation*), for which $U \to 0$. The wave functions to be considered represent delocalized states, and again the Pauli principle has to be respected. Treating U and J_D as small perturbations, the exchange constant J turns out to be [16]

$$J \;\approx\; \frac{U}{4} \;+\; J_D \;-\; |t|\,. \tag{1.28}$$

Consistently with previous findings, interatomic hopping destroys ferromagnetic spin alignment. Since J_D and $|t|$ decrease with increasing interatomic distance but U remains constant, Eq. (1.28) predicts ferromagnetism above some interatomic distance. Considering that $J_D \ll U$, in the end the phenomenon is regulated by a competition between Coulomb repulsion and interatomic hopping. The independent-electron approximation works best for transition-metal elements and alloys, such as iron, cobalt and nickel. These materials exhibit pronounced interatomic hopping and are often conductors with delocalized wave functions. The considered approximation is the basis for the treatment of the *itinerant electron magnetism* [13, 16].

In a simple one-electron picture, the electrons fill the available delocalized states until the Fermi level is reached. Non-magnetic metals have two equally populated $\uparrow$ and $\downarrow$ sub-bands. In *Pauli paramagnetism*, an applied magnetic field transfers a few electrons from (e.g.) the $\downarrow$ band to the $\uparrow$ band. This results in a linear response of the magnetization as a function of the applied magnetic field. For ferromagnetic metals, the energy (1.28) translates into an effective exchange

field, which determines the transfer of electrons from one sub-band to the other without the need of an applied magnetic field (*exchange splitting effect*). The *Stoner criterion*, derived from the *band structure* of metals, allows predicting the onset of ferromagnetism by knowing the density of states $D(E_F)$ at the Fermi level:

$$UD\left(E_F\right) \, > \, 1. \tag{1.29}$$

As we have seen in the previous paragraph, the hopping energy ($|t| \approx 1/D(E_F)$) competes against U and Eq. (1.28) predicts ferromagnetism for $U/4 + J_D > |t|$, in close analogy to the Stoner criterion.

1.3   The micromagnetic theory

Passing from an isolated one-electron atom to an ensemble of many-electron atoms makes the description way more precise, but the equations governing the system become too difficult to be exactly solved. As far as ferromagnetism is concerned, an ensemble of many-electron atoms can be seen as an ensemble of interacting elementary magnetic moments $\boldsymbol{\delta\mu}_j$, for both localized and itinerant electron magnetism. Then, the interactions give rise to energy terms which concur in determining the equilibrium configuration of any ferromagnetic body. By identifying an appropriate size scale, a *local magnetization* $\mathbf{M(r)}$ can be introduced [11]:

$$\mathbf{M(r)} \, = \, \frac{\sum_j \boldsymbol{\delta\mu}_j}{\delta V_{\mathbf{r}}}. \tag{1.30}$$

The local magnetization represents the average magnetic moment contained in a volume $\delta V_{\mathbf{r}}$ centered at $\mathbf{r}$. Such a volume has to be small enough to allow a *continuous medium approximation*, but it has to contain enough elementary moments in order to make $\mathbf{M(r)}$ a well-defined statistical quantity. Moreover, the local magnetization provides a connection with Maxwell equations, since this is the quantity to be used in Eq. (1.4b). All these considerations led to the development of the *micromagnetic theory* (or *micromagnetics*) [12,18]. For simplifying the notation, the spatial dependence of $\mathbf{M}$ will be shown only in case of ambiguities.

Micromagnetics deals with the *total (Gibbs) free energy* E_{tot} [19]:

$$E_{tot} \, = \, E_Z \, + \, E_{ex} \, + \, E_{mc} \, + \, E_{ms}. \tag{1.31}$$

The *Zeeman energy* E_Z is the interaction energy between a magnetized volume

V and the applied magnetic field $\mathbf{H}$:

$$E_Z \;=\; -\mu_0 \int_V \mathbf{M} \cdot \mathbf{H} d\mathbf{r}. \tag{1.32}$$

The term E_{ex} represents the *exchange energy* in the continuous medium approximation:

$$E_{ex} \;=\; \int_V A \left(|\boldsymbol{\nabla}\mathrm{m}_x|^2 + |\boldsymbol{\nabla}\mathrm{m}_y|^2 + |\boldsymbol{\nabla}\mathrm{m}_z|^2 \right) d\mathbf{r}, \tag{1.33}$$

where the *exchange stiffness* $A \propto J$ describes the local strength of the exchange interaction and $\mathbf{m}(\mathbf{r}) = \mathbf{M}(\mathbf{r})/\mathrm{M}_S$. The saturation magnetization M_S represents the magnitude of $\mathbf{M}(\mathbf{r})$, so $\mathbf{m}(\mathbf{r})$ is a unitary vector. Eventually, the terms E_{mc} and E_{ms} are the *magnetocrystalline anysotropy energy* and the *magnetostatic energy*, respectively, and they will be described in the next two sections.

1.3.1 Magnetocrystalline anisotropy

The magnetocrystalline anisotropy is mainly due to spin-orbit coupling. Through the coupling between the spin and the orbital motion of electrons, when an external magnetic field tries to reorient the spin, the orbit also tend to be reoriented, but, since the orbit is strongly coupled to the lattice, it resists the attempt to rotate the spin direction. The symmetry of the lattice determines crystallographic directions (*easy axes*) along which the spin system aligns at equilibrium. In the continuous medium approximation, this translates to the fact that to rotate the magnetization away from the easy axes costs energy. In the case of a cubic crystal, the *magnetocrystalline anisotropy energy density* $\mathcal{E}_{mc}$ can be expressed as a series expansion of the direction cosines α_1, α_2, α_3 of the magnetization relatively to the crystal axes:

$$\mathcal{E}_{mc} \;=\; K_0 \;+\; K_1 \left(\alpha_1^2\alpha_2^2 + \alpha_2^2\alpha_3^2 + \alpha_3^2\alpha_1^2 \right) \;+\; K_2 \left(\alpha_1^2\alpha_2^2\alpha_3^2 \right) \;+\; \cdots, \tag{1.34}$$

where $K_0, K_1, K_2, \ldots$ are the anisotropy constants, which are given for a particular material at a particular temperature and can be a function of the position. The magnitude and the sign of the significant anisotropy constants determine what directions are easy axes. In the case of *uniaxial anisotropy*, which can be found in hexagonal crystals (like cobalt), the energy density is a function of a single angle ϑ:

$$\mathcal{E}_{mc} \;=\; K_0 \;+\; K_1 \sin^2 \vartheta \;+\; K_2 \sin^4 \vartheta \;+\; \cdots. \tag{1.35}$$

Depending on the relative value and the sign of the anisotropy constants, there can be an easy axis of magnetization, an easy basal plane of magnetization or an easy cone of magnetization. The magnetocrystalline anisotropy energy considered in Eq. (1.31) can be obtained by integrating the relative energy density over the volume V of the sample:

$$E_{mc} = \int_V \mathcal{E}_{mc} d\mathbf{r}. \tag{1.36}$$

1.3.2   Shape anisotropy

The magnetostatic energy originates from the interaction among the elementary magnetic moments which constitute a ferromagnet: being the analogous of the electrostatic energy for electric charges, it represents the energy contribution coming from the fact that each magnetic moment is immersed in the magnetic field $\mathbf{H}_d$ created by the surrounding magnetic moments (i.e. the *demagnetizing field*). For a specimen with magnetization $\mathbf{M}$, the magnetostatic energy E_{ms} can be evaluated as [12]

$$E_{ms} = -\frac{\mu_0}{2} \int_V \mathbf{M} \cdot \mathbf{H}_d d\mathbf{r}, \tag{1.37}$$

where the integration is over the volume V of the sample. The effect of this energy term is mainly to define the magnetic microstructure of an extended ferromagnetic body, but it can also be a source of anisotropy in small particles: the magnetostatic energy depends on the direction of the magnetization because the *shape* of the particle contributes in determining the field produced by the magnetization itself.

In the case of an ellipsoidal particle with uniform magnetization $\mathbf{M}$, the field $\mathbf{H}_d$ can be expressed as

$$\mathbf{H}_d = -\mathfrak{N}_d\mathbf{M}, \tag{1.38}$$

where $\mathfrak{N}_d$ is the *demagnetizing tensor*, characterized by a unitary trace. When the Cartesian coordinates are chosen along the principal axes of the ellipsoid, the energy density extracted from Eq. (1.37) becomes

$$\mathcal{E}_{ms} = \frac{\mu_0}{2} \left(N_x \mathrm{M}_x^2 + N_y \mathrm{M}_y^2 + N_z \mathrm{M}_z^2 \right). \tag{1.39}$$

The quantities N_x, N_y and N_z are called *demagnetizing factors* and, for a spherical particle, it turns out that $N_x = N_y = N_z = 1/3$. If the ellipsoid has two axes

(a) Prolate spheroid   (b) Oblate spheroid
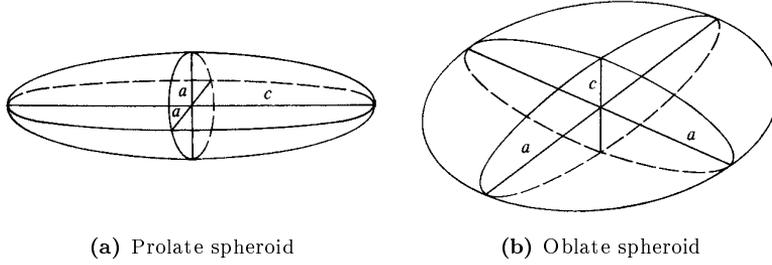
Figure 1.2: Ellipsoids. Adapted from Ref. [10].

of equal length a (see Fig. 1.2), the magnetostatic energy density is given by

$$
\begin{aligned}
\mathcal{E}_{ms} &= \frac{\mu_0}{2}\left[N_c\left(\mathrm{M}\cos\vartheta\right)^2 \ + \ N_a\left(\mathrm{M}\sin\vartheta\right)^2 \right] \\
&= \frac{\mu_0}{2}N_c\mathrm{M}^2 \ + \ \frac{\mu_0}{2}\left(N_a - N_c\right)\mathrm{M}^2\sin^2\vartheta,
\end{aligned}
\tag{1.40}
$$

where ϑ is the angle between the magnetization $\mathbf{M}$ and the third axis of length c. The quantities N_a and N_c are the demagnetizing factors of the corresponding axes, whose values depend on the ratio between c and a, but in general $N_c < N_a$ if $c > a$ (prolate spheroid) and the direction $\vartheta = 0$ is an easy axis. This expression for the magnetostatic energy density has an angle-dependent term of exactly the same form as in the uniaxial magnetocrystalline anisotropy energy density. For a general ellipsoid, the demagnetizing factors can be calculated according to the formulas given by Osborn [10, 20], which have simple analytical expressions for the cases depicted in Fig. 1.2:

- considering $m = c/a > 1$ for a prolate spheroid, then

$$
N_c = \frac{1}{m^2 - 1}\left[\frac{m}{\sqrt{m^2 - 1}}\ln\left(m + \sqrt{m^2 - 1} \right) - 1 \right],
\tag{1.41a}
$$

$$
N_a = \frac{1 \ - \ N_c}{2}.
\tag{1.41b}
$$

- considering $m = a/c > 1$ for an oblate spheroid, then

$$
N_a = \frac{1}{2\left(m^2 - 1\right)}\left[\frac{m^2}{\sqrt{m^2 - 1}}\arcsin\left(\frac{\sqrt{m^2 - 1}}{m} \right) - 1 \right],
\tag{1.42a}
$$

$$
N_c = 1 \ - \ 2N_a.
\tag{1.42b}
$$

In both cases, N_a and N_c only depend on the *aspect ratio m*, a statement which
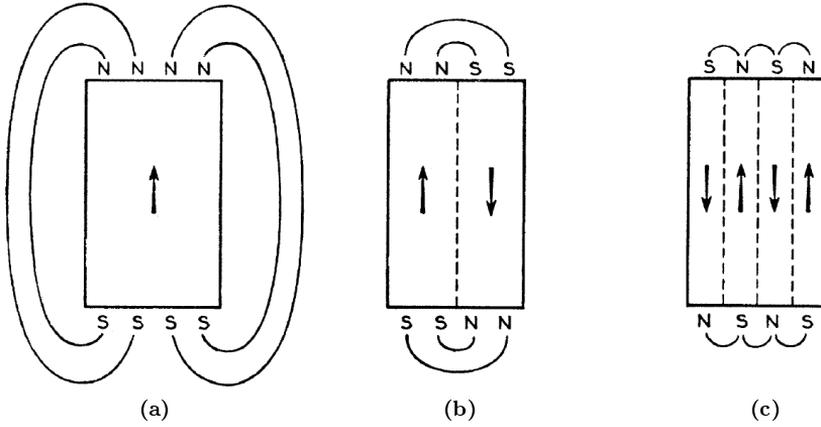
Figure 1.3: Schematic diagrams showing the emergence of magnetic domains from (a) to (c): according to the pole avoidance principle, the configuration depicted in (c) is characterized by lower magnetostatic energy than the ones in (a) and (b). In any case, the whole domain structure of a specimen is governed by the total free energy expressed by Eq. (1.31). Adapted from [22].

is true in general.

The competition between the exchange energy E_{ex} and the magnetostatic energy E_{ms} is characterized by the *exchange length* l_{ex} [19, 21]:

$$l_{ex} = \sqrt{\frac{2A}{\mu_0 M_S^2}}.\qquad(1.43)$$

This is the shortest scale on which the magnetization can be twisted in order to minimize E_{ms}. Considering iron, $A = 2.1 \cdot 10^{-11}$ J $\cdot$ m^{-1} and $M_S = 1700$ kA $\cdot$ m^{-1}, so $l_{ex} \approx 3.4$ nm, whereas for Permalloy, $A = 1.3 \cdot 10^{-11}$ J $\cdot$ m^{-1} and $M_S = 800$ kA $\cdot$ m^{-1}, so $l_{ex} \approx 5.7$ nm.

1.3.3 The Landau–Lifshitz–Gilbert equation

The microstructure of ferromagnetic materials is the result of minimizing the total free energy (1.31). As shown in Fig. 1.3, *magnetic domains* tend to form in the lowest energy state because the system wants to minimize its total self-energy, which is represented by the magnetostatic energy E_{ms}. Equation (1.37) can also be expressed as [12]

$$E_{ms} = \frac{\mu_0}{2} \int_{\text{all space}} H'^2 d\mathbf{r},\qquad(1.44)$$

where $\mathbf{H}'$ is the magnetic field generated by the magnetized material and the

integration is over the whole space. This form of writing the magnetostatic energy demonstrates the *pole avoidance principle*. The integrand is positive everywhere, which makes the magnetostatic energy always positive. So, the smallest possible value for this energy term is zero, a value that can only be achieved when H′ is identically zero everywhere. This fact implies that the magnetostatic energy term always tries to avoid any sort of volume (ρ_m) or surface (σ_m) magnetic charge, since the H-field can be mathematically *interpreted* as generated by fictitious magnetic poles:

$$\rho_m \; = \; -\boldsymbol{\nabla} \cdot \mathbf{M}, \tag{1.45a}$$

$$\sigma_m \; = \; \hat{\mathbf{n}} \cdot \mathbf{M}, \tag{1.45b}$$

where $\hat{\mathbf{n}}$ is the outward-pointing surface normal. A complete avoidance is usually not possible, because the energy minimization is subjected to constrains imposed by the exchange interaction, the external field and the anisotropies. Once the domains are there, the exchange tries to keep a uniform magnetization inside the domains and the anisotropy energy terms try to align the magnetization in each domain along one of the easy axes. However, the domains are separated by regions, the *domain walls*, where the magnetization rotates from one easy direction to another. The presence of domain walls locally enhances the energy, but at equilibrium this is compensated by a net decrease in the total free energy.

Mathematically speaking, the minimization of the total free energy (1.31) requires a variational approach [19]. The solution of the problem takes the form of a stability condition, known as *Brown's equations*, to be fulfilled at equilibrium:

$$\mathbf{m} \times \mathbf{H}_{eff} \; = \; 0, \tag{1.46}$$

where $\mathbf{m}(\mathbf{r}) = \mathbf{M}(\mathbf{r})/\mathrm{M}_S$ and

$$\mathbf{H}_{eff} \; = \; \frac{2}{\mu_0 \mathrm{M}_S} \boldsymbol{\nabla} \cdot (A \boldsymbol{\nabla} \mathbf{m}) \; - \; \frac{1}{\mu_0 \mathrm{M}_S} \frac{\partial \mathcal{E}_{mc}}{\partial \mathbf{m}} \; + \; \mathbf{H}_d \; + \; \mathbf{H}. \tag{1.47}$$

The effective field $\mathbf{H}_{eff}$ exerts a torque on the magnetization and, for a system to be in equilibrium, this torque has to be zero everywhere. However, Eq. (1.46) does not describe how the system will approach the equilibrium after an external perturbation. For this purpose, the *Landau–Lifshitz–Gilbert* (LLG) *equation* has been introduced [23–25]:

$$\frac{\partial \mathbf{m}}{\partial t} \; = \; -\frac{\mu_0 \gamma}{1 + \alpha^2} \left(\mathbf{m} \times \mathbf{H}_{eff} \; + \; \alpha \mathbf{m} \times \mathbf{m} \times \mathbf{H}_{eff} \right). \tag{1.48}$$

The parameter $\gamma > 0$ is the *gyromagnetic ratio* and the time dependence of $\mathbf{m}$ and $\mathbf{H}_{eff}$ is implicitly considered. The first term of Eq. (1.48) describes a precession of the magnetization around the effective field direction. For an electron spin, the (Larmor) precession frequency can be obtained by considering that $\gamma/(2\pi) = g_S e/(4\pi m) \approx 28$ GHz $\cdot$ T^{-1}. The dimensionless parameter $\alpha \geq 0$ controls the strength of the damping mechanism, necessarily involved in any approach to equilibrium. In fact, $\mathbf{m} \times \mathbf{m} \times \mathbf{H}_{eff}$ represents a torque which bends the magnetization towards the equilibrium direction defined by $\mathbf{H}_{eff}$. As a reference, a value often found in literature for Permalloy is $\alpha = 0.01$. Equation (1.46) implies that $\partial\mathbf{m}/\partial t = 0$, thus showing the compatibility between the LLG equation and Brown's equilibrium condition. To be noted that, at any position, the magnitude of the magnetization is conserved during the process, since [24]

$$\frac{\partial}{\partial t}\left(|\mathbf{m}|^2\right) \;=\; 2\mathbf{m} \cdot \frac{\partial\mathbf{m}}{\partial t} \;=\; 0. \tag{1.49}$$

1.4 Single-domain particles

As we have seen in the previous section, magnetic domains appear because of the balance between the energy enhancement due to the presence of domain walls and the reduction in magnetostatic energy. Thinking in these terms, it appears clear that a sufficiently small particle cannot contain domain walls and so it should consist of a single domain. In fact, the magnetostatic energy varies as the volume of the particle, while the wall energy varies as the cross-sectional area of the particle, determining a critical radius below which the single-domain state is energetically favourable. Since there are no domain walls, the magnetization process in an ideal single-domain particle only consists in the *coherent rotation* of the magnetization. This process is described by the *Stoner−Wohlfarth model* [10,26], which is worth to be discussed here because of its historical and physical merit. Let us consider the following free energy E_{SW} for an ideal single-domain particle in form of a prolate spheroid ($N_a > N_c$) of volume V:

$$E_{SW} \;=\; KV\sin^2\vartheta \;-\; \mu_0\mathrm{M}_S HV\cos\left(\psi - \vartheta\right), \tag{1.50a}$$

$$K \;=\; K_1 \;+\; \frac{\mu_0}{2}\Delta N\mathrm{M}_S^2, \tag{1.50b}$$

where $\Delta N = N_a - N_c$ and all the terms constant in ϑ have been neglected. The angle ϑ is the angle between the magnetization $\mathbf{M}_S$ and the easy axis, while ψ is the angle between the applied magnetic field $\mathbf{H}$ and the easy axis. The exchange energy is already taken into account in the assumption of considering an

(a) Free energy ($\psi = 180°$)
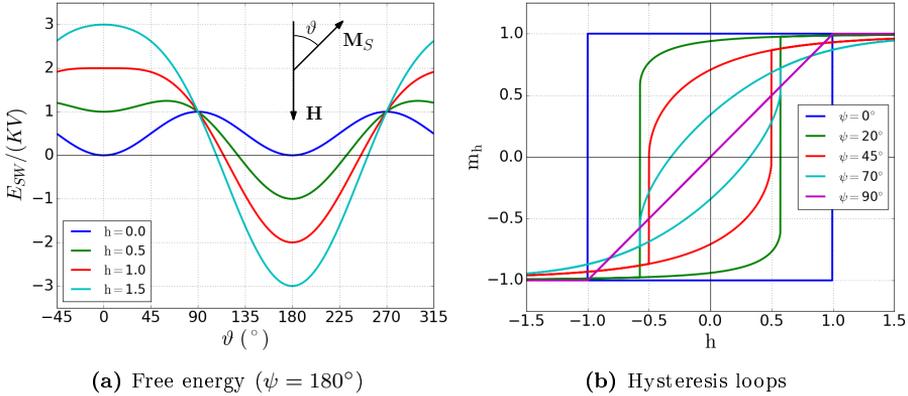
(b) Hysteresis loops

Figure 1.4: (a) Normalized free energy as a function of the magnetization angle ϑ for different values of normalized field h. (b) Hysteresis loops for single-domain particles with energy (1.50a) corresponding to different ψ angles. The value m_h is the normalized component of the magnetization along the magnetic field direction.

ideal single-domain particle: the exchange interaction simply keeps all the spins aligned, forming a sort of *macrospin* with magnetization equal to M_S everywhere in the particle. For a given **H**, the magnetization equilibrium position can be obtained by considering

$$\frac{dE_{SW}}{d\vartheta} = KV \sin 2\vartheta - \mu_0 M_S HV \sin(\psi - \vartheta) = 0 \qquad (1.51)$$

and looking for the solutions corresponding to minima for E_{SW}. A normalized field h = H/H$_K$ can be defined by introducing the *anisotropy field* H$_K$:

$$H_K = \frac{2K}{\mu_0 M_S}. \qquad (1.52)$$

Figure 1.4a illustrates the behaviour of E_{SW} when $\mathbf{M}_S$ is initially aligned with the easy axis ($\vartheta = 0°$) and **H** starts to be reversed ($\psi = 180°$). When h = 0 (blue curve), both $\vartheta = 0°$ and $\vartheta = 180°$ are equilibrium positions for $\mathbf{M}_S$, separated by an energy barrier KV. As the magnetic field ramps up, the minimum at $\vartheta = 180°$ becomes deeper and deeper with respect to the minimum at $\vartheta = 0°$, until h = 1 is reached. At this field value, $\vartheta = 0°$ is no longer a minimum and the magnetization becomes energetically unstable, eventually flipping over to $\vartheta = 180°$ (*magnetization reversal* process). The evolution of the magnetization as a function of **H** for this particular choice of ψ is given by the blue hysteresis loop in Fig. 1.4b, where the normalized component of the magnetization along the magnetic field direction is shown as a function of h. To find the critical field value

H_{cf} at which the magnetization jumps to the opposite direction as a function of ψ, we note that a solution of Eq. (1.51) does not necessarily correspond to a minimum in E_{SW}, but it can also correspond to an energy maximum, depending on the sign of the second derivative: if it is positive the equilibrium is stable, if it is negative the equilibrium is unstable, whereas if it is zero, a condition of stability is just changing to one of instability. Thus the critical field is found by imposing

$$\frac{d^2 E_{SW}}{d\vartheta^2} \; = \; 2KV \cos 2\vartheta \; + \; \mu_0 \mathrm{M}_S HV \cos\left(\psi - \vartheta\right) \; = \; 0. \qquad (1.53)$$

The simultaneous solution of Eqs. (1.51) and (1.53) leads to the following system of equations, from which the critical field $h_{cf} = \mathrm{H}_{cf}/\mathrm{H}_K$ and the corresponding critical angle ϑ_{cf} for the magnetization can be calculated [10]:

$$\begin{cases} \tan^3 \vartheta_{cf} \;=\; -\tan\psi, \\[2mm] \mathrm{h}_{cf}^2 \;=\; 1 \;-\; \dfrac{3}{4}\sin^2 2\vartheta_{cf}. \end{cases} \qquad (1.54)$$

When $\psi = 180°$, $\vartheta_{cf} = 0$ and $h_{cf} = 1$ (that means $\mathrm{H}_{cf} = \mathrm{H}_K$): the hysteresis loop is then rectangular, as shown in Fig. 1.4b. The values of h_{cf} decreases from 1 at $\psi = 0$ to a minimum of 0.5 at $\psi = 45°$ and then increases again to 1 as ψ approaches 90°. For the Stoner–Wohlfarth model, the critical field H_{cf} coincides with the *coercive field* H_C only when $\psi \leq 45°$, since H_C is defined to be the field value for which the component of the magnetization along the magnetic field direction reduces to zero.

1.4.1   Superparamagnetism and stochastic LLG equation

Until now we have neglected the effect of *temperature*. If the particle becomes small enough, the energy barrier (proportional to the particle volume) would become so small that energy fluctuations due to thermal effects could help the system in overcoming the energy barrier and spontaneously reverse the magnetization, giving rise to *superparamagnetism* [27]. In order to quantify the effect of temperature on a particle, we can *statistically* analyze the *rate* at which thermal equilibrium is approached in an ensemble of particles. Let us consider an assembly of N identical single-domain particles described by Eq. (1.50a) with their easy axes all parallel to a common direction, which defines the z-axis. Since only two equilibrium positions are defined in no applied magnetic field ($\vartheta = 0°, 180°$), we can divide the particles into two groups (see Fig. 1.5a):

(a) Energy landscape
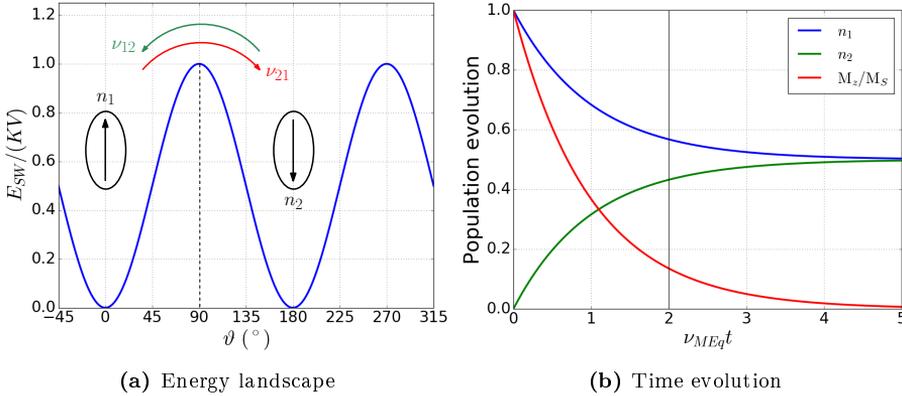
(b) Time evolution

Figure 1.5: (a) Blue curve of Fig. 1.4a showing the two stable states for the magnetization characterizing the populations n_1 and n_2. These states are separated by an energy barrier KV. (b) Time evolution of n_1, n_2 and $\mathrm{M}_z/\mathrm{M}_S$ as predicted by Eqs. (1.57) and (1.58) for $\nu_{21} = \nu_{12}$ and $n_1(0) = 1$.

- n_1 is the fraction of particles whose magnetization is $\hat{\mathbf{z}}\mathrm{M}_S$;

- n_2 is the fraction of particles whose magnetization is $-\hat{\mathbf{z}}\mathrm{M}_S$.

The evolution of these two populations (with $n_1(t)+n_2(t) = 1 \ \forall t$) is well described by a *master equation* (see also Appendix D) [28, 29]:

$$
\begin{cases}
\dot{n_1} &= -\nu_{21}n_1 \ + \ \nu_{12}n_2 \\
\dot{n_2} &= \ \ \ \nu_{21}n_1 \ - \ \nu_{12}n_2
\end{cases}.
\tag{1.55}
$$

The rates ν_{21} and ν_{12} are the *relaxation frequencies* associated with the particle transition from group 1 to 2 and from group 2 to 1, respectively. The relaxation frequency ν_{ij} (or equivalently the relaxation time $\tau_{ij} = 1/\nu_{ij}$) is given by the *Néel–Arrhenius equation* [28]:

$$
\nu_{ij} \ = \ \nu_0 \exp\left(-\frac{\Delta E_{ij}}{k_B T}\right).
\tag{1.56}
$$

The parameter ΔE_{ij} is the energy barrier associated to the considered process and ν_0 represents the *attempt frequency*, which, at this stage, can be considered as constant [28, 30] with a value of about 10^{10} Hz. The solution to the linear

system (1.55) is

$$
\begin{cases}
n_1(t) \;=\; \dfrac{\nu_{12}}{\nu_{MEq}} \;+\; \left[n_1(0) - \dfrac{\nu_{12}}{\nu_{MEq}} \right] \exp\left(-\nu_{MEq} t\right) \\[2mm]
n_2(t) \;=\; 1 \;-\; n_1(t)
\end{cases} \;,\qquad (1.57)
$$

where $\nu_{MEq} = \nu_{21} + \nu_{12}$ and $0 \leq n_1(0) \leq 1$ fully specifies the initial conditions. The average magnetization $\mathbf{M}(t)$ can then be expressed as

$$
\mathbf{M}(t) \;=\; \hat{\mathbf{z}} \mathrm{M}_S \left[n_1(t) \;-\; n_2(t) \right] \;=\; \hat{\mathbf{z}} \mathrm{M}_S \left[2 n_1(t) \;-\; 1 \right]. \qquad (1.58)
$$

For H $= 0$, it turns out that $\Delta E_{21} = \Delta E_{12} = KV$ and $\nu_{21} = \nu_{12}$. In this case, Eqs. (1.57) and (1.58) return M$(t) \to 0$ for $t \to \infty$, meaning that any initial order imposed to the ensemble will be lost after a high-enough time (see Fig. 1.5b). As a measure of this time scale, the value $2\tau_{MEq} = 2/\nu_{MEq}$ is usually chosen. So, for a given energy barrier KV, the average experimental measurement time t_{exp} has to be compared with $2\tau_{MEq}$ in order to define the thermal stability of the considered system:

- if $t_{exp} > 2\tau_{MEq}$, the performed measurement is able to record the statistical nature of thermally activated processes, and each particle appears as superparamagnetic;

- if $t_{exp} < 2\tau_{MEq}$, the particle appears as "blocked" in the initial state during the measurement, as if the temperature does not play any role.

Exploiting these considerations, a *blocking temperature* T_b can be defined as the temperature for which $t_{exp} = 2\tau_{MEq}$ for a given particle:

$$
T_b \;=\; \frac{KV}{k_B \ln\left(\nu_0 t_{exp}\right)}. \qquad (1.59)
$$

In this framework, the effect of an applied magnetic field is to modify the value of the energy barrier. After being initially saturated in the positive z-direction ($n_1(0) = 1$), a field $\mathbf{H}$ is applied to the ensemble of particles in the negative z-direction ($\psi = 180°$), modifying the energy landscape of each particle as shown in Fig. 1.4a. So, the energy barriers for reversal ΔE_{ij} can be derived to be

$$
\Delta E_{21} \;=\; KV \left(1 \;-\; \frac{\mathrm{H}}{\mathrm{H}_K} \right)^2, \qquad (1.60\mathrm{a})
$$

$$
\Delta E_{12} \;=\; KV \left(1 \;+\; \frac{\mathrm{H}}{\mathrm{H}_K} \right)^2, \qquad (1.60\mathrm{b})
$$

where we have made use of Eq. (1.52). The field progressively reduces the energy barrier for the transition from group 1 to group 2 until the process becomes thermally active during the average experimental measurement time, and the magnetization reversal can be effectively recorded. The effect of temperature is then to reduce the magnetic field needed for switching the particle magnetization, since the temperature allows the particle to explore larger portions of the energy landscape around the minimum it resides in. So, the coercive field $H_C(T)$ can be calculated as the field at which (statistically) half of the particles can change state during the average experimental measurement time t_{exp}, i.e. $n_1(t_{exp}) = 0.5$ also implying $M(t_{exp}) = 0$. From Eqs. (1.57) and (1.58), this corresponds to

$$\frac{\nu_{12}}{\nu_{MEq}} \; + \; \left(1 - \frac{\nu_{12}}{\nu_{MEq}} \right) \exp\left(-\nu_{MEq} t_{exp} \right) \; = \; \frac{1}{2}. \tag{1.61}$$

An additional assumption has to be made in order to simplify the result [31]. Since ΔE_{21} becomes smaller and smaller with respect to ΔE_{12} as H increases, we can neglect ν_{12}, so

$$H_C(T) \; = \; H_K \left[1 \; - \; \sqrt{\frac{k_B T}{KV} \ln\left(\frac{\nu_0 t_{exp}}{\ln 2} \right)} \, \right]. \tag{1.62}$$

Equation (1.62) is known as *Sharrock equation* [31, 32].

To be noted that the explicit T appearing in the Sharrock equation is not the only source of temperature dependence for H_C. The energy fluctuations caused by temperature do not only act on the magnetization as defined by Eq. (1.30), but there is a measurable effect on all the involved degrees of freedom (i.e. the elementary magnetic moments $\boldsymbol{\delta\mu}_j$). For this reason, the saturation magnetization magnitude itself is a function of temperature [12]. A far as this thesis in concerned, we consider the following temperature dependence for M_S:

$$M_S(T) \; = \; M_S^{0K} \left(1 \; - \; \frac{T}{T_C} \right)^{\beta}, \tag{1.63}$$

where M_S^{0K}, T_C and β are parameters to be experimentally determined and $T < T_C$.

In general, the thermal fluctuations above descibed can be taken into account inside the framework provided by the micromagnetic theory. Indeed, the effect of a finite temperature can be included in the LLG equation by means of a stochastic term, so identifying the *stochastic* LLG (sLLG) equation [25, 28, 33, 34]. In this

formulation, the effective field $\mathbf{H}_{eff}^{T}(t)$ to be used in Eq. (1.48) takes the form

$$\mathbf{H}_{eff}^{T}(t) \;=\; \mathbf{H}_{eff}(t) \;+\; \mathbf{H}_{fl}(t), \tag{1.64}$$

where a fluctuating field $\mathbf{H}_{fl}(t)$ has been introduced. In order to provide the effect of actual thermal fluctuations, $\mathbf{H}_{fl}(t)$ must be a Gaussian stochastic process, so satisfying the following properties [35–38]:

$$\langle \mathbf{H}_{fl}(t) \rangle \;=\; 0, \tag{1.65a}$$

$$\langle \mathrm{H}_{fl,i}(t)\mathrm{H}_{fl,j}(t') \rangle \;=\; \frac{2\alpha k_B T}{\gamma \mu_0^2 \mathrm{M}_S V} \delta\left(t - t'\right) \delta_{ij}, \tag{1.65b}$$

where $\langle \cdot \rangle$ denotes a time average and $\langle \cdot \cdot \rangle$ a correlation, δ is either a Dirac delta or a Kronecker delta $(i, j = x, y, z)$, T represents the temperature, α is the LLG damping parameter, γ is the gyromagnetic ratio, M_S is the saturation magnetization magnitude and V denotes the volume on which the thermal fluctuations can be considered as spatially correlated. Actually, the absence of any spatial correlation for $\mathbf{H}_{fl}$ is customarily assumed [35], so the elementary magnetic moment $\boldsymbol{\delta\mu}$ should appear in Eq. (1.65b) instead of $\mathrm{M}_S V$, but the methods for numerically solving the sLLG (see Appendix C) implement this requirement only between the various simulation cells (being V their volume). A similar argument can be applied to the time correlation expressed by $\delta\left(t - t'\right)$, since also time has to be make discrete for obtaining a numerical solution. In the end, $\mathbf{H}_{fl}$ can be assumed to be [25]

$$\mathbf{H}_{fl}(i) \;=\; \boldsymbol{\eta}_i \sqrt{\frac{2\alpha k_B T}{\gamma \mu_0^2 \mathrm{M}_S V \Delta t_i}}, \tag{1.66}$$

where Δt_i is the i-th time step and $\boldsymbol{\eta}_i$ is a random vector generated using a standard normal distribution whose value is changed after every i-th step. The effect of thermal fluctuations inside the simulation cells can then be taken into account by considering the $\mathrm{M}_S(T)$ value at the temperature of interest[2] [40–42].

1.5   Spin waves

The dynamic response of the magnetization (for a ferromagnetic material) to a small time-varying magnetic field can be analytically obtained by linearizing the LLG equation (1.48) about a saturated equilibrium state in the approximation of small oscillations [43]. For getting the resonance frequency, the damping term in

---

[2]However, close to the Curie temperature, an alternative approach can be considered: the *Landau–Lifshitz–Bloch equation* [39].

the LLG equation can be neglected ($\alpha = 0$), since its main effect is to determine a finite width for the resonance peak without shifting the peak position (to lowest order). Moreover, we also neglect the magnetocrystalline anisotropy contribution to the effective field (Eq. (1.47)), since it is of no relevance in the framework of this thesis. To solve the linearized LLG equation, we need to separate $\mathbf{H}_{eff}$ and $\mathbf{M}$ in terms of static and time-varying components:

$$\mathbf{H}_{eff}(t) \; = \; \mathbf{H}^0_{eff} \; + \; \mathbf{H}^*_{eff}\mathrm{e}^{-i\omega t}, \tag{1.67a}$$

$$\mathbf{M}(t) \; = \; \mathbf{M}^0 \; + \; \mathbf{M}^*\mathrm{e}^{-i\omega t}, \tag{1.67b}$$

where the time dependence of the time-varying terms has been made explicit. For definiteness, we assume that the static equilibrium fields lie along the z-axis, namely $\mathbf{H}^0_{eff} = \hat{\mathbf{z}}\mathrm{H}^0_{eff}$, and the term given by the the externally applied magnetic field ($\hat{\mathbf{z}}\mathrm{H}$) constitutes a static bias field. Hence, for small deviations from equilibrium ($\mathrm{M}^* \ll \mathrm{M}^0$ and $\mathrm{H}^*_{eff} \ll \mathrm{H}^0_{eff}$), the z-component of the magnetization results to be unchanged, so that $\mathbf{M}^0 \approx \hat{\mathbf{z}}\mathrm{M}_S$. Making these assumptions and neglecting second-order terms in small quantities, the no-damping linearized LLG equation reads [43, 44]

$$i\omega\mathbf{M}^* \; = \; \omega_{\mathrm{M}}\hat{\mathbf{z}} \times \left(\mathbf{H}^* \; - \; \frac{\omega_{\mathrm{H}}}{\omega_{\mathrm{M}}}\mathbf{M}^* \; - \; \mathfrak{N}_d\mathbf{M}^* \; + \; \lambda_{ex}\boldsymbol{\nabla}^2\mathbf{M}^* \right), \tag{1.68}$$

where

$$\omega_{\mathrm{M}} \; = \; \mu_0\gamma\mathrm{M}_S, \tag{1.69a}$$

$$\omega_{\mathrm{H}} \; = \; \mu_0\gamma\left(\mathrm{H} - N_z\mathrm{M}_S\right), \tag{1.69b}$$

$$\lambda_{ex} \; = \; \frac{2A}{\mu_0\mathrm{M}_S^2}. \tag{1.69c}$$

The field $\mathbf{H}^*$ denotes the term in $\mathbf{H}^*_{eff}$ associated to the externally applied magnetic field, so it represents the external small perturbation we are exploiting for getting the magnetization dynamic response. The tensor $\mathfrak{N}_d$ is the demagnetizing tensor introduced in Sec. 1.3.2. For simplicity, we are considering the $\mathfrak{N}_d$ principal axes to be parallel to the coordinate axes, so that N_z is the demagnetizing factor along the z-axis. Eventually, the quantity $\lambda_{ex}\mathrm{M}_S$ is called the *spin-wave stiffness* [45]. If the spatial dependence of $\mathbf{H}^*$ and $\mathbf{M}^*$ is of the form $\mathrm{e}^{i\mathbf{k}\cdot\mathbf{r}}$, the operator $\boldsymbol{\nabla}^2$ can be substituted by $-\mathrm{k}^2$ and Eq. (1.68) can be inverted to return the magnetic susceptibility tensor for the time-varying x- and y-components

(*generalized Polder tensor*) [43]:

$$\chi_m = \frac{1}{D} \begin{bmatrix} \omega_{\mathrm{H}} + \omega_{\mathrm{M}} \left(N_y + \lambda_{ex} \mathrm{k}^2 \right) & -i\omega \\ i\omega & \omega_{\mathrm{H}} + \omega_{\mathrm{M}} \left(N_x + \lambda_{ex} \mathrm{k}^2 \right) \end{bmatrix} \qquad (1.70)$$

where

$$D = \left[\omega_{\mathrm{H}} + \omega_{\mathrm{M}} \left(N_x + \lambda_{ex} \mathrm{k}^2 \right) \right] \left[\omega_{\mathrm{H}} + \omega_{\mathrm{M}} \left(N_y + \lambda_{ex} \mathrm{k}^2 \right) \right] - \omega^2. \qquad (1.71)$$

The resonance frequency ω_0 can be found by imposing $D = 0$ [43, 45, 46]:

$$\left(\frac{\omega_0}{\mu_0 \gamma} \right)^2 = \left[\mathrm{H} + \left(N_x - N_z \right) \mathrm{M}_S + \lambda_{ex} \mathrm{M}_S \mathrm{k}^2 \right] \left[\mathrm{H} + \left(N_y - N_z \right) \mathrm{M}_S + \lambda_{ex} \mathrm{M}_S \mathrm{k}^2 \right]. \tag{1.72}$$

In case $\lambda_{ex} = 0$, Eq. (1.72) reduces to the *Kittel equation* for the *ferromagnetic resonance frequency* [11, 47].

The tensor (1.70) can be applied both to bulk isotropic ferromagnetic materials (for which all the demagnetizing factors are zero) and to thin films (where the demagnetizing factor corresponding to the film growth direction can be taken as equal to one). As we have just seen, it defines the response of a ferromagnetic material to a time-varying field. Hence, it can be combined with the Maxwell equations (1.1) in order to describe the propagation of electromagnetic waves within a ferromagnetic medium. Detailed solutions to this problem can be found in Ref. [43]. The most interesting thing for us is the fact that such a material, when perturbed out of equilibrium, can sustain magnetization oscillations, generally called *spin waves*. In case of confined dimensions, as in nanostructures, these oscillations can give rise to standing-wave patterns which can give information on the magnetization reversal process, as we will see in Chap. 6. As a reference, for the materials and the geometries considered in this thesis, the relevant resonance frequencies lie in the range $1 - 10$ GHz.

1.6   Optics in metals: plasmonics

Whereas magnetism mainly deals with the relation between $\mathbf{M}$ and $\mathbf{H}$ (see Eq. (1.8)), *plasmonics* arose from the study of the optical properties of metals [48–50]. As such, Eq. (1.4a) is now the equation to be considered and the transfer function for optical properties is represented by the dielectric susceptibility tensor $\boldsymbol{\chi}$, as shown by Fig. 1.6:

$$\mathbf{P} = \varepsilon_0 \boldsymbol{\chi} \mathbf{E}. \qquad (1.73)$$
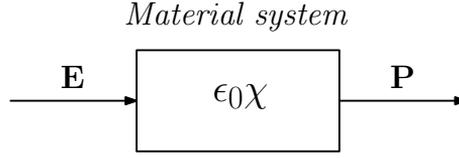
Material system

Figure 1.6: Block diagram outlining the action of an electric field **E** on a material system. To be compared with Fig. 1.1.

An expression for $\boldsymbol{\chi}$ can be derived in the framework of classical physics by considering the *Drude–Lorentz model* for an electron system [51]:

$$\ddot{\mathbf{r}} + \Gamma\dot{\mathbf{r}} + \omega_0^2\mathbf{r} = -\frac{e}{m}\mathbf{E}, \tag{1.74}$$

where m is the electron mass, e is its charge, $\mathbf{r}$ denotes the displacement of the electron from its equilibrium position, $\mathbf{E}$ is the electric field, Γ is the damping parameter and ω_0 is the resonance frequency. This model will be used in Chap. 2, where magnetism and optics are going to be combined in order to explain the origin of *magneto-optical effects* [52]. In case of an optically isotropic and homogeneous material subjected to an oscillating electric field, in the form of $\mathbf{E} = \mathbf{E_0}e^{-i\omega t}$, the dielectric susceptibility tensor $\boldsymbol{\chi}$ reduces to a diagonal tensor whose non-zero elements are equals to

$$\chi = \frac{ne^2}{\varepsilon_0 m}\left(\frac{1}{\omega_0^2 - \omega^2 - i\Gamma\omega}\right) = \frac{ne^2}{\varepsilon_0 m}\left[\frac{\omega_0^2 - \omega^2 + i\Gamma\omega}{\left(\omega_0^2 - \omega^2\right)^2 + \Gamma^2\omega^2}\right], \tag{1.75}$$

where n is the average number of electrons per unit volume. In the end, the Drude–Lorentz model says that, when an electromagnetic wave impinges on a material described as a system of electrons, the j-th electron responds to the oscillating electric field $\mathbf{E}$ by developing an electric dipole moment $\boldsymbol{\delta}\mathbf{p}_j = -e\mathbf{r}_j$, where $\mathbf{r}_j$ is solution of Eq. (1.74): $\mathbf{r} = -\varepsilon_0\chi\mathbf{E}/(ne)$. The net effect per unit volume is expressed by the electric polarization $\mathbf{P}(\mathbf{r})$:

$$\mathbf{P}(\mathbf{r}) = \frac{\sum_j \boldsymbol{\delta}\mathbf{p}_j}{\delta V_{\mathbf{r}}} = n\langle\boldsymbol{\delta}\mathbf{p}(\mathbf{r})\rangle, \tag{1.76}$$

where the sum runs over the electric dipole moments contained in a volume $\delta V_{\mathbf{r}}$ centered at $\mathbf{r}$ and $\langle\boldsymbol{\delta}\mathbf{p}(\mathbf{r})\rangle$ represents the average electric dipole moment contained in that volume. The j-th electric dipole moment $\boldsymbol{\delta}\mathbf{p}_j$ itself represent a source of electromagnetic radiation, which is then emitted giving rise to the *scattered radiation*. However, this is not the only process which can occur: due

to the presence of damping, part of the energy the electron receives from the incident field is dissipated through other mechanisms, eventually turning into heat. This is what is usually defined as *absorption*. Scattering and absorption of electromagnetic radiation are the two general categories in which the light-matter interaction phenomena can be subdivided. While working with metals, Eq. (1.75) can be expressed in a slightly different way:

$$\chi \;=\; -\frac{\omega_p^2}{\omega^2 + i\Gamma_D\omega} \;+\; \omega_p^2 \sum_j \frac{f_j}{\omega_{0j}^2 - \omega^2 - i\Gamma_j\omega}, \qquad (1.77a)$$

$$\omega_p \;=\; \sqrt{\frac{ne^2}{\varepsilon_0 m}}. \qquad (1.77b)$$

The first term in Eq. (1.77a) can be obtained by starting from the *Drude model* and takes into account the effect of *free electrons* (i.e. *conduction electrons*), for which the equation of motion does not contain the elastic term responsible for the appearance of the resonance (i.e. $\omega_{0D} = 0$) and $\tau_D = 1/\Gamma_D$ represents the electron mean free time [53]. The parameter ω_p denotes the *plasma frequency* and represents the maximum frequency the system of free electrons can respond to. Above this frequency, the metal becomes transmitting, a phenomenon known as the *ultraviolet transparency* of metals [51]. The sum appearing in the second term of Eq. (1.77a) can be used to fit any kind of transition (like *interband transitions*) leading to a resonant behaviour described by a resonance frequency ω_{0j} and a lifetime proportional to $1/\Gamma_j$. For this purpose, a phenomenological *oscillator strength* f_j can be assigned to each term in order to express the "relevance" of the associated j-th process.

1.6.1   Plasmonics of metallic nanostructures

When a metal is moulded into a nanostructure, the confinement of the conduction electrons starts playing a role. The surface of the nanostructure exerts an effective restoring force on the driven electrons, so that a resonance can arise. This resonance is called *localized surface plasmon* (LSP) *resonance* [48, 54, 55]. For the purpose of this thesis, the most interesting feature of LSPs is the fact that hitting the resonance is the most effective way for transferring energy from the incident electromagnetic field to the nanostructure. For better describing these concepts, we can consider a homogeneous and isotropic metallic sphere whose radius a is much smaller than the wavelength λ of the incident electric field $\mathbf{E}_b = \mathbf{E_{0}}_b e^{i(\mathbf{k}\cdot\mathbf{r} - \omega t)}$. The magnitude of the wavevector $\mathbf{k}$ is given by $k = 2\pi/\lambda$, since we are considering the sphere to be in vacuum. The condition $a \ll \lambda$ en-

sures that the electric field is approximately uniform through the volume of the sphere, so a quasi-static approach can be used. The field $\mathbf{E}_{int}$ inside the sphere is given by the superposition of the applied field $\mathbf{E}_b$ and the depolarization field $\mathbf{E}_d$ given by $\mathbf{E}_d = -\mathbf{P}/(3\varepsilon_0)$. The field $\mathbf{E}_d$ plays, for optical phenomena, the same role the demagnetizing field of Eq. (1.38) plays for magnetic nanostructures. So, $\mathbf{E}_{int}$ can be retrieved by imposing

$$\mathbf{E}_{int} \;=\; \mathbf{E}_b \;+\; \mathbf{E}_d \;=\; \mathbf{E}_b \;-\; \frac{\varepsilon_r - 1}{3}\mathbf{E}_{int}, \tag{1.78}$$

having defined $\varepsilon_r = 1 + \chi$ (*relative dielectric permittivity*) and considering Eq. (1.73). In case of a sphere, the electric polarization $\mathbf{P}$ is uniform through the whole volume $V = 4\pi a^3/3$, whence the total electric dipole moment $\mathbf{p}$ is

$$\mathbf{p} \;=\; V\mathbf{P} \;=\; 4\pi\varepsilon_0 a^3 \frac{\varepsilon_r - 1}{\varepsilon_r + 2}\mathbf{E}_b \;=\; \varepsilon_0 \alpha_p \mathbf{E}_b, \tag{1.79}$$

where α_p is called *polarizability*. We introduced the electric dipole moment since it is the source of the electromagnetic radiation produced by the nanostructure in question, namely the *scattered radiation*. For a sphere embedded in a homogeneous and isotropic medium with relative dielectric permittivity ε_{env}, Eq. (1.79) has to be accordingly modified:

$$\mathbf{p} \;=\; 4\pi\varepsilon_0\varepsilon_{env}a^3 \frac{\varepsilon_r - \varepsilon_{env}}{\varepsilon_r + 2\varepsilon_{env}}\mathbf{E}_b \;=\; \varepsilon_0\varepsilon_{env}\alpha_p\mathbf{E}_b. \tag{1.80}$$

All these formulas can be generalized considering an ellipsoid with semiaxes a_x, a_y and a_z. The polarizabilities $\alpha_{p,i}$ along the principal axes ($i = x, y, z$) turn out to be [48,56]

$$\alpha_{p,i} \;=\; 4\pi a_x a_y a_z \frac{\varepsilon_r - \varepsilon_{env}}{3\varepsilon_{env} + 3L_i\left(\varepsilon_r - \varepsilon_{env}\right)} \tag{1.81}$$

and the geometrical factors L_i (*depolarization factors*) are given by

$$L_i \;=\; \frac{a_x a_y a_z}{2} \int_0^\infty \frac{dr}{(r + a_i^2)\sqrt{(r + a_x^2)\left(r + a_y^2\right)\left(r + a_z^2\right)}}. \tag{1.82}$$

To be noticed that the factors L_i are the same as the demagnetizing factors N_i calculated according to Ref. [20]. The behaviour of $\alpha_{p,i}$ reflects both the optical material properties and the nanostructure geometry. Even if the material does not show a resonant behaviour at the considered frequencies, the size and the shape of the nanostructure, leading to Eq. (1.81), can determine the appearance of a resonance.
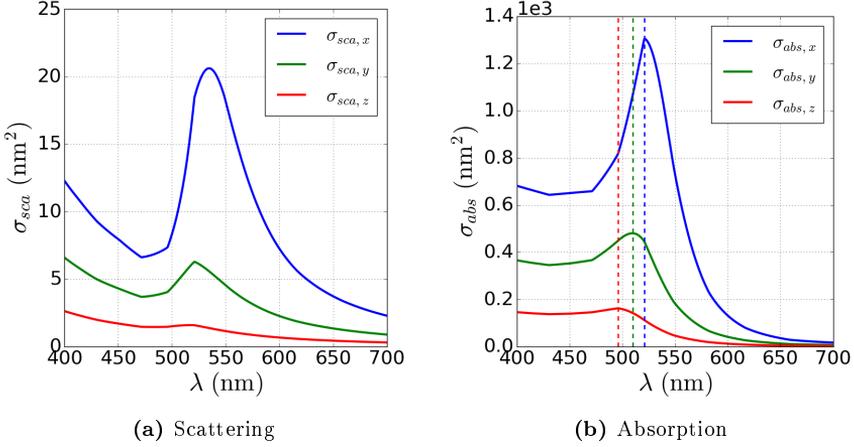
(a) Scattering   (b) Absorption

Figure 1.7: Cross sections for a gold ellipsoid of semiaxes $a_x = 20$ nm, $a_y = 15$ nm and $a_z = 10$ nm in vacuum. The dashed lines in (b) indicate the peak positions. The gold refractive index has been taken from Ref. [58].

From the viewpoint of optics (and for the sake of this thesis), it is much more interesting to highlight the fact that a resonantly enhanced polarizability leads to an enhancement in the efficiency with which a metal nanostructure scatters and absorbs light. For quantifying this effect, the *scattering* (σ_{sca}) and *absorption* (σ_{abs}) *cross sections* can be calculated [48, 57]:

$$\sigma_{sca,i} = \frac{k_{env}^4}{6\pi} |\alpha_{p,i}|^2 \,, \tag{1.83a}$$

$$\sigma_{abs,i} = k_{env} \Im(\alpha_{p,i}) \,, \tag{1.83b}$$

where $k_{env} = 2\pi\sqrt{\varepsilon_{env}}/\lambda$. The sum of scattering and absorption cross sections defines the *extinction cross section* σ_{ext}:

$$\sigma_{ext,i} = \sigma_{sca,i} + \sigma_{abs,i}. \tag{1.84}$$

A cross section represents an "effective area" crossing the incident electromagnetic wave. For a wave with intensity I_b and linearly polarized along the i-axis ($i = x, y, z$), $\sigma_{sca,i} I_b$ returns the power scattered by the nanostructure, whereas $\sigma_{abs,i} I_b$ corresponds to the absorbed power (eventually turning into heat). Figures 1.7a and 1.7b show the scattering and absorption cross sections for a gold ellipsoid of semiaxes $a_x = 20$ nm, $a_y = 15$ nm and $a_z = 10$ nm in vacuum. The peaks denote the presence of a resonance (the LSP resonance) and the relative length of the axes (i.e. the *aspect ratio*) determines both the peak position and the peak

relative intensity: the longer the axis, the higher the peak and its position shifts towards longer wavelengths.

All these results are valid as long as $a_i \ll \lambda$. When the size of the nanostructure starts becoming comparable with the wavelength (few hundreds of nanometers for visible radiation), the incident electric field cannot be considered uniform through the whole nanostructure volume (*retardation effects* [5,59]). Moreover, the nanostructures are usually fabricated on top of a suitable substrate and so they are not embedded in a uniform medium. All the general considerations developed through this section remain valid, but several simulation techniques have been developed through the years in order to take into account all the experimental conditions and to obtain a numerical solution when the analytical one is not available [59]. After all, the whole problem "reduces" to find a solution to the Maxwell equations (1.1), having (i) properly described the behaviour of the materials under the influence of an electromagnetic field (see Eq. (1.4)) and (ii) properly defined the *boundary conditions*.

Chapter 2

Magneto-optical Effects

Light interacts with matter in many different ways. The phenomena that occur as a result of this interaction can be affected by material properties and external effects, like an applied magnetic field or the magnetization of the body itself, giving rise in this case to magneto-optic effects. In 1845, Michael Faraday was able to verify that the polarization plane of the light transmitted in a dielectric medium in the direction of an external applied magnetic field was rotated by an angle that depends on the strength of the magnetic field [60]. Almost 30 years later, in 1877, John Kerr showed that a change in the state of polarization occurred on reflection from a polished, soft iron pole-piece of a strong electromagnet [61]. Although the physical origin is the same, they are called *magneto-optical Faraday effect* and *magneto-optical Kerr effect* (MOKE), respectively, and they became rapidly a mean to probe the magnetic properties of matter. Indeed, theory and experiments have shown that, in ferromagnetic materials, magneto-optical effects are proportional to the net magnetization of the sample and not to the applied magnetic field as in the case of non-ferromagnetic specimens.

2.1 Classical approach to magneto-optical effects in dielectrics

In order to better understand the physics behind these phenomena, it is useful to start analyzing the explanation of the Faraday and Kerr effects in dielectric, non-magnetic media in terms of the *Drude–Lorentz model* for dispersion, in which an electron is considered harmonically bound to the nucleus and subjected to a damping force [62]. The goal is to obtain the susceptibility tensor, from which one

can determine how the electromagnetic field is modified during the interaction with such a material by the presence of an externally applied magnetic field.

2.1.1   The susceptibility tensor

The equation of motion for an electron of (effective) mass m and charge e subjected to an oscillating electric field, in the form of $\mathbf{E} = \mathbf{E_0} e^{-i\omega t}$, and a static magnetic field $\mathbf{H}$ is

$$m\ddot{\mathbf{r}} \ + \ b\dot{\mathbf{r}} \ + \ k\mathbf{r} \ = \ - \ e\mathbf{E} \ - \ e\mu_0\dot{\mathbf{r}} \times \mathbf{H}, \tag{2.1}$$

where $\mathbf{r}$ is the displacement of the electron from its equilibrium position, k is the elastic-force constant, b is the damping coefficient and μ_0 is the vacuum permeability, as we are working with non-magnetic media. $\mathbf{E}$ has been chosen in this form in order to be compatible with the electric field of a propagating plane wave. The solution we are looking for is the steady state condition for which the displacement $\mathbf{r}$ has the same time dependence as the electric field, hence Eq. (2.1) becomes

$$- \ m\omega^2\mathbf{r} \ - \ i\omega b\mathbf{r} \ + \ k\mathbf{r} \ = \ - \ e\mathbf{E_0} \ + \ i\omega e\mu_0\mathbf{r} \times \mathbf{H}. \tag{2.2}$$

Defining the z-axis as the direction of the applied magnetic field, Eq. (2.2) leads to three equations, one for each Cartesian coordinate:

$$\mathfrak{M} \cdot \begin{pmatrix} x \\ y \\ z \end{pmatrix} \ = \ -\frac{e}{m} \begin{pmatrix} E_{0x} \\ E_{0y} \\ E_{0z} \end{pmatrix}, \tag{2.3}$$

where

$$\mathfrak{M} \ = \ \begin{bmatrix} \omega_0^2 - \omega^2 - i\Gamma\omega & -i\omega\omega_C & 0 \\ i\omega\omega_C & \omega_0^2 - \omega^2 - i\Gamma\omega & 0 \\ 0 & 0 & \omega_0^2 - \omega^2 - i\Gamma\omega \end{bmatrix}. \tag{2.4}$$

In writing the tensor $\mathfrak{M}$, we have used the following notations:

$$\omega_0 \ = \ \sqrt{\frac{k}{m}} \qquad \text{(resonance frequency)},$$

$$\Gamma \ = \ \frac{b}{m} \qquad \text{(damping parameter)},$$

$$\omega_C \ = \ \frac{e\mu_0\mathrm{H}}{m} \qquad \text{(cyclotron frequency)}.$$

If n is the average number of electrons per unit volume, the electric polarization $\mathbf{P}$ of the medium is given by $\mathbf{P} = -ne\mathbf{r}$ and can be obtained from Eq. (2.3):

$$\mathbf{P} = \frac{ne^2}{m}\mathfrak{M}^{-1}\mathbf{E_0}. \tag{2.5}$$

The *(dielectric) susceptibility tensor* $\boldsymbol{\chi}$ is the quantity relating the electric polarization to the applied electric field through the relation

$$\mathbf{P} = \varepsilon_0\boldsymbol{\chi}\mathbf{E_0}, \tag{2.6}$$

where ε_0 is the vacuum permittivity. Combining Eqs. (2.5) and (2.6), $\boldsymbol{\chi}$ turns out to be given by

$$\boldsymbol{\chi} = \frac{ne^2}{\varepsilon_0 m}\mathfrak{M}^{-1} = \begin{bmatrix} \chi_{xx} & i\chi_{xy} & 0 \\ -i\chi_{xy} & \chi_{xx} & 0 \\ 0 & 0 & \chi_{zz} \end{bmatrix}, \tag{2.7}$$

where

$$\chi_{xx} = \omega_p^2\left[\frac{\omega_0^2 - \omega^2 - i\Gamma\omega}{(\omega_0^2 - \omega^2 - i\Gamma\omega)^2 - \omega^2\omega_C^2}\right], \tag{2.8a}$$

$$\chi_{xy} = \omega_p^2\left[\frac{\omega\omega_C}{(\omega_0^2 - \omega^2 - i\Gamma\omega)^2 - \omega^2\omega_C^2}\right], \tag{2.8b}$$

$$\chi_{zz} = \omega_p^2\left[\frac{1}{\omega_0^2 - \omega^2 - i\Gamma\omega}\right]. \tag{2.8c}$$

The parameter ω_p, expressed by Eq. (1.77b), represents the plasma frequency, a quantity exclusively defined for a metal, but useful here since the model is quite general. The effect of the applied field is to introduce *non-diagonal antisymmetric* terms in the susceptibility tensor. In case of zero applied field, the susceptibility is reduced to a diagonal tensor with all the elements equal to each other, a typical form for isotropic media.

2.1.2 The indices of refraction

The propagation of the electromagnetic wave in a non-conductive, non-magnetic and electrically neutral dielectric is determined by solving the relevant Maxwell

equations [62]:

$$\boldsymbol{\nabla} \times \mathbf{E} \;=\; -\;\mu_0 \frac{\partial \mathbf{H}}{\partial t}, \tag{2.9}$$

$$\boldsymbol{\nabla} \times \mathbf{H} \;=\; \varepsilon_0 \frac{\partial \mathbf{E}}{\partial t} \;+\; \frac{\partial \mathbf{P}}{\partial t}. \tag{2.10}$$

The wave equation for $\mathbf{E}$ is obtained by taking the curl of Eq. (2.9) and the time derivative of Eq. (2.10) and combining them to eliminate $\mathbf{H}$:

$$\boldsymbol{\nabla} \times \boldsymbol{\nabla} \times \mathbf{E} \;=\; -\;\frac{1}{c^2}\frac{\partial^2 \mathbf{E}}{\partial t^2} \;-\; \frac{\chi}{c^2}\frac{\partial^2 \mathbf{E}}{\partial t^2}, \tag{2.11}$$

where we have used Eq. (2.6) to define $\mathbf{P}$ and the fact that the speed of light in vacuum c is related to μ_0 and ε_0 by means of $1/c^2 = \mu_0\varepsilon_0$. In order to describe the Faraday effect, we are interested in the propagation of a monochromatic electromagnetic wave in the direction of the applied magnetic field, namely the z-axis considering the susceptibility tensor expressed by Eq. (2.7). Therefore, we can choose a solution in the form $\mathbf{E} = \mathbf{E_0}e^{i(kz-\omega t)}$, where the wave vector $\mathbf{k}$ is in the z-axis direction. Equation (2.11) gives

$$\left[k^2 - \frac{\omega^2}{c^2}\left(1+\chi_{xx}\right)\right] E_{0x} \;-\; \left(\frac{\omega^2}{c^2}i\chi_{xy}\right) E_{0y} \;=\; 0, \tag{2.12a}$$

$$\left(\frac{\omega^2}{c^2}i\chi_{xy}\right) E_{0x} \;+\; \left[k^2 - \frac{\omega^2}{c^2}\left(1+\chi_{xx}\right)\right] E_{0y} \;=\; 0, \tag{2.12b}$$

$$\frac{\omega^2}{c^2}\left(1+\chi_{zz}\right) E_{0z} \;=\; 0. \tag{2.12c}$$

The last equation merely gives $E_{0z} = 0$, while the determinant of the coefficients of the first two equations must vanish for a non-trivial solution, giving the condition

$$\left[k^2 - \frac{\omega^2}{c^2}\left(1+\chi_{xx}\right)\right]^2 \;-\; \left(\frac{\omega^2}{c^2}\chi_{xy}\right)^2 \;=\; 0. \tag{2.13}$$

Solving for k, we find

$$k \;=\; \frac{\omega}{c}\sqrt{1 \;+\; \chi_{xx} \;\pm\; \chi_{xy}}, \tag{2.14}$$

that in combination with Eqs. (2.12a) and (2.12b) yields

$$E_{0y} \;=\; \mp i E_{0x}. \tag{2.15}$$

The above result means that the two values of k given by Eq. (2.14) correspond to *right* (R) and *left* (L) *circularly polarized light*, respectively. The indices of

refraction are, accordingly,

$$n_R = \sqrt{1 + \chi_{xx} + \chi_{xy}}, \tag{2.16a}$$

$$n_L = \sqrt{1 + \chi_{xx} - \chi_{xy}} \tag{2.16b}$$

and allow describing how the polarization of the electromagnetic wave is affected by the propagation in the medium. Through Eqs. (2.8a) and (2.8b), the indices of refraction are given by

$$\sqrt{1 + \chi_{xx} \pm \chi_{xy}} \approx \sqrt{1 + \frac{\omega_p^2}{\omega_0^2 - \left(\omega \pm \frac{\omega_C}{2}\right)^2 - i\Gamma\omega}}, \tag{2.17}$$

expressions valid under the assumption $|\chi_{xy}| \ll 1$. The effect of the applied magnetic field is to shift the dispersion curves for circularly polarized light by an amount equal to $\omega_C/2$ (with respect to the unperturbed case) and so proportional to H.

2.1.3 The Faraday and Kerr effects

Equation (2.12c) implies that the electric field vector $\mathbf{E_0}$ lies in the plane normal to the direction of the applied field, namely the xy-plane in this case, so we can consider as reference a monochromatic plane wave with wavelength λ_0 which at $z = 0$ is lineraly polarized in the x-direction. During propagation in the presence of on applied magnetic field, the initial linear polarization state is progressively distorted to an elliptical polarization state, characterized by a *rotation* ϑ and an *ellipticity* ε [63]. The definition of these two parameters is given in Sec. B.2.

A linearly polarized wave in the x-direction can be expressed through Jones vectors and can be resolved into left and right circularly polarized waves (see Eq. (B.10)):

$$E_0 \begin{pmatrix} 1 \\ 0 \end{pmatrix} = \frac{1}{2} E_0 \begin{pmatrix} 1 \\ i \end{pmatrix} + \frac{1}{2} E_0 \begin{pmatrix} 1 \\ -i \end{pmatrix}. \tag{2.18}$$

This means that we can analyze the propagation considering the superposition of the propagation of circularly polarized waves, which can be described by using the refractive indices given by Eqs. (2.16b) and (2.16a):

$$\frac{1}{2} E_0 \begin{pmatrix} 1 \\ i \end{pmatrix} \mathrm{e}^{i\frac{2\pi n_L}{\lambda_0}z} + \frac{1}{2} E_0 \begin{pmatrix} 1 \\ -i \end{pmatrix} \mathrm{e}^{i\frac{2\pi n_R}{\lambda_0}z} = E_0 \mathrm{e}^{i\psi} \begin{pmatrix} \cos(\delta) \\ \sin(\delta) \end{pmatrix}, \tag{2.19}$$

where

$$\psi \;=\; \frac{\pi z}{\lambda_0} \left(n_R \;+\; n_L \right), \qquad\qquad (2.20\text{a})$$

$$\delta \;=\; \frac{\pi z}{\lambda_0} \left(n_R \;-\; n_L \right). \qquad\qquad (2.20\text{b})$$

After propagating a distance l through the medium, the wave will be elliptically polarized with the major axis of the ellipse rotated through the angle (see Eq. (B.17a))

$$\vartheta_F \;=\; \Re\left(\delta\right) \;=\; \frac{\pi l}{\lambda_0}\Re\left(n_R \;-\; n_L\right) \qquad\qquad (2.21)$$

and an ellipticity (see Eq. (B.17b))

$$\tan\left(\varepsilon_F\right) \;=\; \tanh\left[\Im\left(\delta\right)\right] \;=\; \tanh\left[\frac{\pi l}{\lambda_0}\Im\left(n_R \;-\; n_L\right)\right], \qquad\qquad (2.22)$$

where the subscript F points out that we are considering the Faraday effect. From these equations, it can be seen that ϑ_F and ε_F come from a difference between the indices of refraction for left and right circularly polarized light, which are the propagation modes for a light wave traveling in the direction of the applied magnetic field through a dielectric medium characterized by the susceptibility tensor (2.7). Equation (2.22) also leads to the fact that the light becomes elliptically polarized only if the indices of refraction are complex quantities, namely if the medium is absorbing. Expanding n_L and n_R for $|\chi_{xy}| \ll 1$ and substituting them back in Eq. (2.21), ϑ_F becomes

$$\vartheta_F \;\approx\; \frac{\pi l}{\lambda_0}\Re\left(\frac{\chi_{xy}}{\sqrt{1+\chi_{xx}}}\right) \;=\; Vl\mathrm{H}, \qquad\qquad (2.23)$$

where the coefficient V is the Verdet constant: it is a characteristic of the material, it depends on the wavelength of the light and it may also depend on temperature [63]. So, the amount of rotation is proportional to the applied magnetic field intensity and to the distance travelled in the medium.

This analysis can also lead to the evaluation of rotation and ellipticity in the case of the Kerr effect while considering normal incidence. The effect arises from the reflection a light wave undergoes when it impinges on a medium with susceptibility given by Eq. (2.7). Such a phenomenon can be described through the Fresnel coefficient r for normal reflection [62]:

$$r \;=\; -\;\frac{n_r - 1}{n_r + 1}, \qquad\qquad (2.24)$$

where n_r is the ratio between the index of refraction of the medium the wave impinges on and the index of refraction of the medium the wave initially propagates into. In this case, we take as reference a monochromatic plane wave $\mathbf{E_0}$ with wavelength λ_0 which is lineraly polarized in the x-direction and propagates in vacuum (with $n_{Vacuum} = 1$). The reflection is evaluated in terms of the superposition (2.18), so using Eqs. (2.16b) and (2.16a) to calculate r we obtain

$$\frac{1}{2}E_0 \begin{pmatrix} 1 \\ i \end{pmatrix} \left(-\frac{n_L - 1}{n_L + 1} \right) + \frac{1}{2}E_0 \begin{pmatrix} 1 \\ -i \end{pmatrix} \left(-\frac{n_R - 1}{n_R + 1} \right) \propto \begin{pmatrix} 1 \\ i \left(\frac{n_R - n_L}{1 - n_R n_L} \right) \end{pmatrix}, \quad (2.25)$$

where we have disregarded a factor common to both the components. We can rewrite Eq. (2.25) as

$$\begin{pmatrix} 1 \\ i \left(\frac{n_R - n_L}{1 - n_R n_L} \right) \end{pmatrix} = \begin{pmatrix} 1 \\ \vartheta_K + i\varepsilon_K \end{pmatrix}, \quad (2.26)$$

where

$$\vartheta_K = -\Im \left(\frac{n_R - n_L}{1 - n_R n_L} \right) \approx \Im \left(\frac{\chi_{xy}}{\chi_{xx}\sqrt{1 + \chi_{xx}}} \right), \quad (2.27a)$$

$$\varepsilon_K = \Re \left(\frac{n_R - n_L}{1 - n_R n_L} \right) \approx -\Re \left(\frac{\chi_{xy}}{\chi_{xx}\sqrt{1 + \chi_{xx}}} \right) \quad (2.27b)$$

and the subscript K points out that we are considering the Kerr effect. The expansion used in obtaining Eqs. (2.27) implies that $n_R - n_L$ is of the order of χ_{xy} if $|\chi_{xy}| \ll 1$. Under this assumption we can identify ϑ_K as the Kerr rotation and ε_K as the Kerr ellipticity for the case of normal incidence. Again we see that these effects are proportional to the applied magnetic field and that the plane of polarization of light is rotated only if the interaction is occurring with an absorbing medium.

2.1.4   The full susceptibility tensor

The susceptibility tensor in Eq. (2.7) has been obtained under the assumption $\mathbf{H} = \hat{\mathbf{z}}H$, but considering $\mathbf{H} = \hat{\mathbf{x}}H_x + \hat{\mathbf{y}}H_y + \hat{\mathbf{z}}H_z$ the full susceptibility tensor in Cartesian coordinates can be derived [64]:

$$\chi = \frac{\omega_p^2}{L \left(L^2 - \omega^2 \omega_C^2 \right)} \mathfrak{X}, \quad (2.28)$$

where

$$L = \omega_0^2 - \omega^2 - i\Gamma\omega,$$

$$\mathfrak{X} = \begin{bmatrix} L^2 - \omega^2\omega_{Cx}^2 & iL\omega\omega_{Cz} - \omega^2\omega_{Cx}\omega_{Cy} & -iL\omega\omega_{Cy} - \omega^2\omega_{Cx}\omega_{Cz} \\ -iL\omega\omega_{Cz} - \omega^2\omega_{Cx}\omega_{Cy} & L^2 - \omega^2\omega_{Cy}^2 & iL\omega\omega_{Cx} - \omega^2\omega_{Cy}\omega_{Cz} \\ iL\omega\omega_{Cy} - \omega^2\omega_{Cx}\omega_{Cz} & -iL\omega\omega_{Cx} - \omega^2\omega_{Cy}\omega_{Cz} & L^2 - \omega^2\omega_{Cz}^2 \end{bmatrix},$$

$$\omega_{Ci} = \frac{e\mu_0 \mathrm{H}_i}{m} \quad (i = x, y, z).$$

By expanding the components of $\boldsymbol{\chi}$, we can get the relevant terms usually taken into account while considering magneto-optical effects:

$$\boldsymbol{\chi} \approx \boldsymbol{\chi}^{(0)} + \boldsymbol{\chi}^{(1)} + \boldsymbol{\chi}^{(2)}, \tag{2.29a}$$

$$\boldsymbol{\chi}^{(0)} = \frac{\omega_p^2}{\omega_0^2 - \omega^2 - i\Gamma\omega} \begin{bmatrix} 1 & 0 & 0 \\ 0 & 1 & 0 \\ 0 & 0 & 1 \end{bmatrix}, \tag{2.29b}$$

$$\boldsymbol{\chi}^{(1)} = \frac{\omega_p^2\omega}{(\omega_0^2 - \omega^2 - i\Gamma\omega)^2} \begin{bmatrix} 0 & i\omega_{Cz} & -i\omega_{Cy} \\ -i\omega_{Cz} & 0 & i\omega_{Cx} \\ i\omega_{Cy} & -i\omega_{Cx} & 0 \end{bmatrix}, \tag{2.29c}$$

$$\boldsymbol{\chi}^{(2)} = \frac{\omega_p^2\omega^2}{(\omega_0^2 - \omega^2 - i\Gamma\omega)^3} \begin{bmatrix} \omega_C^2 - \omega_{Cx}^2 & -\omega_{Cx}\omega_{Cy} & -\omega_{Cx}\omega_{Cz} \\ -\omega_{Cx}\omega_{Cy} & \omega_C^2 - \omega_{Cy}^2 & -\omega_{Cy}\omega_{Cz} \\ -\omega_{Cx}\omega_{Cz} & -\omega_{Cy}\omega_{Cz} & \omega_C^2 - \omega_{Cz}^2 \end{bmatrix}. \tag{2.29d}$$

The term $\boldsymbol{\chi}^{(0)}$ represents the susceptibility of an isotropic dielectric which can be obtained from Eq. (2.2) in case of no applied magnetic field. The term $\boldsymbol{\chi}^{(1)}$ is the *first order* correction in ω_{Ci} ($\forall i$) to $\boldsymbol{\chi}^{(0)}$. It introduces out-of-diagonal terms in Eq. (2.29a) which depend on the applied magnetic field intensity and direction. The term $\boldsymbol{\chi}^{(2)}$ is the *second order* correction to $\boldsymbol{\chi}^{(0)}$. It causes the appearance of terms depending on the applied magnetic field also in $\boldsymbol{\chi}$'s main diagonal. To be noted that $\boldsymbol{\chi}^{(1)}$ is an antisymmetric tensor, whereas $\boldsymbol{\chi}^{(2)}$ is a symmetric tensor, as it should be according to the symmetry properties of the magnetic field [64,65].

Moreover, until now the susceptibility tensor has only been derived for an ideal material containing electrons characterized by the same resonance frequency and damping parameter in the equation of motion (2.1). In general, an optical medium will have many characteristic resonance frequencies and, given the lin-

earity of the governing equations, the exhaustive form of Eq. (2.6) is

$$\mathbf{P} = \varepsilon_0 \left(\sum_j \boldsymbol{\chi}_j \right) \mathbf{E}, \tag{2.30}$$

where the sum runs over all the susceptibility tensors $\boldsymbol{\chi}_j$ of the involved oscillators. So, considering only the optical properties given by Eq. (2.29b) (for simplicity), we have for each diagonal element [51]:

$$\chi_{ii}^{(0)} = \omega_p^2 \sum_j \frac{f_j}{\omega_{0j}^2 - \omega^2 - i\Gamma_j\omega}. \tag{2.31}$$

This equation takes into account all the transitions in the medium and a set of phenomenological *oscillator strengths* f_j have been introduced to account for the quantum mechanical transition probabilities ($\sum_j f_j = 1$) in our classical model.

2.2 Magneto-optical effects in ferromagnets

The description of the magneto-optical effects in ferromagnets has been focused on the explanation of the unusual large effect showed by ferromagnetic materials, for which magneto-optical effects are up to five orders of magnitude more intense than in non-ferromagnetic bodies under the same external applied magnetic field. These effects are definitely connected to the ferromagnetic properties of the specimen, since for temperature higher than the Curie temperature of the materials they disappear along with the ferromagnetic behaviour.

The classical approach of Sec. 2.1.1 can be extended in order to evaluate the electronic equations of motion in metallic media, for which the conduction electrons play a fundamental role. In this case, the electrons are grouped into two sets, *bound electrons* and *conduction electrons*. For ferromagnetic metals, the effect of the magnetization $\mathbf{M}$ can be included thanks to the presence of an effective magnetic field $\eta\mathbf{M}$ proportional to the magnetization [66]. This field, called *Weiss field*, was postulated by Weiss [15] in order to account for the existence of ferromagnetic order and it is of the correct order of magnitude to justify the observed effects [67]. The theory of itinerant electron magnetism (valid for iron, cobalt, nickel and Permalloy as far as this thesis is concerned; see Sec. 1.2.3) allows us to include a Lorentz-force term only for the conduction electrons whose spins are unbalanced. In view of these considerations, the equations of

motion to be solved are, according to the notations used in Eq. (2.1),

$$m\ddot{\mathbf{r}}_1 \,+\, b_1\dot{\mathbf{r}}_1 \,+\, k_1\mathbf{r}_1 \,=\, -\,e\mathbf{E}, \tag{2.32a}$$

$$m\ddot{\mathbf{r}}_2 \,+\, b_2\dot{\mathbf{r}}_2 \,=\, -\,e\mathbf{E}, \tag{2.32b}$$

$$m\ddot{\mathbf{r}}_3 \,+\, b_3\dot{\mathbf{r}}_3 \,=\, -\,e\mathbf{E} \,-\, e\mu_0\dot{\mathbf{r}}_3 \times (\eta\mathbf{M}), \tag{2.32c}$$

for the bound electrons, the spin-balanced conduction electrons and the spin-unbalanced conduction electrons, respectively. The polarization of the medium can be obtained by the averaged effect given by the three groups of electrons, in the form of $\mathbf{P} = -\,(1-\alpha-\beta)\,ne\mathbf{r}_1 - \alpha ne\mathbf{r}_2 - \beta ne\mathbf{r}_3$, where $\alpha(\beta)$ are the fraction of spin-(un)balanced conduction electrons out of a total electron density n. This leads to an antisymmetric susceptibility tensor, in which the off-diagonal terms are proportional to the various components of the magnetization $\mathbf{M}$, as in the case of the tensor (2.7) obtained for a dielectric in an external applied magnetic field. All the electrons contribute to the susceptibility tensor, but in the presence of magnetism only the contribution from the spin-unbalanced conduction electrons is affected by the presence of the effective magnetic field $\eta\mathbf{M}$.

After the advent of quantum mechanics, Heisenberg was able to ascribe the Weiss field to the exchange interaction among electrons, providing an established description for ferromagnetic phenomena in terms of an effective field capable of aligning the individual spins. However, this effective field cannot be used to explain magneto-optical effects, since it is not coupled to the electron motion which determines the dielectric properties of a material and, consequently, the optical behaviour. This problem was solved by Hulme [68] introducing the fact that the spin-orbit interaction (see Sec. 1.2.1) couples the motion of an electron to its spin, providing the connection between magnetic and optical properties of a ferromagnetic material. Spin-orbit coupling results from the interaction of the electron spin $\mathbf{s}$ with the magnetic field the electron "sees" as it moves through the electric field $-\boldsymbol{\nabla}V(\mathbf{r})$ inside a medium with momentum $\mathbf{p}$. This coupling is expressed by a term proportional to $\mathbf{S} \cdot (\boldsymbol{\nabla}V(\mathbf{r}) \times \mathbf{p})$, which, to a certain extent, can be thought of as an effective magnetic field of vector potential proportional to $\mathbf{S} \times \boldsymbol{\nabla}V(\mathbf{r})$ acting on the motion of the electron [64, 69, 70]. For non-magnetic materials, this effect is not strong, although the spin-orbit interaction is present, because the equal number of spin-up and spin-down electrons cancels the effect. For ferromagnetic materials, the effect manifest itself because of the unbalanced population of electron spins. Kittel was able to show that in case of quenching of the orbital angular momentum, which leads to a weak spin-orbit coupling, the magneto-optic effects arise because of the change in the electronic wave function

due to spin-orbit interaction and induced by an externally applied magnetic field.

2.2.1 Argyres' theory

A full derivation of these effects in ferromagnets was given by Argyres [69] using the band theory of metals and the time-dependent perturbation theory in order to evaluate the effect of the spin-orbit interaction on the optical properties of ferromagnets, within the framework provided by the semiclassical theory of radiation. The assumptions taken by Argyres make his theory applicable only to visible and ultraviolet frequencies, which is not a limit, because this range of the electromagnetic spectrum is characterized by energies that indeed allow probing magneto-optical effects in ferromagnetic materials. To begin with, a one-electron Hamiltonian $\mathcal{H}$ can be used for describing the ground and the excited states of the system [69]:

$$\mathcal{H} \; = \; \mathcal{H}_0 \; + \; \mathcal{H}' \; + \; \mathcal{H}'', \tag{2.33}$$

where

$$\mathcal{H}_0 \; = \; \frac{1}{2m}\mathbf{p}^2 \; + \; V(\mathbf{r}), \tag{2.34a}$$

$$\mathcal{H}' \; = \; \frac{1}{2m^2c^2}\mathbf{S} \cdot \left(\boldsymbol{\nabla}V(\mathbf{r}) \times \mathbf{p}\right), \tag{2.34b}$$

$$\mathcal{H}'' \; = \; \frac{e}{m}\mathbf{A}(\mathbf{r},t) \cdot \mathbf{p}. \tag{2.34c}$$

In these expressions, m is the mass of the electron and $-e$ is its charge, $\mathbf{p} = -i\hbar\boldsymbol{\nabla}$ is the momentum operator and $\mathbf{S} = \hbar\boldsymbol{\sigma}/2$ is the electron spin operator. $V(\mathbf{r}) = -e\phi(\mathbf{r})$ is the potential energy of an electron in the crystal in the absence of radiation and it represents the averaged influence of the nuclei and all the other electrons on the electron under consideration. $\mathbf{A}(\mathbf{r},t)$ is the vector potential of the electromagnetic field inside the material. For a monochromatic wave of angular frequency ω, such a potential is

$$\mathbf{A}(\mathbf{r},t) \; = \; \mathbf{a}(\mathbf{r})\exp\left(-i\omega t\right) \; + \; \mathbf{a}^*(\mathbf{r})\exp\left(i\omega t\right). \tag{2.35}$$

Equation (2.34b) represents the spin-orbit interaction, whereas Eq. (2.34c) describes the interaction of an electron with the electromagnetic field in the material (only the largest term being kept). So, Eq. (2.33) is a simplified form of Eq. (1.16a).

Since the Hamiltonian operator $\mathcal{H}$ in Eq. (2.33) has to be used for solving the Schrödinger equation, $\mathcal{H}''$ can be treated as a perturbation of $\mathcal{H}_0 + \mathcal{H}'$ by

making use of the *time-dependent perturbation theory* [71]. The equation to be considered is

$$i\hbar \frac{d}{dt} |\Psi(t)\rangle = (\mathcal{H}_0 + \mathcal{H}' + \mathcal{H}'') |\Psi(t)\rangle. \tag{2.36}$$

Let us assume we know a complete set of unperturbed eigenstates satisfying

$$(\mathcal{H}_0 + \mathcal{H}') |\Phi_n\rangle = E_n^{(0)} |\Phi_n\rangle, \tag{2.37}$$

where the kets $|\Phi_n\rangle$ are taken to be time independent. So, the solution of Eq. (2.36) is given by

$$|\Psi(t)\rangle = \sum_n c_n(t) \exp\left(-\frac{iE_n^{(0)}t}{\hbar}\right) |\Phi_n\rangle, \tag{2.38}$$

where we have expanded $|\Psi(t)\rangle$ in terms of the complete set of eigenstate $|\Phi_n\rangle$ and

$$c_n(0) = \delta_{nk}, \tag{2.39a}$$

$$c_n(t) = \frac{1}{i\hbar} \int_0^t \exp(i\omega_{nk}\tau) \langle \Phi_n | \mathcal{H}''(\tau) | \Phi_k \rangle \, d\tau, \tag{2.39b}$$

$$\omega_{nk} = \frac{E_n^{(0)} - E_k^{(0)}}{\hbar}. \tag{2.39c}$$

$|\Phi_k\rangle$ represents the initial unperturbed state, whereas $|c_n(t)|^2$ (for $n \neq k$) is the probability that at time t a measurement of the state $|\Psi(t)\rangle$ yields the quantum numbers of the state $|\Phi_n\rangle$. The matrix element $\langle \Phi_n | \mathcal{H}''(t) | \Phi_k \rangle$ takes into account the transition between the states $|\Phi_n\rangle$ and $|\Phi_k\rangle$ induced by $\mathcal{H}''(t)$ and its symmetry properties give rise to transition rules. The fact that the these transitions occur between states whose energy is influenced by the spin-orbit interaction and the presence of a spin-unbalanced electron population determine the appearance of magneto-optical effects. Indeed, for calculating the total current density induced in the system, the current density that can be obtained in the one-electron approximation has to be summed over all the occupied states. Argyres divided the sums over states into (i) an integral over all states occupied by electrons with both spin directions (i.e. spin-balanced electrons) and (ii) an integral over states occupied by electrons with only one spin direction (i.e. spin-unbalanced electrons, which are responsible for the magnetic properties of the material), providing the foundation for the division of electrons into groups carried out in order to obtain Eqs. (2.32). In other words, the appearance of magneto-optical effects requires
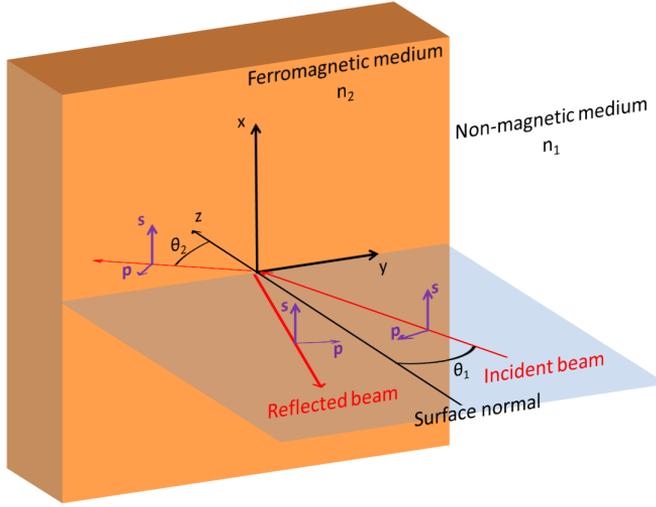
Figure 2.1: Coordinate system used in the description of the incidence of light which travels through a non-magnetic medium (with complex index of refraction n_1) and impinges on a ferromagnetic medium (with complex index of refraction n_2).

both the spin-orbit interaction and the exchange splitting effect.

From the conductivity and polarizability tensors relating the total current density to the elecromagnetic field represented by Eq. (2.35), a dielectric tensor ε for a ferromagnetic medium with magnetization **M** can be obtained, which for a cubic crystal has the following form [72]:

$$\boldsymbol{\varepsilon} \;=\; \boldsymbol{\varepsilon}^{(0)} + \boldsymbol{\varepsilon}^{(1)} \;=\; \varepsilon_{xx} \begin{bmatrix} 1 & -iQ\mathrm{m}_z & iQ\mathrm{m}_y \\ iQ\mathrm{m}_z & 1 & -iQ\mathrm{m}_x \\ -iQ\mathrm{m}_y & iQ\mathrm{m}_x & 1 \end{bmatrix}, \qquad (2.40)$$

where ε_{xx} is a factor independent from the magnetization and $Q \in \mathbb{C}$ is the *(Voigt) magneto-optical constant*, which is proportional both to the magnitude M of the magnetization and to the spin-orbit coupling strength, and it is frequency dependent [69]. The m_x, m_y and m_z components of **m** are the direction cosines of **M** in the coordinate system showed in Fig. 2.1. Actually, Agryres' theory has been developed considering a saturated ferromagnetic domain and the integral over the spin-unbalanced electrons returns a term proportional to the magnitude M_S of the saturation magnetization. So, Q results to be a *material property*. Experimentally, this fact has been exploited in order to get the critical exponent β through magneto-optical measurements of the temperature dependence of the magnetization, obtaining values in agreement with the theory of phase transitions

[73].

The tensor given in Eq. (2.40) for a cubic crystal can also be justified from considerations regarding the time reversal symmetry: the magnetic field changes sign under the time reversal operation [64, 65]. It follows that the Onsager's relation requires $\varepsilon_{ij}(\mathbf{M}) = \varepsilon_{ji}(-\mathbf{M})$ and expanding the dielectric tensor retaining up to linear terms in $\mathbf{M}$ (and so in Q), it can be seen that the antisymmetric part of $\boldsymbol{\varepsilon}$ is generated by the magnetization. Moreover, symmetries allows quickly determining also the form of the quadratic (second order in M) magneto-optical tensor $\boldsymbol{\varepsilon}^{(2)}$:

$$\boldsymbol{\varepsilon}^{(2)} = \begin{bmatrix} B_1 \mathrm{m}_x^2 & B_2 \mathrm{m}_x \mathrm{m}_y & B_2 \mathrm{m}_x \mathrm{m}_z \\ B_2 \mathrm{m}_x \mathrm{m}_y & B_1 \mathrm{m}_y^2 & B_2 \mathrm{m}_y \mathrm{m}_z \\ B_2 \mathrm{m}_x \mathrm{m}_z & B_2 \mathrm{m}_y \mathrm{m}_z & B_1 \mathrm{m}_z^2 \end{bmatrix} - B_1^* \mathbf{I}, \qquad (2.41)$$

where B_1 and B_2 describe the *Voigt effect*, whereas B_1^* does not depend on the magnetization direction and can be absorbed in the zero-order magneto-optical tensor $\boldsymbol{\varepsilon}^{(0)}$, so retrieving Eq. (2.41) in the form given by Ref. [72]. Equations (2.40) and (2.41) have the same structure owned by Eq. (2.29a), which has been obtained considering a classical approach to magneto-optical effects in dielectrics.

2.3 Macroscopic formalism for the MOKE

The MOKE is a powerful mean to probe the magnetization of ferromagnetic media which are opaque to visible light. Since the magnetic information depth of the MOKE is below 50 nm in metals, it can be employed to analyze the superficial region of bulk materials or to investigate magnetic thin films and nanostructures. Kerr rotation and ellipticity can be obtained for an arbitrary angle of light incidence, generalizing the approach described in Secs. 2.1.2 and 2.1.3, where only normal incidence is considered. Figure 2.1 shows the geometry considered in order to solve Maxwell equations in the case of reflection from a boundary between a non-magnetic medium and a medium characterized by the dielectric tensor (2.40). The polarization of the electromagnetic wave is described in terms of the component of the electric field vector along the p-axis, that lies in the scattering plane, and along the s-axis, that is normal to the scattering plane. So, the electric field vector $\mathbf{E}^i$ of the incident wave is connected to the electric field vector $\mathbf{E}^r$ of the reflected wave through the Fresnel reflection matrix $\mathfrak{R}$:

$$\begin{pmatrix} E_p^r \\ E_s^r \end{pmatrix} = \mathfrak{R} \begin{pmatrix} E_p^i \\ E_s^i \end{pmatrix} = \begin{bmatrix} r_{pp} & r_{ps} \\ r_{sp} & r_{ss} \end{bmatrix} \begin{pmatrix} E_p^i \\ E_s^i \end{pmatrix}, \qquad (2.42)$$

where the Fresnel coefficients are given by [74–76]

$$r_{pp} = \frac{n_2 \cos \vartheta_1 - n_1 \cos \vartheta_2}{n_2 \cos \vartheta_1 + n_1 \cos \vartheta_2} - \frac{2in_1 n_2 \cos \vartheta_1 \sin \vartheta_2 \mathrm{m}_x Q}{\left(n_2 \cos \vartheta_1 + n_1 \cos \vartheta_2 \right)^2}, \tag{2.43a}$$

$$r_{ps} = -\frac{in_1 n_2 \cos \vartheta_1 \left(\mathrm{m}_y \sin \vartheta_2 - \mathrm{m}_z \cos \vartheta_2 \right) Q}{\left(n_2 \cos \vartheta_1 + n_1 \cos \vartheta_2 \right) \left(n_1 \cos \vartheta_1 + n_2 \cos \vartheta_2 \right) \cos \vartheta_2}, \tag{2.43b}$$

$$r_{sp} = \frac{in_1 n_2 \cos \vartheta_1 \left(\mathrm{m}_y \sin \vartheta_2 + \mathrm{m}_z \cos \vartheta_2 \right) Q}{\left(n_2 \cos \vartheta_1 + n_1 \cos \vartheta_2 \right) \left(n_1 \cos \vartheta_1 + n_2 \cos \vartheta_2 \right) \cos \vartheta_2}, \tag{2.43c}$$

$$r_{ss} = \frac{n_1 \cos \vartheta_1 - n_2 \cos \vartheta_2}{n_1 \cos \vartheta_1 + n_2 \cos \vartheta_2}. \tag{2.43d}$$

In the above equations, n_1 is the complex index of refraction of the non-magnetic medium, n_2 is the complex index of refraction of the ferromagnetic medium, ϑ_1 is the complex angles of incidence and ϑ_2 is the complex angle of refraction, as given by Snell's law. Equation (2.42) has been derived by means of the dielectric tensor (2.40) and only terms up to first order in Q has been considered [75]. The Kerr rotation ϑ_K and ellipticity ε_K are defined through the Fresnel coefficients as

$$|\vartheta_{Kp}| = \Re \left(\frac{r_{sp}}{r_{pp}} \right), \tag{2.44a}$$

$$|\vartheta_{Ks}| = \Re \left(\frac{r_{ps}}{r_{ss}} \right), \tag{2.44b}$$

$$|\varepsilon_{Kp}| = \Im \left(\frac{r_{sp}}{r_{pp}} \right), \tag{2.44c}$$

$$|\varepsilon_{Ks}| = \Im \left(\frac{r_{ps}}{r_{ss}} \right). \tag{2.44d}$$

The subscripts p and s refer to the fact that this definition are strictly effective only for linearly p-polarized and linearly s-polarized incident light, respectively. Since a multiplicity of sign conventions for rotation and ellipticity appears in literature, the above equations express only the modulus of the rotation and ellipticity, while the sign must be chosen in agreement with the adopted convention [77]. The definitions in Eqs. (2.44) are strictly valid only if $\vartheta_K, \varepsilon_K \ll 1$, as derived in Sec. B.2. However, this is indeed the case for typical materials, as shown in the next paragraphs.

As we have already seen, the effect of the magnetization is contained in Q:

if $Q = 0$, only the Fresnel coefficients r_{pp} and r_{ss} are different from zero and they are reduced to the usual form valid for the reflection between dielectric media. In this case, the Kerr rotation and ellipticity are zero, for both p- and s-polarization of the incoming light. When $Q \neq 0$, different kind of MOKEs can be distinguished, depending on the relative direction of the magnetization with respect to the scattering plane:

- **polar MOKE**, characterized by $m_z = 1$ and $m_x = m_y = 0$, i.e. the magnetization is parallel to the surface normal;

- **longitudinal MOKE**, characterized by $m_y = 1$ and $m_x = m_z = 0$, i.e. the magnetization is parallel to the surface of the interface and lies on the scattering plane;

- **transversal** (or **equatorial**) **MOKE**, characterized by $m_x = 1$ and $m_y = m_z = 0$, i.e. the magnetization is parallel to the surface of the interface and normal to the scattering plane.

According to the direction of the magnetization to be probed, the relevant Fresnel coefficients are different, but in all cases the effects are proportional to the intensity of the magnetization [76]. To be noted the fact that the trasversal MOKE does not produce Kerr rotation and ellipticity for linearly s- or p-polarized impinging light, but it only induces a change in the intensity of linearly p-polarized light, since r_{ss} does not depend on Q and from $m_y = m_z = 0$ follows that $r_{ps} = r_{sp} = 0$.

In order to point out the overall features of Eqs. (2.42) and (2.44) and the strength of the effects, Figs. 2.2a, 2.2b, 2.3a and 2.3b show the dependence from the incidence angle ϑ_1 of Kerr rotation and ellipticity in both polar and longitudinal configurations for red visible light of 635 nm wavelength in bulk Permalloy ($n_2 = 1.93 + 3.11i$, $Q = 0.0094 - 0.0081i$) [78]. Since $|Q| \ll 1$, the assumption of retaining terms up to first order in Q is valid. Polar ϑ_K and ε_K are even functions of the incidence angle, for both p and s polarization of the incident light, while longitudinal ϑ_K and ε_K are odd functions of the incidence angle and so they are equal to zero for $\vartheta_1 = 0$, for both p and s polarization. These features are very important in defining the geometry of the apparatus that can be used to measure MOKEs. Indeed, through the dependence of ϑ_K and ε_K from ϑ_1, the angle of incidence of light can be optimized in order to maximize the measured effect: a good general choice for the polar MOKE configuration is to work with an angle of incidence close to $\vartheta_1 = 0$, while this is a condition to be avoided for the longitudinal MOKE configuration, being the effect null in this case. Moreover, Figs.

2.4a and 2.4b show the fact that (for bulk Permalloy at $\vartheta_1 = 35°$) the Kerr rotation and ellipticity in the longitudinal configuration are function of the incidence wavelength λ, since both n_2 and Q are wavelength-dependent [78]. Generally, it is true that (i) what effect should be measured (ϑ_K or ε_K), (ii) what polarization of incident light should be employed (p or s polarization) and (iii) what incidence wavelength has to be chosen are factors which are material-dependent and which must be carefully taken into account during the design of the measurement setup.

(a) p polarization

(b) s polarization
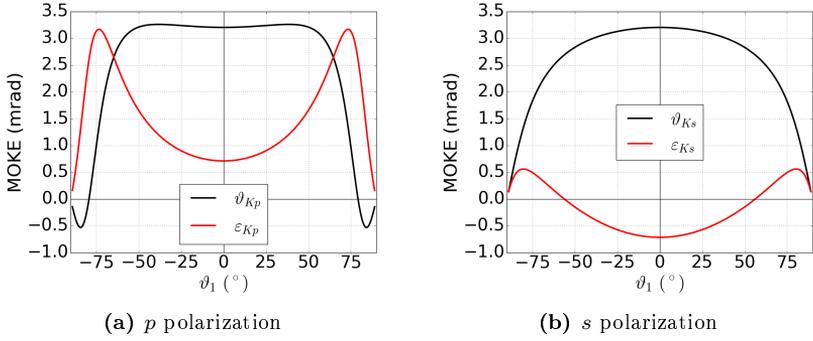
Figure 2.2: Angular dependence in bulk Py of the polar Kerr rotation ϑ_K and elliptic-ity ε_K for both p and s linearly polarized light of 635 nm wavelength ($n_2 = 1.93 + 3.11i$, $Q = 0.0094 - 0.0081i$).

(a) p polarization

(b) s polarization
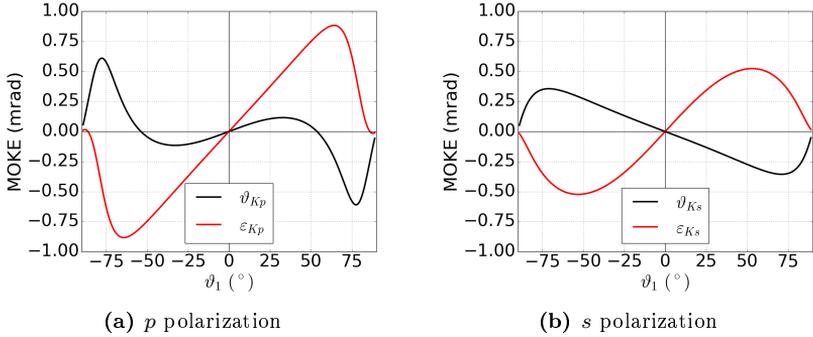
Figure 2.3: Angular dependence in bulk Py of the longitudinal Kerr rotation ϑ_K and ellipticity ε_K for both p and s linearly polarized light of 635 nm wavelength ($n_2 = 1.93 + 3.11i$, $Q = 0.0094 - 0.0081i$).

(a) p polarization
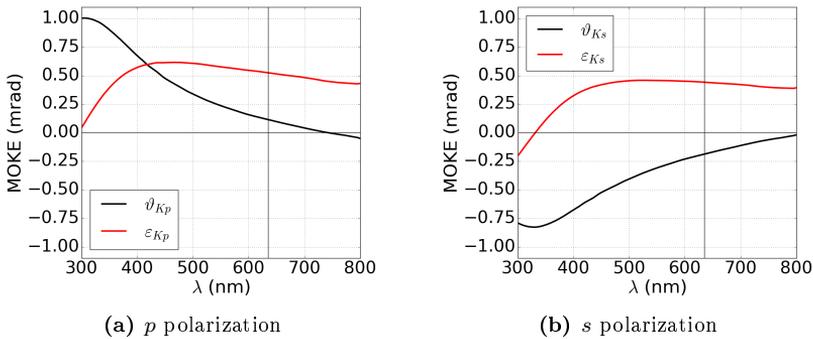
(b) s polarization

Figure 2.4: Wavelength dependence in bulk Py of the longitudinal Kerr rotation ϑ_K and ellipticity ε_K for both p and s linearly polarized light ($\vartheta_1 = 35°$). The black vertical lines correspond to $\lambda = 635$ nm.

Chapter 3

Fabrication and Characterization

Nanotechnology, although envisioned almost sixty years ago, is at the forefront of the current technological and scientific innovation. In his famous talk *There's Plenty of Room at the Bottom* (1959) [4], Richard P. Feynman discussed "the problem of manipulating and controlling things on a small scale". The word "nanotechnology" was coined much later, but Feynman's words nicely introduce two fundamental aspects of this field: *manipulation* and *control*. This chapter deals with both of them, according to what has been done for achieving the results summarized in this thesis. In particular, through advanced nanofabrication techniques, we were able to *fabricate* arrays of magnetic nanostructures, which have been properly *characterized* in order to verify the achievement of the designed properties.

3.1 Nanofabrication: electron beam lithography

The study of nanostructures paved the way for the emergency of many interesting behaviours not occurring while considering bulk materials. These emergent properties are due to *confinement*, i.e. the reduction of at least one dimension of the considered structure down to nanometer size. Actually, the definition of confinement can be made more precise if stated in terms of the *mesoscopic condition* [2]

$$L \approx \rho_C, \tag{3.1}$$

where ρ_C is the characteristic length scale of the involved phenomenon and L is the nanostructure confinement length. So, it is the interplay between ρ_C and L which determines the nanostructure properties. The phenomena we are interested in include both ferromagnetism in metallic nanostructures and their interaction with visible/NIR light, determining a confinement length in the range $10-1000$ nm. For this reason, fabrication techniques with a resolution of ≈ 10 nm are required in order to produce ensembles of nanostructures showing the desired properties.

Electron beam lithography (EBL) is the fabrication technique we selected for this purpose, because of some key features matching our needs:

- **nominal resolution of $\approx$ 20 nm**, which is by far enough for the properties we want to investigate (as shown in the following chapters);

- **very high flexibility in the design of extended samples** (maskless lithography), which is of utmost importance in the fabrication of nanostructures for research purposes;

- **in-house availability of EBL systems** (RAITH150 Two and eLINE by Raith), which allowed us to produce sample batches in a reasonable amount of time.

The EBL technique is conceptually derived from the *scanning electron microscopy* (SEM) technique, which has been complemented with the hardware and electronics needed for generating arbitrary patterns by sweeping the electron beam (e-beam) in a controlled way.

Appendix A contains a schematic workflow of the nanofabrication process (see Fig. A.1) and the recipes we used for fabricating the samples related to this thesis. The following sections are devoted to summarize some relevant concepts in EBL in order to properly understand the most important workflow steps.

3.1.1   The role of electrons

EBL systems exploit the electron-matter interaction in order to deposit energy in the desired pattern in a sample covered by an e-beam resist film. As the electrons produced in the EBL column enter the sample, they interact as negatively charged particles with the electromagnetic fields of the sample atoms. The positive charge of protons is highly concentrated in the nucleus, while the negative charge of the atomic electrons is much more dispersed in a shell structure. The interaction between beam electrons and sample atoms can deflect the beam electrons along new trajectories, causing them to spread out laterally from

the incident beam footprint. This kind of scattering, which is elastic (no kinetic energy loss), can result in beam electrons leaving the sample after numerous events, a process called *backscattering*. The cross section for elastic scattering increases along with the atomic number Z, approximately as Z^2, since heavier atoms possess a much stronger positive charge in their nucleus, and decreases as the electron energy E increases, approximately as $1/E^2$ [79]. Backscattering is quantified by the backscatter coefficient η, which is defined as

$$\eta \ = \ \frac{n_{BSe}}{n_{beam}}, \tag{3.2}$$

where n_{BSe} is the number of backscattered electrons and n_{beam} is the number of beam electrons incident on the sample.

Simultaneously with elastic scattering, the beam electrons lose energy and transfer this energy in various ways to the sample atoms (*inelastic scattering*), but the transfer takes place gradually, so that the beam electrons propagate through many atom layers into the sample before losing all their energy and getting trapped. The rate of energy loss dE with respect to the traveled distance dr can be described by the Bethe formula for electrons [80], whose main features are:

$$\frac{dE(r)}{dr} \ \propto \ -\frac{nZ}{E(r)} \ln\left(\frac{E^2(r)}{c_1 Z^2}\right), \tag{3.3}$$

where n is the number of sample atoms per unit volume, Z is the atomic number, $E(r)$ is the electron energy at point r and c_1 is a constant with energy dimensions. Both electrons (*secondary electrons*) and x-rays are emitted from the sample atoms during inelastic scattering, but only secondary electrons are of particular relevance in the EBL framework. Secondary electrons are loosely bound outer shell electrons from the sample atoms which receive sufficient kinetic energy during inelastic scattering events to be ejected from the atom and set into motion. The kinetic energy associated with these events is low (usually less than 50 eV) with respect to the beam electrons energy (several keV) and so 50 eV represents the (arbitrary) limit below which electrons travelling in the sample are considered secondary electrons. Despite their low energy and depending where they are generated (the closer to a surface, the better), secondary electrons can reach the sample surface and escape from it, along with backscattered electrons. Secondary electrons are produced along the entire beam electron trajectories within the sample, so the path of beam electrons within the sample is a continuous occurrence of elastic and inelastic scatterings, losing energy inside the sample (production of secondary electrons) and changing direction, until they get

trapped or can leave the sample (as backscattered electrons).

To clarify these concepts, let us consider two practical cases. An e-beam with 5 nm diameter and an energy $E_0 = 20$ keV (typical parameters for EBL) strikes the surface of both a silicon ($Z = 14$, $n \approx 5.0 \cdot 10^{22}$ atoms $\cdot$ cm^{-3}) and a gold ($Z = 79$, $n \approx 5.9 \cdot 10^{22}$ atoms $\cdot$ cm^{-3}) sample. Figures 3.1a and 3.1b show the interaction volume produced by the beam electrons as they enter the samples. The *interaction volume* represents the sample volume in which the beam electrons undergo elastic and inelastic scatterings, until they lose all their energy. Each figure has been obtained through a Monte Carlo electron trajectory simulator [81] and shows 1000 traces out of the 500 000 simulated ones. The path color goes from yellow to blue according to the reduction in the electron kinetic energy, while the red traces represent electron trajectories emerging as backscattered electrons. The first thing to be noted is the huge difference in the interaction volume between silicon and gold (approximately two orders of magnitude). This can be understood in terms of Eq. (3.3), which predicts higher energy losses for gold and so a shorter path average length. Moreover, the simulations allow for extracting the backscatter coefficients (see Eq. (3.2)):

$$\eta_{Si} = 0.14,$$
$$\eta_{Au} = 0.45.$$

The obtained values reflect the fact that the probability of elastic scattering events increases along with the atomic number Z. The difference in the backscatter coefficients can also be seen by comparing Fig. 3.1a and the inset of Fig. 3.1b (zoom in of the gold interaction volume), where the number of red traces normalized to the total number of depicted traces indeed represents the backscatter coefficient (and visually appears as a "density" of red traces). The last interesting information on electron-matter interaction comes from Fig. 3.1c, where the normalized number of backscattered electron traces is shown as a function of the kinetic energy these electrons possess when leaving the samples. Since the beam electrons in silicon are characterized by longer paths with respect to gold, the backscattered electrons emerging from the silicon sample have lost more energy with respect to beam electrons travelling through gold, which instead corresponds to a peaked distribution around an energy value of $\approx 0.93 E_0$.
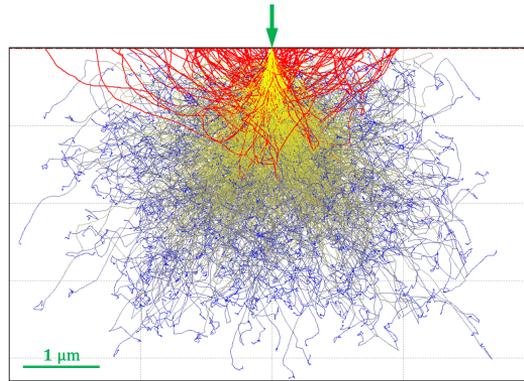
(a) Silicon
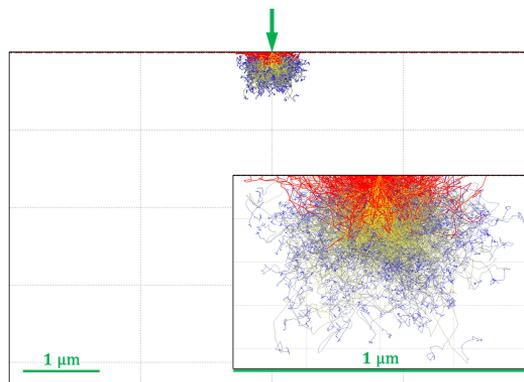
(b) Gold
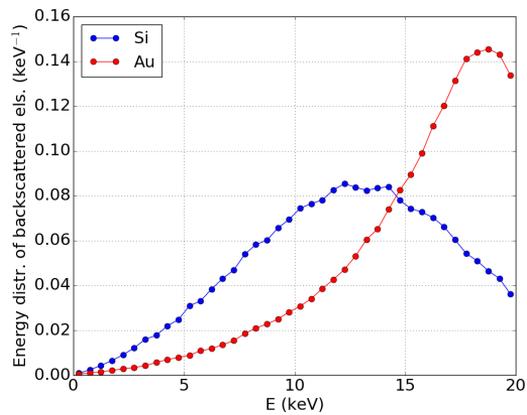
(c) Energy distribution

Figure 3.1: (a),(b) Calculated interaction volume for a 20 keV e-beam striking silicon and gold, respectively. The green arrows show the striking point. The path color goes from yellow to blue according to the reduction in the electron kinetic energy. The beam electron trajectories emerging as backscattered electrons are shown as red traces. (c) Backscattered electrons energy distribution for silicon (blue-dotted line) and gold (red-dotted line).

3.1.2   The role of e-beam resists

E-beam *resists*, composed by long polymer molecules, play an active and fundamental role during the EBL process. The sample to be patterned has to be covered by an e-beam resist film in order to generate the desired mask after e-beam exposure. As in photolithograpy, the resist volume interacting with beam electrons undergoes structural changes which modify the resist solubility in the proper solvent (a process called *development*), so the patterned structures can be imprinted in the resist film.

Resist materials are classified into two broad categories, *positive* and *negative* [82]. Positive resists dissolve preferentially during development in regions which have been exposed, while the reverse is true for negative resists. Positive-resist materials consist of long polymer molecules which are degraded by chain scission during exposure, thereby becoming more soluble in the developing solution. Negative-resist materials also consist of polymer molecules, but, upon exposure, the dominant reaction is the formation of bound polymer molecules by cross linking, making the exposed volume more resistant to the developing solution. To be noted that the *developing time* (and not only what happens during the exposure process) is an important parameter for EBL fabrication, since the time a sample is dipped in the developing solution determines the amount of removed exposed resist.

Figure 3.2 helps in clarifying how the exposure process of e-beam resists works. It shows the simulated interaction volume [81] determined by a 5 nm diameter e-beam with 20 keV energy impinging on the surface of a silicon substrate covered by a 100 nm thick polymethyl methacrylate (PMMA) layer, a widely used positive resist [83]. As for Fig. 3.1, 1000 traces are depicted out of the 500 000 simulated ones. Comparing the interaction volume in Fig. 3.2a with the one shown in Fig. 3.1a and extracting the backscatter coefficient from the simulation ($\eta_{PMMA|Si} \approx 0.14$), it can be seen that such a thin PMMA layer is of little (or no) influence on the scattering events occurring in the substrate material. This implies that the substrate itself plays a fundamental role during e-beam exposure. In particular, for insulating substrates, (i) the lack of a conductive path to ground, (ii) the additional capacitance of the substrate and (iii) a significant additional charge coming from the stopping of beam electrons can lead to *substrate charging* [79]. It consists in the accumulation of negative charges, whose parasitic electric fields deflect the impinging beam electrons making, in the worst case, the patterning impossible, since the deflection is time dependent and not practically predictable.

The quantity that controls the exposure (and so the change in solubility) of an
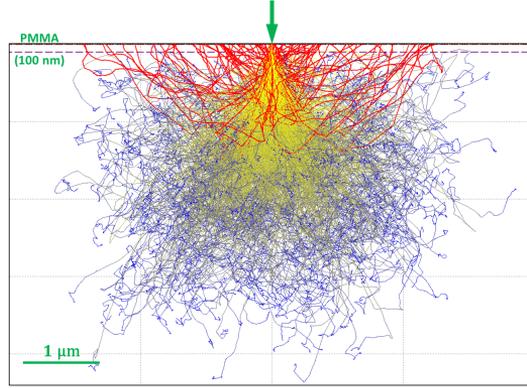
(a) PMMA|Si traces
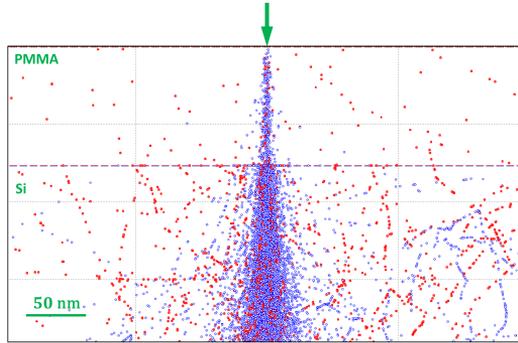
(b) PMMA|Si events

Figure 3.2: (a) Calculated interaction volume for a 20 keV e-beam striking a PMMA(100 nm)|Si bilayer. The path color goes from yellow to blue according to the reduction in the electron kinetic energy. The beam electron trajectories emerging as backscattered electrons are shown as red traces. (b) Zoom in of (a) in which each open dot (red for backscattered electrons) represents a scattering event. The green arrows show the striking point.

e-beam resist is the total energy absorbed per unit volume (energy density $\mathcal{E}$) and each resist is characterized by a critical value $\mathcal{E}_C$ needed to get a proper exposure. Considering only the PMMA layer in Fig. 3.2b, the blue-open dots represent the scattering events associated with the striking electrons in their "forward" propagation through the resist. The inelastic subset of these events deposits the average energy ΔE_F per incident electron in the resist layer, contributing to its structural modification. Moreover, the red-open dots in Fig. 3.2b represent the scattering events associated with backscattered electrons. Because of the oblique trajectories of backscattered electrons and their lower energies with respect to impinging electrons, they are a factor β ($\approx 4 - 5$) more efficient at generating secondary electrons, and so on depositing energy in the resist layer [82]. For this

reason, the average energy loss ΔE_{BSe} per backscattered electron in the resist layer is given by $\Delta E_{BSe} = \beta\eta\Delta E_F$, where η is the backscatter coefficient from Eq. (3.2). Assuming that the energy is absorbed uniformly in a resist volume V during the exposure time Δt_{exp}, the absorbed energy density $\mathcal{E}$ can be obtained by the expression [82]

$$\mathcal{E} \ = \ \frac{(1+\beta\eta)\,\Delta E_F}{e\ V} I_{beam}\Delta t_{exp}, \qquad\qquad (3.4)$$

where e is the electron charge magnitude and I_{beam} is the current associated with the impinging electron beam. The assumption related to a uniform absorption of energy in the resist, justified in case of a thin resist layer, allowed transforming the integration of elementary events in a simple sum: at each point, the relevant absorbed energy density $d\mathcal{E}$ is given by the forward energy deposited in that point and the energy deposited by the backscattered electrons produced while scanning the e-beam over the resist surface S designed for patterning. In this case, the average effect is precisely given by Eq. (3.4). Hence, considering a resist of thickness z, the interaction volume V can be expressed as $V = S \cdot z$, and Eq. (3.4) can be modified to

$$\mathcal{E} \ = \ \frac{(1+\beta\eta)\,\Delta E_F}{e\ z} \cdot \frac{I_{beam}\Delta t_{exp}}{S} \ \equiv \ \frac{(1+\beta\eta)\,\Delta E_F}{e\ z} \cdot D, \qquad (3.5)$$

where we have defined the *exposure dose D*. In the contest of EBL, the compact forward-scattered energy distribution determines the ultimate resolution. However, a limiting factor for the EBL resolution is given by the *proximity effect*, caused by the exposure of the resist by backscattered electrons and constituting a background on which the designed pattern is superimposed. The proximity effect can be mitigated by varying the dose according to the position on the sample and by optimizing the development time.

The exposure dose allows quantifying two important properties which can be used to further classify e-beam resists and to express their performances. Figure 3.3 shows a typical plot of the fraction of positive e-beam resist thickness left after its development as a function of D (for fixed development time). In case of a negative resist, the blue curve is mirrored with respect to a symmetry plane parallel to the y-axis and intersecting the curve at $y = 0.5$ (i.e. all the negative resist thickness is retained for high doses). For a positive resist, the critical dose (related to $\mathcal{E}_C$) is the D value at which, for a given development time, all the exposed resist volume dissolves and the resist thickness left in the patterned area is zero. Actually, the transition from exposed to unexposed resist is not abrupt,
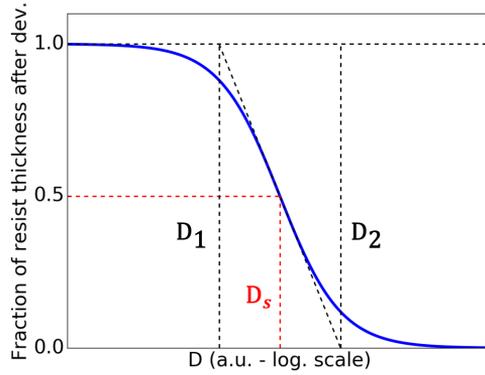
Figure 3.3: Typical plot of the fraction of positive e-beam resist thickness left (y) after development as a function of the exposure dose (for fixed development time). D_1 and D_2 are determined by the intersection between the line having the slope of the blue curve in its central part and the $y = 0$, $y = 1$ lines. D_s is the point corresponding to $y = 0.5$ according to the blue curve.

but it occurs with a certain slope. So, the dose D_2 can be taken as a measure of the critical dose and the values D_1 and D_2 allow defining the *contrast* γ of an e-beam resist [82]:

$$\gamma \;=\; \left[\log_{10}\left(\frac{D_2}{D_1} \right) \right]^{-1}. \tag{3.6}$$

The contrast of a resist determines its capacity of producing arrays of steep and close nanostructures. The *sensitivity* of an e-beam resist indicates the "ease" of being modified by the exposure process: an high sensitivity resist needs a lower value of $\mathcal{E}$ (and so of D) with respect to a low sensitivity resist in order to be properly exposed. To quantify this aspect, the dose D_s in Fig. 3.3 is usually considered and it corresponds to a fraction of resist thickness left after development of 0.5. It can be seen that [82]

$$D_s \;=\; \sqrt{D_1 D_2}. \tag{3.7}$$

Fixing the e-beam current and the exposed area, high sensitivity resists require a lower exposure time than low sensitivity resists, so allowing for faster patterning.

PMMA is a high-resolution high-contrast resist and it constitutes the standard positive resist for EBL. The blue-open dots in the PMMA layer depicted in Fig. 3.2b show an interesting phenomenon: the volume exposed by the forward-scattered beam electrons has a conical shape, since the beam diameter at the PMMA|Si interface is larger than the striking diameter. This feature leads to a conical shape of the developed patterned structures, where the base of the

trench (or pillar for negative resist) results wider than the top. The resulting profile (*undercut*) is helpful during the lift-off process (the resist removal after depositing the target material), since it allows for a safe and fast resist detachment. Nonetheless, a too pronounced undercut can lead to the merging of the developed structure bases in case of a densely packed array of repeated entities. Better results in this respect can be achieved by using the ZEP positive e-beam resist [84], the choice for most of the samples described in this thesis. Moreover, ZEP is characterized by higher sensitivity than PMMA, so allowing for shorter exposure times.

3.2   The MOKE measurement technique

The interaction of an electromagnetic wave with a ferromagnetic body produces a change in the wave polarization whose extent is proportional to the magnetization of the probed volume (see Chap. 2). Since the penetration depth of visible/NIR light is below 50 nm in metals, the measurement of the magneto-optical Kerr effect (MOKE) is an effective mean for obtaining information about the magnetic properties of the surface of bulk metallic materials or to investigate magnetic thin films and nanostructures. It is possible to design experimental setups that allow performing a quantitative evaluation of the magneto-optic effects and the complete magneto-optical characterization of a sample, in terms of both magnetization orientation and magneto-optical constants [66,67,85–87]. The experimental MOKE setup used in order to obtain the measurements presented in this thesis is based on the *polarization modulation technique* [86], in which the polarization state of the light reflected from the sample is modulated in order to extract both the *rotation* and the *ellipticity* coming from the interaction with the sample. The definition of these two parameters is given in Sec. B.2. Before describing in detail the polarization modulation technique, it is quite useful considering the basic aspects of the MOKE measurement technique.

The MOKE is described by Eq. (2.42), where the effect of the light-sample interaction is contained in each one of the Fresnel coefficients, whose main features can be summarized (at first order) as:

$$r_{pp} = A - B\mathrm{m}_x, \tag{3.8a}$$

$$r_{ps} = -C\mathrm{m}_y + D\mathrm{m}_z, \tag{3.8b}$$

$$r_{sp} = C\mathrm{m}_y + D\mathrm{m}_z, \tag{3.8c}$$

$$r_{ss} = E, \tag{3.8d}$$

where $A, B, C, D, E \in \mathbb{C}$ are proportionality factors depending on the angle of incidence and on material properties, whereas the m_x, m_y and m_z components of $\mathbf{m}$ are the direction cosines of the magnetization $\mathbf{M}$ in the coordinate system showed in Fig. 2.1. All the magnetization components appear in the Fresnel coefficients, so by selecting a proper MOKE configuration is possible to define an appropriate sensitivity direction (in the scattering plane or perpendicular to it) and to perform magneto-optical vectometry [66, 86, 87]. However, in the framework of this thesis, the most relevant magnetization components are the ones lying in the scattering plane (i.e. corresponding to m_y and m_z), so we restrict our description to impinging s-polarized light. Making use of Jones calculus for modelling the optical path (see Sec. B.1), the interaction between a monochromatic linearly s-polarized incident wave $\mathbf{E}^i$ and the sample gives rise to an elliptically polarized reflected wave $\mathbf{E}^r$ expressed by

$$\begin{pmatrix} E_p^r \\ E_s^r \end{pmatrix} = \begin{bmatrix} r_{pp} & r_{ps} \\ r_{sp} & r_{ss} \end{bmatrix} \begin{pmatrix} 0 \\ E_s^i \end{pmatrix} = E_s^i \begin{pmatrix} r_{ps} \\ r_{ss} \end{pmatrix} \propto \begin{pmatrix} \frac{r_{ps}}{r_{ss}} \\ 1 \end{pmatrix}, \qquad (3.9)$$

having neglected a factor common to both the components which does not depend on the magnetization. From Eqs. (2.44b) and (2.44d) follows that

$$\begin{pmatrix} \frac{r_{ps}}{r_{ss}} \\ 1 \end{pmatrix} = \begin{pmatrix} \vartheta_{Ks} + i\varepsilon_{Ks} \\ 1 \end{pmatrix}, \qquad (3.10)$$

where ϑ_{Ks} and ε_{Ks} are the Kerr rotation and ellipticity for impinging s-polarized light, respectively. The analysis of the light polarization state is performed through optical elements which allow modifying the polarization of the wave in a controlled way, in order to extract information from a subsequent intensity measurement through a photodetector. The direct evaluation of the intensity of the vector (3.10) provides a signal that is proportional to the square of the magnetization, losing the distinction between the two saturation states. A first improvement consist in the insertion of a *linear polarizer* between the sample and the detector. The effect of this optical element is described by the Jones matrix in Eq. (B.12) and the intensity I of the resulting vector is given by

$$I \propto \left| \begin{bmatrix} \cos^2\alpha & \cos\alpha\sin\alpha \\ \cos\alpha\sin\alpha & \sin^2\alpha \end{bmatrix} \begin{pmatrix} \vartheta_{Ks} + i\varepsilon_{Ks} \\ 1 \end{pmatrix} \right|^2, \qquad (3.11)$$

where α is the angle of the polarization axis of the polarizer with respect to the direction of extinction for linearly s-polarized light. The evaluation of Eq. (3.11)

gives

$$I \ \propto \ \left(\vartheta_{Ks}^2 + \varepsilon_{Ks}^2\right)\cos^2\alpha \ + \ \sin^2\alpha \ + \ \vartheta_{Ks}\sin\left(2\alpha\right), \tag{3.12}$$

showing that, up to first order in ϑ_{Ks} and ε_{Ks}, the intensity is proportional to the Kerr rotation and so to the magnetization. However, through this setup only the Kerr rotation is attainable and it can be a limit either when the Kerr ellipticity is dominant over the Kerr rotation (as in the case of Permalloy) or when both these effects have to be measured for the same sample. In order to achieve sensibility to both the components, a *linear retarder* can be inserted between the sample and the polarizer. If the Jones matrix in Eq. (B.13) is inserted in the optical train of Eq. (3.11), the intensity of the resulting vector is given by

$$I \ \propto \ \left\| \begin{bmatrix} \cos^2\alpha & \cos\alpha\sin\alpha \\ \cos\alpha\sin\alpha & \sin^2\alpha \end{bmatrix} \begin{bmatrix} 1 & 0 \\ 0 & \mathrm{e}^{i\phi} \end{bmatrix} \begin{pmatrix} \vartheta_{Ks} + i\varepsilon_{Ks} \\ 1 \end{pmatrix} \right\|^2, \tag{3.13}$$

where the fast-axis of the linear retarder is parallel to the s-axis and the phase of the fast-axis wave advances the slow-axis wave by ϕ. Equation (3.13) becomes

$$\begin{aligned} I \ \propto \ & \left(\vartheta_{Ks}^2 + \varepsilon_{Ks}^2\right)\cos^2\alpha \ + \ \sin^2\alpha \\ & + \ \left(\vartheta_{Ks}\cos\phi + \varepsilon_{Ks}\sin\phi\right)\sin\left(2\alpha\right). \end{aligned} \tag{3.14}$$

When $\phi = 0$ or $\phi = \pi/2$, a signal proportional to the Kerr rotation or to the Kerr ellipticity can be obtained, respectively, and for each choice of the retardation, the intensity is proportional to the magnetization, up to first order in ϑ_{Ks} and ε_{Ks}. Moreover, given ϑ_{Ks} and ε_{Ks}, the maximum detected intensity as a function of α occurs when

$$\tan\left(2\alpha\right) \ = \ \frac{2\left(\vartheta_{Ks}\cos\phi + \varepsilon_{Ks}\sin\phi\right)}{\vartheta_{Ks}^2 + \varepsilon_{Ks}^2 - 1}, \tag{3.15}$$

which corresponds to Eq. (B.5), showing that in this case the polarization axis of the polarizer coincides with the major axis of the ellipse swept by the electric field vector of the reflected light during its propagation towards the photodetector.

3.2.1   The polarization modulation technique

The polarization modulation technique provides a powerful way for measuring and *quantifying* both ϑ_{Ks} and ε_{Ks}. Equation (3.15) suggests a possible method: the angle α, which can be experimentally controlled and determined, is directly related to ϑ_{Ks} and ε_{Ks}, depending on the considered ϕ value. However, there are two major drawbacks:

- rotation and ellipticity needed to be measured are small, usually below 1 mrad, and directly measuring such small angles with enough resolution for probing the MOKE (of the order of 0.01 mrad) is not possible;

- the measure of small electric signals requires a technique capable of distinguishing them from noise.

Both these issues can be addressed and solved by the polarization modulation technique: instead of fixing the phase retardation ϕ in Eq. (3.14), this parameter is modulated at a constant frequency ω. By doing so, both ellipticity and rotation can be obtained during the same measurement and two *lock-in amplifiers* can be utilized to reject all the electronic signals lying out of a narrow frequency band around ω and 2ω, respectively.

The modulation of the phase ϕ can be experimentally performed by means of a *photoelastic modulator* (PEM). It relies on *birefringence*, i.e. the optical property related to the variation of the refractive index of a crystalline material according to the different crystallographic directions. When light of arbitrary polarization propagates through a crystal, it can be considered to consist of two independent waves that are polarized orthogonally with respect to each other and characterized by different refractive indices in case of a birefringent crystal [62]. These two directions defines the *fast* and *slow axes*, whose names recall the fact that a refractive index variation corresponds to a speed difference in the propagation of monochromatic light. Consequently, the speed difference produces a phase difference between the electric field components along these two axes at the crystal exit point, and the resulting action in terms of Jones calculus is the one given by Eq. (B.13). In this framework, the phase modulation capability comes from the fact that a mechanical stress can induce birefringence and, by coupling the active crystal with a piezoelectric transducer, the extent of the modulation can be electronically controlled through the control of the stress. In a PEM, the piezoelectric transducer is driven by an oscillating voltage, determining a phase retardation ϕ having the form [66]

$$\phi \;=\; \frac{2\pi Al}{\lambda}\cos\left(\omega t\right) \equiv \; \phi_m \cos\left(\omega t\right), \qquad (3.16)$$

where A is proportional to the amplitude of the driving voltage, l is the thickness of the PEM birefringent crystal, λ is the wavelength of the considered light and ϕ_m is defined to be amplitude of the phase modulation at frequency ω. Plugging

Signal	Frequency	Measured amplitude
S_0	DC comp.	$RI^* \sin^2 \alpha$
S_ω	ω	$\sqrt{2} RI^* \varepsilon_{Ks} \sin(2\alpha) J_1\left(\phi_m^0\right)$
$S_{2\omega}$	2ω	$-\sqrt{2} RI^* \vartheta_{Ks} \sin(2\alpha) J_2\left(\phi_m^0\right)$

Table 3.1: Amplitudes of the measured signals in the polarization modulation technique listed according to their frequency.

Eq. (3.16) into Eq. (3.13), the intensity I to be calculated becomes

$$I = I^* \left| \begin{bmatrix} \cos^2 \alpha & \cos \alpha \sin \alpha \\ \cos \alpha \sin \alpha & \sin^2 \alpha \end{bmatrix} \begin{bmatrix} 1 & 0 \\ 0 & \mathrm{e}^{i\phi_m \cos(\omega t)} \end{bmatrix} \begin{pmatrix} \vartheta_{Ks} + i\varepsilon_{Ks} \\ 1 \end{pmatrix} \right|^2, \quad (3.17)$$

where we introduced the proportionality factor I^* which depends both on the incident intensity and on $|r_{ss}|^2$. Making use of the Jacobi-Anger expansion and considering only up to the second harmonic of ω, Eq. (3.17) returns

$$\begin{aligned} I = I^* \Big\{ & \left(\vartheta_{Ks}^2 + \varepsilon_{Ks}^2\right) \cos^2 \alpha + \sin^2 \alpha \\ & + 2\varepsilon_{Ks} \sin(2\alpha) J_1(\phi_m) \cos(\omega t) \\ & + \vartheta_{Ks} \sin(2\alpha) \left[J_0(\phi_m) - 2J_2(\phi_m) \cos(2\omega t)\right] \Big\}, \end{aligned} \quad (3.18)$$

where $J_0(\phi_m)$, $J_1(\phi_m)$ and $J_2(\phi_m)$ are Bessel functions of the first kind evaluated at ϕ_m. Equation (3.18) can be simplified by neglecting second order terms in ϑ_{Ks}, ε_{Ks} and by considering a phase modulation amplitude ϕ_m^0 such that $J_0\left(\phi_m^0\right) = 0$:

$$\begin{aligned} I = & I^* \sin^2 \alpha + 2I^* \varepsilon_{Ks} \sin(2\alpha) J_1\left(\phi_m^0\right) \cos(\omega t) \\ & - 2I^* \vartheta_{Ks} \sin(2\alpha) J_2\left(\phi_m^0\right) \cos(2\omega t). \end{aligned} \quad (3.19)$$

The voltage signal at the output of the photodetector is proportional to the intensity corresponding to Eq. (3.19) and it is the sum of three parts, corresponding to three different frequencies, as summarized in Table 3.1. The R proportionality factor (*responsivity*) introduced in the table accounts for the photodiode working principle: the generation of a photocurrent (and so a voltage on a load) in response to incident light power. At this stage, the use of two lock-in amplifiers phase-locked to the photodiode voltage signal at frequency ω and 2ω allows measuring the amplitudes S_ω and $S_{2\omega}$ corresponding to the respective modulation frequencies. Since lock-in amplifiers are programmed to return the root mean square of the measured voltage, a further factor $\sqrt{2}/2$ has been introduced in Table 3.1. Finally, through the value of the S_0 DC component is possible to
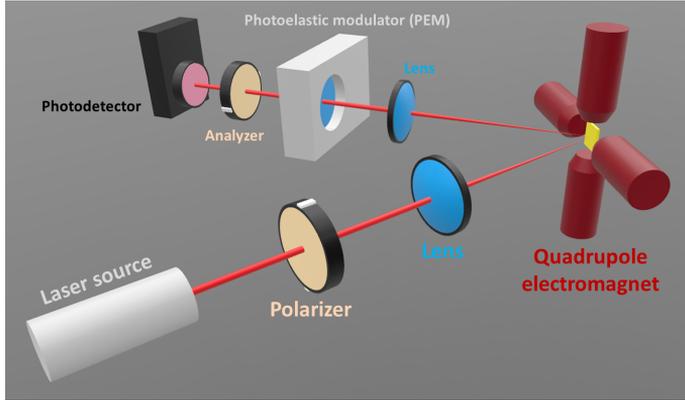
Figure 3.4: Scheme of the longitudinal MOKE setup used for obtaining the measurements presented in this thesis.

normalize the measured amplitudes S_ω and $S_{2\omega}$ in order to get a quantitative evaluation of ϑ_{Ks} and ε_{Ks}:

$$\varepsilon_{Ks} = \frac{\tan\alpha}{2\sqrt{2}J_1\left(\phi_m^0\right)}\frac{S_\omega}{S_0}, \tag{3.20a}$$

$$\vartheta_{Ks} = -\frac{\tan\alpha}{2\sqrt{2}J_2\left(\phi_m^0\right)}\frac{S_{2\omega}}{S_0}. \tag{3.20b}$$

3.2.2 The experimental setup

The experimental setup implementing the optical train described by Eq. (3.17) and corresponding to a *longitudinal* MOKE setup is schematically shown in Fig. 3.4. The light coming from a CW diode laser ($\lambda = 532$ nm or $\lambda = 635$ nm) passes through a Glan–Thompson polarizer to be subsequently focused on the sample by means of a converging lens. The angle of incidence is about 35°. The sample can be mounted inside a quadrupole electromagnet allowing for the generation of a magnetic field up to 2000 Oe (per axis) in the plane of the sample. Both the magnetic field and the sample can be rotated around the sample surface normal, in order to perform measurements along different directions on the sample without modifying the scattering plane, which defines the sensitivity plane for the considered MOKE configuration. The reflected light is then collimated using a second converging lens in order to avoid the light spot diameter to be bigger than the diameter of the photodetector active area (3.6 mm). Before reaching the photodetector, the light beam passes through the PEM optical head and through a second Glan–Thompson polarizer, usually defined "analyzer". The PEM modulation frequency is $\omega = 50$ kHz, so the bandwidth of the photodetector
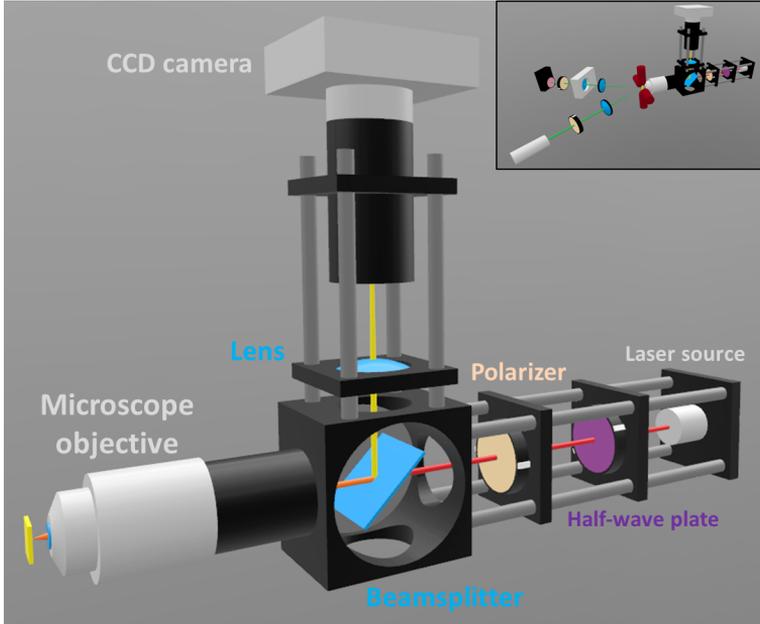
Figure 3.5: The thermoplasmonic heating stage designed to be combined with our MOKE setup, as shown in the inset.

have to be broad enough to resolve the signal component at $2\omega = 100$ kHz. The analyzer angle is usually kept in a range of $\pm 10°$ with respect to the extinction position (i.e. when the polarization axis of the incident radiation is at $90°$ with respect to the transmission axis of the analyzer), since it has been demonstrated to be the best compromise in terms of *signal-to-noise ratio* [88]. The signal coming from the photodetector is fed both to two lock-in amplifiers, phase-locked at ω and 2ω, and to a digital multimeter for the measurement of S_0 (see Table 3.1). The whole systems is controlled by a LabVIEW software, which synchronizes the applied magnetic field with the measured signal in order to get hysteresis loops. The typical time for sweeping a complete hysteresis loop is of the order of 60 s.

For the thermoplasmonic heating of artificial spin ice systems (see Chap. 5), we developed an heating stage to be fitted in our MOKE setup, as shown in Fig. 3.5. The (pump) light produced by a CW diode laser ($\lambda = 785$ nm or $\lambda = 808$ nm) has to be focused onto the sample in order to convey energy in selected sample region. The whole setup is mounted on a XYZ translation stage in order to move the pump beam independently from both the sample and the MOKE setup (probe) beam. The active area of the photodetector in the MOKE setup has to be covered by a laser-line optical filter, in order to pick only the probe beam, so avoiding any unwanted signal coming from the pump beam.

The pump spot diameter can be adjusted in the range $1 - 30$ μm for varying the illuminated area and so the delivered intensity (i.e. power density per unit area). A drawback of working with such a small spot diameter is the necessity of using a microscope objective which makes the distance between the objective front lens and the sample of about 2 mm. A Glan–Laser polarizer placed after the laser source allows having a well defined polarization axis, since working with linearly polarized light is mandatory for getting a proper thermoplasmonic heating in our implementation, as we will see in Chap. 5. In case of using the linearly polarized $\lambda = 785$ nm laser source, a polymer zero-order half-wave plate (at $\lambda = 780$ nm) rotates the polarization axis of the incident light in order to avoid a loss of intensity while changing the polarizer orientation (see Eq. (B.14)). For the $\lambda = 808$ nm laser source, an unpolarized light exits from a multi-mode optical fiber, so the zero-order half-wave plate would have no effect. Through a beamsplitter, part of the light coming back from the sample can be deviated towards a CCD camera, allowing for the formation of an image of the sample. An integrated system of view is convenient when working with nanostructure arrays, since it helps in observing where the beams are impinging on and makes the beam alignment easier.

3.3   Anti-reflection coating for ultrafast MOKE measurements

Following the development of intense, coherent laser-based sources of terahertz radiation [89], the past decade has witnessed an increased interest in the use of this type of radiation to control the properties of materials on the sub-picosecond time scale. Terahertz photons (with energies in the meV range) can drive nonlinear dynamics without significantly increasing the entropy of the system [90–94]. In the field of condensed matter physics, the investigation of ultrafast dynamics driven by strong terahertz fields is frequently performed using terahertz pump radiation (usually in the $1 - 10$ THz range, 300 to 30 μm in wavelength) and visible or NIR probing light (typically a sub-100 fs pulse). To study the effects in the strong-field limit, the strength of the terahertz field can be locally enhanced exploiting near-field effects in meta-materials [90,95–101], which typically consist of micrometer-sized metallic structures deposited on the sample surface. However, since the area of the sample to be measured is often significantly smaller than the area of the metallic structures composing the meta-materials, the reflectivity of the probe in the visible/NIR frequency range is dominated by the meta-material

building blocks. As a consequence, it is extremely challenging to isolate the sample response, despite the enhancement provided by the meta-material itself. This problem can be mitigated by using dielectric and absorbing coatings, for instance to enhance the magneto-optical activity in magnetic thin films and to reduce the background reflections [102–104]. This solution greatly boosts the signal up to a point where single nano-structures can be measured [105–107]. The drawback of this approach is that it imposes constraints on the choice of the layers underneath the target structure. This limitation can become crucial if these underlayers are utilized to tune the important properties of the investigated thin films. In this case, a more suitable solution is to deposit an anti-reflection (AR) coating only on the metal structures forming the meta-material, to minimize the reflection from those areas, which is the main factor affecting the intensity of the measured signal. At the same time, the AR layer should not perturb the terahertz radiation that still needs to be enhanced by the metal layers.

In this framework, we propose a simple single-layer anti-reflection coating design that can be implemented on arbitrary meta-material structures comprising highly conducting and reflective metallic layers. The coating suppresses the NIR reflection typically utilized to probe the response of the sample, without noticeably affecting the terahertz radiation at much larger wavelengths. The work has been mainly performed during a four-month research stay at Stockholm University (Sweden), in the "Ultrafast Dynamics in Condensed Matter" group led by Dr. Stefano Bonetti. The following discussion, which derives from Ref. [108], is of relevance for this chapter, since the experimental verification of the AR coating working principle has been performed through MOKE measurements. In other words, the introduced AR coating represents a simple solution that can be implemented (during the sample fabrication stage) in order to prevent unwanted reflections in general MOKE measurements.

3.3.1   The design of the anti-reflection coating

Terahertz meta-materials can be fabricated by depositing metallic (typically gold) layers that can locally enhance the electromagnetic field of the incident radiation. One of the simplest realization of such structure consists of two metallic strips separated by a small gap, i.e. a dipole antenna, as the ones shown in Fig. A.2. For a suitable geometry of the antenna and polarization of the incident radiation, opposite charges can be induced by the electromagnetic field at the opposite edges of the gap, producing a local enhancement of the electric field within the gap [54].
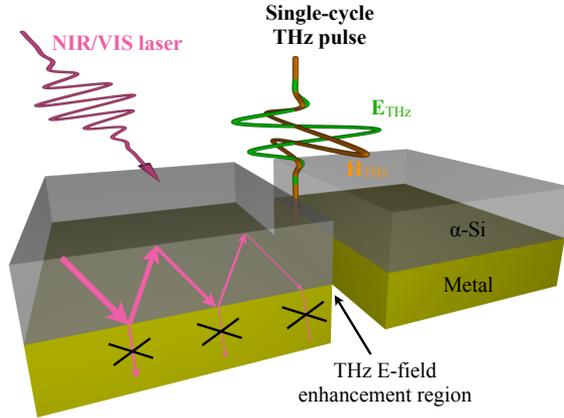
Figure 3.6: Design of the dipole antenna for terahertz near-field enhancement in the gap between two metallic electrodes, covered by an AR coating for NIR and visible radiation. A single-cycle of the terahertz field, with the suitable polarization for the optimal coupling to the antenna, is sketched. The pink arrows schematically show the working principle of the AR coating for a metal, where destructive interference (zig-zag arrows within the top layer) is combined with dielectric losses to compensate for the forbidden transmission through the metallic electrodes (crossed-out arrows in the metal layer), as detailed in the body of the text. Adapted from [108].

In the standard AR coatings, designed to minimize the reflection from dielectric materials, one exploits the phenomenon of destructive interference of the waves reflected at the two interfaces, to cancel out the total electric field that propagates in the backward direction. Since the energy of the electromagnetic wave is conserved, the transmission through the dielectric is maximized. However, this mechanism cannot be implemented for coatings on metals, since the wave cannot propagate through the metal, and hence the reflection cannot be eliminated. For an AR coating to work for a metal, it is necessary to create destructive interference (to suppress Fresnel reflections) and to simultaneously absorb the radiation, as shown schematically in Fig. 3.6. In other words, the dielectric layer needs to be sufficiently lossy in the visible/NIR region, so that the wave decays after multiple reflections at the interfaces. This idea was proposed decades ago by Hass et al. [109], who demonstrated that lossy double dielectric layers can suppress the reflectivity of aluminum and copper in the visible range, while maintaining high reflectivity in the mid-infrared range, up to a wavelength of 10 μm. Moreover, they also highlighted the fact that absorption in single-layer AR coatings is necessary to reduce the high reflectance of metals in the visible range. In a later related work by Yoshida [110], a single-layer AR coating for metals was described mathematically. He considered a non-absorbing dielectric layer

with real refractive index $n_1 > 1$ and thickness d_1, deposited on top of a metallic substrate characterized by a complex refractive index $n_2 + ik_2$. The reflectance R for monochromatic light impinging at normal incidence on the three-layer stack composed by air ($n_0 = 1$), the non-absorbing dielectric coating and the metal substrate can be analytically evaluated and it turns out [108, 110, 111] it can be reduced to zero for a proper d_1 value when

$$ n_1 \;=\; \sqrt{n_2 \;+\; \frac{{k_2}^2}{n_2 - 1}}. \tag{3.21}$$

Equation (3.21) imposes a constraint on the n_2 and k_2 values, since $n_1 > 1$. The effect of this constraint is that, according to Yoshida [110], "zero reflection cannot be achieved with a single dielectric film coating for metals with large extinction coefficient $k \gtrsim 3$, such as silver and gold". In this case, zero reflectance can be obtained by allowing the dielectric coating to be slightly absorbing.

Indeed, in the following, we experimentally confirm that the reflection from gold (and hence from any good metal) can be suppressed by using a single layer of sputtered amorphous silicon (α-Si). In the visible/NIR range, a thin α-Si film acts as a dielectric with a relatively large imaginary part of the refractive index, since the electronic states are not characterized by well-defined momentum, enhancing the radiation absorption in α-Si as compared to its crystalline form [112]. On the other hand, low absorption in the terahertz range (for wavelengths $\gtrsim 100\ \mu\mathrm{m}$) and the small thickness compared to the radiation wavelength make these layers practically invisible, thus maintaining the high reflectivity characteristics of gold in this frequency range.

We first used the transfer matrix method (TMM) [6] to simulate the feasibility of this approach. We simulated the Air|α-Si|Au|Si(substrate)|Air multilayer, where the outermost air layers were semi-infinite and the substrate was 500 μm thick. The radiation was assumed to be monochromatic with a wavelength of 800 nm (the typical center-wavelength of a Ti:sapphire laser) and impinging at normal incidence onto the multilayer stack. We considered the refractive indices $n_\mathrm{Air} = 1$, $n_{\alpha-\mathrm{Si}} \approx 3.90 + 0.11i$, $n_\mathrm{Au} \approx 0.15 + 4.91i$ and $n_\mathrm{Si} \approx 3.681 + 0.005i$ [113]. In Fig. 3.7 we plot the reflectance of the stack as a function of the α-Si thickness, for two gold layers of different thickness. For thin gold (20 nm), part of the radiation can be transmitted into the substrate and ≈ 30 nm of amorphous silicon on top of it can efficiently suppress the reflectance. For thick gold (100 nm), enough to prevent any transmission, a thicker amorphous silicon layer (≈ 230 nm) is needed to achieve the same suppression. In the same figure, we also plot the
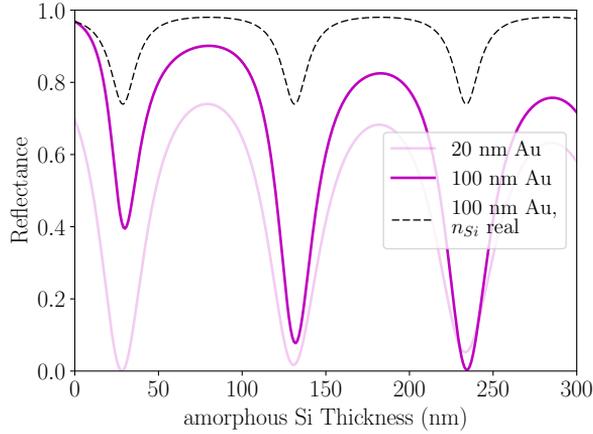
Figure 3.7: Solid curves: calculated reflectance at a wavelength of 800 nm for the Air|α-Si|Au|Si(substrate)|Air multilayer, as a function of the α-Si thickness, for two different Au thickness values at normal incidence. Dashed curve: calculated reflectance at a wavelength of 800 nm for an ideal dielectric on top of a 100 nm thick gold layer, characterized by $n = 3.9$ and zero imaginary part of the refractive index. Adapted from [108].

reflectance (dashed line) of a fictitious dielectric layer with zero imaginary part of the refractive index, but with magnitude equal to that of the the amorphous silicon, so representing a conventional dielectric with negligible losses. It is evident that such a dielectric on top of a 100 nm thick gold layer cannot efficiently suppress the reflectance, demonstrating that cumulative losses after multiple reflections are necessary to realize the anti-reflection configuration. We also noted that a single α-Si AR coating remains efficient over a broad range of incidence angles, as shown in Fig. E.1. We used the TMM to check that, when varying the incidence angle from 0° to 37.5° in case of thin gold (20 nm), the optimal thickness for the α-Si layer varies by less than 2 %. Furthermore, at the optimal α-Si thickness ($\approx$ 30 nm), the 800 nm reflectance remains below 0.05 (an acceptable value for the coating to properly work) at angles of incidence as high as 50°. This can be understood as a consequence of the large refractive index of silicon, which causes the electromagnetic wave to strongly refract when entering the AR coating layer. As a result, the optical path in the silicon layer noticeably increases only at very large angles of incidence.

3.3.2   Experimental and numerical verification

Figure 3.8 shows the calculated and the measured reflectances for several Air|α-Si(t)|Au(20 nm)|Si(substrate)|Air multilayers, as a function of t, both for
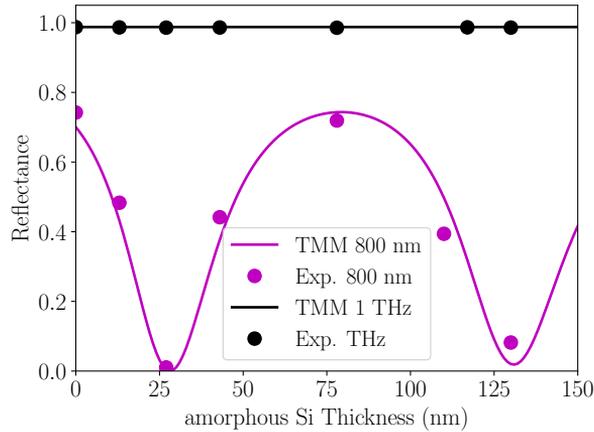
Figure 3.8: Experimental (symbols) and calculated (lines) reflectances for several α-Si|Au(20 nm)|Si(substrate) samples at wavelengths of 800 nm (magenta) and 300 μm (black), the latter corresponding to a radiation frequency of 1 THz. Adapted from [108].

the 800 nm light and the terahertz radiation impinging on the sample at an incidence angle of 10°. The 800 nm radiation was produced by a Ti:sapphire-based regenerative amplifier in 40 fs pulses, corresponding to a 30 nm FWHM bandwidth around the central 800 nm wavelength, as measured by a grating spectrometer. The reflectance at 800 nm was measured directly using a photodiode. The signal was scaled using the known reflectance value of a commercial gold mirror. On the other hand, the reflectance R of the terahertz radiation, generated by optical rectification in a OH1 organic crystal [114], was determined from the measured transmittance T, using the relation $R = 1 - A - T$, where the absorption A was calculated through the TMM. The transmittance was taken to be proportional to the square of the normalized amplitude of the maximum electro-optical sampling signal in a 100 μm thick, 110-cut GaP crystal. The excellent agreement between the data and the calculations directly demonstrates the functionality of the proposed design in suppressing the NIR reflectivity, with the appropriate thickness of α-Si, i.e. 27 nm and 127 nm in the considered case of 800 nm radiation. We emphasize the fact that the experiment demonstrates efficient suppression of the broadband 40 fs pulses of 800 nm radiation. This is not surprising, considering that the bandwidth-to-carrier ratio is less than 4 %. This result confirms the suitability of this design for conventional ultrafast experiments. At the same time, the terahertz reflectance results to be unchanged by the α-Si layer, suggesting that the terahertz near-field enhancement is also likely to be unaffected by the α-Si layer. However, since the measured reflectance is a
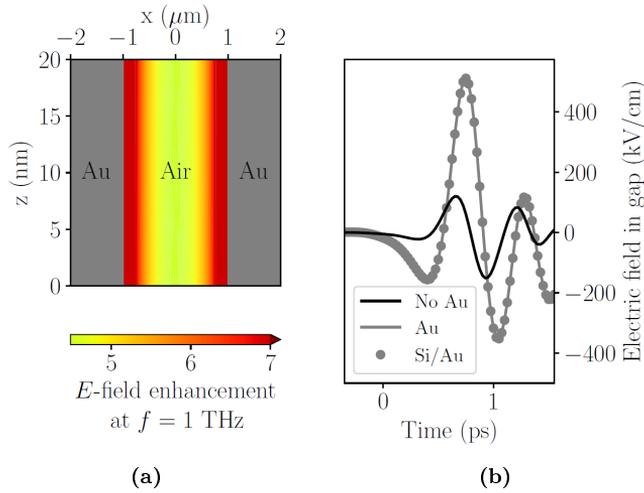
Figure 3.9: (a) Frequency-domain, finite element analysis of the enhancement map for a monochromatic electromagnetic field with frequency $f = 1$ THz incident on two gold plates separated by a gap. (b) Time-domain finite element simulations of the x-component of the electric field for a single-cycle (broadband) terahertz field at the center of the gap, without gold plates (black-solid curve), with gold plates (gray-solid curve) and with α-Si|Au plates (gray-filled dots). In all the calculations, the electric field of the incident radiation is linearly polarized along the $x-$axis and the propagation direction is along the $z-$axis, normal to the sample plane. Adapted from [108].

far-field property and near-field properties are in general very sensitive to inter-face effects, one needs to perform a more detailed investigation of the possible effects of the AR coating on the terahertz radiation in the near-field regime.

Hence, to analyze the near-field effects of the coating, we have performed finite-element numerical calculations using COMSOL Multiphysics [115]. In Fig. 3.9a, we plot the electric field enhancement at a frequency of 1 THz, for a set of two infinitely long, 65 μm wide, 20 nm thick gold plates separated by a gap of 2 μm. The terahertz electric field is applied along the $x-$axis in this figure. The field enhancement is computed by dividing the electric field value in the gap region by the electric field value at the Air|Si interface, in the absence of gold plates. Figure 3.9b shows the time dependence of the x-component of the terahertz electric field in the middle of the gap ($x = 0$) and at $z = 10$ nm above the silicon substrate. For this simulation, we used the experimental time profile of the impinging terahertz field, measured by electro-optical sampling, with a peak value of $\approx 300 \text{ kV} \cdot \text{cm}^{-1}$. For the bare Air|Si interface, the terahertz field is reduced to approximately half of its free-space magnitude, consistent with the relative amplitude t of the transmitted wave at an Air|Si interface computed as

$t = 2/(n + 1)$, with $n \approx 3.4$[1]. The presence of the gold plates introduces a slight temporal shift and enhances the amplitude of the terahertz field to more than 500 kV$\cdot$cm^{-1}, consistent with the ≈ 4 times enhancement observed in the frequency domain simulations of Fig. 3.9a[2]. Most importantly, the addition of the α-Si layer on top of the gold plates does not noticeably affect the field, confirming the intuitive conclusion based on the negligible effect of the α-Si layer on the terahertz reflectance (see Fig. 3.8).

To test the functionality of the AR coating in a practical situation, we measured the polar MOKE hysteresis loops (exploiting the polarization modulation technique of Sec. 3.2.1) from a 3 nm thick CoNi film patterned into a 1 μm wide, 100 μm long wire. The CoNi stack is formed by a Ta(3)|Ni(0.5)|[Ni(1)|Co(0.2)]$_3$|Cu(2)|Ta(2) multilayer (from top down, thickness in nm) with perpendicular magnetic anisotropy. As shown in Fig. 3.10a, the wire is located in the 2 μm wide gap between two 100 μm long and 65 μm wide gold plates, coated with a 27 nm thick α-Si layer. By analyzing the magneto-optical response, we can unambiguously identify the signal coming from the embedded CoNi wire, with no contribution from the non-magnetic electrodes. As the MOKE signal typically results in a tiny intensity variation on top of a large background, this specific system implementation also demonstrates the general suitability of the proposed design for the detection of small effects other than the magneto-optical ones. The polar MOKE hysteresis loops from the embedded wire are plotted in Figs. 3.10b and 3.10c for two different wavelengths of the probing radiation, 550 nm and 800 nm. The AR coating is expected to completely suppress the reflectivity of the gold electrodes at 800 nm (since it has been optimized for this wavelength), while at 550 nm a substantial reflection from the gold plates is expected. Using radiation of different wavelengths is geometrically equivalent to studying samples with different AR coating thickness (as shown in Fig. E.2), with the advantage that the very same sample can be used and the wavelength can be tuned very accurately. The data plotted with symbols in Fig. 3.10c clearly show that the AR coating significantly enhances the signal-to-background ratio, resulting in a ten-fold increase of the relative amplitude of the hysteresis loops at the design wavelength (with respect to a non-optimized case). We have checked that the increase in the relative signal is not caused by the difference between the magneto-optical constants

---

[1]Since we were impinging on the Air|Si interface at normal incidence with a wavelength of ≈ 300 μm, the amplitude of the electric field at $z = 10$ nm above the silicon substrate is almost equal to the amplitude of the transmitted electric field, because of the $\mathbf{\hat{n}} \times (\mathbf{E}_{Si} - \mathbf{E}_{Air}) = 0$ boundary condition.

[2]The discrepancy between the two simulated enhancement values has to do with the fact that the single-cycle field is broadband and so different frequencies are amplified differently by a fixed-geometry design.
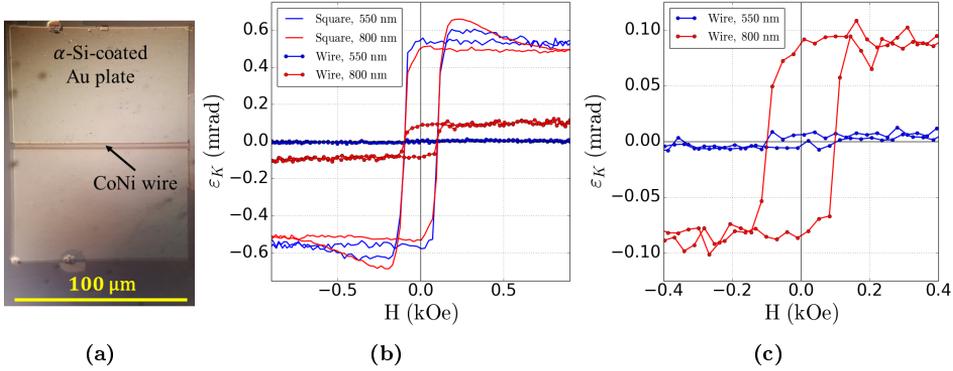
Figure 3.10: (a) Optical microscopy image of the measured structure, consisting in a CoNi wire located in the 2 μm wide gap between two 100 μm long and 65 μm wide gold plates, coated with a 27 nm thick α-Si layer. (b) Polar MOKE hysteresis loops for the 550 nm (blue lines) and 800 nm (red lines) wavelengths of the probing light. Symbols: average of 25 hysteresis loops for the CoNi wire. Solid curves: average of 4 hysteresis loops for a reference 100 μm $\times$ 100 μm CoNi square, at the same wavelengths. (c) Zoom in on the CoNi wire hysteresis loops depicted in (b). Adapted from [108].

of CoNi between the considered wavelengths (550 nm and 800 nm) by measuring the polar MOKE signal from a 100 μm $\times$ 100 μm CoNi square of 3 nm thickness, with no gold electrodes surrounding the structure. The resulting hysteresis loops are shown as solid curves in Fig. 3.10b.

To quantitatively analyze our observations, we noted that when the areas and the reflectivities of different reflecting regions are known, one can predict the ratio in the total measured Kerr ellipticity ε_K between the CoNi square (which is larger than the probing spot) and the wire-shaped sample, according to [105]

$$\eta \equiv \frac{\varepsilon_K^{\text{wire}}}{\varepsilon_K^{\text{square}}} = \frac{A_{\text{wire}}}{A_{\text{wire}} + A_{\text{Si}}\frac{R_{\text{Si}}}{R_{\text{CoNi}}} + A_{\alpha-\text{Si|Au}}\frac{R_{\alpha-\text{Si|Au}}}{R_{\text{CoNi}}}}, \tag{3.22}$$

where A_j is the total area occupied by a certain material j illuminated by the laser beam and R_j denotes the corresponding reflectance that can be measured experimentally or calculated using the Fresnel equations. Table 3.2 summarizes the relationship between the ellipticity of the wire and the ellipticity of the square, assuming that the probing light is focused into a uniform circular spot with diameter $\phi = 75$ μm and the various probed areas are $A_{\text{wire}} = A_{\text{Si}} \approx \phi h = 75$ μm^2 ($h = 1$ μm), $A_{\alpha-\text{Si|Au}} \approx \pi(\phi/2)^2 - 2\phi h \approx 4300$ μm^2. The area occupied by the wire is therefore about 2 % of the total area. Indeed, for the 550 nm wavelength, at which the gold reflectivity is not suppressed by the AR coating, the ellipticity

Wavelength	R_{CoNi}	R_{Si}	$R_{\alpha-\mathrm{Si|Au}}$	η
550 nm − *theory*	0.49	0.40	0.50	0.017
550 nm − *experiment*	0.46	0.40	0.50	0.016
800 nm − *theory*	0.47	0.36	0.020	0.24
800 nm − *experiment*	0.49	0.34	0.031	0.19

Table 3.2: Summary of the ellipticity ratios (η) between a CoNi wire and a CoNi square calculated according to Eq. (3.22). Adapted from [108].

signal for the wire is about 1.6 % of that for the large square, both theoretically and experimentally. In contrast, for the 800 nm wavelength, we expected and observed an increase of this ratio by an order of magnitude. The deviation between the theoretically expected value ($\eta = 0.24$) and the experimental value ($\eta = 0.19$) can be explained by a combination of (i) a few-nm uncertainty in the deposited material thickness, (ii) deviations of the optical properties of the various layers from their nominal values and (iii) the effect of the wire and gold plates edges, whose scattering properties were not taken into account in the calculations reported in Table 3.2.

3.3.3   Conclusions

We have designed and experimentally demonstrated an AR coating for highly reflective metals, which are typically utilized in the fabrication of terahertz meta-materials. The AR coating can efficiently suppress the reflection of light in the visible/NIR range, typically used in the studies of ultrafast phenomena by pump-probe techniques. At the same time, the coating does not perturb the propagation of terahertz radiation and it does not affect the near-field enhancement in the considered meta-material. Our results are expected to open a path for time-resolved experiments aimed at probing the ultrafast dynamics driven in nanostructures by strong terahertz fields, by using table-top femtosecond NIR laser sources.

Chapter 4

Thermal Simulations of Artificial Spin Ice Systems

Artificial spin ice systems represent model systems for the study of geometrical frustration. They consist in arrays of close-enough magnetic nanostructures subjected to magnetostatic interactions, a key ingredient for the appearance of frustration. The strength of these systems resides in the fact that all the relevant parameters influencing the global behaviour can be easily tuned through the advanced fabrication techniques described in Chap. 3. Hence, a systematic study of geometrical frustration can be performed, and the acquired knowledge can be exploited to provide active control on the system behaviour for future frustration-based devices. After reviewing the birth of the field devoted to the study of artificial spin ice systems, this chapter describes our approach to the simulation of the thermally-activated magnetization reversal events occurring in the nanostructures forming geometrically-frustrated arrays.

This chapter will constitute the frame for setting-up a research article in collaboration with J. Leliaert, S. Koraltan, D. Suess, D. De Sancho, and P. Vavassori.

4.1 Geometrical frustration

Frustration in physics is the inability of a system to simultaneously satisfy (i.e. energetically minimize) all the pairwise interactions within it [116–118]. To better clarify this definition, we can inspect the behaviour of three Ising-like magnetic moments with magnitude μ disposed on the vertices of a triangular lattice with lattice parameter a. The triangular lattice defines the xy-plane,

(a) Ferromagnetic order

(b) Frustrated system
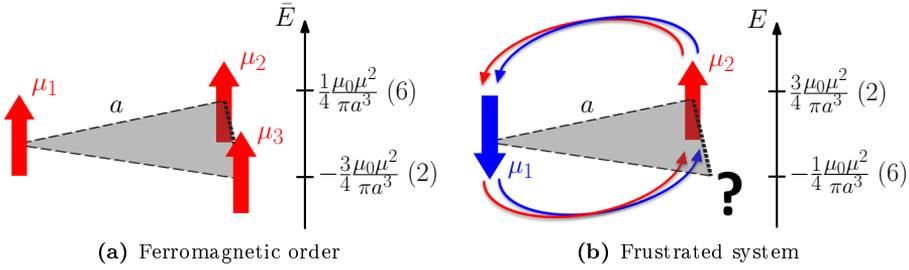
Figure 4.1: (a) Ferromagnetic order in a triangular lattice as given by Eq. (4.2). (b) Frustrated system in a triangular lattice as determined by the local antiferromagnetic interaction imposed by Eq. (4.1). Along the vertical axes, the energies of the eight possible states are shown. The numbers in parenthesis represent the degeneracy of the corresponding configuration.

while the magnetic moments are aligned along the z-direction and only the up-down orientations are allowed. Considering the magnetic moments as point-like magnetic dipoles, their interaction energy E_{ij} is given by [5]

$$E_{ij} \;=\; \frac{\mu_0}{4\pi}\left[\frac{\boldsymbol{\mu}_i\cdot\boldsymbol{\mu}_j}{\mathrm{r}_{ij}^3} \;-\; 3\frac{\left(\boldsymbol{\mu}_i\cdot\hat{\mathbf{r}}_{ij}\right)\left(\boldsymbol{\mu}_j\cdot\hat{\mathbf{r}}_{ij}\right)}{\mathrm{r}_{ij}^3}\right], \tag{4.1}$$

where $\mathbf{r}_{ij}$ represents the distance vector between the i-th and j-th dipoles. For the sake of this example, we neglect the exchange interaction (if any) and we can define a fictitious "anti-dipolar" interaction, whose interaction energy $\bar{E}_{ij}$ consists in

$$\bar{E}_{ij} \;=\; -E_{ij} \;=\; \frac{\mu_0}{4\pi}\left[3\frac{\left(\boldsymbol{\mu}_i\cdot\hat{\mathbf{r}}_{ij}\right)\left(\boldsymbol{\mu}_j\cdot\hat{\mathbf{r}}_{ij}\right)}{\mathrm{r}_{ij}^3} \;-\; \frac{\boldsymbol{\mu}_i\cdot\boldsymbol{\mu}_j}{\mathrm{r}_{ij}^3}\right]. \tag{4.2}$$

Figure 4.1a shows the ground state (GS) determined according to Eq. (4.2): the minimum energy is achieved for a parallel alignment of magnetic moments, favouring ferromagnetic ordering. In case of a triangular lattice composed by N sites, the ferromagnetic order can be extended to the whole lattice, so determining a doubly degenerate GS, with a zero-point entropy per site of $k_B \ln 2/N$ (negligible for macroscopic systems as $N \to \infty$). On the other end, the equilibrium configuration induced by Eq. (4.1) is completely different. Two magnetic moments can be easily accommodated as shown in Fig. 4.1b, since the anti-parallel alignment in now favoured. But what about the third magnetic moment? In both cases (up or down alignment), either E_{13} or E_{23} is not minimized, so determining a GS with higher energy than the ferromagnetic GS of Fig. 4.1a. Moreover, the GS is more degenerate than before, since all the six configurations with two par-
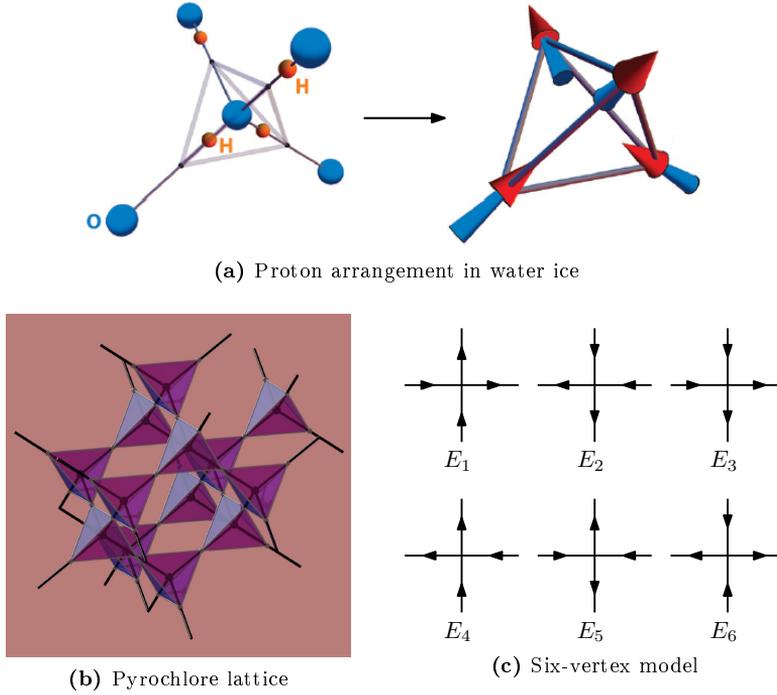
(a) Proton arrangement in water ice

(b) Pyrochlore lattice

(c) Six-vertex model

Figure 4.2: (a) The proton arrangement in water ice can be mapped into a system of arrows in a tetrahedral unit. Adapted from [121]. (b) Scheme of the pyrochlore lattice. Adapted from [122]. (c) Allowed configurations for the six-vertex model, each one associated to an interaction energy E_j, for $j = 1, \ldots, 6$. Adapted from [123].

allel magnetic moments and one anti-parallel to them are valid GSs with equal energy. Extending these finding to a lattice with N sites results in a very peculiar behaviour, which can happen in frustrated systems: the GS degeneracy grows along with N, so resulting in a *finite* zero-point entropy per site $S(0)$ given by [119]

$$S(0) \;=\; \frac{2k_B}{\pi} \int_0^{\frac{\pi}{3}} \ln\left(2\cos x\right) dx \;\approx\; 0.338 k_B. \tag{4.3}$$

In general, frustration can be caused either by competing interactions [120] or by the lattice structure as in Fig. 4.1b, defining the concept of *geometrical frustration* in the latter case. A typical example of geometrical frustration in a real system is given by the proton arrangement in water ice (see Fig. 4.2a), where both GS degeneracy and finite zero-point entropy can be retrieved [121]. The oxygen atoms form a periodic lattice with coordination number 4, isomorphic to the center of the tetrahedra in the *pyrochlore* structure shown in Fig. 4.2b. Each hydrogen nucleus (a proton) is placed between two neighbouring oxygen atoms along the line connecting them. Because of the equilibrium O–O and O–H bond

lengths, the lowest energy state has two protons positioned close to the oxygen and two protons positioned farther away, forming a so-called *two-in–two-out* state (*ice rule*) [124]. For every tetrahedron, there are six ways of achieving this state and, since the tetrahedra are corner-sharing, the associated degeneracy cannot be lifted by long-range order [125]. The arrangement of protons determined by this rule can be mapped into a system of arrows lying along the axes connecting the centers of adjacent tetrahedra, as shown in Fig. 4.2a. This one-to-one correspondence between protons and arrows has to be completed by pointing each arrow towards the oxygen atom closer to the proton the arrow represents. So, the equilibrium properties of such a system of arrows can be studied by considering the *six-vertex model*, a well-known two-dimensional model in statistical mechanics which can be exactly solved in order to get the relevant thermodynamical quantities [123]. This model considers arrow arrangements on a two-dimensional square lattice. At each lattice vertex, four arrows meet and only six out of the sixteen possible vertex configurations satisfy the two-in–two-out rule, as depicted in Fig. 4.2c. For the behaviour of water ice to be reproduced, the energies of the six possible configurations have to be considered equal, i.e. $E_1 = \ldots = E_6$. With this prescription, the zero-point entropy per proton (i.e. per arrow) in water ice can be calculated [126]:

$$S(0) \;=\; \frac{3}{4} k_B \ln\left(\frac{4}{3}\right) \;\approx\; 0.216 k_B. \tag{4.4}$$

4.2   Spin ice and artificial spin ice systems

The mapping of water ice into a system of arrows can be made, in a certain sense, more "real" and not only a mere mathematical strategy for the calculation of statistical quantities. Being the arrows in Fig. 4.2a representative of magnetic moments, a ferromagnetic coupling between neighbouring arrows would determine the same type of frustration and GS degeneracy described by the six-vertex model. This has been demonstrated to be the case for the rare-earth titanate pyrochlores $Dy_2Ti_2O_7$ and $Ho_2Ti_2O_7$ [125, 127], whence the name *spin ice systems*. In these compounds, the rare-earth magnetic moment (with magnitude $\mu \approx 10\mu_B$) resides on the sites of the pyrochlore lattice (with a nearest-neighbour distance $a \approx 3.54$ Å) and points along the axis joining the centers of the two tetrahedra it belongs to [128]. Because of the size of a and the magnitude of μ, both the exchange interaction and the dipolar (magnetostatic) interaction have to be taken into account. At the level of nearest-neighbour interactions, the balance between exchange and dipolar interactions determines a ferromagnetic

coupling, which is necessary for obtaining geometrical frustration in the rare-earth titanate pyrochlores. Indeed, when the ferromagnetic coupling is not present (as for $Tb_2Ti_2O_7$), the spin arrangement does not show geometrical frustration [128]. Even if the situation gets more complicated because of the long-range nature of the dipolar interaction, this long-range nature has been demonstrated to be a needed condition for having frustration in spin ice systems and so GS degeneracy [128, 129].

The specific-heat measurement performed by Ramirez et al. on $Dy_2Ti_2O_7$ below 20 K [125] shows a zero-point entropy of $\approx 0.232k_B$ per magnetic moment, in good agreement with Eq. (4.4). Moreover, as the temperature grows, the measured entropy per magnetic moment approaches the value of $k_B \ln 2 \approx 0.693k_B$, which corresponds to the *full* entropy per magnetic moment, since there are only two possible orientations. This fact suggests that, even if the low-temperature equilibrium GS can be described by the six-vertex model, all the possible sixteen configurations can occur when $T > 0$ K. So, the most general *sixteen-vertex model* (see Fig. 4.3), obtained by removing the ice rule, has to be considered for a proper description of the static properties of the system at an arbitrary temperature [130–133].

A drawback of spin ice systems is the fact that the interesting features given by frustration are not easy to inspect, since they occur close to a temperature of 0 K and on a scale of few tens of angstrom. In 2006, Wang et al. introduced the square *artificial spin ice* (ASI) system [3], consisting in a planar array of elongated magnetic nanostructures arranged along the edges of a square lattice, as shown in Fig. 4.4a. The mapping between ASI vertices and the sixteen-vertex model can be defined by identifying each nanostructure with a magnetic moment, and the dipolar interactions between these magnetic moments create a two-dimensional analogue to spin ice. This has been achieved thanks to a proper tuning of the ASI system parameters through the use of advanced fabrication techniques (EBL, see Sec. 3.1). In fact, as discussed in Sec. 1.3.2, the shape of a magnetic nanostructure is a source of anisotropy. By fabricating elongated structures (small enough to be single domain), it is possible to obtain a magnetic entity behaving like a "giant" magnetic moment (*macrospin*) with only two stable directions (along the major axis of the nanostructure). The typical magnitude of the macrospin magnetic moment in ASI systems is $\mu \approx 10^7 \mu_B$, so the macrospins can effectively interact by means of the dipolar interaction (4.1) at distances of few tens of nanometers. Then, the coupling strength can be varied by modifying the distance between adjacent nanostructures, up to a regime where each entity can be considered as isolated. In the end, the high flexibility in the design of ASI systems results in
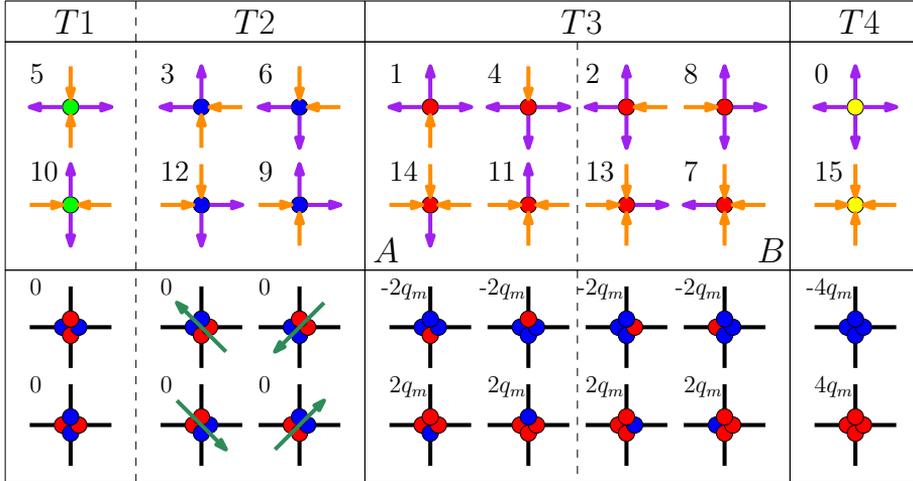
Figure 4.3: The sixteen possible configurations considering four Ising-like magnetic moments. They are divided in 4 groups ($T1$, $T2$, $T3$, $T4$) according to the energy they can be associated to. Only $T1$ and $T2$ vertices satisfy the two-in–two-out rule. In the upper row, each group has been marked with a color (the filled dot inside the vertices). The vertex numbering (from 0 to 15) represents the convention adopted during this thesis. In the bottom row, the description in terms of effective vertex charge is depicted. Here, a red-filled dot represents a magnetic charge q_m, while a blue-filled dot represents a magnetic charge $-q_m$. The numbers correspond to the total charge sitting on the vertex center. Moreover, $T2$ and $T3$ vertices also posses a net magnetic moment, represented by green arrows only for $T2$ vertices.

the capability of building systems where the interesting low-temperature states of spin ices can be obtained at the desired temperature, even at room temperature. Moreover, the size of the involved magnetic nanostructures (hundreds of nanometers) allows using well-established imaging techniques in order to record the configuration of an extended system at the level of the single nanostructure, in some cases also as a function of time. These techniques comprise magnetic force microscopy (MFM) [3], Lorentz transmission electron microscopy [134] and x-ray photoemission electron microscopy [135, 136].

The emergence of frustration in square ASI systems can be seen at a single-vertex level. The different distances between first nearest-neighbours and second nearest-neighbours remove part of the degeneracy characteristic of spin ice systems, so separating the six vertices satisfying the ice rule in $T1$ and $T2$ vertices. The minimum energy is achieved by $T1$ vertices, but not all the pairwise interaction energies are minimized, since the minimum energy configuration for the second nearest-neighbours is the one depicted in the bottom part of Fig. 4.4b. The impossibility of simultaneously satisfying all the interaction fits with the
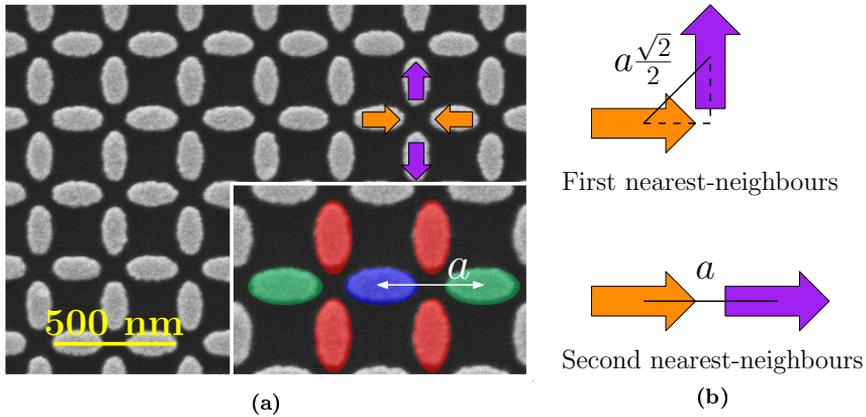
Figure 4.4: (a) SEM image of a square ASI system, where the scale bar displays a typical size-scale. The coloured arrows show how the mapping to the sixteen-vertex model works: each nanostructure can be identified with a magnetic moment. Inset: definition of the lattice parameter a and of the nearest-neighbours. For the blue nanostructure, the four red islands represent the *first* nearest-neighbours (with distance $a\sqrt{2}/2$), whereas the two green ones are the *second* nearest-neighbours (with distance a). (b) Minimum energy configurations for first and second nearest-neighbours.

definition of frustration given at the beginning of this chapter. However, the GS of square ASI systems is not highly degenerate, since it consists in a full $T1$ tiling formed by an alternation of $T1-5$ and $T1-10$ vertices (see Figs. 4.3 and 4.6a), and there are only two extended configurations associated with this type of tiling. So, the zero-point entropy per nanostructure is $k_B \ln 2/N$, which is negligible as $N \to \infty$.

Besides the square ASI, many other geometries have been investigated [135, 137–144]. Of these, the *artificial kagome spin ice* consists in placing the magnetic nanostructures on the edges of a honeycomb lattice. The resulting GS is highly degenerate, since each vertex is formed by three nanostructures meeting at an angle of 120°, so determining the equivalence of the three pairwise interactions and an energy hierarchy similar to the one depicted in Fig. 4.1b. Farhan et al. [135, 145] have been able to image the time evolution of the kagome ASI GS in few basic units of the honeycomb lattice, so exploring for the first time the energy landscape of a *thermally active* ASI system.

4.2.1 Energy levels in the sixteen-vertex model

Figure 4.5b shows the energies of all the sixteen basic vertices for a square ASI system in the *macrospin approximation*: the interaction energy is calculated

according to Eq. (4.1) as if the macrospin would reside in the center of the corresponding nanostructure. The general model for the calculation of the vertex energies is schematically depicted in Fig. 4.5a, where a rectangular lattice of lattice parameters a and b with a height offset h is considered. According to this model, the vertex energies are:

$$E_{T1} = \frac{\mu_0 \mu^2}{2\pi} \left[\frac{1}{a^3} + \frac{1}{b^3} - \frac{48ab}{(a^2 + b^2 + 4h^2)^{\frac{5}{2}}} \right], \tag{4.5a}$$

$$E_{T2} = -\frac{\mu_0 \mu^2}{2\pi} \left(\frac{1}{a^3} + \frac{1}{b^3} \right), \tag{4.5b}$$

$$E_{T3}^A = \frac{\mu_0 \mu^2}{2\pi} \left(\frac{1}{b^3} - \frac{1}{a^3} \right), \tag{4.5c}$$

$$E_{T3}^B = \frac{\mu_0 \mu^2}{2\pi} \left(\frac{1}{a^3} - \frac{1}{b^3} \right), \tag{4.5d}$$

$$E_{T4} = \frac{\mu_0 \mu^2}{2\pi} \left[\frac{1}{a^3} + \frac{1}{b^3} + \frac{48ab}{(a^2 + b^2 + 4h^2)^{\frac{5}{2}}} \right]. \tag{4.5e}$$

Figure 4.5b has been obtained by considering $a = b$ and $h = 0$ (*planar square ASI system*). In this case, the four normalized energy levels (with respect to E_{T4}) take values which are independent from a: 0, $1/2 - 2\sqrt{2}/12$, $1/2 - \sqrt{2}/12$ and 1. The high degeneracy of the spin ice system GS can be retrieved by introducing a height offset h^* in a square ASI system, which can be calculated by imposing $E_{T1} = E_{T2}$ in Eqs. (4.5) [146–148]:

$$h^* = a\sqrt{\left(\frac{3}{8} \right)^{\frac{2}{5}} - \frac{1}{2}} \approx 0.419a. \tag{4.6}$$

The vertex energies calculated considering $a = b$ and $h = h^*$ (*three-dimensional square ASI system*) are shown in Fig. 4.5c. Now, there are only three energy levels and the corresponding normalized energies are 0, 1/4 and 1. By further increasing the height offset (e.g. to $2h^*$ as in Fig. 4.5d), the second nearest-neighbour interactions become prevalent, and so the $T2$ vertices result to be in a lower energy state than the $T1$ vertices. Moreover, $E_{T1} = E_{T2}$ can also be obtained for a planar system ($h = 0$) in case of a rectangular lattice (*rectangular ASI system*). If we define $K = a/b$, the condition to be fulfilled is [149]

$$\left(1 + K^3 \right) \left(1 + K^2 \right)^{\frac{5}{2}} - 24K^4 = 0. \tag{4.7}$$
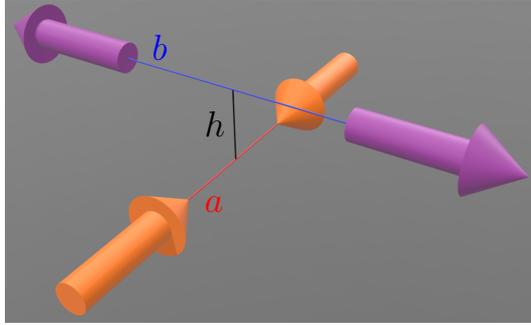
(a) Generalized $T1 - 10$ vertex
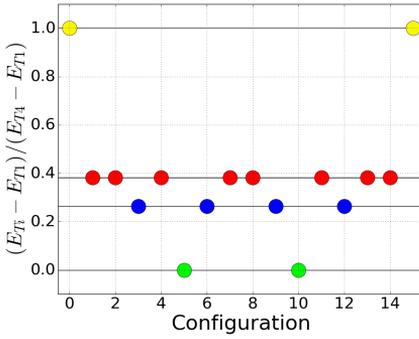
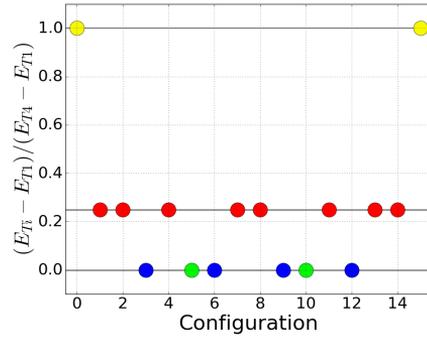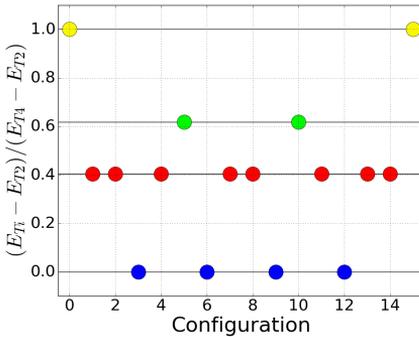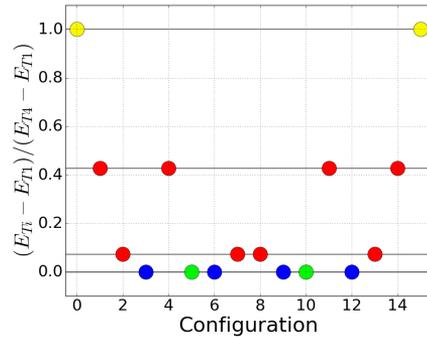**(b)** Planar square ASI

(c) 3D square ASI – h^*

(d) 3D square ASI – $2h^*$

(e) Planar rectangular ASI – $a = K_1 b$

Figure 4.5: Normalized vertex energies in the macrospin approximation. The filled-dot colors correspond to Fig. 4.3. (a) Definition of a, b and h considering the $T1 - 10$ vertex. (b) Normalized energies for a planar square ASI system ($a = b$ and $h = 0$). (c) Normalized energies for a three-dimensional square ASI system ($a = b$ and $h = h^*$). (d) Normalized energies for a three-dimensional square ASI system with $h > h^*$ ($a = b$ and $h = 2h^*$). The $T2$ vertices are now energetically favoured with respect to $T1$ vertices. (e) Normalized energies for a planar rectangular ASI system ($a = K_1 b$ and $h = 0$).

(a) Square ASI GS   (b) Dirac string
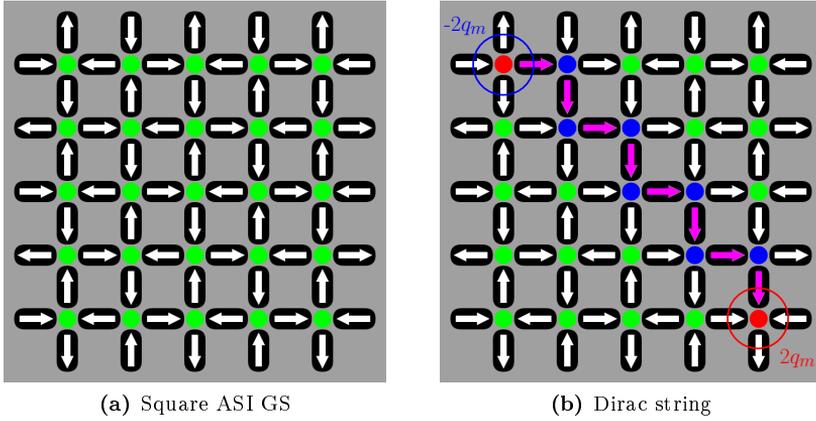
Figure 4.6: (a) Square ASI system GS formed by an alternation of $T1-5$ and $T1-10$ vertices. (b) On top of the GS, a couple of $T3$ excitations can be formed, corresponding to two effective magnetic charges of magnitude $2q_m$ and $-2q_m$. These charges can be separated, but they remain connected by a string of magnetic moments belonging to $T2$ vertices (magenta-filled arrows).

The solutions of interest are $K_1 \approx 0.556$ and $K_2 = 1/K_1 \approx 1.797$. For $a = K_1 b$, the normalized energies are depicted in Fig. 4.5e and it is apparent that the high degeneracy related to the ice rule is again recovered. Both h^* obtained according to Eq. (4.6) and the values for K obtained from Eq. (4.7) are exact only in the macrospin approximation. The finite size of the considered nanostructures and their internal structure do play a role in the vertex energy landscape, as we will see in the following sections.

An alternative way of modelling square ASI consists in the *dumbbell approximation* [122]. A uniformly magnetized nanostructure can be seen to host a $\pm q_m$ magnetic charge at its far ends according to Eq. (1.45b), so resembling a charge dumbbell. Obviously, the net magnetic charge owned by a nanostructure is zero, but there could be an effective magnetic charge located in the region where four islands meet to form a vertex, as schematically depicted in the bottom row of Fig. 4.3. A compensation effect leads to zero effective charge for both $T1$ and $T2$ vertices, but whereas the $T1$ vertex charge shows a quadrupole configuration, the $T2$ vertex charge distribution determines the appearance of a net magnetic moment, represented by the green arrows in Fig. 4.3. On the other hand, $T3$ vertices can be associated to an effective charge of $\pm 2q_m$ (and to a net magnetic moment), whereas $T4$ vertices correspond to $\pm 4q_m$. This description, also valid for spin ice compounds, allowed for studying the magnetic properties of ASI systems in terms of *magnetic monopoles* joined by *Dirac strings* [122,150]. Figure

4.6a shows the GS for square ASI system composed by twenty-five vertices. By flipping the magnetization of a nanostructure, a couple of $T3$ excitations can be formed, corresponding to two effective magnetic charges of magnitude $2q_m$ and $-2q_m$. These effective charges behave like magnetic monopoles, interacting according to Coulomb's law. When the $\pm 2q_m$ charges separate, they remain connected by strings (Dirac strings) composed by a sequence of magnetic moments oriented from the negative charge to the positive charge, as shown by the magenta-filled arrows in Fig. 4.6b. The string formation is associated with the appearance of $T2$ vertices, a fact that further enhances the energy above the GS. This additional energy can be associated to the string tension and constitutes a correction to a pure coulombic interaction between magnetic charges [150].

4.2.2   Vertex-frustrated lattices

The high degeneracy characteristic of spin ice systems resides in the existing degeneracy at the vertex level. Indeed, the energy degeneracy between $T1$ and $T2$ vertices goes beyond a simple magnetic moment inversion, and the GS of such a system is characterized by a highly-degenerate mixture of $T1$ and $T2$ vertices. On the contrary, the fact that $E_{T1} < E_{T2}$ in planar square ASI systems leads to a well-defined antiferromagnetic GS (i.e. a full $T1$ tiling). A part by introducing geometrical modification to the planar square ASI as shown in the previous section, an higher level of degeneracy can be recovered by *decimating* the full lattice, removing properly defined nanostructures as suggested by Morrison et al. [151]. According to the authors, "the zero-point entropy follows not from a freedom of choice at the vertex level, but from the non-trivial relative arrangement of the non-degenerate vertices themselves". In this kind of systems, it is impossible to find a global arrangement of magnetic moments such that all the vertices are in their lowest energy configuration. Equivalently, the GS must contain excited vertices. However, these excited vertices are not excitations of the global system, but they are excited by the topology of the lattice, since their energy is constrained to be higher than the minimum energy for a vertex. In a sense, they are topologically-protected excitations which cannot be eliminated from the GS. This form of frustration is called *vertex frustration*, because it arises from the frustrated attempt to allocate each vertex of the array in its minimum energy configuration, rather than from the frustration in the local pairwise interactions. So far, two vertex-frustrated systems have been experimentally realized: the *shakti lattice* of Fig. 4.7a [152] and the *tetris lattice* of Fig. 4.7b [153].
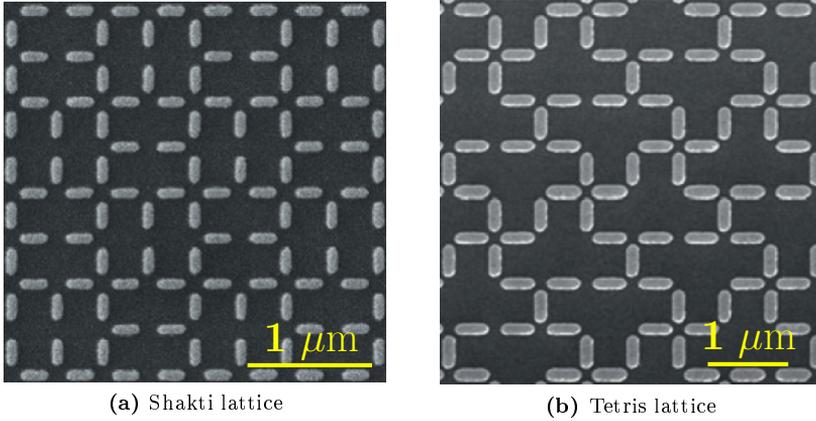
(a) Shakti lattice

(b) Tetris lattice

Figure 4.7: (a) Shakti lattice, obtained by properly removing 1/4 of the nanostructures composing the planar square ASI system. Adapted from [152]. (b) Tetris lattice, obtained by properly removing 3/8 of the nanostructures composing the planar ASI system. Adapted from [153].

4.3   Accessing the ground state

The first square ASI systems were designed to be in a "frozen" state at room temperature, which is one of the interesting features of ASIs. Indeed, since these systems are thermally stable (or frozen) at room temperature, the interesting low-temperature states can be obtained and imaged already at ambient conditions, without the need of approaching a temperature of 0 K as for spin ice compounds. Once the desired pattern has been fabricated, it retains its magnetic configuration for an average relaxation time t given by Eq. (1.56):

$$t \;=\; \frac{1}{\nu_0} \exp\left(\frac{KV}{k_B T}\right),   \tag{4.8}$$

where T is the considered temperature, V is the nanostructure volume and K is determined by Eq. (1.50b). For typical nanostructures considered in ASIs, only the shape anisotropy has to be included ($K_1 = 0$ in Eq. (1.50b)) and it turns out that $t >> 10^8$ s at room temperature [3], so the pattern can practically be considered as thermally stable (i.e. as if $T = 0$ K). Even if this stability is desired for probing the frozen state, the involved energy barriers prevent any kind of observable thermal evolution towards the GS, which is the low-temperature equilibrium state. To stimulate the evolution of a frozen pattern towards the GS, Wang et al. [154] proposed a protocol based on *field demagnetization*. The target sample is initially saturated in a fully polarized $T2$ tiling by applying a

high-enough magnetic field along a main diagonal of the square ASI pattern. Then, the sample is rotated at constant speed inside an alternate magnetic field of decreasing amplitude. However, this protocol turned out to be not suitable for bringing the square ASI to its GS. Indeed, Nisoli et al. [155] demonstrated that the demagnetization protocol generates a well-defined (albeit *not* thermally equilibrated) disordered state which restores the macroscopic degeneracy, but on a manifold characterized by higher energy than the GS. Starting from a full $T2$ tiling, the demagnetization protocol does not significantly reduce the average vertex energy, but it moves the configuration about within the energy manifold the initial state resides in. So, the end result consists in the formation of a disordered mixture composed by $T1$, $T2$ and $T3$ vertices in defined proportions, resulting in a final state with extensive frozen-in zero-point entropy. Despite the achievements of this approach, the demagnetization protocol failed in obtaining the square ASI GS.

In 2011, Morgan et al. [156] discovered that a carefully-prepared as-fabricated Py sample showed a frozen state very closely approaching the GS, as displayed in Fig. 4.8a. In the figure, it is possible to identify large ordered areas of alternating $T1-5$ and $T1-10$ vertices (the GS signature) separated by *domain walls* composed by $T2$ and $T3$ vertices. The considered pattern (with a lattice parameter of 400 nm) was formed by Py bars of 280×85 nm^2 area and 26 nm thickness. For such islands, the stability time at room temperature is practically infinite. However, during the evaporation of Py in the last part of the fabrication process (with a deposition rate of 0.6 Å $\cdot$ s^{-1}), the volume of each nanostructure goes from zero to the final value, so determining a variation of the energy barrier in Eq. (4.8). At the first stage of the material deposition, the very thin Py islands are free to fluctuate at the growth temperature (estimated to be 350 K), so having the possibility of sampling their whole energy landscape. At a certain point, the volume will be big enough to determine sizeable interactions but still leaving the nanostructures free to fluctuate. Hence, the vertices try to order according to their Boltzmann factors [158], which dictate GS ordering for this particular sample. A further increase in the island volume causes the freezing of the obtained order, which can be imaged at the end of the process. The formation of domains is due to the double degeneracy of the GS: the nucleation of a $T1$ tiling can happen anywhere in the pattern and two colliding $T1$ domains can merge only if they have a compatible stacking (i.e. the same kind of alternation of $T1-5$ and $T1-10$ vertices). This process resembles the order-disorder transition in a two-component system [159, 160].

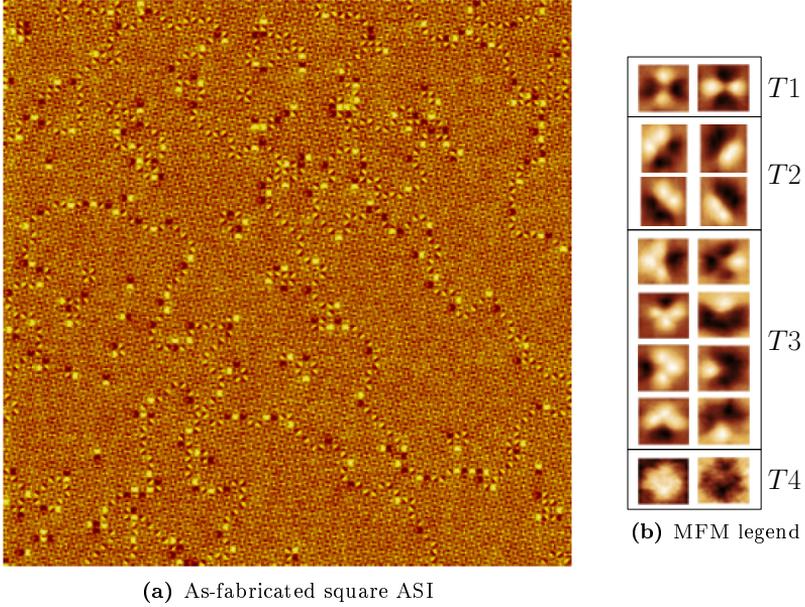The drawback of Morgan's discovery is that one sample corresponds to just

(a) As-fabricated square ASI

(b) MFM legend

Figure 4.8: (a) MFM image of a 30×30 μm^2 region of the as-fabricated square ASI. Large ordered areas of alternating $T1-5$ and $T1-10$ vertices are separated by domain walls composed by $T2$ and $T3$ vertices. Adapted from [156]. (b) Legend for interpreting MFM images of square ASI systems. Adapted from [157].

one measurement, since the order is imposed during fabrication, preventing further configuration evolutions at room temperature. In 2013, both Porro et al. [157] and Zhang et al. [161] proposed a method for thermalizing ASI systems based on an actual *heating* of existing patterns, so not just relying on what happens during the material deposition stage. While reaching a temperature close to T_C, the huge decrease in the saturation magnetization almost suppresses the shape anisotropy barrier, leaving the nanostructures composing the pattern in the superparamagnetic state. This process corresponds to a "melting" of the ASI system and the islands are free to fluctuate and sample their whole energy landscape. Upon cooling down, the fluctuation dynamics slows down, until the system sits in a configuration that turns out to be quite similar to that obtained in as-fabricated samples, as shown in Fig. 4.9a, where once again large $T1$ domains appear. By comparing this figure with Fig. 4.9b (state generated by field demagnetization), it is possible to note a different behaviour between the heat thermalization process and the demagnetization protocol: the thermalization by heating is more effective in getting states close to the GS (a full $T1$ tiling), as also highlighted by the fractional vertex populations in Fig. 4.9c. Moreover, this thermally-induced melting-freezing protocol can be repeated as many times as

(a) Thermalization by heating

(b) Demagnetization protocol
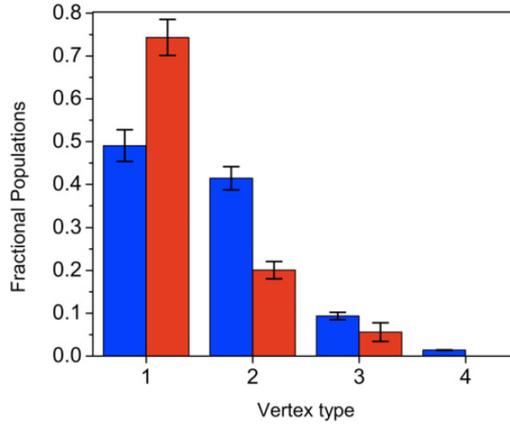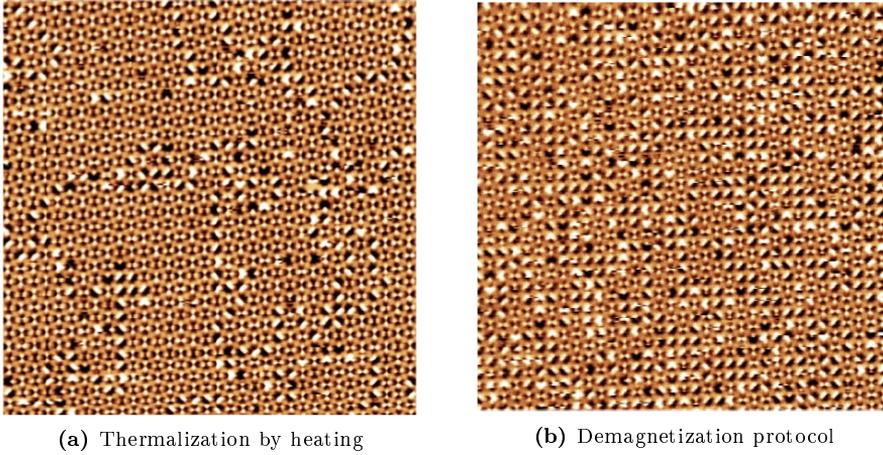
(c) Vertex populations

Figure 4.9: (a) MFM image of a 15×15 μm^2 region of a square ASI sample subjected to the heat thermalization process. (b) MFM image of a 15×15 μm^2 region of a square ASI sample which underwent the demagnetization protocol. Image (a) shows ordered GS domains, whereas (b) is characterized by a disordered state mainly formed by $T1$, $T2$ and $T3$ vertices. (c) Fractional vertex populations corresponding to protocol (a) (red columns) and protocol (b) (blue columns). The error bars come from the analysis of various regions on the samples. Adapted from [157].

desired on the same sample, since the needed temperature is not high enough to determine structural modifications[1] [157]. Thereby, this approach paved the way for the systematic experimental study of thermally-induced frozen states in ASI systems. In literature, various materials, nanostructure sizes and shapes and lat-

---

[1] Actually, the first annealing can determine an irreversible change in the magnetic properties. However, the results of subsequent heat thermalization processes have been verified to be reproducible.

tice parameters have been considered, but an extended GS in square ASI systems
has been obtained only in few cases [136, 161]. Most of the time, the end state
is similar to Fig. 4.9a, where $T1$ domains are separated by domain walls whose
distribution, composition and evolution might be exploited for the realization of
nanodevices [140].

4.4   Design of square artificial spin ice systems

Giving (i) the importance of the thermalization process by heating, whose
outcomes strongly depend on the parameters governing the systems, and (ii) the
need for predicting and controlling these outcomes, a method for properly design-
ing the involved nanostructures is mandatory. For square ASI systems, the GS
and the equilibrium configuration are determined by the energy associated to the
vertex configurations in Fig. 4.3, while the energy barriers for the magnetization
reversal of the considered nanostructures set the time-scale for the evolution. The
evaluation of the relevant energies requires the definition of few aspects governing
the whole system:

- the **size** and the **shape** of the nanostructures;

- the choice of the (magnetic) **material**;

- the **lattice parameter** of the square grid.

Even if they are all of utmost importance, the work connected to this thesis
deeply explored the impact of the nanostructure size and shape on the global
behaviour, as we will se in what follows. Regarding the material, a model for
$M_S(T)$ has been obtained by fitting the experimental data from Ref. [157]:

$$M_S(T) \;=\; M_S^{0K}\left(1 \;-\; \frac{T}{T_C}\right)^{\beta}, \quad \text{where} \quad \begin{cases} M_S^{0K} = 725 \text{ kA} \cdot \text{m}^{-1} \\ T_C = 764 \text{ K} \\ \beta = 0.35 \end{cases} . \quad (4.9)$$

This set of parameters is not intended to describe the behaviour of M_S close
to T_C (as for the definition of critical exponents [12]), but it has been obtained
by fitting the experimental data in a broad temperature range, namely from
300 K to T_C. The lattice parameter controls the strength of interactions. At this
stage, we would like to have as strong as possible interactions, to be far from the
isolated nanostructure behaviour and to have sizeable interactions even at high
temperatures. The limit we pose is to work with a minimum separation between

neighbouring nanostructures that can be safely fabricated by EBL, so of the order
of 50 nm.

4.4.1   The single-vertex approximation

The most common approach found in literature for calculating the energy
barriers is the one described by Farhan et al. [135]:

$$\Delta E \ = \ \Delta E_0 \ + \ \frac{E_f \ - \ E_i}{2}. \tag{4.10}$$

To get the actual energy barrier ΔE, the isolated island energy barrier ΔE_0
(calculated following Ref. [20] or Ref. [162]) is linearly modified according to the
initial (E_i) and final (E_f) configuration energies. These energies usually refer to
vertex energies and can be calculated through Eqs. (4.5) in the macrospin approx-
imation. Even if Eq. (4.10) can indeed be derived inside the framework provided
by the macrospin approximation, things start changing when considering (i) the
actual shape of the involved nanostructures and (ii) the fact that each island is
shared between two vertices.

As a first step in our design strategy, we analyzed the energy landscape of
a single vertex by relaxing one of the hypothesis associated to the macrospin
approximation in order to take into account the actual nanostructure shape.
Nonetheless, at this stage each island is still considered to be uniformly mag-
netized and to reverse by coherent rotation of the magnetization. The energies
evaluated in this *single-vertex approximation* (SVA) are improved with respect
to the values obtained by means of Eqs. (4.5), but the validity of the uniform
magnetization assumption strongly depends on the nanostructure size, shape and
temperature.

To illustrate the results of the SVA, we considered a shape frequently encoun-
tered in literature, namely the *stadium-like* shape. The size of each nanostruc-
tures has been tuned to be easily fabricated by EBL and to show a superpara-
magnetic behaviour far from T_C (see the material parameters in Eq. (4.9)): the
major axis is 150 nm, the minor axis is 100 nm and the thickness is 3 nm. The
resulting lattice parameter is $a = 260$ nm, as described in Fig. 4.10. The process
to be analyzed, as shown in Fig. 4.11a, is the magnetization reversal of one of the
nanostructures composing the vertex (*single-flip event*), from $\vartheta = 0°$ to $\vartheta = 180°$
and viceversa. The magnetostatic energy has been calculated according to the
method developed by Newell at al. [162], which allows taking into account the
actual nanostructure shape (cell-size of 5 nm $\times$ 5 nm $\times$ 3 nm), while the interac-
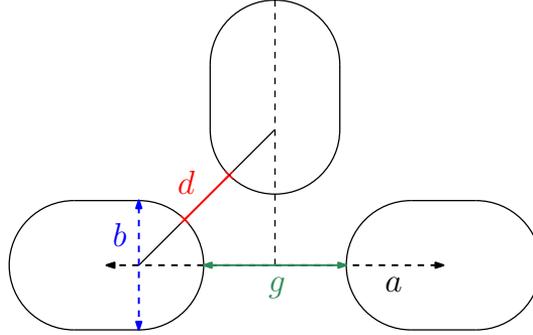
Figure 4.10: Stadium-like nanostructures composing a vertex. If the major axis is 150 nm and the minor axis is $b = 100$ nm, a gap $g = d\sqrt{2} + b(\sqrt{2} - 1) \approx 110$ nm results in a separation d between neighbouring nanostructures of 50 nm, so justifying the value $a = 260$ nm. Playing with the nanostructure shape, g can be further reduced while maintaining the d target value.

tion energy between islands has been evaluated as described in Sec. C.2. All the above parameters lead to a relaxation time of 1 s at $T_b = 388$ K for an isolated nanostructure (corresponding to an energy barrier of $\approx 23 k_B T_b$ for $\nu_0 = 10^{10}$ Hz), considered to be the relevant blocking temperature criteria for these systems.

Figure 4.11b shows the energies involved in the single-flip magnetization reversal and allows us to describe several general aspects. The energy barriers can be calculated by subtracting the energy of the starting state ($\vartheta = 0°$ or $\vartheta = 180°$) from the maximum energy obtained during the reversal process ($\vartheta = 90°$ or $\vartheta = 270°$). These barriers can be compared with the purple bar in Fig. 4.11b, representing the energy barrier in case of an isolated nanostructure. Moreover, it turns out that not all the sixteen possible configurations associated to a vertex can be connected by means of a single-flip event. Despite the chosen island, only three base transitions can be identified: $T_1 \leftrightarrow T_3$, $T_2 \leftrightarrow T_3$ and $T_3 \leftrightarrow T_4$. Hence, the $T3$ vertices result to be key states for the achievement of a full $T1$ tiling, since $T2$ and $T4$ vertices can be converted in $T1$ vertices only passing through $T3$. The $T_2 \leftrightarrow T_3$ transition points out another interesting feature: the energy barriers for $\vartheta = 90°$ or $\vartheta = 270°$ are not always equal, meaning that the neighbouring nanostructures can induce a preferential rotation direction for the reversal.

From the energy barriers, Eq. (4.8) allows calculating the switching frequencies (as the inverse of the relaxation time). Figure 4.11c shows their values obtained for $\nu_0 = 10^{10}$ Hz and considering all the possible configurations involving the three black nanostructures in Fig. 4.11a. Each one of the eight configurations is associated to four switching frequencies, since there are two starting states and
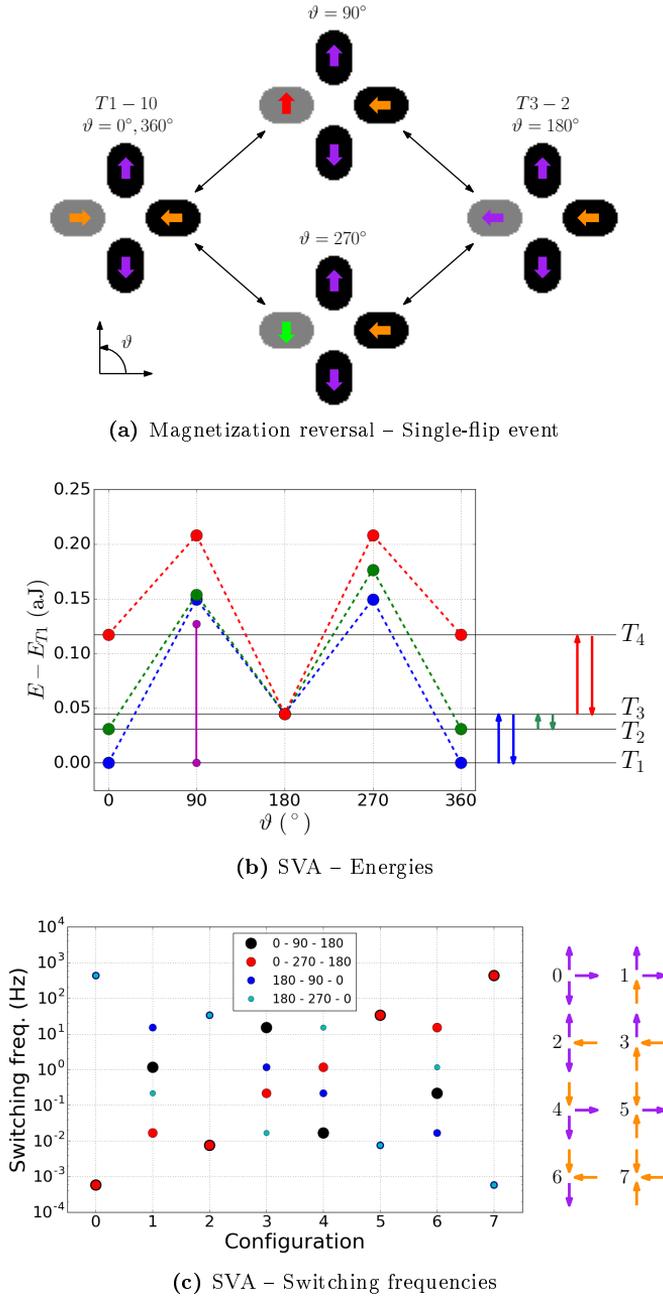
(a) Magnetization reversal – Single-flip event

(b) SVA – Energies

(c) SVA – Switching frequencies

Figure 4.11: (a) Schematic of a single-flip event showing the magnetization reversal leading to a $T_1 \leftrightarrow T_3$ transition. This event corresponds to the blue-dashed curve in (b) and to configuration 2 in (c). (b) Calculated SVA energies at $T_b = 388$ K for the four configurations depicted in (a) when the three possible transitions connected to a single-flip event are considered. The value $\vartheta = 360°$ has been repeated for clarity. The purple bar corresponds to the energy barrier of the isolated nanostructure. (c) Switching frequencies for all the possible configurations involving the three black nanostructures in (a). The numbers in the legend represent "initial-state angle – barrier angle – final-state angle" for the gray nanostructure.
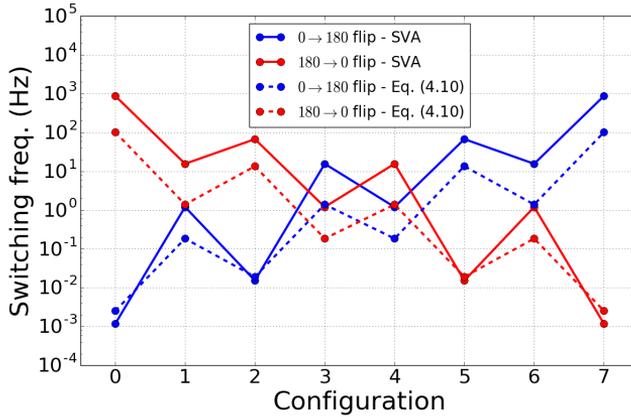
Figure 4.12: Comparison between the SVA and Eq. (4.10). The continuous lines represent the combined switching frequencies taken from Fig. 4.11c (the SVA), whereas the dashed lines show the switching frequencies calculated according to the energy barriers given by Eq. (4.10) and Ref. [162]. More details are given in the body of the text.

two rotation directions for the reversal, as indicated by the legend. The vertical order of the coloured dots is related to the symmetry of the configurations (what equilibrium state and what rotation direction are preferred), whereas their positions indicate the transition type. Indeed, neglecting the colors, there are only three scenarios (e.g. configurations 0, 1 and 2), corresponding to the three base transitions in Fig. 4.11b. Moreover, four distinct switching frequencies (see, e.g., configuration 1) are the signature of a preferential rotation direction as in the case of $T_2 \leftrightarrow T_3$ transitions.

The switching frequencies so calculated can be compared to the approach described by Eq. (4.10) and Ref. [162] for the calculation of energy barriers. Since Eq. (4.10) does not provide a distinction between flipping events occurring through $\vartheta = 90°$ and through $\vartheta = 270°$, the two transitions corresponding to the same starting state in the SVA have been combined by *summing* the relative switching frequencies. This assumption can be justified by considering these events as independent transition channels, as stated in Eq. (D.2).

4.4.2   The double-vertex approximation

When calculating energy barriers for nanostructures composing a square ASI system, the SVA does not take into account neither the lattice geometry (i.e. the fact that each island is shared between two vertices) nor the long-range nature of the dipolar interaction. However, it turns out to be enough to consider only
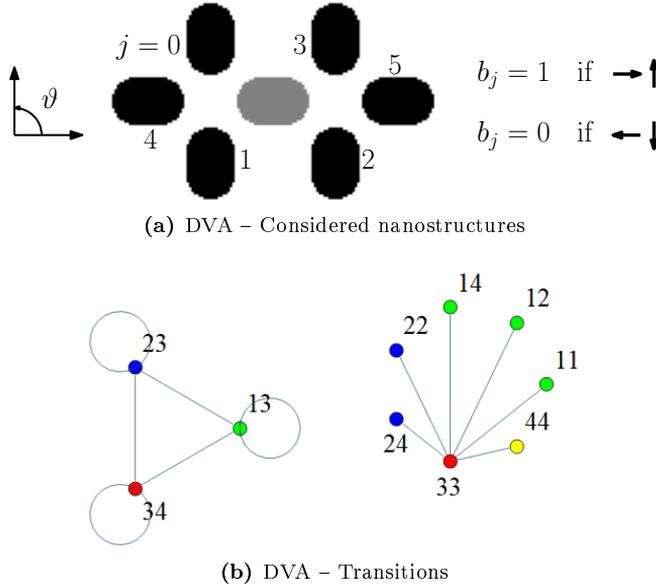
(a) DVA – Considered nanostructures

(b) DVA – Transitions

Figure 4.13: (a) Considered nanostructures in the DVA. Energy barriers and switching frequencies can be calculated for all the sixty-four possible configurations involving the six black nanostructures. The island index j and the island coefficient b_j help in assigning a unambiguous configuration index, as explained in the body of the text. (b) The twelve allowed transitions $T_i T_j \leftrightarrow T_k T_l$ in the DVA (so considering single-flip events). The node colors represent the less energetic vertex involved in the pair, whereas the numbers identify the vertex types i, j and k, l.

first and second nearest-neighbours (see Fig. 4.4a) for the evaluation of proper interaction energies [163, 164]. This fact led us to introduce a second step in our design strategy, the *double-vertex approximation* (DVA). Retaining all the assumptions leading to the SVA, we are now considering the interactions between all the seven nanostructures in Fig. 4.13a in order to evaluate energies and energy barriers. Hence, the switching frequencies can be calculated as before for all the sixty-four possible configurations for the six considered neighbours, as shown in Fig. 4.14. A rule has been devised in order to classify all the configurations: an index j has been associated to each one of the six neighbouring nanostructures, as depicted in Fig. 4.13a. Then, a coefficient b_j has been defined, according to the magnetization direction of each black nanostructure along its major axis: $b_j = 1$ if the magnetization lies either at $\vartheta = 0°$ for horizontal nanostructures or at $\vartheta = 90°$ for vertical nanostructures, whereas $b_j = 0$ if the magnetization lies either at $\vartheta = 180°$ for horizontal nanostructures or at $\vartheta = 270°$ for vertical nanostructures. Hence, the configuration index c_i (for $i = 0, \ldots, 63$) can be found
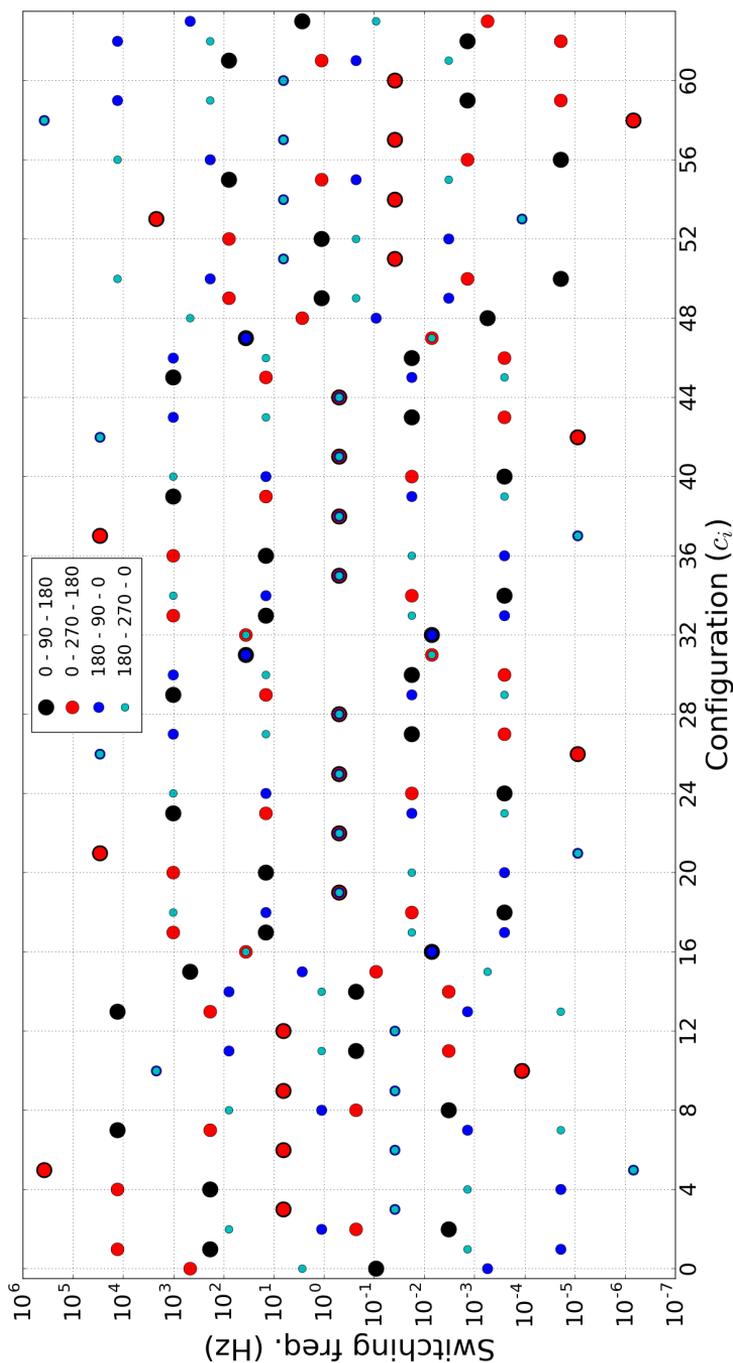
Figure 4.14: Switching frequencies at $T_b = 388$ K with $\nu_0 = 10^{10}$ Hz for all the possible configurations involving the six black nanostructures in Fig. 4.13a. The numbers in the legend represent "initial-state angle – barrier angle – final-state angle" for the gray nanostructure, as detailed in Fig. 4.11a.

according to

$$c_i = \sum_{j=0}^{5} b_j 2^j. \tag{4.11}$$

Once the DVA calculation strategy has been implemented, it is possible to easily vary all the relevant parameters governing square ASI systems (see the beginning of Sec. 4.4), in order to see the impact on the switching frequencies. Figure 4.14 also allows visualizing some general symmetries, which are related to the distribution of the magnetization in the six neighbouring islands rather than to the system parameters. Indeed, it turns out there are only *twelve* transitions to be considered (i.e. twelve significant arrangements of coloured dots), corresponding to all the possible transitions involving two adjacent vertices for single-flip events taking place in the shared island, as shown in Fig. 4.13b. Moreover, regarding the number of distinct switching frequencies associated with each configuration, there are only *three* cases. Four different switching frequencies (e.g. configuration $c_i = 4$) mean that the four transitions are characterized by different energy barriers. Two different switching frequencies indicate a certain symmetry in the process. Configuration $c_i = 12$ shows a case in which flipping through $\vartheta = 90°$ is equivalent to pass through $\vartheta = 270°$, but one of the two minima (here $\vartheta = 180°$) is more stable than the other ($\vartheta = 0°$). On the contrary, for configuration $c_i = 16$ the two minima correspond to the same energy, but flipping through $\vartheta = 270°$ is a more probable process than flipping through $\vartheta = 90°$. Eventually, for configurations like configuration $c_i = 28$ the four transitions are associated with the same switching frequency, which does coincide with the switching frequency determined by considering the isolated nanostructure energy barrier ΔE_0.

4.4.3 The time evolution of the vertex populations

The calculation of energy barriers and switching frequencies is driven by the need for investigating the thermalization process by heating. Starting from a given initial state for a square ASI system at a given temperature, the idea is to predict the evolution of the vertex populations as a function of time, in order to see the impact of the various system parameters on the formation of the equilibrium state. Some questions can be posed: *what determines the appearance of GS domains instead of a complete T1 tiling? How do the domain boundaries (composed by T2 and T3 vertices) form and develop?* To provide answers, we decided to employ *kinetic Monte Carlo* (kMC) simulations [29, 165–167].

The usual goal in Monte Carlo simulations is the calculation of the expecta-

tion value of some observable quantity at thermal equilibrium [165]. In the past, Monte Carlo simulations have been used for obtaining the equilibrium state for square ASI systems [168, 169]. However, not all the Monte Carlo algorithms are suitable for a dynamical interpretation of the results, i.e. for extending the findings to out-of-equilibrium states. For this purpose, the kMC algorithm proved to be an invaluable method for investigating the thermal behaviour of ASI systems [131, 135, 136, 170–172]. As detailed in Appendix D, the kMC needs the switching frequencies to be formulate as rates with physical meaning [167]. This requirement nicely match with our DVA, which has been precisely developed for providing actual switching frequencies.

The main limitation of the DVA resides in the assumption regarding the considered magnetization reversal process: the coherent rotation of a uniformly magnetized magnetic nanostructure. While this mechanism allows us to quickly calculate all the needed switching frequencies, it is unlikely to happen in a real sample. Indeed, it is well known that the field-induced magnetization reversal process in magnetic nanostructures does depend on their size and shape, demonstrating the existence of reversal paths characterized by lower energy barriers than the coherent rotation process [173–175]. Even if the magnetization reversal is not field-induced while considering the thermal behaviour of ASI systems, there are experimental evidences pointing out the existence of low-energy reversal paths. In two related works (Kapaklis et al. [176] and Andersson et al. [177]), the comparison between calculations and experimental data required the use of a reduced nanostructure magnetization with respect to the value obtained for a continuous thin film of the same material. The reduction (about 65 % [177]) has been ascribed to the non-collinearity of the magnetization close to the edges of a magnetic nanostructure, resulting in a smaller effective magnetic moment for the islands. For nanostructures fabricated with isotropic materials, the bending of the edge magnetization originates from the balance between exchange and magnetostatic interaction energies. This balance is not only responsible of the magnetization equilibrium state, but it also has a deep impact on the development of the reversal mechanism [45]. Similar conclusions have been obtained also by Morley et al. [178], according to whom "whilst reduced magnetization or volume can explain some of this discrepancy, it seems clear once again that a pure coherent rotation mechanism is unlikely to be strictly followed".

For these reasons, we decided to investigate the *thermally-activated magnetization reversal mechanism* by making use of micromagnetic simulations performed at finite temperature.

4.4.4 Micromagnetic simulations at finite temperature

As we have seen in Sec. 1.3, micromagnetics is the theory describing magnetization processes [12]. Through *micromagnetic simulations* (i.e. the numerical solution of the LLG equation (1.48)), it is possible to get an insight into the magnetization time evolution in magnetic nanostructures, both isolated and interacting. In particular, the sLLG equation (see Sec. 1.4.1) allows taking into account the effect of temperature by adding a properly-defined fluctuating magnetic field (given by Eq. (1.66)) to the LLG effective field. The goal of this analysis is to obtain a quantitative evaluation of the discrepancy between the coherent reversal mechanism and what could happen in a real magnetic nanostructure because of temperature. In other words, the calculation of the DVA switching frequencies provides a way of quickly getting input values for kMC simulations, but the level of approximation provided by the DVA has to be improved in order to include the effect of thermal fluctuations on the energy barriers. Hence, we simulated what happens to the magnetization of an isolated nanostructure (the same one described in Sec. 4.4.1) in no applied magnetic field as a function of time and temperature, for obtaining switching frequencies in case of a thermally-activated magnetization reversal process. As simulation parameters, we considered the saturation magnetization given by Eq. (4.9) [41], $A = 13$ pJ $\cdot$ m^{-1} as exchange stiffness, $\alpha = 0.01$ and a cell size of 5.234 nm $\times$ 5.125 nm $\times$ 3 nm.

The micromagnetic simulation program we decided to use was *mumax*^{3} [25], because of its key characteristics. The capability of performing simulations at finite temperatures, by solving the sLLG equation, is one of its core functionalities [36]. Moreover, being GPU-based, it is faster than conventional micromagnetic solvers relying exclusively on the CPU (e.g. *OOMMF* [179]). This is of extreme importance for us, since we need to simulate long time intervals (at least 10 μs) in order to have enough statistics (i.e. enough reversal events) for extracting the switching frequencies. All the micromagnetic simulations performed for this chapter have been realized in collaboration with Dr. Jonathan Leliaert (Ghent University, Belgium), who is member of the *mumax*^{3} development team.

Figure 4.15 shows the time evolution of the normalized x-component of the magnetization (m$_x$) at $T = 700$ K. Since the x-axis coincides with the easy axis induced by the shape anisotropy, the jumps between stable states (m$_x \approx 1$ and m$_x \approx -1$) clearly appears in the plotted stream. By counting how many times the m$_x$ value crosses the line given by m$_x = 0$, it is possible to count the number of switching events and the time distance between successive crossing points is a measure of the switching time for the corresponding jump. It is worthwhile to
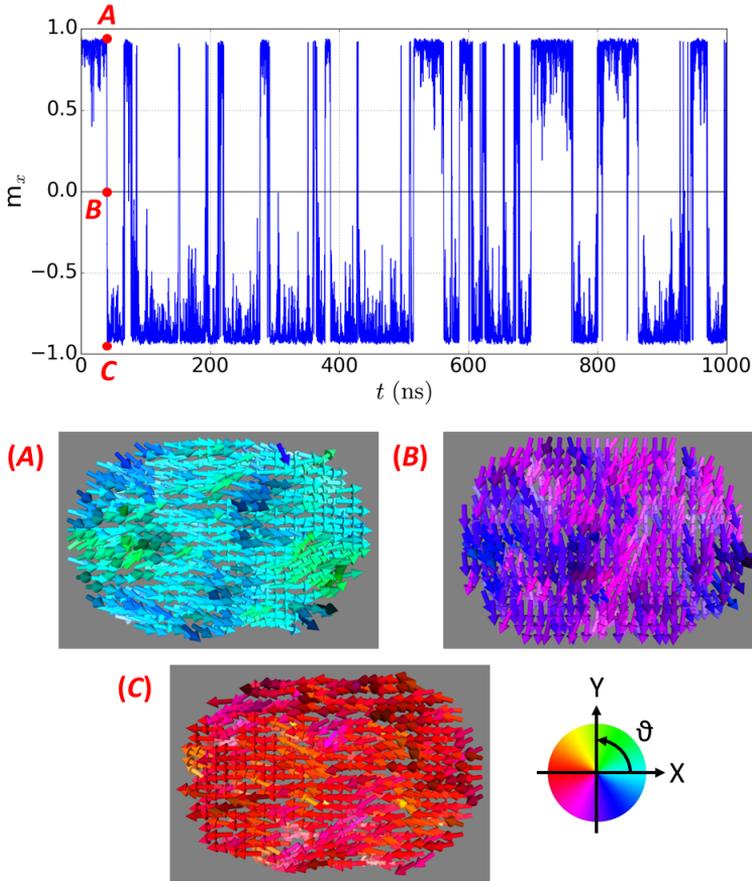
Figure 4.15: Simulated magnetization evolution for an isolated nanostructure at $T = 700$ K. The normalized x-component of the magnetization m_x has been plotted in a time interval of 1 μs to show the jumps between stable states. The A, B and C frames correspond to the red-filled dots depicted in the plot.

stress here the fact that "switching time" refers to the time the magnetization resides close to an equilibrium state and not to the duration of the reversal itself (i.e. the sharp jumps in Fig. 4.15). In case of an isolated island, there is no need for identifying the transition type, since the absence of neighbouring islands makes the four switching frequencies all equal and so all the jumps contribute to the statistical analysis of the same event. Figure 4.15 also shows three magnetization configurations corresponding to a jump from $\vartheta = 0°$ (A) to $\vartheta = 180°$ (C). The non-uniformity of the magnetization comes from the fact that here we are considering both all the relevant energy terms (the exchange energy and the magnetostatic energy) and the effect of thermal fluctuations, as described by Eq. (1.66). The actual simulated stream at $T = 700$ K corresponds to a time interval
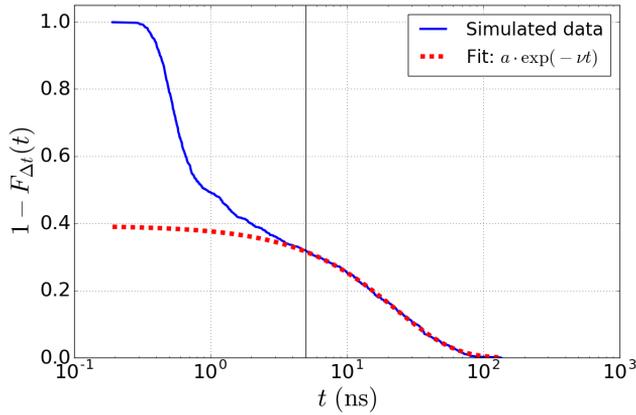
(a) Switching time cCDF at $T = 700$ K
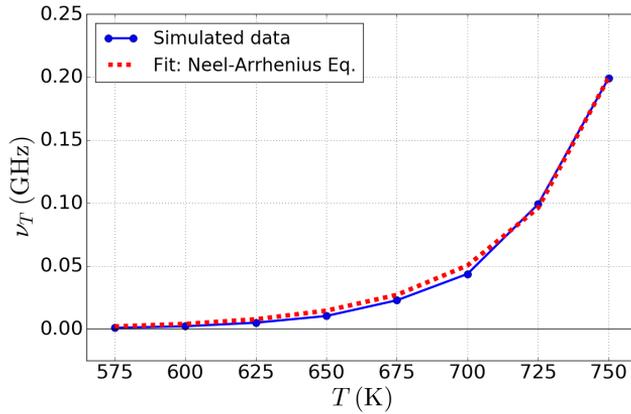
(b) Switching frequency as a function of temperature

Figure 4.16: (a) cCDF for the switching times extracted from the simulation shown in Fig. 4.15 and best fit according to Eq. (D.10b). The black vertical line corresponds to $t = 5$ ns. (b) Switching frequency ν_T as a function of temperature and best fit according to the Néel–Arrhenius equation. More details are given in the body of the text.

of 10 μs, allowing us to get 1061 switching events. Each event has been associated to a switching time Δt as described above and Fig. 4.16a shows the *complementary cumulative distribution function* (cCDF). As explained in Appendix D, the expected cCDF can be derived from Eq. (D.10b), but the obtained cCDF is characterized by two modes. Below a switching time of 1 ns, the recorded events reflect both the statistics of the thermally-activated magnetization reversal and the presence of "immediate switch-back" events. As noted by Brown [180], the thermal energy leading to the reversal process can be high enough to determine a double reversal, bringing the magnetization configuration back to the starting

state. Having no net effect, this double events can be neglected in our analysis (in first approximation). Anyway, the two contributions are difficult to disentangle, but the mode we are interested in extends to long switching times (i.e. the tail of the simulated cCDF). Hence, the fit can be performed according to the equation $a \cdot \exp(-\nu t)$ for the data satisfying $t \geq 5$ ns, a limit chosen by looking for the best agreement. The quantity to be retrieved is the average switching frequency ν, whereas a only takes into account the fact we are considering a portion of the simulated cCDF in order to exclude the contribution from immediate switch-back events. All the analysis so far described has been repeated at multiple temperatures, in order to extract the switching frequency ν_T as a function of temperature (see Figs. F.1–F.7). Table 4.1 and Fig. 4.16b summarize the main results. The errors for ν_T correspond to one standard deviation and have been calculated as the square root of the diagonal elements of the covariance matrix returned by the fitting function [181]. For ν_T as a function of T, the Néel–Arrhenius equation (1.56) represents the proper fitting function, since we are dealing with thermal activated events. However, we considered a slightly different form, since we are interested in capturing the difference with respect to a coherent magnetization reversal:

$$\nu_T \;=\; \nu_0 \exp\left(-\frac{c\Delta E_0}{k_B T}\right), \tag{4.12}$$

where ΔE_0 is the energy barrier for an isolated nanostructure in case of coherent reversal and $(\nu_0,\ c)$ are the fitting parameters. So, we calculated ΔE_0 with $mumax^3$ at the needed temperatures (where the only temperature effect is given by the fact that M = M(T)) for using the quantity $\Delta E_0/(k_B T)$ as the fitting

T (K)	t_{Sim} (μs)	N_{Tot}	N_{Fit}	ν_T (Hz)	$\Delta E_0/(k_B T)$
575	50	62	37	$(8.3 \pm 0.3) \cdot 10^5$	9.17
600	10	34	20	$(2.10 \pm 0.12) \cdot 10^6$	7.96
625	10	70	42	$(4.90 \pm 0.11) \cdot 10^6$	6.80
650	10	195	98	$(1.025 \pm 0.010) \cdot 10^7$	5.69
675	10	449	187	$(2.273 \pm 0.015) \cdot 10^7$	4.61
700	10	1061	339	$(4.367 \pm 0.011) \cdot 10^7$	3.53
725	10	2183	540	$(9.901 \pm 0.018) \cdot 10^7$	2.41
750	10	4391	560	$(1.992 \pm 0.003) \cdot 10^8$	1.14

Table 4.1: Switching frequency ν_T as a function of temperature T. The parameter t_{Sim} refers to the total time considered in the micromagnetic simulations, N_{Tot} is the total number of switching events occurred in t_{Sim}, N_{Fit} denotes the number of events contributing to the fit (i.e. with a switching time greater than 5 ns) and ΔE_0 is the energy barrier for an isolated nanostructure in case of coherent magnetization reversal.

independent variable (see the last column in Table 4.1). By considering $\ln(\nu_T)$ as the dependent variable, we were able to exploit the *weighted linear regression* [182] in order to give more relevance to the high-temperature data, supported by the highest number of events (reflecting in the lowest relative errors). Eventually, we obtained

$$\nu_0 = (3.84 \pm 0.07) \cdot 10^8 \text{ Hz}, \qquad (4.13a)$$

$$c = 0.576 \pm 0.013. \qquad (4.13b)$$

The main result of this analysis is the fact that $c < 1$: the thermally-activated magnetization reversal is associated with an energy barrier lower than the coherent rotation energy barrier by a factor of c. As discussed in Sec. 4.4.3, $c < 1$ qualitatively agrees with the results reported in literature. Another interesting conclusion emerges from this analysis: the energy barrier reduction factor c has been found while considering perfectly defined nanostructures in our simulations, i.e. without considering defects. So, the fact that $c < 1$ both in simulations and in experiments seems to be primarily related to the nature of the thermally-activated magnetization reversal. Defects certainly contribute in lowering the energy barrier, but, according to our analysis, to a much lesser extent. In the following, we will refer to the corrected-energy-barrier version of the DVA (SVA) as *corrected DVA (SVA)*.

Nonetheless, the value for c has been obtained for a certain combination of geometrical shape and material parameters, and the requirement of having enough jumps in the simulated time interval restricted the range of possible simulation temperatures ($T > 575$ K in this case). Then, up to this point, we cannot say too much on how c and ν_0 could be influenced by the temperature range of analysis and by geometrical and material parameters. Regarding ν_0, it is well known it can depend on several parameters (see, e.g., Ref. [183]) and a recent analysis on similar nanostructures returned a ν_0 value of the same order of magnitude as Eq. (4.13a) [184]. However, we are mainly interested in the behaviour of c, since it resides inside the exponential function and it can determine huge changes in the switching frequency order of magnitude.

4.4.5   Comparison with literature data

Our findings allowed us to analyze and interpret the experimental results available in Ref. [136]. This research article has been chosen since it provides a complete set of data we can try to reproduce by using our approach, namely the
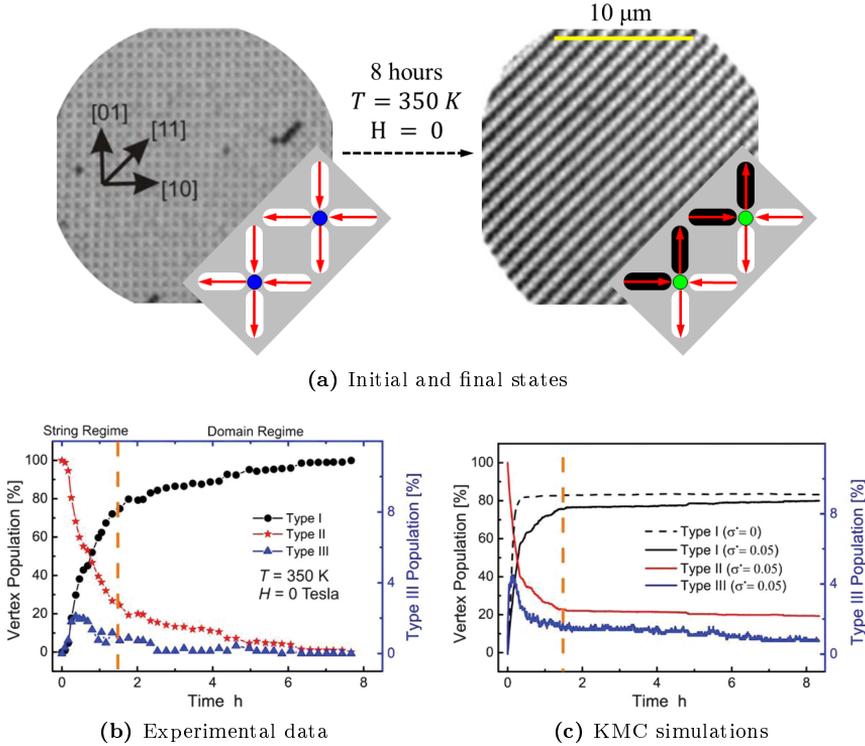
(a) Initial and final states

(b) Experimental data

(c) KMC simulations

Figure 4.17: (a) Initial (left) and final (right) XMCD images recorded during the experiment reported in Ref. [136]. The dark and bright contrast in the images is a measure of the orientation of the nanostructure magnetization, as schematically shown in the insets. In 8 hours at $T = 350$ K, the array evolved from a full $T2$ tiling to a full $T1$ tiling. (b) Time evolution of the vertex populations extracted from the recorded XMCD images. (c) KMC simulations aimed at obtaining a reasonable agreement with the experimental data. Adapted from [136].

calculation of the energy barriers in the DVA, the use of a correction factor c and the simulation of the time evolution of the vertex populations through the kMC method.

The considered sample consists in a 40 μm × 30 μm square ASI system formed by stadium-like Permalloy ($Ni_{83}Fe_{17}$) nanostructures whose major axis is 470 nm, the minor axis is 170 nm and the thickness is 3 nm. The lattice parameter is $a = 600$ nm, corresponding to a $g = 130$ nm gap size. The array has been brought to a full $T2$ tiling by applying a saturating magnetic field along the [11] direction, as shown in the left part of Fig. 4.17a. Then, the time evolution of the vertex populations has been recorded by collecting x-ray magnetic circular dichroism (XMCD) images [185] while the sample was left for 8 hours at $T = 350$ K in no applied magnetic field. The XMCD image taken at the

end of the experiment (right part of Fig. 4.17a) shows the formation of a full $T1$ tiling, which corresponds to the GS. The inspection of the obtained images allowed the authors to calculate the relative vertex populations and to extract the time evolution for $T1$, $T2$ and $T3$ vertices, as shown in Fig. 4.17b. The experimental data have been compared with kMC simulations, where the relevant parameters have been adjusted in order to get a reasonable agreement with the experiment: $M_S = 350$ kA $\cdot$ m^{-1}, $\nu_0 = 5 \cdot 10^{11}$ Hz and $\Delta E_0^* = 0.168$ aJ. The simulation results are shown in Fig. 4.17c. The parameter ΔE_0^* represents the intrinsic energy barrier for the considered nanostructures, which indeed is the parameter we considered in the micromagnetic analysis performed in Sec. 4.4.4. Moreover, for better reproducing the experimental data, the authors introduced a certain degree of disorder by randomly varying the intrinsic energy barrier of each nanostructure using a Gaussian distribution centered on ΔE_0^* with a standard deviation of $\sigma^* = 0.05\Delta E_0^*$. If we now calculate the ΔE_0 value (i.e. the energy barrier for an isolated nanostructure in case of coherent reversal) to be used in the DVA by considering the geometrical and material parameters above declared, we obtain $\Delta E_0 = 0.346$ aJ, which corresponds to $\Delta E_0^*/0.49$. The use of a reduced energy barrier for the magnetization reversal, which was introduced in the research article for getting a reasonable agreement with the experimental results, can possibly be justified through the micromagnetic analysis described in Sec. 4.4.4. It is not surprising we find here a different value ($c = 0.49$) with respect than before ($c = 0.58$), since c can depend on size, shape, material parameters, defects and temperature.

Knowing all the relevant parameters, we were able to run kMC simulations in the framework provided by the corrected DVA to test all our findings. For this purpose, we considered a square array having the same size as the fabricated one (40 μm $\times 30$ μm) and we took into account its finite size by calculating the switching frequency of the nanostructures composing the boundaries according to the corrected SVA, given that the boundary nanostructures are not shared between two adjacent vertices. Since c and ν_0 have been obtained in Sec. 4.4.4 for considerably different nanostructures, we decided to maintain the values extracted form the research article: $c = 0.49$ and $\nu_0 = 5 \cdot 10^{11}$ Hz. Figure 4.18a shows four images extracted form the XMCD measurement sequence. By combining them with the time evolution reported in Fig. 4.17b, it is possible to identify two regimes:

- in the *string regime*, chains (or strings) composed by $T1$ vertices form along the [11] direction and tend to merge with neighbouring strings;
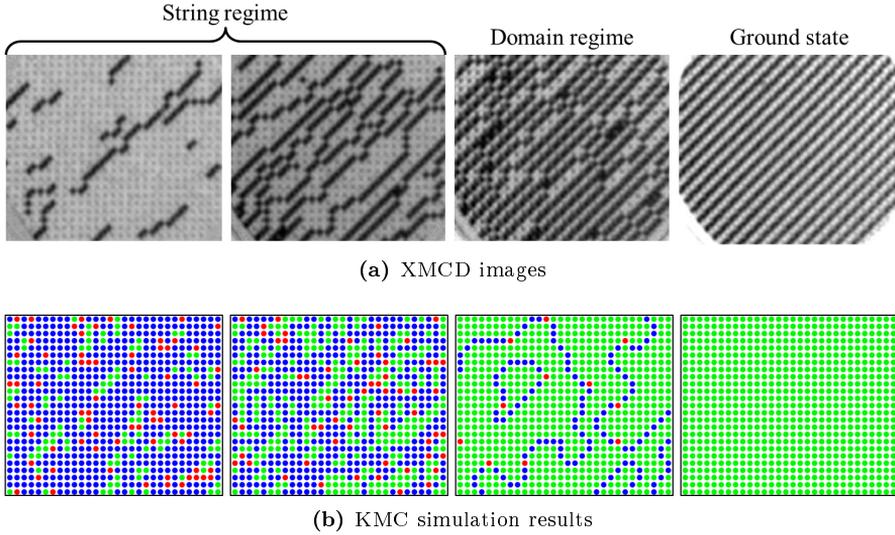
(a) XMCD images

(b) KMC simulation results

Figure 4.18: (a) XMCD images corresponding to the time evolution shown in Fig. 4.17b. The labels "string regime" and "domain regime" indicates different steps in the the array evolution, as described in the body of the text. Adapted from [136]. (b) Sequence of images extracted from our kMC simulations and corresponding to the regimes in (a). The colors associated to each vertex type can be found in Fig. 4.3.

- after joining together, the strings cluster and form extended domains of $T1$ vertices. We already saw this phenomenon, e.g. in Fig. 4.8a, since two colliding $T1$ domains can merge only if they have a compatible stacking. This stage is called *domain regime*.

If the domain walls could shrink or be expelled from the (finite-size) array, the final state would be the GS, i.e. a full $T1$ tiling, as happened in the experiment. For comparison, Fig. 4.18b shows four images extracted from our kMC simulations and corresponding to the above-described regimes. Each dot corresponds to a vertex, according to the color-legend depicted in Fig. 4.3, and the field of view has been adjusted to match the experimental one. In the first image, small $T1$ strings (green-filled dots) can be seen to develop along the [11] direction. The strings grow and merges until $T1$ domains appear in the third image, and they are separated by domain walls composed by $T2$ and $T3$ vertices (blue- and red-filled dots, respectively). Finally, also the kMC simulations show the formation of the GS. Although the sequence of regimes seems to be well reproduced, this is not the case for the corresponding time-scale, as shown in Fig. 4.19. The curves refer to the time evolution of the vertex populations in the whole array and they have been obtained as the average of the results coming form five kMC simulations. Basically, our method is able to predict the formation of the GS, but on a wrong
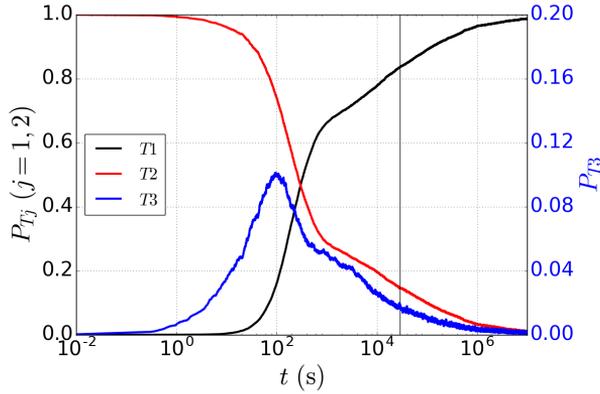
Figure 4.19: Time evolution of the vertex populations. The parameter P_{Tj} ($j = 1, 2, 3$) denotes the occupation probability for each vertex type. The curves have been obtained as the average of five kMC simulations. The black vertical line corresponds to 8 hours.

time-scale, since the equilibrium is reached in $\Delta t \approx 10^7$ s and not in 8 hours.

The reasons leading to this discrepancy can be several, since the path to kMC simulations goes through many stages. However, the fact that the various regimes are well reproduced (including the GS) but on a too long time-scale seems to imply that something went wrong in the energy barrier calculations. Indeed, we were forced to use parameters coming from the research article ($c = 0.49$ and $\nu_0 = 5 \cdot 10^{11}$ Hz) instead of calculating them through our approach (the corrected DVA), and this could determine the observed discrepancy. It is true that the parameters given in the research article have been derived from the experiment, but there is not a unique way for tuning c and ν_0 in order to get a reasonable agreement with the measured data. What we would like to achieve is the determination of these parameters through our approach (i.e. giving them a physical justification), which resulted to be impossible because of the considered temperature: the statistical analysis of the switching frequency cannot be performed through micromagnetic simulations for a stadium-like 470 nm $\times$ 170 nm $\times$ 3 nm nanostructure at $T = 350$ K. For this purpose, we identified a different method which provides the direct evaluation of energy barrier values: the *string method*.

4.4.6 The string method

The time evolution of the thermally-activated magnetization reversal allowed us to get a statistical evaluation of the energy barrier. On the other hand, the energy barrier considered for the DVA is based on a direct calculation: since the whole reversal path is known in the magnetization configuration space (whose co-
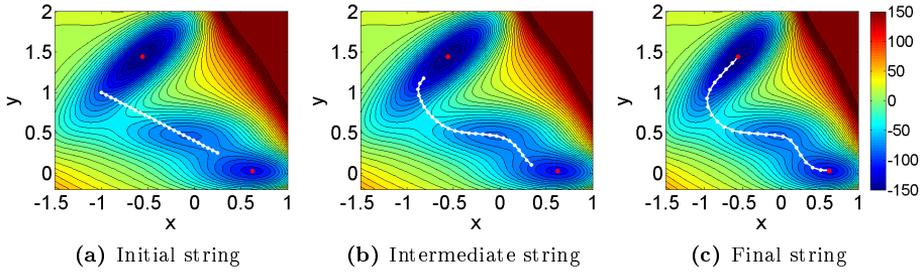
(a) Initial string   (b) Intermediate string   (c) Final string

Figure 4.20: String method applied to the Müller potential [186] considering a string composed by 25 states (the white-dotted lines). The red dots represent the energy minima to be considered. Adapted from [187].

ordinates are given by the components of $\mathbf{M}(\mathbf{r})$ $\forall \mathbf{r}$), the energy at each relevant point can be calculated according to Eq. (1.31), which represents the micromagnetic energy as a function of the magnetization. However, as we have seen, the advantage of a direct calculation is overshadowed by the fact that the configuration path associated to the lowest energy barrier cannot be easily identified: the assumption of a coherent magnetization reversal mechanism has been found to be not correct (from the micromagnetic simulations at high temperature and from the reduction in the energy barrier needed for reproducing the experimental results). By considering only two coordinates (x and y), a similar situation can be visualized in form of a two-dimensional color plot, as depicted in Fig. 4.20a. This plot represents the value of the Müller potential [186], a two-parametric model potential having three minima and two saddle points constituting a benchmark for this kind of problems. The white dotted line corresponds to the initial *string*: a guessed sequence of 25 states in the configuration space connecting two defined states at opposite boundaries. Neither the string is associated to the minimum energy barrier, nor the boundary states constitute equilibrium states sitting in energy minima (marked as red dots in Fig. 4.20a). However, being this problem of general interest (i.e. the search of minima and minimum energy paths in a multi-dimensional space), mathematical methods have been developed for numerically solving this task. In particular, we considered the *string method* [187–189] and its application to magnetic nanostructures [190, 191]. The working principle of this method is explained in detail in the former references, but Fig. 4.20 again helps in sketching the general idea. Starting from the guessed string shown in Fig. 4.20a, the string method provides a recipe for evolving each one of the states composing the string towards a path (i) joining two energy minima and (ii) corresponding to the minimum energy barrier between them. Essentially, considering a potential

energy $V(x, y)$, a minimum energy path $\varphi : \mathbb{R} \to \mathbb{R}^2$ is a curve connecting two minima and satisfying [188]

$$\boldsymbol{\nabla} V^\perp |_\varphi \ = \ 0, \tag{4.14}$$

where $\boldsymbol{\nabla} V^\perp$ is the component of $\boldsymbol{\nabla} V$ normal to φ. So, the initial curve is iteratively evolved under the action of $-\boldsymbol{\nabla} V$ until Eq. (4.14) results to be satisfied. For micromagnetic problems, the stopping criterion is based on the energy difference between each state and the corresponding state calculated in the previous iteration [191]. Figure 4.20c shows the obtained minimum energy path, whereas Fig. 4.20b shows an intermediate string still evolving towards the final path.

Back to our system, a string composed by states extracted from the coherent magnetization reversal mechanism constitutes the starting string, and the string method described in Ref. [190] can be applied to it in order to calculate the magnetization reversal path associated to the minimum energy barrier. This path is of particular relevance, since the energy barrier resides inside the exponential function for the calculation of the switching frequency, and so it corresponds to the most probable process for the thermally-activated magnetization reversal. Moreover, the effect of temperature can be taken into account just by considering the appropriate saturation magnetization value at the temperature of interest, changing nothing in the string method recipe. This part is still work in progress, so no results will be presented here. All the string method calculations we are considering will be performed in collaboration with Sabri Koraltan and Dr. Dieter Suess (TU Wien, Austria).

4.5   Conclusions

Through this chapter, we outlined a consistent method for the calculation of the switching frequencies related to thermally-activated processes in ASI systems. For this kind of processes, the switching frequency is well described by the Néel–Arrhenius equation, so the associated energy barrier is a key quantity to be determined. Our first step, leading to the SVA, consisted in evaluating the energy barrier at a vertex level taking into account the correct shape of the involved nanostructures. We soon recognized that this approximation was too stringent, since each nanostructure is shared in between two adjacent vertices. Hence, we introduced the DVA and we calculated all the 64×4 switching frequencies to be used as input for kMC simulations. However, both the DVA and the SVA are based on the magnetization reversal by coherent rotation, since this is the fastest way for calculating the quantities we need. To check this fact, the magnetization

reversal process to be considered was inspected by micromagnetic simulations at finite temperature, which returned an interesting conclusion: even if we were simulating perfectly defined nanostructures, the thermal activation of the reversal process caused the reduction of the energy barrier value to be used in the Néel–Arrhenius equation for retrieving the simulated switching frequencies. Then, we coded this information in form of an energy barrier reduction factor c. The fact that $c < 1$ can often be encountered in literature, but we tried here to give a more robust physical justification despite the presence of defects in real samples.

Chapter 5

Thermoplasmonic Heating of Artificial Spin Ice Systems

Chapter 4 has been devoted to the analysis of thermally-induced processes in square ASI systems. In literature, all the experiments involving the heating of ASI systems are performed through the use of conventional heaters [157, 161], namely by putting the sample in contact with a surface whose temperature can be precisely controlled. Here, we exploit the principles of plasmonics to optimize the absorbed power in metallic nanostructures that can be used as building blocks for ASI systems. The heating process is given by the dissipation of the absorbed power in form of heat. Such kind of mechanism offers several advantages with respect to the conventional heating by contact. First of all, the anisotropy in the optical properties of elongated metallic nanostructures allows controlling the delivered heat by means of the polarization direction of the incident electromagnetic radiation, providing *selective* heating: the extent of the absorbed power depends on the relative orientation between the light polarization and the major axis of the nanostructures. Furthermore, by focusing the beam to small spots (up to 1 μm in diameter) a *local* heating can be obtained. Finally, the thermal inertia, which sets an upper limit to the heating (or cooling) rate, is not given by bulky heating devices, but it is determined by the sample thermal properties, so allowing for studies on a wider temporal scale. All these features are of interest both for fundamental research and for possible opto-activated ASI-based devices.

This chapter will constitute the frame for setting-up a research article in collaboration with C. Rufo and P. Vavassori.

5.1   Thermoplasmonics

The field of *thermoplasmonics* deals with heating metal nanostructures with light [59, 192, 193]. This apparently simple sentence contains all the elements we need for the heating of ASI systems. The key physical principle consists in what happens when light is shone on a metal nanostructure: the electric field of the incident light put the free electrons in an oscillatory motion (i.e. an oscillatory electric current) and a resonance, called localized surface plasmon (LSP) resonance, can appear. As briefly discussed in Sec. 1.6.1, the interaction with the electromagnetic radiation is enhanced when a LSP resonance is excited and energy is transferred to the nanostructure in the most efficient way. Part of this energy is re-emitted in form of electromagnetic waves (*scattered radiation*) and part is dissipated inside the nanostructure in form of heat via the Joule effect. We are interested in this second mechanism (i.e. *absorption*) for our purposes. The most important quantity to be determined in order to compute the resulting temperature field is the total (heat) power absorbed by the nanostructure, which is given by $\sigma_{abs}I_b$ for an incident electromagnetic wave with intensity I_b, since we defined the absorption cross section σ_{abs} as an "effective area" crossing the incident electromagnetic wave and quantifying the absorbed power. By using linearly polarized light and elongated nanostructures, it is possible to tune the absorbed power by changing the direction of the polarization axis, as shown in Fig. 1.7b.

When delivering energy to a metal nanostructure fabricated on top of a substrate, the main mechanism governing the temperature field evolution is *heat diffusion*. For a medium with thermal conductivity κ, mass density ρ and specific heat at constant pressure c_p, the heat diffusion equation reads [59]

$$\rho c_p \frac{\partial T(\mathbf{r},t)}{\partial t} \; - \; \boldsymbol{\nabla} \cdot \kappa \boldsymbol{\nabla} T(\mathbf{r},t) \; = \; q_h(\mathbf{r},t), \tag{5.1}$$

where $q_h(\mathbf{r},t)$ is the heat power density (per unit volume). The steady-state solution of Eq. (5.1) provides the equilibrium temperature field for a metallic nanostructure embedded in a homogeneous medium with thermal conductivity κ and illuminated with CW radiation. For a spherical nanostructure of radius a, the temperature variation with respect to the reference boundary temperature is given by [59]

$$\Delta T(\mathrm{r}) \; = \; \begin{cases} \dfrac{Q_h}{4\pi\kappa a} & \text{for } \mathrm{r} \leq a, \\[2ex] \dfrac{Q_h}{4\pi\kappa \mathrm{r}} & \text{for } \mathrm{r} > a, \end{cases} \tag{5.2}$$

where r denotes the distance with respect to the center of the sphere and Q_h is the integral of the heat power density q_h over the volume of the sphere. Actually, Eq. (5.2) neglects temperature variations inside the sphere itself, but this is a very good approximation in case the thermal conductivity of the nanostructure was much higher than the thermal conductivity of the surrounding medium. The validity of this assumption, which actually is not limited to spherical nanostructures, is a general trend for metallic nanostructures and it is rather independent from size or morphology [59]. From the viewpoint of thermoplasmonics, the power absorbed by the incident field constitutes the heating source, so we can take $Q_h = \sigma_{abs}I_b$. In case of a nanostructure array, we consider N identical spherical nanostructures of radius a, delivering the heath power $\sigma_{abs}I_b$ at the position $\mathbf{r}_j$ ($j = 1, \ldots, N$), and so the steady-state temperature increase ΔT_j experienced by each nanostructure results to be [59]

$$\Delta T_j \; = \; \Delta T_j^{self} \; + \; \Delta T_j^{ext} \; = \; \frac{\sigma_{abs}I_b}{4\pi\kappa a} \; + \; \sum_{\substack{i=1 \\ i\neq j}}^{N} \frac{\sigma_{abs}I_b}{4\pi\kappa \left|\mathbf{r}_j - \mathbf{r}_i\right|}, \qquad (5.3)$$

whereas the temperature increase anywhere in the surrounding medium is

$$\Delta T(\mathbf{r}) \; = \; \sum_{i=1}^{N} \frac{\sigma_{abs}I_b}{4\pi\kappa \left|\mathbf{r} - \mathbf{r}_i\right|}. \qquad (5.4)$$

The term ΔT_j^{self} in Eq. (5.3) represents the self-contribution to the temperature increase of the j-th nanostructure and the term ΔT_j^{ext} contains the temperature variation induced by the other $N-1$ nanostructures at the position $\mathbf{r}_j$. The interplay between ΔT_j^{self} and ΔT_j^{ext} determines the appearance of two regimes:

- if ΔT_j^{self} is dominant, the temperature significantly increases only in the vicinity of each nanostructure (*localization regime*);

- if ΔT_j^{ext} is dominant, thermal collective effects occur and tend to homogenize the temperature through the whole array, despite the nanometric nature of the heat sources (*collective regime*).

For a two-dimensional array of nanostructures, a dimensionless parameter ξ_2 can be defined for discriminating between the two regimes [59, 194]:

$$\xi_2 \; = \; \frac{p^2}{3La}, \qquad (5.5)$$

where p is the average neighbouring nanostructure period (i.e. center-to-center

distance) and L stands for the characteristic size of the illuminated area, namely the beam diameter in case of a circular uniform beam or the beam FWHM for Gaussian illumination. So, $\xi_2 \gg 1$ identifies the localization regime, whereas for $\xi_2 \ll 1$ the temperature tends to be homogeneous through the whole array. Another interesting fact is that, for practical samples, the nanostructures are not embedded in a homogeneous medium, but they are usually fabricated on top of a suitable substrate, so residing at the interface between two media. In this case, the thermal conductivity κ in all the above formulas has to be substituted by the average thermal conductivity $\bar{\kappa}$ [195]:

$$\bar{\kappa} = \frac{\kappa_1 + \kappa_2}{2}, \tag{5.6}$$

where κ_1 and κ_2 are the thermal conductivities of the two media. According to Baffou [59], "this important conclusion is at the basis of a current assumption in thermoplasmonics: when conducting numerical simulations involving plasmonic structures lying on a substrate, one can consider the structures as embedded in a uniform medium with thermal conductivity $\bar{\kappa}$, simplifying a lot the simulations".

When illuminating a portion of the whole array and for uniformly distributed nanostructures, it is possible to find an approximate solution to Eq. (5.3) representing the temperature increase ΔT_0 at the center of the illuminated region (see also Appendix G) [59, 194]:

$$\Delta T_0 \approx \frac{\sigma_{abs}\mathcal{P}}{\pi^2 D^2 \bar{\kappa} a} + \frac{\sigma_{abs}\mathcal{P}}{\pi \bar{\kappa} D S}\left(1 - \frac{2\sqrt{S}}{D\sqrt{\pi}}\right), \tag{5.7a}$$

$$\Delta T_0 \approx \frac{\sigma_{abs}\mathcal{P}\ln(2)}{\pi^2 H^2 \bar{\kappa} a} + \frac{\sigma_{abs}\mathcal{P}}{2\bar{\kappa} H S}\sqrt{\frac{\ln(2)}{\pi}}\left(1 - \frac{4\sqrt{S\ln(2)}}{\pi H}\right), \tag{5.7b}$$

where $\mathcal{P}$ is the source power reaching the sample and S denotes the unit cell area of the nanostructure array. Equation (5.7a) applies for a circular uniform beam of diameter D, whereas Eq. (5.7b) is valid for a Gaussian beam having a FWHM of size H. A last extension to the theory has to be done while considering non-spherical nanostructures. It turns out the radius a in the above formulas has to be substituted with the factor βa_0, where the correction factor β usually lies in the range $1-2$ and a_0 is the radius of a sphere having the same volume as the considered nanostructure [59, 195, 196].

Equations (5.7) can be used both in the localization regime and in the collective regime, only changing the weight of the various terms. However, for very packed nanostructure arrays, optical interactions might also play a role, and the

array is no more constituted by an ensemble of optically independent heaters, as Eqs. (5.3) and (5.7) assume. The regime of near-field optical interactions in thermoplasmonics has been poorly explored until now, but it is quite relevant to us when considering ASI systems, as we will see in Sec. 5.3.

5.2   Heating of isolated nanostructures

To implement the thermoplasmonic heating of ASI systems in a reliable way, the process has to be investigated by steps. We started from the elementary unit usually composing these systems, which consists in an elongated magnetic nanostructure designed according to what we reported in Chap. 4. As discussed in Sec. 1.6.1, an elongated metal nanostructure shows an anisotropic behaviour in the optical properties. In particular, the absorption cross section can be tuned depending on the nanostructure aspect ratio (AR), i.e. the ratio in between the nanostructure geometrical axes. The main idea consists in exploiting this optical anisotropy for providing *selective* heating: in case of linearly polarized light, both the resonance peak position and the absorbed power depend on what nanostructure axis the polarization direction is parallel to, as shown in Fig. 1.7b. Hence, the selectivity comes from the fact that, by changing wavelength and polarization direction, the power transferred to a metallic elongated nanostructure (and thus the delivered heat power) can be properly tuned.

For testing this principle, we fabricated arrays of magnetically and optically non-interacting metallic nanostructures characterized by sizes and shapes usually encountered in ASI systems. Figure 5.1 shows SEM images of six arrays fabricated on top of the same glass substrate. The geometrical parameters are detailed in Table 5.1. This sample has been fabricated according to recipe A.3. In particular, the whole surface of the substrate has been coated with a 4 nm thick titanium film,

Array name	Array size (μm^2)	d_x (nm)	d_y (nm)	x-axis pitch (nm)	y-axis pitch (nm)
$A1 - 1.50$	200×200	100	150	330	380
$B1 - 1.75$	200×200	100	175	330	405
$C1 - 2.00$	200×200	100	200	330	430
$A2 - 1.50$	200×200	100	150	330	760
$B2 - 1.75$	200×200	100	175	330	810
$C2 - 2.00$	200×200	100	200	330	860

Table 5.1: Geometrical parameters for the arrays shown in Fig. 5.1. The parameters d_x and d_y are the nanostructure diameters along the x- and y-axis, respectively.

(a) Array $A1-1.50$

(b) Array $B1-1.75$

(c) Array $C1-2.00$

(d) Array $A2-1.50$

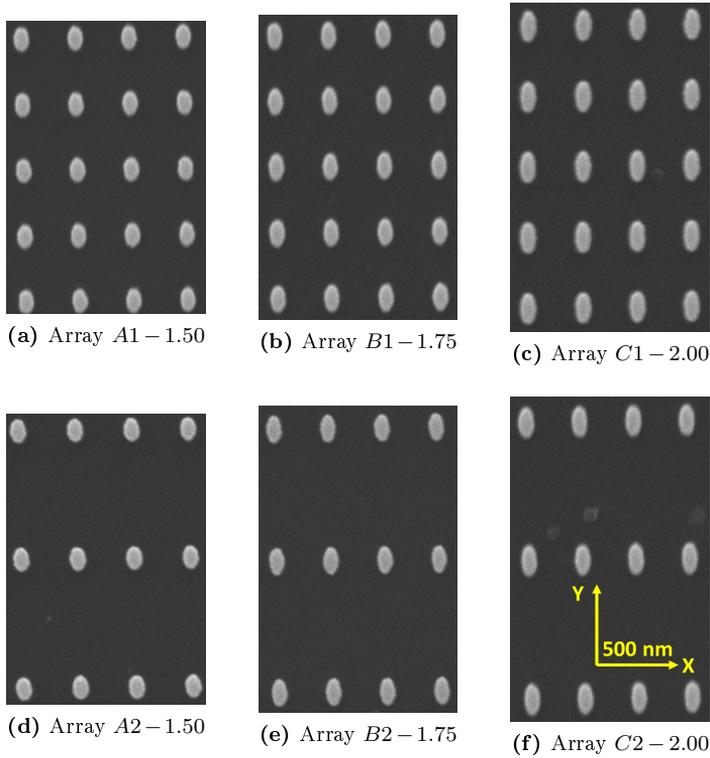**(e)** Array $B2-1.75$

(f) Array $C2-2.00$

Figure 5.1: SEM images of the arrays fabricated for testing the thermoplasmonic heating of nanostructures to be used in square ASI systems. The material stack for each nanostructure is, from top down, Au(5 nm)|Py(10 nm)|Au(25 nm). The geometrical parameters are detailed in Table 5.1.

in order both to avoid the charging effect during the EBL process and to improve the nanostructure adhesion. After the EBL patterning and the resist development steps, a trilayer film has been deposited: Au(5 nm)|Py(10 nm)|Au(25 nm), listed from top down. The 5 nm thick gold layer on top serves as a protective capping layer, whereas the 25 nm thick gold bottom layer constitutes an efficient nanoantenna interacting with the incident electromagnetic field. The chosen thickness for gold and Permalloy comes from the theoretical and experimental search of the best stack for optimizing the interaction with the electromagnetic field in the wavelength range we are interested in. The optical properties have been tested by measuring the extinction spectra in case of linearly polarized light for samples $A1-1.50$, $B1-1.75$ and $C1-2.00$. The quantity $1-T$ shown in Fig. 5.2a (and representing extinction) comes from the measurement of the transmittance T, which has been normalized to the transmittance of a substrate region without arrays.
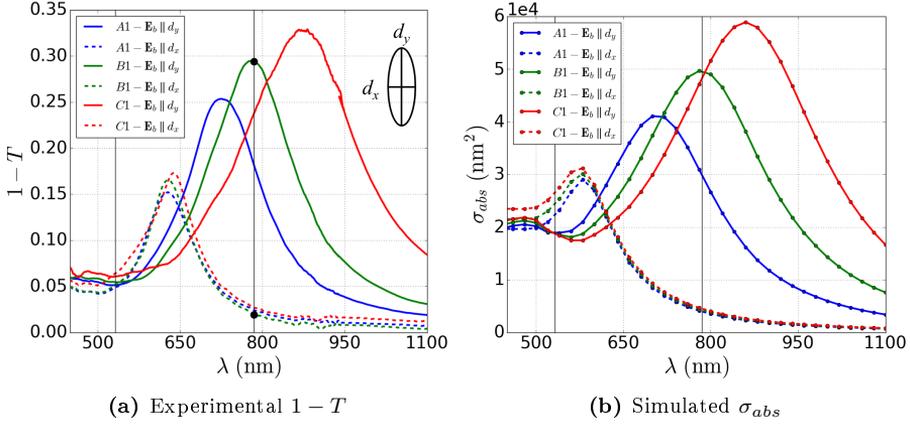
(a) Experimental $1 - T$ **(b)** Simulated σ_{abs}

Figure 5.2: (a) Experimental extinction spectra $(1 - T)$ measured using linearly polarized light. The incident electric field $\mathbf{E}_b$ was parallel either to the major axis d_y or to the minor axis d_x of the nanostructures composing the arrays. (b) Simulated absorption cross section σ_{abs} corresponding to the cases shown in (a). In both images, the black vertical lines correspond to $\lambda = 532$ nm and $\lambda = 785$ nm.

Considering, e.g., array $A1 - 1.50$ in case of perpendicular polarization directions (blue-solid line and blue-dashed line in Fig. 5.2a), the resonance peak obtained when the incident electric field $\mathbf{E}_b$ is parallel to the major axis d_y ($\mathbf{E}_b \parallel d_y$) corresponds to higher extinction than the resonance peak obtained for $\mathbf{E}_b$ parallel to the minor axis d_x ($\mathbf{E}_b \parallel d_x$). Moreover, the $\mathbf{E}_b \parallel d_y$ resonance peak sits at a longer wavelength, as expected according to the theory discussed in Sec. 1.6.1. This general behaviour is also followed by the other two arrays (i.e. $B1 - 1.75$ and $C1 - 2.00$), even if with relevant differences. In particular, when comparing the $\mathbf{E}_b \parallel d_y$ resonance peak for the three arrays (coloured solid lines in Fig. 5.2a), we can see the expected peak-position shift towards higher wavelengths which mirrors the growth in the AR. The theory also predicts the enhancement of the resonance-peak height according to the AR (and the volume) trend, as indeed observed. Hence, from these measurements, the concept of selective heating can be clearly understood. Let us suppose our sample consists in a $B1 - 1.75$ array. If we shine the array with a linearly polarized light corresponding to $\lambda = 785$ nm, the nanostructures can either efficiently remove energy form the incident beam or become almost transparent, depending on the orientation of the nanostructure with respect to the polarization direction. For $\lambda = 785$ nm, we are very close to the major-axis resonance ($\mathbf{E}_b \parallel d_y$), but we are quite far from it when $\mathbf{E}_b \parallel d_x$ (as marked by the black-filled dots in Fig. 5.2a), and the extinctions differ by an order of magnitude. This is what we mean by selectivity in this context: the

ability of varying the optical behaviour by changing the polarization direction of the incident light. Even if we discussed the principle for sample $B1 - 1.75$, the conclusion is valid for all the three samples we considered, the only difference being the resonance wavelength. Actually, this kind of selectivity is nothing new [52,197], but what is interesting for us is the fact that the reported behaviour is mirrored by the absorption cross section σ_{abs}, which is the quantity appearing in Eqs. (5.7) and quantifying the temperature increase. Indeed, Fig. 5.2b shows the σ_{abs} curves simulated using COMSOL Multiphysics [115] and corresponding to the cases depicted in Fig. 5.2a. The refractive indices have been taken from Ref. [58] for gold and from Ref. [198] for Permalloy. Through σ_{abs}, the selectivity in the optical properties transfers to a selectivity in the nanostructure heating, since the temperature increase results to be dependent on the light polarization direction. In other words, at a given wavelength, not only the incident power $\mathcal{P}$ determines the amount of heat power delivered by the nanostructures, but also the polarization direction through the behaviour of σ_{abs}. In case of optimal conditions, as for array $B1 - 1.75$ at $\lambda = 785$ nm, the polarization direction plays the role of a "switch" due to the huge difference in the σ_{abs} values, so allowing us to basically turn on and off the interaction. A fundamental role is played by the 25 nm thick gold layer, since the optical properties of gold determine sharp and strong LSP resonances for the geometries and wavelengths we are interested in. This fact translates into an efficient coupling with the incident electromagnetic field, providing the basis for the effective selective heating just described. This is not the case for Permalloy alone, for which the interaction with the electromagnetic field is too weak to provide effective heating under the same experimental conditions, as shown in Fig. G.1.

The validity of our statements has been verified by exploiting the temperature dependence of the coercive field H_C, as described by the Sharrock equation (1.62). The measurement of the temperature increase has been indirectly performed by measuring the coercive field variation ΔH_C as a function of the incident power. For each array, eight hysteresis loops have been recorded through the experimental setup described in Sec. 3.2.2. The wavelength of the probe laser ($\lambda = 532$ nm) lies in a region of inefficient thermoplasmonic heating for both polarization directions (see Fig. 5.2a), in order to not perturb the measurement results. The pump laser ($\lambda = 785$ nm) was linearly polarized along the major axis of the nanostructures composing the arrays and its power has been varied between 0 and 60 mW. By fixing the pump wavelength, we verified the effect of the nanostructure AR on the heating. Considering a pump beam FWHM of $H = 30$ μm as L in Eq. (5.5), it turns out that $\xi_2 < 0.075$ for all the fabricated arrays, so
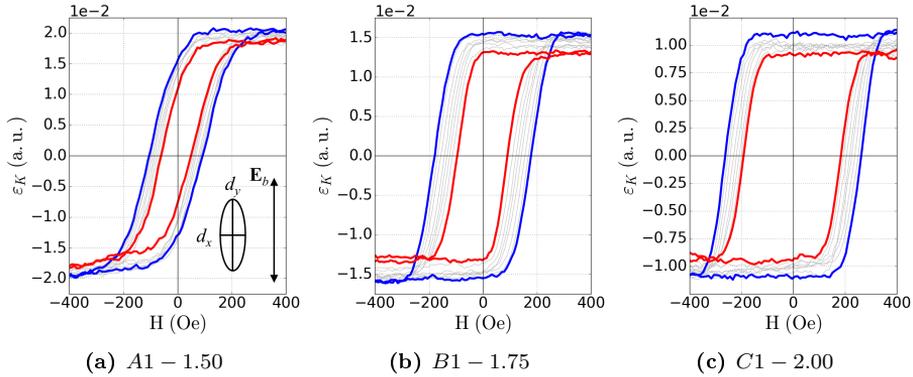
Figure 5.3: Hysteresis loops recorded along d_y at increasing incident power ($\lambda = 785$ nm). The inset in (a) shows the polarization axis of the incident electric field $\mathbf{E}_b$, which is parallel to d_y. For each sample, the blue hysteresis loop corresponds to $\mathcal{P} = 0$ mW, whereas the red hysteresis loop corresponds to $\mathcal{P} = 60$ mW. The gray hysteresis loops contained between the limiting loops have been obtained at intermediate powers, as summarized in Fig. 5.4.

we always are in the collective regime, corresponding to a homogeneous heating. The probe beam was made smaller ($H = 15$ μm) than the pump beam in order to probe only the central region of the pump spot, where the temperature (given by Eq. (5.7b)) is most likely to be uniform. An image of these spots can be found in Fig. G.2. The measured hysteresis loops are shown in Fig. 5.3. As expected from the AR dependence of the demagnetizing field (shape anisotropy, see Sec. 1.3.2), at room temperature (blue hysteresis loops, $\mathcal{P} = 0$ mW) sample $C1 - 2.00$ shows the highest coercive field (H$_C \approx 263$ Oe), followed by sample $B1 - 1.75$ (H$_C \approx 178$ Oe) and then by sample $A1 - 1.50$ (H$_C \approx 105$ Oe). At maximum power (red hysteresis loops, $\mathcal{P} = 60$ mW), all the samples are characterized by narrower hysteresis loops, but sample $B1 - 1.75$ shows the largest variation, followed by sample $C1 - 2.00$ and then by sample $A1 - 1.50$, as summarized in Fig. 5.4. If the heat power delivered by the nanostructures was the same at fixed incident power (i.e. same σ_{abs} for the three cases), the temperature increase would be the same and, from the Sharrock equation, we would get a higher ΔH$_C$ for the nanostructures characterized by the highest AR (sample $C1 - 2.00$). Nonetheless, this is not the case, and the ΔH$_C$ behaviour follows the $1 - T$ hierarchy at $\lambda = 785$ nm (see Fig. 5.2a).

Even if a quantitative evaluation of the correspondence between temperature and ΔH$_C$ is very difficult, a fit to the Sharrock equation (1.62) could express the consistency of our results. The incident power $\mathcal{P}$ can be considered as the
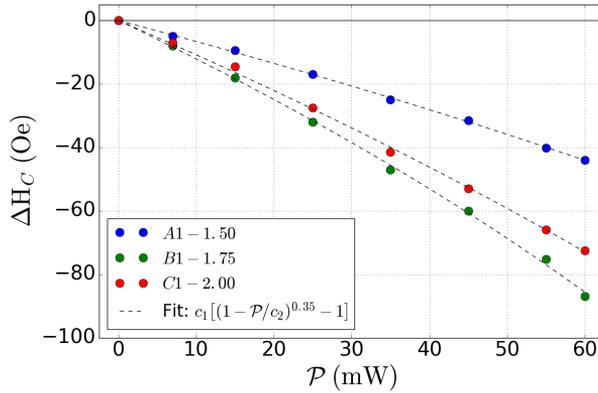
Figure 5.4: Coercive field variation as a function of the incident power. For each sample, the reference coercive field at zero power corresponds to the one extracted by the blue hysteresis loop in Fig. 5.3. The coefficients returned by the fitting function are summarized in Table 5.2.

independent parameter (instead of the temperature) by noticing that Eq. (5.7b) returns $\Delta T \propto \mathcal{P}$. If we stay far from the nanostructure blocking temperature, the coercive field variation is mainly given by the temperature dependence of the saturation magnetization in the anisotropy field H_K, so Eq. (1.62) can be recast to provide a reasonable fit function in the form

$$\Delta H_C(\mathcal{P}) \;=\; c_1 \left[\left(1 - \frac{\mathcal{P}}{c_2} \right)^{\beta} - 1 \right],\tag{5.8}$$

having considered Eq. (1.63) for the temperature dependence of M_S ($\beta = 0.35$) and imposing $\Delta H_C(0) = 0$. The black-dashed lines in Fig. 5.4 show the fit results and Table 5.2 lists the returned values for c_1 and c_2. The errors correspond to one standard deviation and have been calculated as the square root of the diagonal elements of the covariance matrix returned by the fitting function [181]. The parameter c_2 represents a power scale for the coercive field variation ΔH_C: the smaller c_2, the higher the variation that can be produced at a given inci-

Array name	c_1 (Oe)	c_2 (mW)
$A1 - 1.50$	$(3.5 \ \pm \ 0.8) \cdot 10^2$	$(1.9 \ \pm \ 0.4) \cdot 10^2$
$B1 - 1.75$	$(4.3 \ \pm \ 0.7) \cdot 10^2$	$(1.3 \ \pm \ 0.2) \cdot 10^2$
$C1 - 2.00$	$(5.1 \ \pm \ 1.4) \cdot 10^2$	$(1.7 \ \pm \ 0.4) \cdot 10^2$

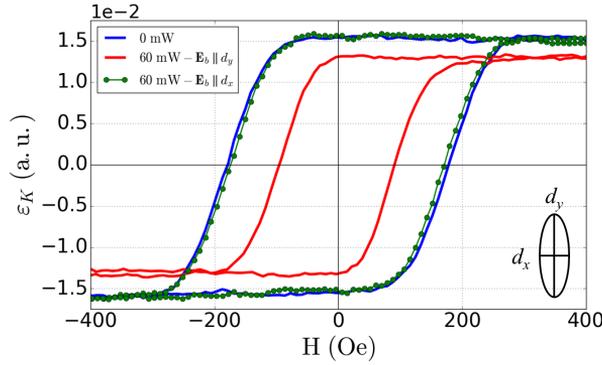**Table 5.2:** Coefficients returned by the fitting function (5.8).

Figure 5.5: Measured hysteresis loops along d_y on array $B1 - 1.75$. The blue and red hysteresis loops have been taken from Fig. 5.3b and correspond to measurements performed at $\mathcal{P} = 0$ mW and at $\mathcal{P} = 60$ mW for $\mathbf{E}_b \parallel d_y$. The green-dotted hysteresis loop has been recorded on the same sample at $\mathcal{P} = 60$ mW, but considering $\mathbf{E}_b \parallel d_x$. The same incident power (at $\lambda = 785$ nm) determines different $\Delta \mathrm{H}_C$ according to the polarization direction, as marked by the black-filled dots in Fig. 5.2a.

dent power. Indeed, the c_2 values reflect the $1 - T$ hierarchy, being the array $B1 - 1.75$ characterized by the lowest c_2 value and the highest coercive field variation. Moreover, since we are considering a model taking only into account the temperature variation of the anisotropy field H_K in the Sharrock equation, the parameter c_1 should grow along with the AR of the considered nanostructures. Indeed, this is what the fits return: the smallest c_1 value corresponds to array $A1 - 1.50$ and the value gets bigger for bigger ARs. The maximum temperature variation we have induced can be estimated from the incident power $\mathcal{P}$ through Eq. (5.7b). At $\lambda = 785$ nm, for the nanostructures forming array $B1 - 1.75$ we can consider $\sigma_{abs} = 5 \cdot 10^4$ nm^2, $\bar{\kappa} = 0.7$ W $\cdot$ m$^{-1} \cdot$ K^{-1} (the average between the values for glass and air), an effective radius $a_0 = 50$ nm and a correction factor $\beta = 1$. So, for $H = 30$ μm and $\mathcal{P} = 60$ mW, the first term in Eq. (5.7b) gives $\Delta T_{0,1^{st}} \approx 7$ K, whereas the second term gives $\Delta T_{0,2^{nd}} \approx 248$ K, corresponding to a total temperature variation of $\Delta T_0 \approx 255$ K.

After having analyzed the effect of the nanostructure AR on the heating, we inspected the dependence of σ_{abs} from the light polarization direction. The blue and red hysteresis loops in Fig. 5.5 have been taken from Fig. 5.3b and represent the hysteresis loops measured at $\mathcal{P} = 0$ mW and at $\mathcal{P} = 60$ mW on array $B1 - 1.75$ when it is illuminated by a $\lambda = 785$ nm light, linearly polarized along d_y. When rotating the polarization direction to bring it parallel to d_x, the nanostructures are no more in resonance (as shown by the black-filled dots in Fig. 5.2a) and the heating should be much less efficient in this configuration. Indeed,
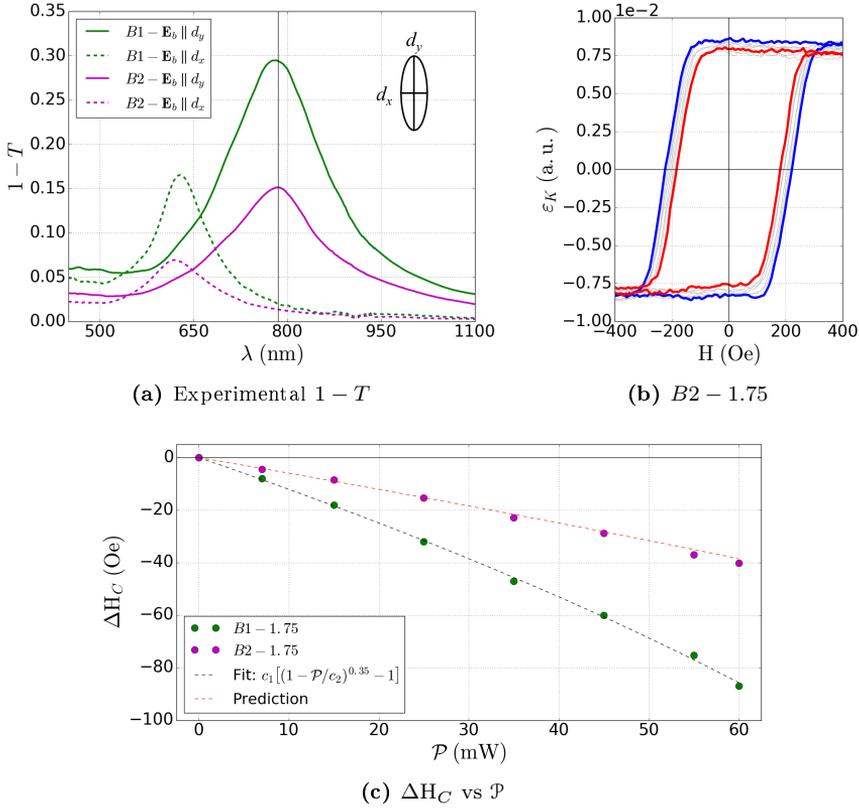
(a) Experimental $1 - T$

(b) $B2 - 1.75$

(c) $\Delta \mathrm{H}_C$ vs $\mathcal{P}$

Figure 5.6: Influence of the array filling factor on the thermoplasmonic heating: comparison of arrays $B1 - 1.75$ and $B2 - 1.75$. (a) Experimental extinction spectra $(1 - T)$ measured using linearly polarized light. (b) Hysteresis loops recorded along d_y at increasing incident power ($\lambda = 785$ nm) for array $B2 - 1.75$ and $\mathbf{E}_b \parallel d_y$. (c) Coercive field variation as a function of the incident power. The coloured dots represent experimental data, the black-dashed line is a fit to the $B1 - 1.75$ data and the red-dashed line shows the prediction discussed in the body of the text.

this is demonstrated by the green-dotted hysteresis loop in Fig. 5.5, which has been obtained at $\mathcal{P} = 60$ mW, but for linearly polarized light along d_x: the $\Delta \mathrm{H}_C$ variation with respect to the unperturbed hysteresis loop is minimal.

However, the absorption cross section is not the only parameter influencing the temperature increase. Also the *filling factor* (i.e. the fraction of array area covered by the nanostructures) does play a role. This dependence appears in S, the unit cell area of the nanostructure array. The parameter S resides in the second term of Eq. (5.7b), which is the most relevant term in case of homogeneous heating: by doubling S, the corresponding ΔT_0 should be halved. Hence, all the previous analysis has been repeated for array $B2 - 1.75$, fabricated as array $B1 - 1.75$, but

with a unit cell area as twice as big. Figure 5.6a shows the comparison between the extinction spectra of arrays $B1-1.75$ and $B2-1.75$. The values for $B2-1.75$ are approximately half of the values for $B1-1.75$ and, since the nanostructure size and shape are the same, the difference can be ascribed to the difference in S, which is indeed a factor of 2 smaller for $B2-1.75$. Figure 5.6b shows the hysteresis loops performed under the same conditions of those in Fig. 5.3b, and Fig. 5.6c summarizes the behaviour of ΔH_C as a function of the power $\mathcal{P}$. For comparison, the ΔH_C values for array $B1-1.75$ have been taken from Fig. 5.4 and repeated here. The black-dashed line represents the same fit performed before, but now the red-dashed line corresponds to a prediction we made in order to test our assumptions on the fit parameters. Basically, the red-dashed line has been calculated through Eq. (5.8) by considering the following observations. Since the parameter c_1 mainly depends on the AR, we chose to maintain the same value we found for array $B1-1.75$, being the involved nanostructures characterized by the same AR. On the other hand, the parameter c_2 represents a power scale for the coercive field variation. Because of the variation in S, we estimated that twice the power should be needed in order to get for array $B2-1.75$ the same effects we saw in $B1-1.75$. Hence, we considered $c_2(B2) = 2c_2(B1)$. The end result is given by the red-dashed line in Fig. 5.6c, which is in good agreement with the experimental data.

5.3 Heating of isolated vertices

After having investigated the thermoplasmonic heating of non-interacting nanostructures, we focused on isolated vertices formed by the nanostructures in array $B1-1.75$ ($d_x = 100$ nm, $d_y = 175$ nm). A vertex is composed by four nanostructures, aligned in pairs along two perpendicular directions. Figure 5.7 shows SEM images of three arrays fabricated on top of the same glass substrate. The geometrical parameters are detailed in Table 5.3. This sample has been fab-

Array name	Array size (μm^2)	Gap (nm)	Pitch (nm)
$V1-100$	200×200	100	680
$V2-150$	200×200	150	730
$V3-200$	200×200	200	780

Table 5.3: Geometrical parameters for the arrays shown in Fig. 5.7. The *gap* refers to the edge-to-edge distance g shown in Fig. 4.10. The *pitch* denotes the side of the square lattice formed by the vertex centers.

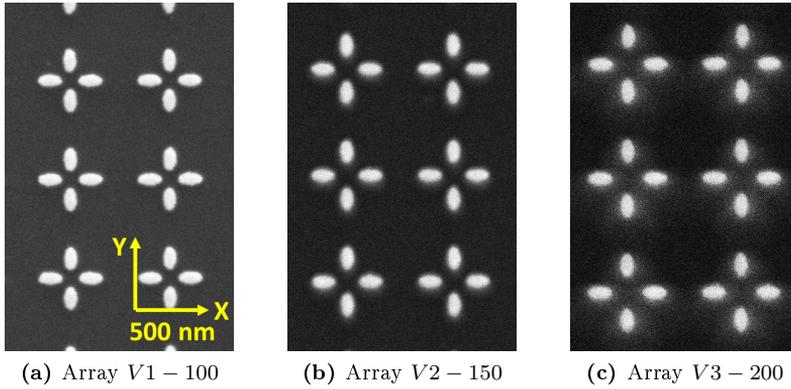**(a)** Array $V1 - 100$ **(b)** Array $V2 - 150$ **(c)** Array $V3 - 200$

Figure 5.7: SEM images of the arrays fabricated for testing the thermoplasmonic heating of isolated vertices. The material stack for each nanostructure is, from top down, Au(5 nm)|Py(10 nm)|Au(25 nm). The geometrical parameters are detailed in Table 5.3.

ricated according to the same recipe used for the previous sample. Each vertex can be considered as magnetically and optically isolated from the other vertices in the array. As shown in Fig. 5.8a, we measured the extinction spectra for arrays $V1 - 100$ and $V3 - 200$ in case of linearly polarized light along the side of the square lattice formed by the vertex centers. Since both the nanostructure orientations considered before are present in the array, both the resonance peaks appear during the same measurement. However, a slightly shift in the peak positions can be observed: the peak corresponding to the nanostructure minor axis blueshifts, whereas the peak corresponding to the nanostructure major axis red-shifts. This fact is the signature of a near-field optical interaction occurring in between the nanostructures forming the vertex. Indeed, the peak separation increases as the gap size decreases [54], being larger for array $V1 - 100$. For matching the $V1 - 100$ resonance peak, the thermoplasmonic heating of isolated vertices has been performed with a $\lambda = 808$ nm pump beam and the same wavelength has been used for array $V3 - 200$ in order to make easy the side-to-side comparison. For consistency with all the previous analysis, Fig. 5.8b shows the simulated absorption cross sections σ_{abs}, but it is much more interesting to disentangle the contributions coming from the two pairs of nanostructures composing a vertex. So, the absorption cross sections characterizing the nanostructure pair parallel to the incident electric field $\mathbf{E}_b$ have been extracted from the simulations and shown in Fig. 5.9 as coloured solid lines. On the other hand, the coloured dashed lines represent the absorption cross sections for the nanostructure pair perpendicular to the incident electric field $\mathbf{E}_b$. At an incident wavelength of $\lambda = 808$ nm the
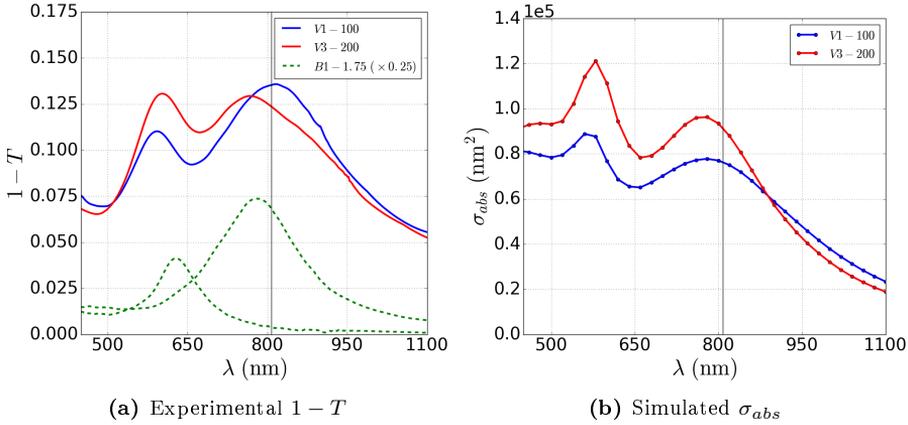
(a) Experimental $1 - T$

(b) Simulated σ_{abs}

Figure 5.8: (a) Experimental extinction spectra $(1 - T)$ measured using light linearly polarized along the side of the square lattice. As a reference, the green-dashed lines represent the extinction spectra for array $B1 - 1.75$ taken from Fig. 5.2a. (b) Simulated vertex absorption cross section σ_{abs} corresponding to the cases shown in (a). In both images, the black vertical lines correspond to $\lambda = 808$ nm.

optical selectivity is preserved, being the σ_{abs} values different by more than one order of magnitude for both the simulated vertices. In Sec. 5.2, we saw that a certain degree of optical selectivity also implies heating selectivity, but this was true in case of elongated nanostructures oriented along the same direction. However, when working with isolated vertices, the nanostructures composing the array are arranged along two perpendicular directions. The pair arranged along the pump beam polarization direction interacts more effectively with the incident field and so it absorbs more energy, but the heat is diffusively redistributed until a steady state is reached. The net result is that, even if only a pair of nanostructures operates as an active heater, the whole vertex temperature will substantially raise. The hysteresis loops shown in Fig. 5.10 seem to confirm this view, both for array $V1 - 100$ and for array $V3 - 200$. The blue hysteresis loops represent measurements performed with no pump beam ($\mathcal{P} = 0$ mW), so corresponding to room-temperature hysteresis loops. The red hysteresis loops have been measured for a $\mathcal{P} = 60$ mW, $\lambda = 808$ nm pump beam whose electric field $\mathbf{E}_{b1}$ lies in the MOKE setup sensitivity plane. Eventually, the green hysteresis loops show the measurements obtained by rotating the pump beam polarization direction by 90°. In case of $\mathbf{E}_{b1}$ pumping (red hysteresis loops), the coercive field variation for array $V1 - 100$ results to be $\Delta\mathrm{H}_C \approx 25$ Oe, whereas for array $V3 - 200$ we get $\Delta\mathrm{H}_C \approx 30$ Oe. Indeed, the extinction values for the two arrays at $\lambda = 808$ nm coming from Fig. 5.8a are not too different and thus the corre-
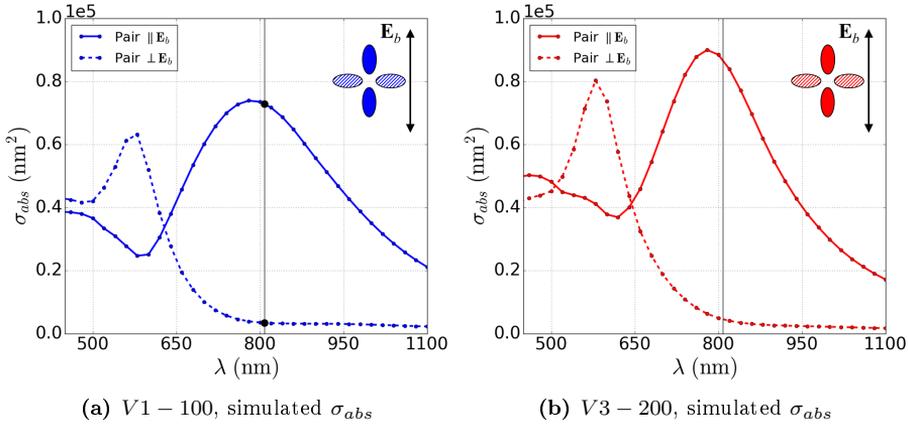
(a) $V1 - 100$, simulated σ_{abs}

(b) $V3 - 200$, simulated σ_{abs}

Figure 5.9: Contributions to the simulated absorption cross section σ_{abs} coming from the two orthogonal nanostructure pairs forming an isolated vertex, for (a) array $V1-100$ and (b) array $V3 - 200$. In both images, the black vertical lines correspond to $\lambda = 808$ nm.

sponding ΔH_C values are expected to be the same. Another interesting fact is that, for each array, there is almost no difference in between the coercive fields obtained for the two pump polarization directions (the red and the green hysteresis loops). This fact is a direct consequence of being in the homogeneous heating regime. The coercive field is mainly determined by the jump in the elementary hysteresis loop characterizing the nanostructures whose major axis lies in the MOKE setup sensitivity plane. Indeed, the hysteresis loops collected during the performed measurements (in longitudinal configuration) represent the average magnetization behaviour coming from the component of the nanostructure magnetization lying in the sensitivity plane, which also contains the applied magnetic field. For this reason, the nanostructures whose major axis lies in the sensitivity plane contribute to the average magnetization with an *easy-like* hysteresis loop, characterized by a jump in correspondence of the coercive field. On the other hand, the nanostructures whose major axis is perpendicular to the sensitivity plane show (on the average) no hysteresis and so no contribution to the average coercivity. Despite the fact we made measurements with the pump beam linearly polarized both in the sensitivity plane ($\mathbf{E}_{b1}$) and perpendicular to it ($\mathbf{E}_{b2} \perp \mathbf{E}_{b1}$), the coercive field variation we measure is almost the same, meaning we are reaching a similar temperature for the nanostructures lying in the sensitivity plane for both the heating conditions.

To prove this fact, we performed a COMSOL Multiphysics [115] simulation of the temperature field in case of a finite array (7×7 vertices) designed to have

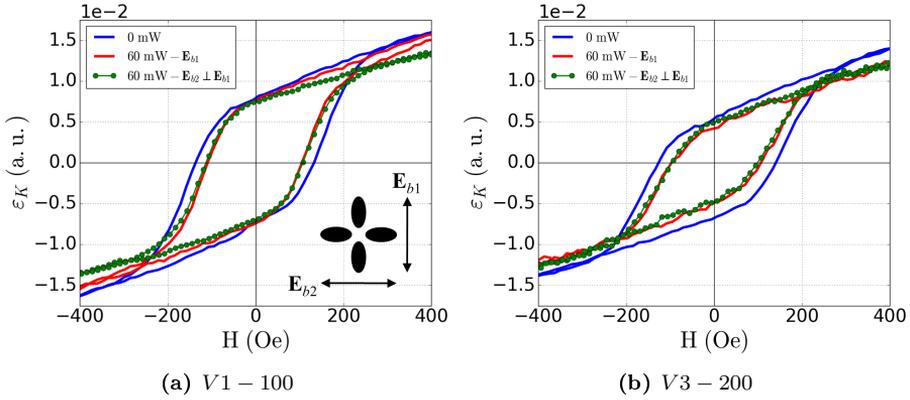**(a)** $V1 - 100$ **(b)** $V3 - 200$

Figure 5.10: (a) Measured hysteresis loops along the direction parallel (red) and perpendicular (green) to $\mathbf{E}_{b1}$ on array $V1 - 100$ for a $\lambda = 808$ nm pump beam. (b) Measured hysteresis loops along the direction parallel (red) and perpendicular (green) to $\mathbf{E}_{b1}$ on array $V3 - 200$ for a $\lambda = 808$ nm pump beam.

the same geometrical parameters as $V1 - 100$. Since the simulated array is much smaller than the measured one, we aim at understanding the general behaviour without expecting to get the actual array temperature. However, the performed simulation can be well representative of what happens when working with very focused pump beam, so that few vertices are involved. For each nanostructure, the thermal properties needed for the simulations (i.e. the thermal conductivity, the mass density and the specific heat at constant pressure) have been calculated as a volume average of the characteristic values for gold and nickel. Regarding the substrate, the value $\kappa = 1.4 \ \mathrm{W \cdot m^{-1} \cdot K^{-1}}$ has been considered. Moreover, all the ΔT values returned by the simulation have to be referred to $T_0 = 300$ K. The nanostructures lying along the simulation y-axis and x-axis have been associated to half the σ_{abs} values corresponding to the upper black-filled dot and to the lower black-filled dot in Fig. 5.9a, respectively. By doing so, we define a preferential direction (the y-axis) for the interaction with the incident electromagnetic field, so implementing the optical selectivity. The incident power has been spatially modulated with a Gaussian profile of growing FWHM, but the average beam intensity has been kept fixed to the maximum value used during the measurements, corresponding to a total power $\mathcal{P} = 60$ mW for a beam FWHM of 30 μm. Figures 5.11a-5.11d show the ΔT temperature field when the pump beam FWHM corresponds to 680 nm, 1360 nm, 2720 nm and 5440 nm, respectively. The wider the area in which the incident power is distributed, the higher the number of structures contributing to the total heating. In the homogeneous heating regime,
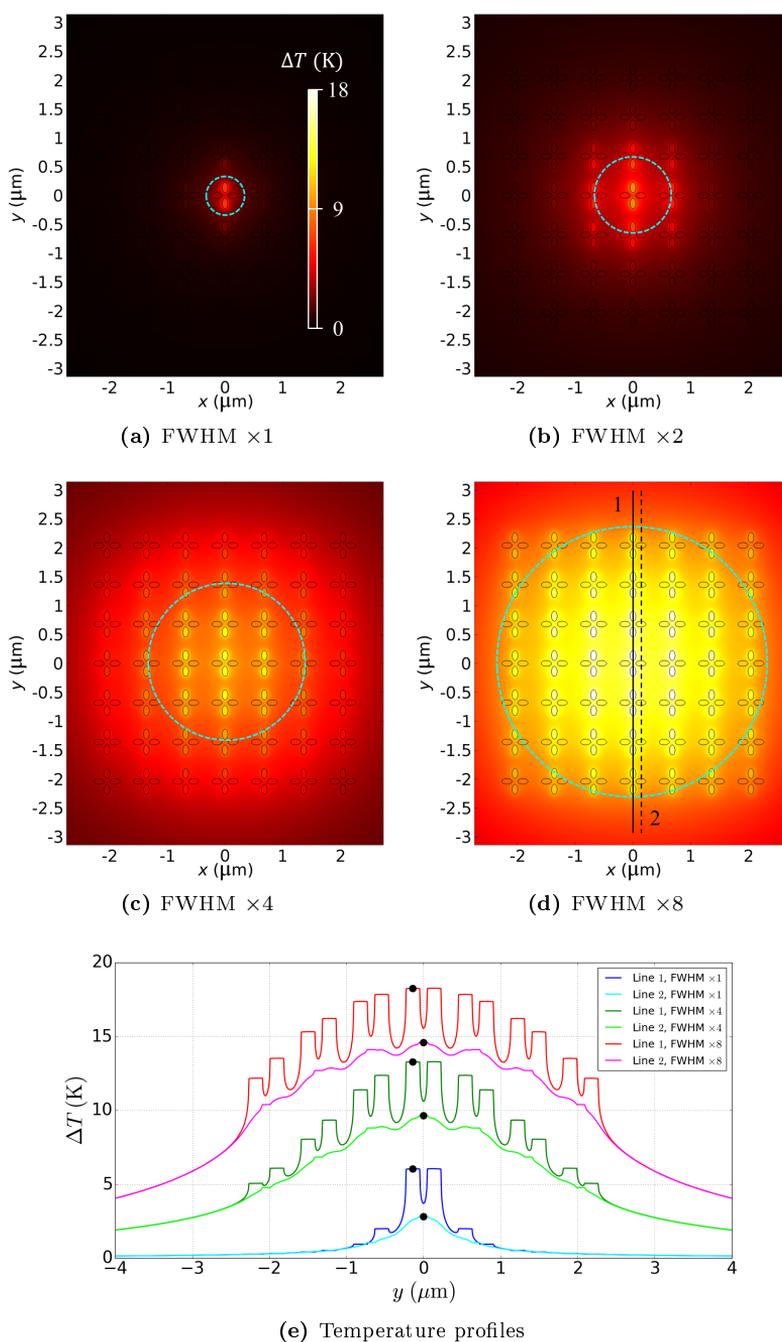
(a) FWHM ×1

(b) FWHM ×2

(c) FWHM ×4

(d) FWHM ×8

(e) Temperature profiles

Figure 5.11: (a)-(d) Simulation of the temperature field for a finite array with the same geometrical parameters as $V1 - 100$. The light-blue dashed-line circles represent the considered pump beam FWHM in each case, in units of the array pitch (i.e. 680 nm). (e) Temperature profiles along the black lines depicted in panel (d).

this fact reflects in the increase of the background temperature, which is made visible by the yellow halo in Fig. 5.11d. This point can be further clarified by extracting the temperature profiles along the black lines depicted in Fig. 5.11d: line 1 crosses a row of nanostructures which are actively interacting with the incident field, while line 2 is associated to the orthogonal nanostructures. The resulting profiles are shown in Fig. 5.11e. Even if the growing number of involved vertices determines the rise of the average ΔT, the temperature difference in between the nanostructures composing the central vertex (i.e. the differences in between the values marked by black-filled dots in Fig. 5.11e for a given beam FWHM choice) seems to be constant. This temperature difference is quite relevant since it quantifies the degree of heating selectivity.

To better inspect this point, we simulated one more time the temperature field corresponding to Fig. 5.11c, but after having removed the central vertex. The result is shown in Fig. 5.12a, where the central vertex has been drawn only as a guide. On the other hand, Fig. 5.12b shows the "complementary" simulation, namely a simulation only involving the central vertex, but maintaining the same beam FWHM. The temperature profiles along the white lines marked in Fig. 5.12a are depicted in Fig. 5.12c, where also the profiles relative to the single vertex case have been traced. By looking at the region where the central vertex resides ($|y| < 225$ nm), it can be seen that all the other vertices produces the diffuse temperature background, which is almost constant in all the central vertex region, while the temperature difference is mainly determined by what happens inside the vertex itself. This finding is in agreement with Eq. (5.3), where the self-contribution can be separated from the contribution coming from the rest of the array. Moreover, the additivity of the two contributions can be verified by adding together the retrieved profiles and by comparing the result with the outcome of the full simulation, as we did for getting Fig. 5.12d. If we performed the same simulations with a power N times higher, we would get the same results, but all the values would be N times bigger. All these conclusions helped us in identifying the most important control parameters for a useful selective heating process. The beam intensity determines the temperature difference in between the nanostructures forming a vertex, so the intensity is the parameter to be considered in order to tune the heating selectivity at a vertex level. For the case depicted in Fig. 5.12c, the intensity used in the simulation led to a vertex temperature difference of 3.6 K for a background ΔT of 6.8 K. Increasing ten times the intensity would return a vertex temperature difference of 36 K. Nonetheless, for a given FWHM, the intensity also controls the background temperature caused by the response of all the other illuminated nanostructures. Considering the ten-fold
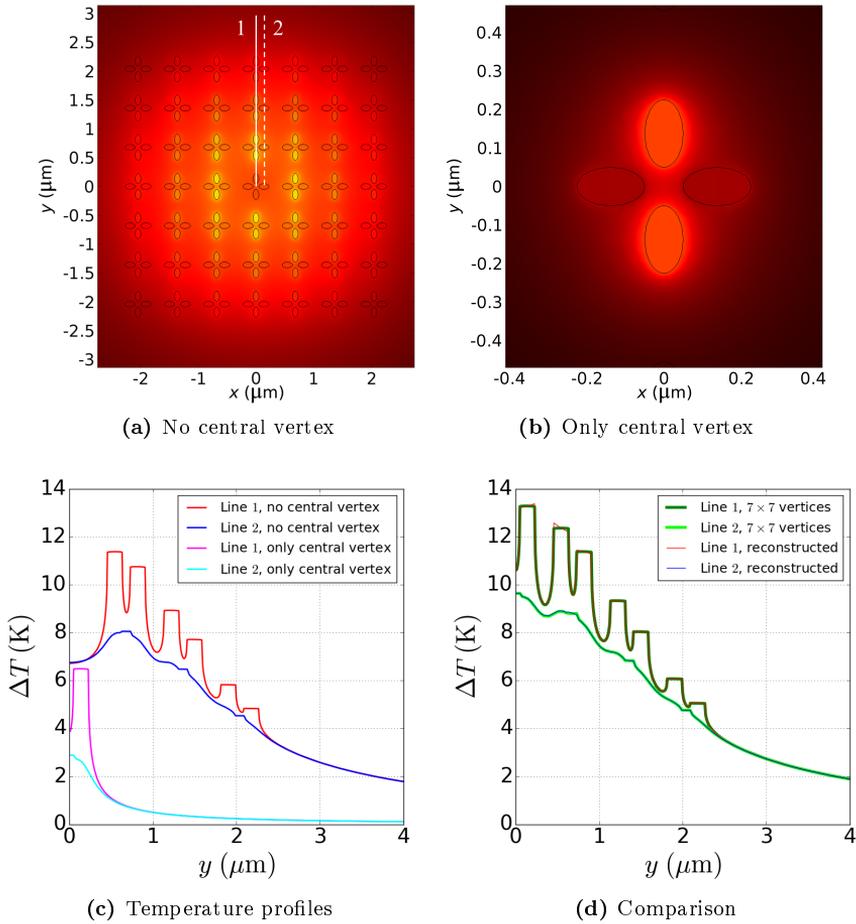
(a) No central vertex

(b) Only central vertex

(c) Temperature profiles

(d) Comparison

Figure 5.12: (a) Simulation of the temperature field corresponding to Fig. 5.11c (FWHM ×4) obtained by removing the central vertex (drawn here only as a guide). (b) Simulation of the temperature field under the same conditions, but considering only the central vertex. The colors still refer to the color bar in Fig. 5.11a. (c) Temperature profiles along the white lines depicted in panel (a) for both the simulations. (d) Reconstructed temperature profiles (i.e. sum of the appropriate profiles) and comparison with the result obtained for the full 7 × 7 array (green and light-green plots in Fig. 5.11e).

intensity increase just discussed, we would also get a background ΔT of 68 K. Even if there would be an increase in the heating selectivity at the vertex level, the background ΔT could become too high to ensure the proper functioning of our approach (e.g. by reaching the Curie temperature of the nanostructure magnetic material). The solution is then to play with the FWHM at fixed intensity: by reducing the illuminated area (i.e. by further focusing the beam), the number of involved nanostructures is reduced, so it is the background temperature.

However, the restriction on the FWHM is not a limit, since it allows us to get a *local* selective heating, concentrating the effect of the thermoplasmonic heating approach on a reduced number of vertices.

Going back to Fig. 5.10, what we learnt from the simulations on a finite array can anyway explain why, despite we performed measurements with the pump beam linearly polarized along two perpendicular directions, the coercive field variation was almost the same. The reason is that, for a pump beam FWHM of 30 μm, the temperature difference at the vertex level (estimated to be below 10 K) results to be much smaller than the background ΔT (estimated to be above 100 K), so there is almost no selectivity as long as ΔH_C is concerned.

5.4   Conclusions

The work summarized in this chapter represents a preliminary but complete investigation paving the way for the thermoplasmonic heating of ASI systems. The first step of the study consisted in identifying the proper nanostructure geometry and material to be used. The planar size and shape have been chosen according to what is usually found in ASI systems, whereas the Au|Py|Au stack has been derived from the optimization of the optical properties. The measurements performed on arrays of non-interacting nanostructures showed we could achieve the most important feature we were looking for: selective heating. By fabricating arrays characterized by nanostructures of different AR and filling factor, we were able to verify all the effects predicted by the theory regarding the temperature increase, so becoming aware of the fact we were considering a robust and reliable method. However, this was not enough, since ASI systems are characterized by densely-packed nanostructures aligned along different directions (perpendicular in case of square systems). Hence, as a next step, we studied the behaviour of non-interacting vertices composed by four nanostructures, where we found signatures of optical interaction and the loss of heating selectivity. Anyway, supported by measurements and guided by simulations, we identified the parameters which can play a fundamental role in the selective heating of ASI systems: the beam intensity determines the degree of selectivity, but the beam FWHM has to be accordingly adjusted to get the right temperature scale, since the heating regime is also determined by the beam size. The restriction on the FWHM size is not a limit, but, rather, it goes hand in hand with the requirement of having a local heating. This feature is of interest when thinking at the possibility of fabricating opto-activated ASI-based devices, where the thermal properties can be locally altered by scanning a focused beam on the desired region.

Chapter 6

The Role of Asymmetric Magnetostatic Interactions

When a magnetic nanostructure is immersed in an externally applied magnetic field, spatially uniform over the length-scale of the nanostructure, a wide variety of field-induced behaviours are observed, both experimentally and using micromagnetic simulations. They include reversal via vortex nucleation and annihilation [175], domain wall nucleation and motion [199] and coherent rotation [173]. The sequence of stable and metastable states through which a magnetic nanostructure evolves during field-induced processes depends on and can be controlled by size, shape, material parameters and field history. However, it is important to realize that, under the action of a uniform (according to the above-mentioned definition) applied magnetic field, a magnetic nanostructure can only explore a limited portion of the energy landscape determined by geometry and material properties. Whatever the field history would be, some of the possible reversal paths and metastable (in zero field) magnetization configurations cannot be induced in a magnetic nanostructure using a spatially uniform applied magnetic field. In this chapter, we show that, by subjecting a magnetic nanostructure to properly designed competing magnetostatic interactions leading to asymmetric and inhomogeneous local magnetic fields, the magnetization reversal process can be tuned beyond geometry and material properties engineering. This study is not confined to academic interest alone, but it might also have a relevant technological impact, since magnetostatic interactions have been successfully exploited to provide interconnectivity in arrays of closely-spaced magnetic nanostructures, as in nanomagnetic logic devices [200] and in ASI systems. In

particular, vertex-frustrated lattices (see Fig. 4.7) have been derived from the decimation of full square ASI systems: the vertices are no more all constituted by four nanostructures, but a subset of them is formed by removing either one or two nanostructures, so leaving those vertices subjected to asymmetric and inhomogeneous local magnetic fields.

This chapter will constitute the frame for setting-up a research article in collaboration with A. Crespo, J. M. Porro, P. Landeros, V. Metlushko, A. Berger, and P. Vavassori.

6.1   The magnetization energy landscape

As we saw in Sec. 1.3, the balance between the exchange and the magnetostatic interactions determines the equilibrium magnetization configuration in magnetic nanostructures[1]. While the exchange interaction tries to keep parallel all the magnetic moments, the magnetostatic interaction favours the reduction of the stray field spatial extent, so forcing the magnetization to be parallel to the nanostructure surface. Through Eq. (1.31), each magnetization configuration can be associated to a scalar value which represents its (free) energy, and the set of all the possible energies for a given nanostructure represents its *energy landscape*. The factors governing the form of the energy landscape are the nanostructure size, shape and material. Once the material has been fixed, the nanostructure geometry defines the stable (and metastable) magnetization configurations [173–175]. In case of elongated magnetic nanostructures, two stable configurations are of particular relevance: the *quasi-uniform* (QU) magnetization state and the magnetic *vortex* state. Figure 6.1a shows a QU magnetization state in a stadium-like Permalloy nanostructure of $710\,\text{nm} \times 180\,\text{nm} \times 25\,\text{nm}$ size: the average magnetization along the major axis (i.e. the easy axis determined by the shape anisotropy) corresponds to $\approx 0.97 \text{M}_S$. On the other hand, for the magnetic vortex state in Fig. 6.1b, the average magnetization along both the major and the minor axes is close to zero. Despite the differences, both these configurations constitute stable magnetization configurations for the considered nanostructure, but their energy values allow separating the ground state from the metastable one. Hence, we started our study by performing a systematic analysis of the magnetization energy landscape for stadium-like Permalloy nanostructures of 25 nm thickness as a function of both the length of the minor axis and the aspect ratio (AR). We fixed the thickness to a smaller value than the planar dimensions

---

[1]As we have done until now, for the sake of this thesis we continue neglecting any kind of magnetocrystalline anisotropy.
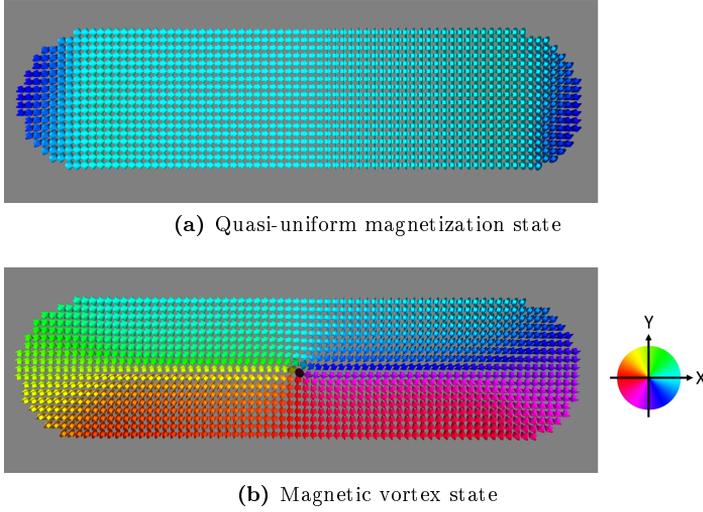
(a) Quasi-uniform magnetization state

(b) Magnetic vortex state

Figure 6.1: Energetically stable magnetization states in no applied magnetic field for a stadium-like Permalloy nanostructure of 710 nm × 180 nm × 25 nm size.

we are interested in, which typically are above 100 nm due to fabrication limitations (i.e. in order to be able to fabricate nanostructures with a well-defined shape). The analysis of the energy landscape in no applied magnetic field has been conducted by using the *OOMMF* micromagnetic solver [179], since the LLG equation (1.48) describes the magnetization evolution towards the effective field $\mathbf{H}_{eff}$, which corresponds to the equilibrium condition stated by Brown's equations (1.46). Clearly, by introducing a predefined magnetization configuration as an input for the simulation, the evolution ended up in the closest energy minimum, since the simulations have been performed at zero temperature. For this reason, we proceeded according to the following steps [201]:

- chose the nanostructure minor axis length and AR;

- initialize the magnetization configuration with a uniform magnetization state and let the system evolve according to the LLG equation. If the final state corresponds to a QU magnetization state, record the energy value, otherwise it does not represent a stable magnetization configuration for the chosen geometric parameters;

- initialize the magnetization configuration with a magnetic vortex state. If the final state still corresponds to a magnetic vortex state, record the energy value, otherwise it does not represent a stable magnetization configuration for the chosen geometric parameters;
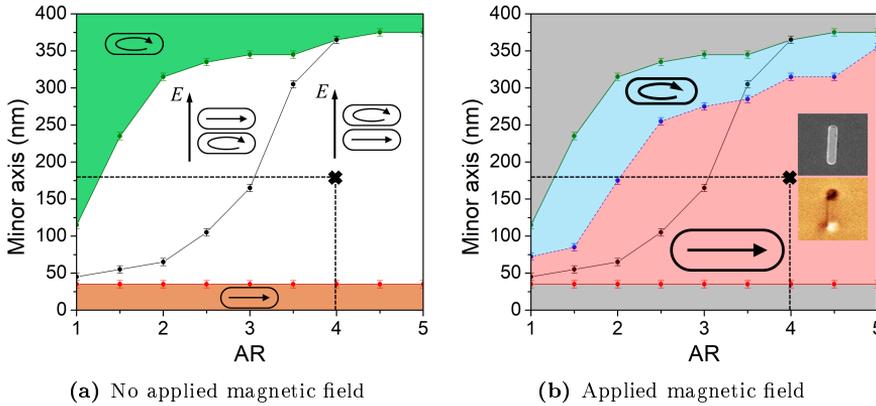
(a) No applied magnetic field   (b) Applied magnetic field

Figure 6.2: (a) Magnetization state phase diagram in no applied magnetic field for a stadium-like Permalloy nanostructure of 25 nm thickness. Four regions can be identified, as indicated by the schematics. In the coloured regions (orange and green), either the QU magnetization or the magnetic vortex are stable states, whereas both can coexist in the white region, but they are associated to different energy values E. (b) Magnetization states that can be induced through a uniform applied magnetic field: in the light-red region, only the QU magnetization can be obtained at remanence, while in the light-blue region also the magnetic vortex can be produced. In both the diagrams, the points marked with a black cross correspond to the case depicted in Fig. 6.1. The insets in (b) show both a SEM image of the corresponding fabricated nanostructure and the MFM image relative to the QU magnetization state.

- repeat all the previous steps for the needed minor axis lengths and ARs.

As simulation parameters for Permalloy, we considered $M_S = 860$ kA $\cdot$ m^{-1}, $A = 13$ pJ $\cdot$ m^{-1}, $\alpha = 0.05$, a stopping criterion given by $\max_{j\in\{\text{cells}\}} |\partial \mathbf{m}_j/\partial t| < 0.1° \cdot$ ns^{-1} and a cell size of 5 nm $\times$ 5 nm $\times$ 25 nm. The end result has been summarized in the phase diagram shown in Fig. 6.2a, and four regions can be identified. In the orange region, corresponding to the smallest minor axis lengths, the QU magnetization is the only energetically stable configuration, meaning that when we input the magnetic vortex as the initial configuration for the simulation, it always evolves towards the QU magnetization states. In the green region, the same behaviour applies to the magnetic vortex: it results to be the only stable state, being the final state also when starting from uniform magnetization. In the white region, representing intermediate sizes, both the states can coexist at equilibrium, but with different energies. In particular, the QU magnetization state possesses higher energy than the magnetic vortex state (at any given dimension) in the white region to the left of the black line. The opposite is true on the right-hand side, where the QU magnetization represents the ground state and the magnetic vortex is only energetically metastable. Even if this phase diagram has

been obtained for a particular choice of shape and thickness, the extracted general behaviour is the same that can be found in literature for elongated Permalloy nanostructures [174].

For practical applications, the nanostructure magnetization state is usually user-controlled through an applied magnetic field. Considering the length-scale of a typical nanostructure, the most common situation corresponds to the use of a magnetic field that can be considered uniform in the space region where the nanostructure resides. So, upon introducing a uniform applied magnetic field, the Zeeman energy term modifies the previously described energy landscape, in a way that depends on the applied magnetic field intensity and direction. However, we are interested in the nanostructure magnetization state at remanence, being the applied field just the mean we have for exploring the energy landscape related to the phase diagram in Fig. 6.2a. So, we simulated hysteresis loops performed at various in-plane angles in order to see, for each one of the previous regions, what magnetization configuration can be induced by an uniform magnetic field. In other words, we perturbed the non-interacting nanostructure energy landscape in order to open paths towards one of the energy minima characterizing the considered geometry. The results are summarized in Fig. 6.2b, which shows the partition of the phase diagram in Fig. 6.2a into two further regions. In the light-red region, no matter what sequence of uniform applied magnetic field we used, we could only get the QU magnetization state at remanence. On the other hand, for nanostructures lying in the light-blue region it is possible to find at least one field sequence leading to a magnetic vortex state when the field is removed. The main conclusion emerging from this analysis is that, both in the light-red and in the light-blue regions of Fig. 6.2b, not all the energy landscape minima can be reached by applying a uniform magnetic field.

In this framework, the nanostructure whose size corresponds to the black cross in Fig. 6.2 (710 nm × 180 nm × 25 nm) has been chosen to demonstrate that, by subjecting it to properly designed competing magnetostatic interactions leading to an asymmetric and inhomogeneous local magnetic field, its magnetization reversal process can include the magnetic vortex state as a stable state after the removal of the applied field. This choice for the size has been dictated by the fact that the black cross lies well inside the light-red region we just identified, since the considered parameters for the micromagnetic simulations might lead to variations in the region boundaries. The MFM image shown as an inset in Fig. 6.2b represents a QU magnetization state at remanence for the non-interacting nanostructure, which also experimentally results to be the only stable remanent magnetization state irrespective of the direction of the uniform applied magnetic
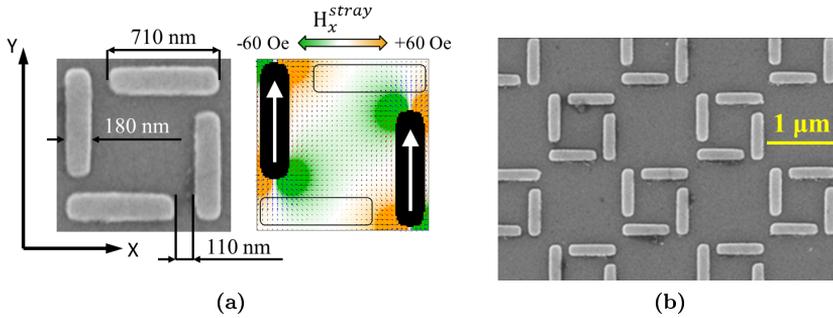
Figure 6.3: (a) Chiral square unit composed by four Py nanostructures of specified size. The color-map shows the spatial distribution of the x-component of the stray field produced by the vertical nanostructures being uniformly magnetized in the direction specified by the white arrows. (b) SEM image of the array considered for the MOKE and MFM measurements reported in Ref. [202]. Adapted from [201].

field. The chiral square unit shown in Fig. 6.3a and composed by four nanostructures could provide the local magnetic field distribution we need for proving our claim. The target nanostructures in which we want to induce the magnetic vortex state are the two horizontal bars (i.e. the nanostructures aligned along the x-axis), whereas the vertical bars are the local magnetic field sources. Indeed, from the color-map in Fig. 6.3a representing the x-component of the stray field $\mathbf{H}^{stray}$ produced by the vertical bars, the local magnetic field in the region where the target bars reside results to be asymmetric and spatially inhomogeneous.

6.2   The experimental evidence

By means of MOKE and MFM measurements carried out on the array shown in Fig. 6.3b, Porro et al. [202] demonstrated that the above described chiral unit indeed facilitates the formation of a magnetic vortex state, in combination with a uniform applied magnetic field. For this reason, we briefly go over the experimental study reported in Ref. [202]. The magnetization reversal process in the chiral unit has been examined by performing hysteresis loops while applying the magnetic field $\mathbf{H}^{appl}$ close to the y-axis, so almost perpendicular to the target bars. For collecting the magnetization signal, the *transverse* MOKE configuration has been employed, so p-polarized light impinged on the sample and the scattering plane was perpendicular to the y-axis. In order to be more sensitive to small changes in the magnetization distribution during the hysteresis loop, the *diffracted* MOKE (DMOKE) geometry [203] has been implemented by collecting the intensity coming from the diffracted beams. As shown in Ref. [204], the in-

tensity of the n-th order diffracted beam is proportional to the *magnetic form factor* $f_n\,(\mathrm{H})$ given by

$$f_n\,(\mathrm{H}) \;=\; \iint_S \mathrm{m}_y\,(x,y,\mathrm{H})\exp\left(inG_x x\right)dxdy, \qquad (6.1)$$

where S denotes the unit cell of the probed array, $\mathrm{m}_y\,(x,y,\mathrm{H})$ is the component of the magnetization spatial distribution which is perpendicular to the scattering plane and $G_x = 2\pi/L_x$, with L_x being the lateral pitch between neighbouring chiral units composing the array (2.2 μm in this case). The upper part of Figs. 6.4a and 6.4b contains the hysteresis loops measured on the 2nd-order diffracted beam (2nd-order DMOKE loops), whereas the lower part contains the corresponding simulated 2nd-order DMOKE loops, obtained by calculating the magnetic form factor $f_2\,(\mathrm{H})$ from the simulated magnetization distribution. Figure 6.4a refers to the case in which $\mathbf{H}^{appl}$ was slightly misaligned (by $\vartheta = -2.5°$) with respect to the y-axis, whereas Fig. 6.4b refers to the aligned case (identified as $\vartheta = -0.1°$ for experimental reasons). Despite the small angular variation, the 2nd-order DMOKE experimental loops show marked differences. Indeed, the applied magnetic field angle ϑ has been chosen for revealing these differences, and we will further discuss this aspect in the next sections. Since it is quite difficult to give a direct interpretation of the features appearing in DMOKE hysteresis loops, the micromagnetic simulations can provide the needed support. Indeed, the side-by-side comparison of the simulated and experimental DMOKE loops permits to confirm the validity of the micromagnetic configurations provided by the simulations or, if required, to revise the assumptions considered in the simulations (i.e. shape details and material parameters) until agreement is achieved. In other words, the agreement between simulated and experimental hysteresis loops allows us to trust the magnetization evolution returned by the micromagnetic simulations.

The relevant micromagnetic configurations, characterizing the two cases depicted in Fig. 6.4 and corresponding to the points marked by letters in the bottom panels, are shown in Fig. 6.5. Starting from positive saturation where the configuration is substantially the same for both cases (A), the magnetization reversal follows two completely different paths after reducing the field. In the misaligned case ($\vartheta = -2.5°$), the formation of an S-state can be observed in the horizontal bars (B). As the field is further reduced, the S-state rotates according to what is shown in configurations C, D, E and F. As a result, all the elements in the chiral unit remain in a single-domain state during the complete reversal process. The bottom-left MFM image in Fig. 6.5 shows the magnetization state at remanence (C) and can be interpreted as corresponding to four nanostructures in a QU
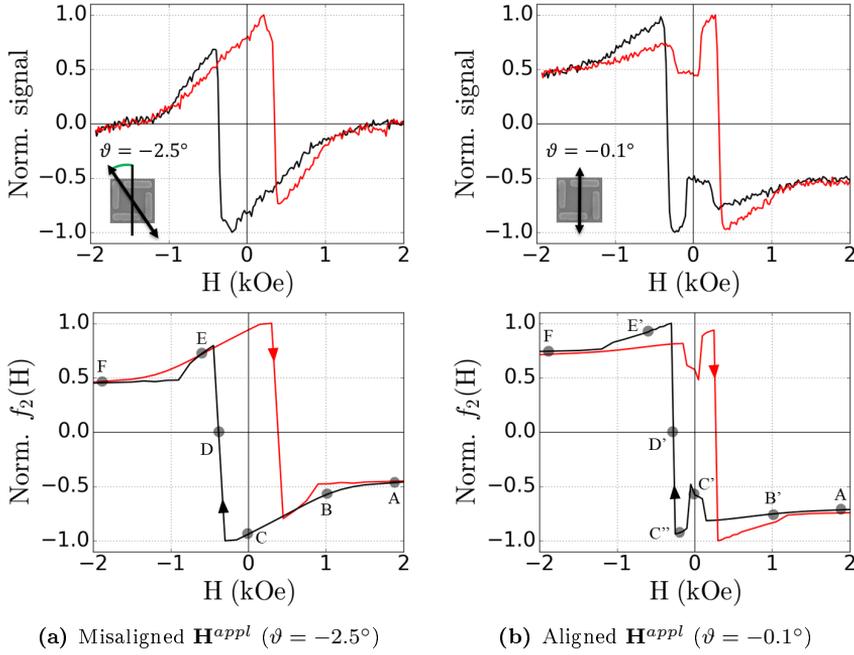
(a) Misaligned $\mathbf{H}^{appl}$ ($\vartheta = -2.5°$)   (b) Aligned $\mathbf{H}^{appl}$ ($\vartheta = -0.1°$)

Figure 6.4: (a) Measured (top panel) and simulated (bottom panel) 2nd-order DMOKE loops for misaligned $\mathbf{H}^{appl}$. (b) Measured (top panel) and simulated (bottom panel) 2nd-order DMOKE loops for aligned $\mathbf{H}^{appl}$. The SEM images appearing as insets in the top panels help in visualizing the applied magnetic field direction. In both the simulated hysteresis loops, the letters refer to the micromagnetic configurations shown in Fig. 6.5. Adapted from [202].

magnetization state. These findings demonstrate that, in the misaligned case, the magnetostatic interaction is not enough relevant in order to cause a deviation from the behaviour induced in a non-interacting nanostructure by a uniform applied magnetic field. A completely different picture emerges in the aligned case ($\vartheta = -0.1°$). Here, the magnetostatic interaction is able to induce a C-state into each one of the horizontal bars (B') rather than a S-state as the applied magnetic field is reduced from positive saturation. The C-state subsequently nucleates a single magnetic vortex in each horizontal bar as the applied field goes to zero (C'). The presence of magnetic vortex states at remanence is confirmed by the MFM image shown in the bottom-right part of Fig. 6.5. As the external field reverses, the vortex cores are displaced horizontally towards the opposite end of each horizontal bar (C''), a process which produces the notable peaks in the 2nd-order DMOKE loop. By further increasing the field in the reverse direction, the magnetization in the vertical bars switches (D' and E') and then the vor-
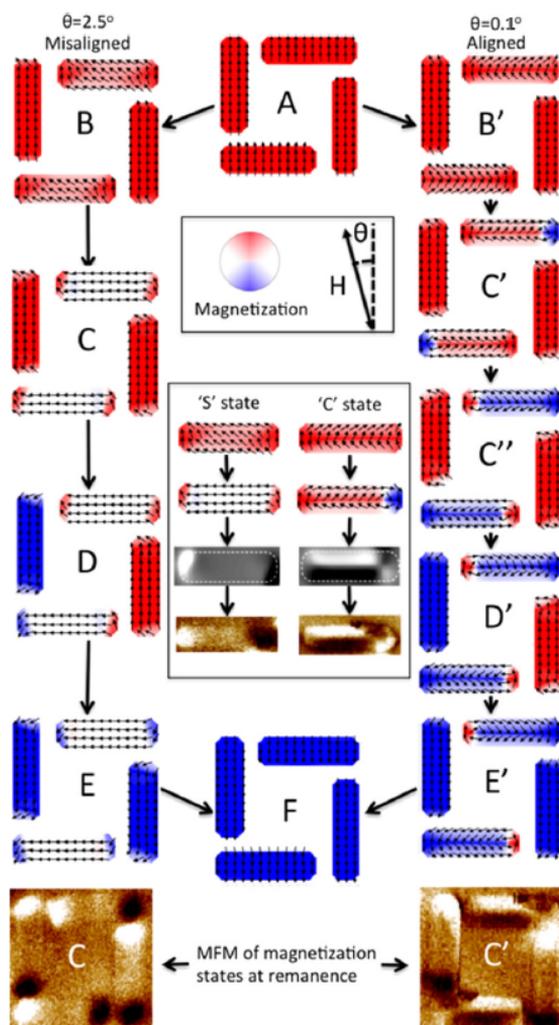
Figure 6.5: *OOMMF* simulations of the magnetization states corresponding to the marked points in the hysteresis loops of Fig. 6.4 and characterizing the magnetization reversal process for the misaligned (left) and aligned (right) cases. The upper inset contains sketches of the magnetization color-scale and of the applied magnetic field direction. The lower inset shows the evolution of the horizontal bar magnetic state for the misaligned and aligned cases. The sequence begins with the seed S-state (misaligned) and C-state (aligned), followed by their corresponding remanent states, the calculated MFM images of these magnetic states and the experimental MFM images showing a QU magnetization state (misaligned) and a magnetic vortex state (aligned). Finally, the lower MFM images show the magnetic states at remanence for the whole chiral unit. Adapted from [202].

tices annihilate before reaching saturation (F). In conclusion, this experimental study confirmed the presence of two magnetization reversal paths. In particular, the asymmetry and spatial inhomogeneity of the magnetostatic interaction field causes the formation of magnetic vortex states in the nanostructures having the minor axis "sufficiently" parallel to the uniform applied magnetic field.

6.3 The detailed study of the magnetization reversal process

6.3.1 Further MOKE measurements

The analysis performed in the framework of the Ph.D. project leading to this thesis started by associating a quantitative meaning to the word "sufficiently". For this purpose, we designed further MOKE measurements in order to perform a systematic study of the angles characterizing the separation in between the two above-mentioned reversal paths. The array shown in Fig. 6.3b has been mounted inside the gap of the quadrupole electromagnet which is part of the longitudinal MOKE setup described in Sec. 3.2.2. Before starting the measurements, we ran micromagnetic simulations[2] for identifying the best field protocol to be employed, which resulted to be the one schematically shown in Fig. 6.6a. At the beginning, the unit cell is rotated at an angle ϑ with respect to the y-axis, since the $\mathbf{H}^{appl}$ magnetic field sequence will be applied by using the two depicted electromagnet poles, which are perpendicular to the scattering plane. Then, the four electromagnet poles are used to apply a saturating magnetic field at $\vartheta = 45°$, in order to bring (or to "reset") the horizontal bars to the QU magnetization state at remanence, providing a reproducible starting state for the following field sequence. Eventually, the field generated by the vertical poles is swept from zero to H^{appl}_{max} and then back to zero, simultaneously measuring a signal proportional to the average magnetization component m_t lying in the scattering plane. We decide to measure m_t, i.e. the magnetization component *transverse* to the applied field direction, since it lies along the major axis of the horizontal bars, allowing us to be more sensitive to magnetization changes in our target nanostructures without having to deal with the vertical bars. Indeed, for the considered field protocol, the vertical bars remain saturated along the major axis, being subjected to almost no magnetization changes. On the other hand, the horizontal

---

[2]As simulation parameters, we considered the values reported in Sec. 6.1, a part for modifying the cell size to 10 nm × 10 nm × 25 nm. We verified that the use of a bigger cell size does not affect the conclusions of our analysis by simulating few selected cases with the previous cell size (5 nm × 5 nm × 25 nm).

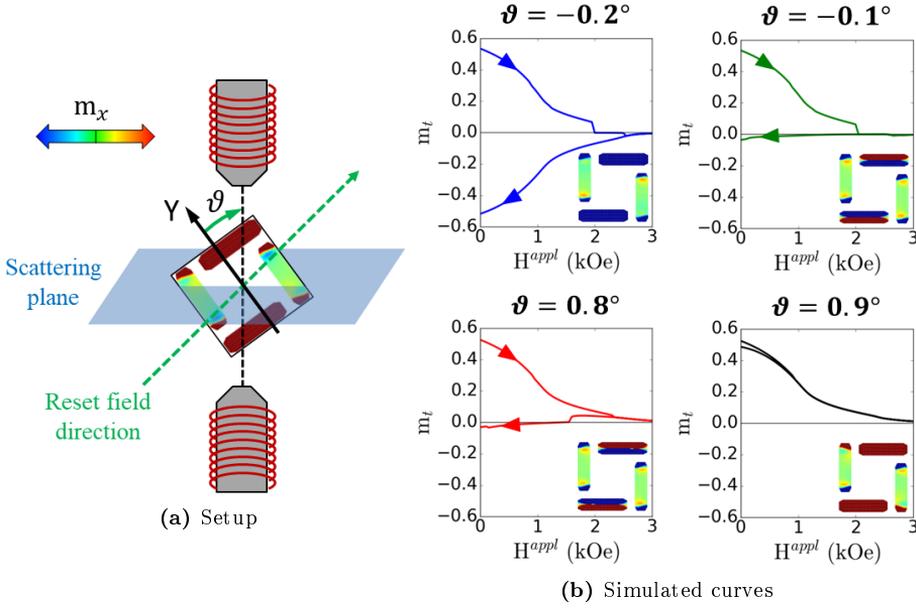**(a)** Setup

(b) Simulated curves

Figure 6.6: Description and simulation of the performed longitudinal MOKE measurements. (a) After resetting the magnetic configuration of the horizontal bars to the QU magnetization state, a magnetic field is applied to the array in Fig. 6.3b at an angle ϑ with respect to the y-axis. The schematic inside the electromagnet poles shows the starting magnetization configuration after the reset. (b) The four curves (swept as indicated by the filled triangles) depict the simulation results obtained at the corresponding angles. The insets show the x-component of the final magnetization configurations: the horizontal bars are either in the magnetic vortex state or in the QU magnetization state.

nanostructures go through major changes, since the final configuration can be either the magnetic vortex state or the QU magnetization state. The simulated curves reported in Fig. 6.6b show the expected results. The angles $\vartheta = -0.2°$ and $\vartheta = -0.1°$ constitute the boundary between the two reversal paths: below $\vartheta = -0.2°$, at the end of the field sequence the horizontal bars result to be in the QU magnetization state, whereas above $\vartheta = -0.1°$ the final configuration is the magnetic vortex state, as indicated by the magnetization configurations shown as insets. Moreover, another boundary appears between $\vartheta = 0.8°$ and $\vartheta = 0.9°$. From these simulations, an interesting aspect emerged, namely the existence of two *critical angles* ϑ_C^- and ϑ_C^+ separating the two reversal paths: for an applied magnetic field angle $\vartheta_C^- < \vartheta < \vartheta_C^+$ (the "aligned" condition of Sec. 6.2), the remanent configuration is the magnetic vortex state, whereas for $\vartheta < \vartheta_C^- \ \lor \ \vartheta > \vartheta_C^+$ (the "misaligned" condition of Sec. 6.2), the horizontal bars are characterized by a QU magnetization state. However, the measured experimental curves would
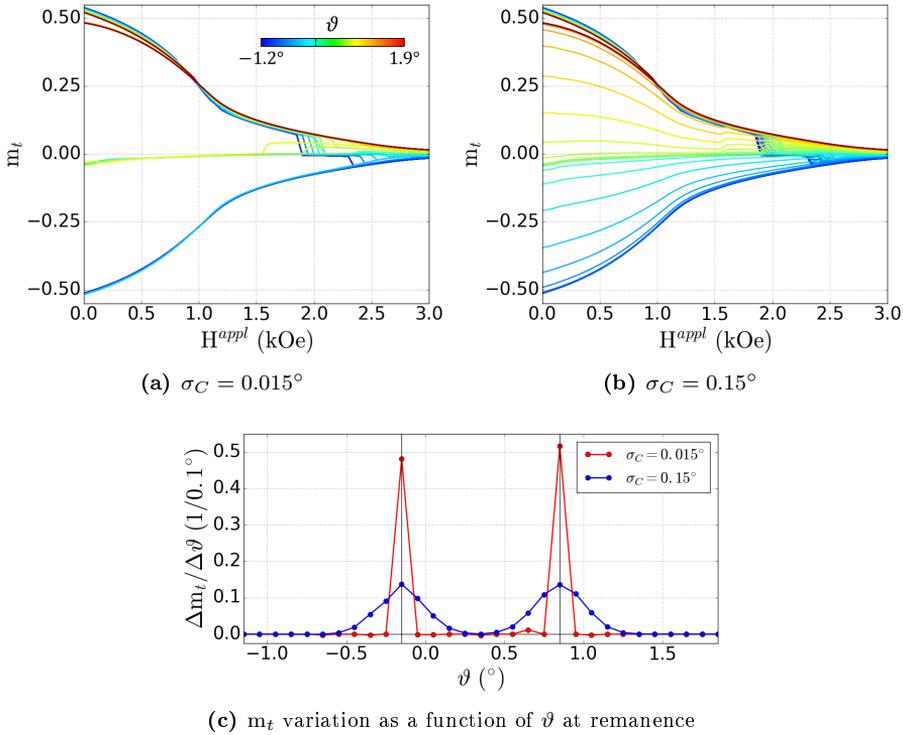
(a) $\sigma_C = 0.015°$

(b) $\sigma_C = 0.15°$

(c) m_t variation as a function of ϑ at remanence

Figure 6.7: (a)-(b) Simulated experimental curves in case of two different σ_C values for the unit cell y-axis direction distribution. In each plot there are 32 curves (from blue to red, gradually), corresponding to ϑ ranging from $-1.2°$ to $1.9°$ with a step size of $0.1°$. (c) "Angular speed" of variation of m_t at remanence, i.e. how "fast" m_t is changing at remanence between subsequent curves.

correspond exactly to the behaviour shown by the simulated curves only in case of perfect (and perfectly aligned) unit cells composing the array. Actually, the limitations in the fabrication process when dealing with arrays of repeated unit cells translate into the statistical distribution of the observed quantities: in this case, the sharp critical angles returned by the simulations will correspond to smooth transitions. To match this fact, we introduced a critical angle distribution in form of a distribution in the unit cell y-axis direction. When considering a measurement to be obtained at angle ϑ, the corresponding simulated experimental curve is the weighted average of the simulated "exact" curves (from Fig. 6.6b) which can be found in an angular range dictated by a Gaussian distribution of standard deviation σ_C around ϑ. Figures 6.7a and 6.7b show the simulated experimental curves corresponding to $\sigma_C = 0.015°$ and $\sigma_C = 0.15°$, respectively. In each plot there are 32 curves (from blue to red, gradually), corresponding to
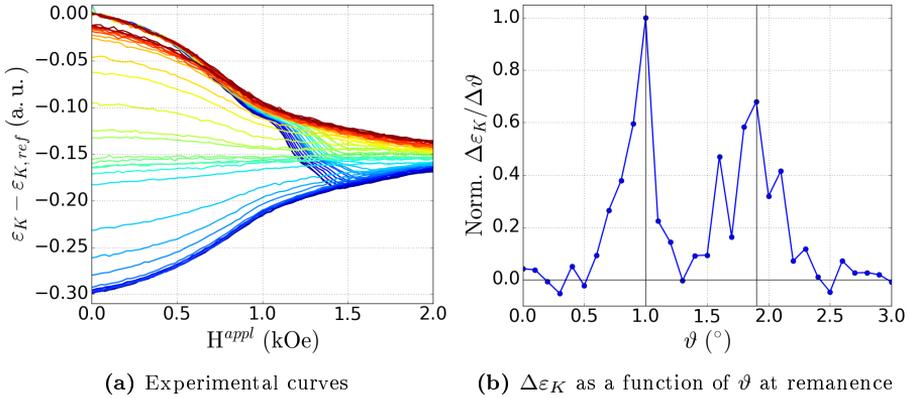
(a) Experimental curves

(b) $\Delta\varepsilon_K$ as a function of ϑ at remanence

Figure 6.8: (a) Measured (single-shot) experimental curves (from blue to red, gradually) corresponding to ϑ ranging from $-0.05°$ to $3.05°$ with a step size of $0.1°$. (b) Normalized "angular speed" of variation of ε_K at remanence, i.e. how "fast" the signal is changing at remanence between subsequent curves.

ϑ ranging from $-1.2°$ to $1.9°$ with a step size of $0.1°$. When σ_C is much smaller than the angular step size (Fig. 6.7a), the simulated measurement sequence is not able to capture the y-axis direction distribution, so the resulting average curves still show the abrupt jumps while crossing the critical angles. On the other hand, if we consider an higher σ_C, comparable with the angular step size (Fig. 6.7b), the average curves are characterized by smoother changes, as can be seen from the m_t trend when $H^{appl} = 0$ Oe. However, despite the differences, the signature left by the critical angles is still present in these plots. Indeed, Fig. 6.7c shows the "angular speed" of variation of m_t at remanence, allowing us to quantify how "fast" m_t is changing at remanence with respect to a variation in ϑ. The red line corresponds to $\sigma_C = 0.015°$: the two visible peaks at $\vartheta = -0.15°$ and $\vartheta = 0.85°$ are consequence of the big changes in the curves depicted in Fig. 6.7a when passing through the critical angles. Even if changes are smoother (i.e. "slower") when considering $\sigma_C = 0.15°$, two peaks are still present (the blue line), and they correspond to the same angles as for $\sigma_C = 0.015°$, confirming that $\Delta m_t/\Delta\vartheta$ is a meaningful quantity to calculate for retrieving the critical angle values.

After having identified how to proceed, we performed the designed MOKE measurements, for which the reset field was 2800 Oe and $H^{appl}_{max} = 2000$ Oe. Figure 6.8a shows the experimental curves, obtained by recording the Kerr ellipticity ε_K. For superimposing all the curves, we subtracted the first ε_K value to each one of them, since the applied field sequence always started from a common and reproducible magnetization configuration. The fact that Fig. 6.8a well compares

with Fig. 6.7b validates all the conclusions inferred from the simulations. Indeed, the "angular speed" of variation of ε_K at remanence plotted in Fig. 6.8b shows two peaks at $\vartheta = 1.0°$ and $\vartheta = 1.9°$, which can be interpreted as corresponding to the critical angles. However, a clarification is mandatory: when working with simulations, we could detect the *absolute* critical angle values since all the considered angles were referred to $\vartheta = 0°$ as the angle of perfect alignment between the unit cell y-axis and $\mathbf{H}^{appl}$. For the measured curves, all the considered ϑ values were referred to an arbitrary $\vartheta = 0°$ reference angle, so we could estimate the critical angles by assuming that the ratio in between the experimental critical angle magnitudes was the same as the simulated one, hence obtaining

$$\vartheta_C^- \approx -0.13°,$$
$$\vartheta_C^+ \approx 0.77°.$$

6.3.2   A simple, but misleading, explanation

To try to figure out the reason of such a sharp transition between the two reversal paths, we started by considering the external magnetic field $\mathbf{H}^{ext}$ felt by the horizontal bar:

$$\mathbf{H}^{ext} = \mathbf{H}^{appl} + \mathbf{H}^{stray}, \tag{6.2}$$

where $\mathbf{H}^{appl}$ is the uniform applied magnetic field and $\mathbf{H}^{stray}$ denotes the stray field produced by the vertical bars. The color-maps in Fig. 6.9a help in visualizing what is going on. For the sake of clarity and for speeding up further simulations, we introduced a modified unit cell obtained by removing the bottom horizontal bar, an operation which does not alter the general behaviour. For the three-bars unit cell, the (positive) critical angle resulted to be $\vartheta_C^+ = 0.94°$ (named ϑ_C from now on), slightly bigger than the value obtained when considering four nanostructures ($\vartheta_C^+ = 0.85°$). The magnetization reversal in confined structures is known to nucleate at the edges [45] and, for the case considered here where $\mathbf{H}^{appl}$ lies close to the y-axis, the top and bottom edges of the horizontal bar (TE and BE, respectively) are the relevant ones. For $\mathbf{H}^{ext}$ being determined by the uniform $\mathbf{H}^{appl}$ alone (e.g. as for a non-interacting bar), the net result would be the formation of a magnetic S-state, which is the seeding state for the formation of a QU magnetization state at remanence. On the other hand, when considering the three-bars unit cell, the stray field generated by the right vertical nanostructure in the bottom-right part of the horizontal bar has a strong negative x-component (filled-green arrow in Fig. 6.9a), whereas in the top-left part the main contribution is given by the strong positive H_x^{stray} coming from the left vertical nanostructure

(a) Modified unit cell and relevant quantities

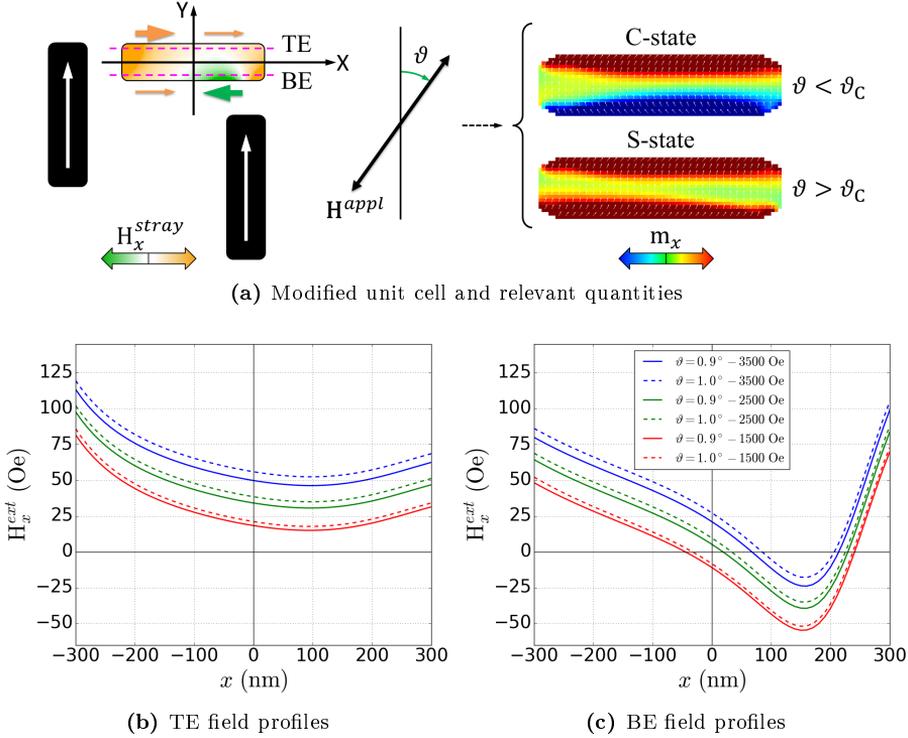(b) TE field profiles

(c) BE field profiles

Figure 6.9: (a) Schematic representation of the relevant characters involved in the magnetization reversal process: according to the applied field angle ϑ, either a magnetic C-state or a magnetic S-state can be nucleated in the horizontal bar, so giving rise to a critical angle ϑ_C separating these two different behaviours. (b) Top-edge (TE) field profiles showing the x-component of $\mathbf{H}^{ext}$ for two applied field angles. (c) Same as (b), but for the bottom-edge (BE) profiles. The field values in the legend refers to the magnitude of $\mathbf{H}^{appl}$.

(filled-orange arrow in Fig. 6.9a). Hence, in the horizontal bar region, $\mathbf{H}^{stray}$ possesses a chirality bestowed by the chiral configuration of the nanostructures composing the unit cell, potentially leading to the formation of a magnetic C-state which is the seeding state for the formation of a magnetic vortex state at remanence. In the end, when considering both these contributions to $\mathbf{H}^{ext}$, each one of them will tend to impose its own symmetry on the magnetization configuration of the horizontal bar and the most relevant term should depend on their relative magnitude. By increasing the angle ϑ, we are increasing the magnitude of H_x^{appl} and, at a certain point, this component will be big enough to counteract the chiral behaviour imposed by the stray field, in particular by balancing the negative H_x^{stray} in the bottom-right part of the horizontal bar. This mechanism, corresponding to a sharp change in the symmetry of $\mathbf{H}^{ext}$,
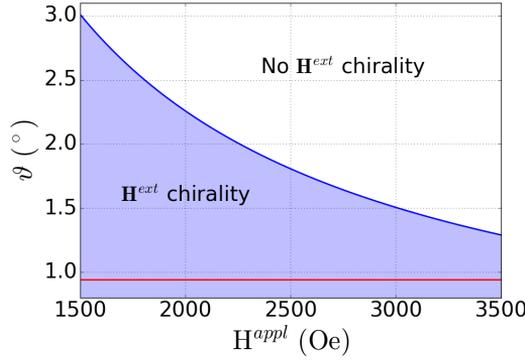
Figure 6.10: Angle ϑ needed for fully balancing H_x^{stray} as a function of H^{appl}. In the blue region, $\mathbf{H}^{ext}$ maintains a chiral character, whereas in the white region $H_x^{ext} \geq 0$ in all the horizontal bar volume. The borderline in between the two regions is determined according to Eq. (6.3). The red horizontal line corresponds to $\vartheta = \vartheta_C = 0.94°$ and completely lies in the blue region.

could explain the existence of a critical angle as the angle at which $\mathbf{H}_x^{ext}$ loses its chiral nature in all the region occupied by the horizontal bar for a given H^{appl} value. To find a confirmation of our reasoning, we plotted the values of H_x^{ext} along both TE and BE for $\vartheta = 0.9°(< \vartheta_C)$ and for $\vartheta = 1.0°(> \vartheta_C)$, as shown in Figs. 6.9b and 6.9c. For the unit cell here considered, saturation corresponds to $H^{appl} = 3500$ Oe, whereas at 1500 Oe either the S-state (for $\vartheta = 1.0°$) or the C-state (for $\vartheta = 0.9°$) have already been nucleated. Therefore, we can identify the $1500 - 3500$ Oe range as the field range in which the symmetry character of $\mathbf{H}^{ext}$ can have an impact on the choice of the magnetization reversal path to be taken. For $\vartheta = 0.9°$ (solid lines), the chiral behaviour of $\mathbf{H}^{ext}$ is present for the whole above-mentioned field range, since $H_x^{ext} < 0$ in the BE profile for $x > 0$ and $H_x^{ext} > 0$ in the TE profile for $x < 0$. Nevertheless, for $\vartheta = 1.0°$ (dashed lines), the chiral character of $\mathbf{H}^{ext}$ is substantially the same, so in the end the alternative formation of either a C-state or an S-state is not evident from this picture. Indeed, the angle ϑ at which $H_x^{ext} \geq 0$ in all the region occupied by the horizontal bar (i.e. the minimum angle needed for fully balancing H_x^{stray}) is given by:

$$\vartheta \;=\; \arcsin \left[\frac{|\min (H_x^{stray})|}{H^{appl}} \right]. \tag{6.3}$$

Figure 6.10 shows the two regions identified by Eq. (6.3): only in the blue region $\mathbf{H}^{ext}$ maintains a chiral character and, for H^{appl} in the $1500 - 3500$ Oe range, the minimum angle needed for suppressing the $\mathbf{H}^{ext}$ chirality is always greater than 1.3°. Thereby, the existence of the calculated $\vartheta_C = 0.94°$ (in particular its

small value) is not simply justifiable through the chiral character of $\mathbf{H}^{ext}$, which appears to be a necessary but not sufficient condition for the observed behaviour.

6.3.3   The dynamical analysis

Since the chirality of $\mathbf{H}^{ext}$ (or, more generally, its symmetry) is certainly a prerequisite for the observed behaviour but it is not sufficient to justify the actual ϑ_C value, we decided to investigate in more details the magnetization dynamics related to the reversal process. According to Leaf et al. [205], changes in the magnetization state can be inferred and identified by analyzing the frequency evolution and the symmetry of the magnetic normal modes of the considered nanostructure during the magnetization reversal process. In Sec. 1.5, we saw that a ferromagnetic material, when perturbed out of equilibrium, can sustain magnetization oscillations, generally called *spin waves*. For waves in confined dimensions, as happens in nanostructures, the resulting standing-wave patterns constitute the nanostructure *normal modes*. However, in case of spin waves, the balance between exchange and magnetostatic interactions determines the appearance of more complex modes [46, 206] which do not fit the standing-wave model description and which can be of utmost importance for the magnetization reversal process. So, for calculating the magnetic normal modes, we implemented the *dynamical matrix method* (DMM) described in Refs. [207, 208]. A magnetic nanostructure can be seen as a collection of N cells characterized by a magnetic moment $\mathrm{M}_S \mathbf{m}_j$ ($j = 1, \ldots, N$) and subjected to various interactions, as described by the following energy density $\mathcal{E}_{tot}$:

$$
\begin{aligned}
\mathcal{E}_{tot} \;=\; &-\mu_0 \mathrm{M}_S \mathbf{H}^{appl} \cdot \sum_{j=1}^{N} \mathbf{m}_j \;+\; \frac{A}{d^2} \sum_{j=1}^{N} \sum_{n}^{n.n.} \left(1 - \mathbf{m}_j \cdot \mathbf{m}_n\right) \\
&+ \frac{\mu_0 \mathrm{M}_S^2}{2} \sum_{i=1}^{N} \sum_{j=1}^{N} \mathbf{m}_i \cdot \mathfrak{N}_{ij} \cdot \mathbf{m}_j.
\end{aligned}
\tag{6.4}
$$

The description of the three contributions to $\mathcal{E}_{tot}$ can be found in Sec. C.1. By expanding the above-defined energy density in power series around the equilibrium magnetization configuration and retaining only the leading terms (2nd-order in the cell magnetization), the search for the magnetic normal modes converts to the calculation of the normal modes associated to a small oscillations problem [9]. Hence, the Hamilton equations lead to an *eigenvalue problem*, where the eigenvalues represent the involved frequencies and the corresponding eigenvectors describe the normal modes, i.e. they give a map of the oscillation amplitude of

the magnetization around the equilibrium configuration. The DMM returns all the normal modes allowed by the geometry and the interactions, but it does not provide any insight regarding the relative amplitude of the modes. This latter information can be retrieved through the Fourier analysis of the time evolution of the nanostructure magnetization obtained by solving the LLG equation [209].

The DMM has been carried out both on the non-interacting bar (as a reference, since there is only one remanent magnetization configuration and no critical angle) and on the three-bars unit cell depicted in Fig. 6.9a. The uniform magnetic field $\mathbf{H}^{appl}$ has been applied at a given angle ϑ and its magnitude has been gradually reduced from saturation (3500 Oe) to zero. From micromagnetic simulations, we could extract the equilibrium magnetization states at any needed $(\vartheta, \mathrm{H}^{appl})$ combination, since the equilibrium state is the input configuration to be used in the DMM calculations. For the non-interacting bar, the input configuration represents a single nanostructure of size $710 \, \mathrm{nm} \times 180 \, \mathrm{nm} \times 25 \, \mathrm{nm}$, which corresponds to $N = 1242$ micromagnetic cells and to a calculation time of about 2 minutes. On the other hand, the input configuration for the interacting case should include the three nanostructures composing the unit cell, corresponding to $N = 3726$ and to a calculation time of about 16 minutes. However, since we were interested in the dynamic behaviour of the horizontal bar, the calculations have been substantially speeded up by performing the analysis taking only into account the 1242 $\mathbf{m}_j$ vectors composing the horizontal bar and then considering $\mathbf{H}^{stray}$ as a background field. In other words, the energy density (6.4) only included $\mathbf{m}_j$ vectors belonging to the horizontal bar and $\mathbf{H}^{appl}$ has been substituted by $\mathbf{H}^{ext}$. The DMM can return all the allowed normal modes, but we are only interested in the lowest frequency modes, since they are the relevant ones, driving the magnetization configuration changes [205, 210]. For this reason, Figs. 6.11a and 6.11b show the out-of-plane component $\delta\mathrm{m}_z$ of the lowest frequency normal modes relative to the non-interacting bar for $\vartheta = 0.9°$: the *edge mode* 1 (EM1) and the *edge mode* 2 (EM2). The dynamical magnetization $\delta\mathrm{m}_z$ represents the initial out-of-plane amplitude of the magnetization oscillation around the equilibrium position in each micromagnetic cell. For both EM1 and EM2, the dynamical magnetization is mainly localized at the edges perpendicular to $\mathbf{H}^{appl}$ [210, 211], but these two modes differ regarding the relative oscillation phase. Whereas the regions of maximum amplitude oscillate in phase for EM2, they are 180° out of phase for EM1, corresponding to a different type of symmetry. The evolution of the edge mode frequencies as a function of H^{appl} is reported in Fig. 6.11c, where the EMs up to EM6 are labelled and the behaviour of EM1 and EM2 is highlighted by blue lines. However, only EM2 results to be active
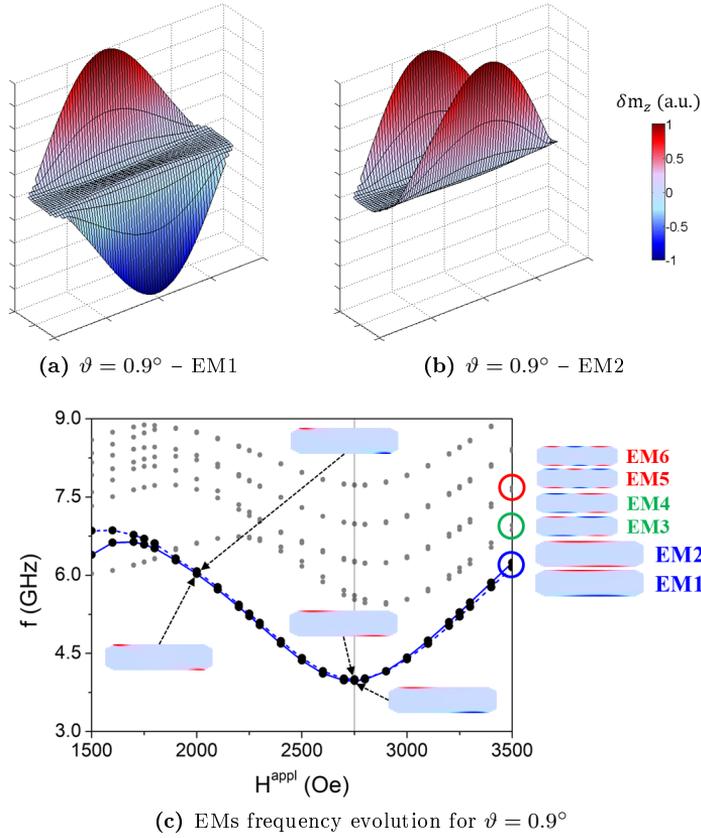
(a) $\vartheta = 0.9°$ – EM1   **(b)** $\vartheta = 0.9°$ – EM2

(c) EMs frequency evolution for $\vartheta = 0.9°$

Figure 6.11: DMM results for a non-interacting bar when $\mathbf{H}^{appl}$ is applied at $\vartheta = 0.9°$. (a) and (b) represent the δm_z mode profiles for the lowest frequency normal modes, i.e. EM1 and EM2. (c) Edge modes frequency evolution as a function of H^{appl}. The blue lines highlight the behaviour of EM1 (dashed line) and EM2 (solid line), for which the mode profiles are shown at 3500 Oe, 2750 Oe and 2000 Oe as insets. The black vertical line corresponds to 2750 Oe.

during the magnetization reversal process, as confirmed by the Fourier analysis of the magnetization evolution performed according to Ref. [209]. The blue-solid line associated with EM2 in Fig. 6.11c allows describing two regions of interest: in the range $2750 - 3500$ Oe, the frequency decreases while decreasing H^{appl}, indicating the building up of an instability area inside the nanostructure (*mode softening*). Indeed, the frequency trend reflects the strength of the restoring force (i.e. the effective field $\mathbf{H}_{eff}$ entering the LLG equation): the lower the frequency, the lower the restoring force on the oscillating magnetic moments and the system is more prone to be influenced by external stimuli. Energetically speaking, the comparison with a simple harmonic oscillator allows the frequency to be iden-

tified with the width of the potential energy well: a higher frequency is related to a narrower potential well, which implies more limited oscillations around the equilibrium position and higher stability (having fixed the total energy). During the mode softening, the localization of this instability area does not change appreciably in this first region. However, below 2750 Oe, the frequency starts rising while decreasing H^{appl}, indicating the recovery of a substantial restoring force. In this region, the spatial localization of the EM2 dynamical magnetization changes, moving towards the lateral edges and becoming more concentrated, following the formation of a magnetic S-state. Thereby, we can identify 2750 Oe as the H^{appl} value corresponding to the S-state nucleation for the non-interacting bar at $\vartheta = 0.9°$. The edge mode softening has also been observed in transversely magnetized Py *stripes*, which correspond to the practical realization of infinitely long bars [212–214]. In this case, the complete softening (i.e. the achievement of zero restoring force) is related to the onset of saturation along the applied magnetic field direction and it occurs at the applied field value needed for balancing the demagnetizing field and aligning the magnetization normal to the edge.

While the DMM calculations for the non-interacting bar constitute a useful reference case, the most interesting information comes from the analysis of the interacting bar. Figure 6.12 shows the summary of the main results, both for the non-interacting bar and for the horizontal (interacting) bar composing the unit cell. For the latter case, the calculations have been performed at $\vartheta = 0.9°(< \vartheta_C)$ and at $\vartheta = 1.0°(> \vartheta_C)$, in order to track the differences in the magnetization dynamical evolution leading to two distinct reversal paths. Each one of the three sections in the figure contains, for selected H^{appl} values, the color-maps representing the x-component of the magnetization m_x and also the δm_z mode profiles for the lowest frequency EMs. As we discussed for the non-interacting bar, EM1 has been greyed out since it is not active during the actual dynamical evolution. The first thing to be noticed is the fact that the nature of the lowest frequency modes for the interacting bar is quite different with respect to what discussed until now: EM1 and EM2 have been replaced by EM1' and EM2', in which the interaction leads to a physical splitting of the modes, so that the maximum for δm_z is mainly concentrated either in the top (EM2') or in the bottom edge (EM1'). As shown in Fig. 6.12 by the blow-up of EM1' and EM2' at $\vartheta = 0.9°$ and $H^{appl} = 3500$ Oe, for the interacting bar at saturation these two modes resemble EM1 and EM2. It is then appealing to consider EM1' and EM2' as a hybridization [211, 215] of the non-interacting bar modes due to the fact that (i) EM1 and EM2 are nearly degenerate in frequency and (ii) the asymmetry introduced by $\mathbf{H}_{stray}$ can determine the activation of EM1. Even though this is
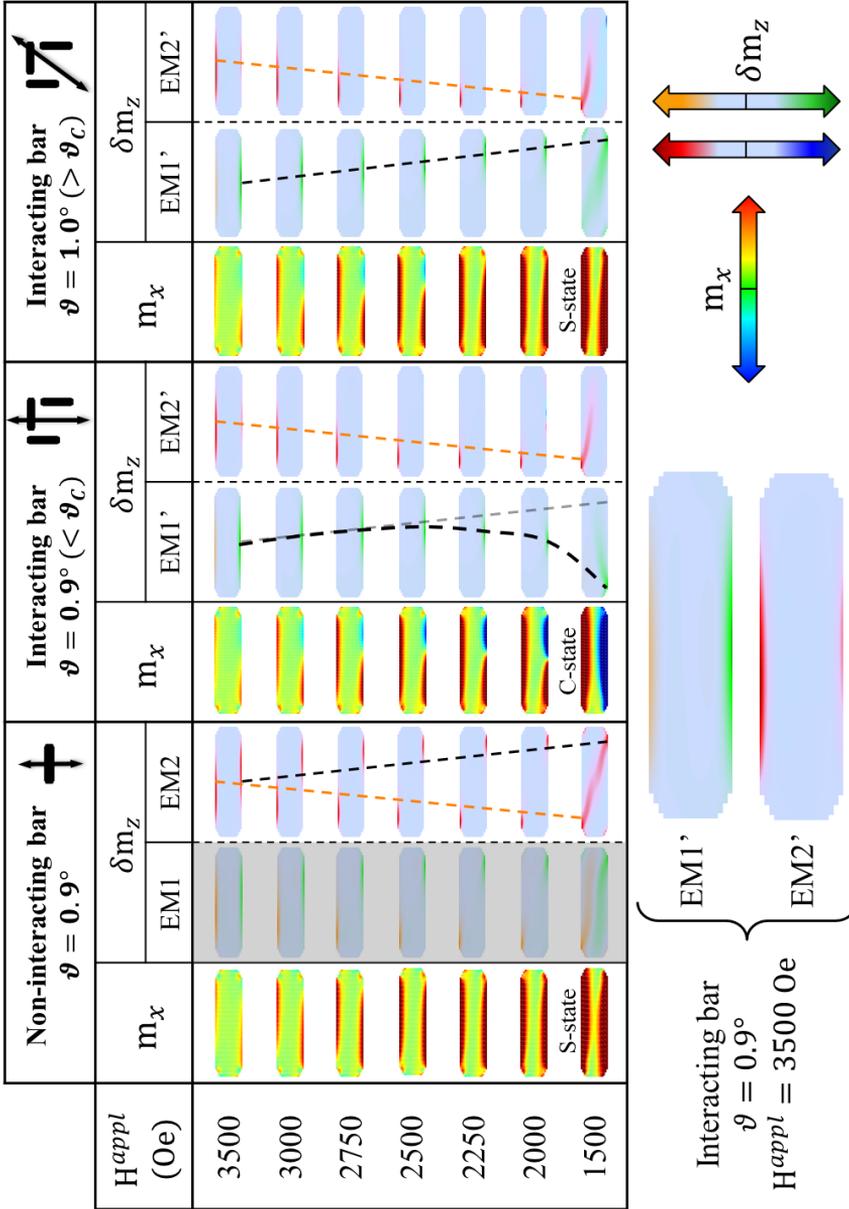
Figure 6.12: Summary of the DMM results for selected H^{appl} values. For each one of the three cases shown here, the first column contains the m_x color-maps, while the two following columns contain the δm_z mode profiles for the lowest frequency EMs. The dashed lines indicate the evolution of the edge mode localization. Two mode profiles (EM1' and EM2' for the interacting bar at $\vartheta = 0.9°$ and $H^{appl} = 3500$ Oe) have been enlarged for showing the similarities with EM1 and EM2 (non-interacting bar) at saturation. For the interacting bar case, the critical angle is $\vartheta_C = 0.94°$.
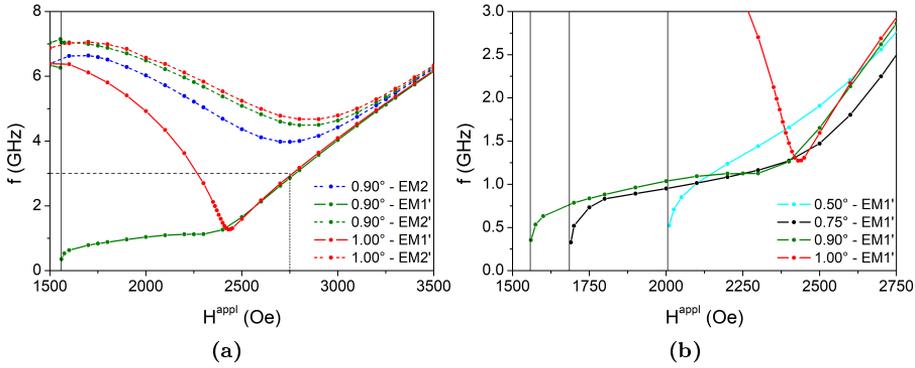
Figure 6.13: (a) Edge modes frequency evolution as a function of H^{appl} for the cases depicted in Fig. 6.12. (b) Blow-up of the region marked by black-dashed lines in (a). Two more angles have been added for showing the approach towards the critical angle. The black vertical lines in (b) correspond to 1560 Oe, 1690 Oe and 2010 Oe.

generally true for the interacting bar case, a difference in the orientation of the externally applied magnetic field leads to a different magnetization evolution. To better understand what is going on, let us focus on the top edge δm_z for the interacting bar case, essentially corresponding to the region where the EM2' mode is confined. The orange-dashed lines in Fig. 6.12 show how the EM2' localization changes as a function of H^{appl}. For both $\vartheta = 0.9°$ and $\vartheta = 1.0°$, EM2' gets more and more localized and moves towards the left-hand side of the bar as the $\mathbf{H}^{appl}$ magnitude is reduced. This is the same evolution undergone by the top-edge part of EM2 for the non-interacting bar case. A confirmation of this similarity can be found in Fig. 6.13a, which shows the edge modes frequency evolution as a function of H^{appl} for the cases depicted in Fig. 6.12. Indeed, the dashed curves are qualitatively associated to the same kind of frequency evolution. Both the green-dashed curve and the red-dashed curve (EM2' modes) go through a mode softening at 2800 Oe, resembling what happens for EM2 (blue-dashed line) and corresponding to the S-state nucleation. A different picture emerges by looking now at EM1' in Fig. 6.12 (as marked by black-dashed lines). This mode tends to be confined in the horizontal bar bottom edge and the existence of a critical angle translates into a variation in its spatial evolution. For $\vartheta = 1.0°$, EM1' progressively concentrates and moves towards the right-hand side of the bar, as happens for the bottom part of EM2. So, the combined field evolution of EM1' and EM2' mirrors the formation of a magnetic S-state. For $H^{appl} \gtrsim 2500$ Oe, this is the same behaviour characterizing EM1' for $\vartheta = 0.9°$, but, by further reducing the applied magnetic field, EM1' shifts towards the left-hand side of

the bar, finally indicating the formation of a magnetic C-state. The different end states obtained above and below the critical angle translate into a peculiar behaviour for the EM1' frequency evolutions, as shown by the solid lines in Fig. 6.13a. The green-solid EM1' curve (interacting bar for $\vartheta = 0.9°$) goes through a discontinuous transition at 1560 Oe, where the frequency approaches zero. As a consequence of this extreme softening, the magnetization oscillation associated to EM1' gets wider and wider (as confirmed by the above-mentioned Fourier analysis), giving rise to a major rearrangement of the magnetization configuration and then to the formation of the C-state. The red-solid curve (interacting bar for $\vartheta = 1.0°$) shows a similar behaviour down to ≈ 2500 Oe, but a substantial restoring force is recovered before reaching the complete softening and the frequency starts rising again (with no discontinuity). Phenomenologically speaking, the emerging picture seems to suggest the horizontal bar magnetization has to be "instructed" on the magnetization reversal path to pursue before overcoming the frequency turning point at ≈ 2500 Oe. The way we have to control this process is through the applied magnetic field orientation, since there is a critical angle separating the two paths. If we identify 2500 Oe as the field corresponding to the ultimate reversal path choice, form the simplistic argument developed in Sec. 6.3.2 and leading to Fig. 6.10, the obtained critical angle would be 1.8°, a value twice as big as the actual critical angle. Moreover, Fig. 6.13b shows a blow-up of the region marked by black-dashed lines in Fig. 6.13a. Two more angles have been added ($\vartheta = 0.5°$ and $\vartheta = 0.75°$) for better showing the approach towards the critical angle. By reducing the angle magnitude, the complete softening occurs at progressively growing H^{appl} values, indicating that the formation of the C-state is anticipated (when coming from saturation).

All this facts further confirm that the chirality of $\mathbf{H}^{ext}$ alone is not sufficient to justify the observed behaviour and the reversal path choice seems to have a dynamical origin. The overall picture emerged so far is quite complex and rather descriptive, but it can be summarized by the following list:

- for the non-interacting bar, EM1 is not active during the magnetization evolution, so we can focus on EM2. During the process, while decreasing the magnitude of $\mathbf{H}^{appl}$ from 3500 Oe to 2750 Oe, we see a decrease in the EM2 frequency, signature of the fact that this mode is getting soft. Since soft modes are characterized by wider oscillation amplitudes with respect to the other modes, they are more prone to influence changes in the magnetization configuration. Indeed, for the non-interacting bar, EM2 is strictly related to the formation of a magnetic S-state, which possesses the same symmetry properties [210];

- when asymmetric and inhomogeneous interactions are introduced, both EM1 and EM2 can in principle be excited. However, since they are almost degenerate in frequency at high H^{appl} values (see the blue curves in Fig. 6.11c), they can hybridize and give rise to different mode profiles. This seems to be the case for the interacting bar, where the EM1' and EM2' appear. These new modes resemble EM1 and EM2 at high fields (e.g. at 3500 Oe), but they get localized either in the top (EM2') or in the bottom edge (EM1') as H^{appl} decreases;

- by looking at the EM1' and EM2' spatial localization in Fig. 6.12 and at their frequency evolution in Fig. 6.13a, it is clear that the dynamics of the bottom and top edges become uncorrelated and, according to the value of ϑ, the bottom and top magnetization evolutions can proceed in different ways. When $\vartheta < \vartheta_C$, both EM1' and EM2' evolve towards the left-hand side of the horizontal bar, following the formation of a C-state. On the other hand, the evolution of these two modes for $\vartheta > \vartheta_C$ is similar to what happens to EM2 in the non-interacting bar, and the magnetization configuration ends up in an S-state. The existence of a critical angle results to be associated with the chirality of $\mathbf{H}^{ext}$, but the actual ϑ_C value seems to have a dynamical origin.

6.3.4 MFM measurements on the unit cell

As a last test on the role of asymmetric and inhomogeneous magnetostatic interactions in the magnetic vortex formation, we decided to fabricate (according to recipe A.2) a sample in which the interaction strength has been properly tuned by playing with the gap size g in between the Py nanostructures composing the unit cell. The first row of Fig. 6.14 shows SEM images of the fabricated nanostructures. We keep calling the target nanostructure as the "horizontal" bar even if it is now the vertical bar for representation purposes. On the same substrate, we placed both the asymmetric unit cell described along the previous sections and a "symmetric" unit cell, where the lateral bars are not displaced relative to one another. In both the cases, the size of the stadium-like nanostructures is still 710 nm × 180 nm × 25 nm, but the gap size has been modified from 110 nm to 75 nm, 150 nm, 225 nm and 300 nm. As a reference, a control isolated bar of the same size has been placed close to the unit cells to be measured. A saturating magnetic field (2000 Oe) has been applied to the sample at various angles ϑ, and the remanent magnetization configurations obtained by reducing the magnetic field to zero have been inspected by recording MFM images (to be interpreted
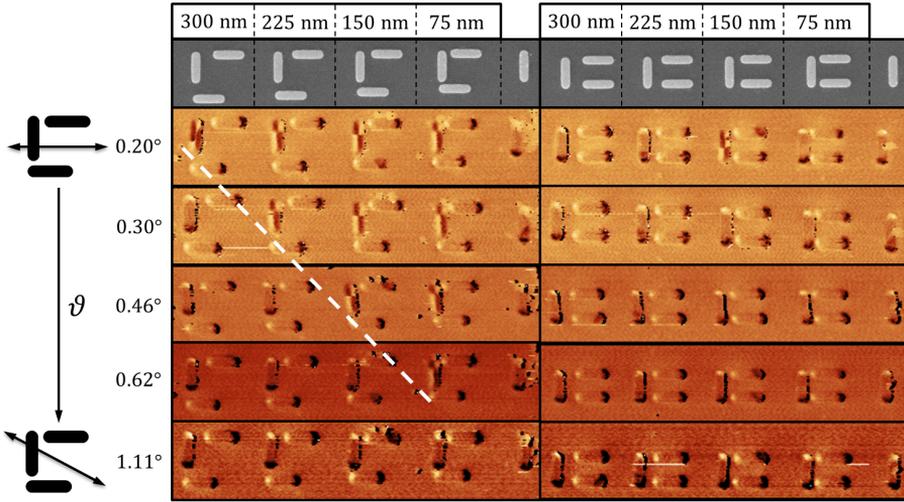
Figure 6.14: MFM measurements as a function of the gap size g and ϑ. The g values are reported in the upper part of the figure and allow identifying columns corresponding to different unit cells. On the other hand, the rows are defined on the basis of the applied magnetic field angle (ϑ). The white-dashed line separates the asymmetric unit cells where the magnetic vortex state can be observed from the ones corresponding to a QU magnetization state.

according to the images reported in the central inset of Fig. 6.5). The results of the MFM measurements as a function of ϑ are shown in Fig. 6.14. Considering the asymmetric unit cell (left-hand part of the figure), when $\vartheta = 0.20°$ all the horizontal bars show the formation of the magnetic vortex state, meaning that $\vartheta_C > 0.20°$ for all the fabricated unit cells. However, when $\vartheta = 0.30°$ the magnetic vortex state is still the remanent configuration for most of the unit cells, but not for the one corresponding to $g = 300$ nm. Then, if we focus on this unit cell ($g = 300$ nm), we can see that for $\vartheta \geq 0.30°$ there is no more evidence of the magnetic vortex state at remanence, being the measured state corresponding to a QU magnetization state. This fact indicates the presence of a critical angle $0.20° < \vartheta_C < 0.30°$ for the $g = 300$ nm unit cell. As marked by the white-dashed line in Fig. 6.14, the same behaviour can be found for all the other asymmetric unit cells, but the critical angle value results to depend on the gap size. On the contrary, neither the non-interacting control bar nor the symmetric unit cells show the formation of the magnetic vortex state at remanence. From these measurements, we can conclude that (i) the formation of the magnetic vortex state is linked to the asymmetry in the magnetostatic interaction due to the relative displacement of the lateral bars and (ii) the value of the critical angle increases as the gap size decreases (corresponding to a stronger interaction field).

6.4   Conclusions

A combination of MOKE measurements, MFM imaging and micromagnetic simulations has been used to investigate the role of asymmetric and spatially inhomogeneous magnetostatic interactions onto the magnetization reversal of elongated Permalloy nanostructures arranged in chiral unit cells. Despite we considered magnetic nanostructures where the magnetic vortex state cannot be induced at remanence by a uniform applied magnetic field because of the chosen geometry, two behaviours have been identified, separated by a critical angle characterizing the direction of the applied magnetic field. Below the critical angle, a magnetic vortex state can be found, at remanence, in the nanostructures whose major axis lies almost perpendicular to the applied magnetic field direction. On the other hand, above the critical angle, the remanent magnetic configuration is the QU magnetization state, as in the case of non-interacting nanostructures. From a different point of view, this study, by unveiling fundamental aspects of the interplay between magnetization dynamics and magnetostatic interactions, demonstrates that localized magnetic field sources can be used to actively induce and finely control the magnetization states and reversal paths of magnetic nanostructures, and that such localized field sources can be easily facilitated within the appropriate array structure.

Chapter 7

Conclusions and Outlook

The results contained in this thesis derive from the most relevant part of the work carried out during my Ph.D. project, so they basically represent the conclusions reached during a productive four-year period. Before summing them up, it is worth explicitly mentioning the most important result, since it is always there but quite hidden: the fact of having absorbed a methodology of work based on the scientific method. Besides the achievements, also the way they have been obtained contributes to build the Ph.D. student's background.

Back to the thesis, Chaps. 1, 2 and 3 collected the basic notions on magnetism needed for understanding the following chapters. In particular, Chap. 2 reported a detailed description of magneto-optical effects in matter and Chap. 3 showed how it is possible to fabricate magnetic nanostructures and then how their behaviour can be characterized.

In Chap. 4 we learnt how to consistently calculate the switching frequencies related to thermally-activated reversal processes in artificial spin ice systems, eventually designing a multiscale simulation scheme. The statistical analysis performed through micromagnetic simulations at finite temperature showed the need for reducing the energy barrier associated to the thermally-activated magnetization reversal with respect to the energy barrier that can be simply calculated by coherent magnetization reversal. This result finds a confirmation in literature, since the magnetization of the involved nanostructures has often to be artificially reduced in order to obtain calculations matching with the measured time scale. However, our analysis is still not complete, since the energy barrier reduction could depend on the considered nanostructure shape/material and the micromagnetic simulations we employed are confined to the high temperature regime, where the switching time is of the order of hundred of nanoseconds. For solving

this issue, we identified a different method (i.e. the string method), which directly calculates energy barrier values instead of relying on the statistical analysis of the switching events. The integration of the string method in our multiscale simulation scheme constitutes the outlook of this research line.

Chapter 5 described the development of a non-standard heating technique for artificial spin ice systems: the thermoplasmonic heating of magnetic nanostructures. Instead of using conventional heaters, the energy is delivered to the nanostructures by exploiting the light-matter interaction and the excitation of localized surface plasmon resonances. A careful choice of the materials and the elongated shape of the involved nanostructures allowed us to implement a selective heating method, since the deposited energy depends both on the radiation wavelength and on the polarization direction. This fact is of extremely interest when considering artificial spin ice systems, where the magnetic nanostructures are aligned along different axes. Moreover, a great advantage of working with light beams is the fact that the illuminated sample area can be controlled by simply focusing or defocusing the beam itself, so providing localized heating. Through the fabrication of nanostructure arrays of progressive complexity, we demonstrated the validity of our approach and we identified the key parameters to be considered for applying this technique to artificial spin ice systems, where the nanostructures are densely packed. Besides the experimental verification, we realized a thermoplasmonic heating stage to be combined with a MOKE setup, for the in-situ heating of samples while tracking the evolution of their magnetic properties. The next step will consist in making this heating stage more compact, in order to be fitted in a MFM setup for the direct imaging of the obtained magnetic configurations.

In the last chapter, Chap. 6, we further highlighted the fundamental role of magnetostatic interactions. Indeed, by subjecting a magnetic nanostructure to properly designed competing magnetostatic interactions (leading to asymmetric and inhomogeneous local magnetic fields), the magnetization reversal process can be tuned beyond geometry and material properties engineering. In other words, the combination of asymmetric and inhomogeneous magnetostatic interactions with a uniform applied magnetic field can induce a magnetic vortex state (metastable) into a magnetic nanostructure designed to behave as a magnetic needle, i.e. whose stable state is given by a quasi-uniform magnetization state. Moreover, the ability of reaching the magnetic vortex state was experimentally found to depend on the direction of the uniform applied magnetic field, so determining the appearance of a critical angle separating two regimes. The transition between these two regimes was investigated by means of the dynamical matrix

method, exploiting the fact that changes in the magnetization state can be inferred and identified by analyzing the frequency evolution and the symmetry of the magnetic normal modes during the magnetization reversal process. It turned out the two reversal mechanism characterizing the regimes are associated to well defined features in the frequency evolution as a function of the applied magnetic field magnitude, which we are planning to measure thanks to a ferromagnetic resonance setup based on a vector network analyzer.

Appendix A

Recipes for Nanofabrication

This appendix contains a list of useful nanofabrication recipes, most of them used for fabricating the samples related to this thesis. Each recipe (from the bare substrate to the final sample) is organized in sequential stages, which are summarized in Fig. A.1. When referring to *dry*, "to gently blow the sample surface with nitrogen" is meant. In the *EBL patterning* step, "base dose" means the suggested central value for performing a *dose test* on the given substrate, since the proper dose also depends on the structures to be patterned. Regarding the *material deposition* step, *e-beam evaporation* has been generally employed (PVD 75 by Kurt J. Lesker Company). Detailed information on the e-beam evaporation technique can be found in Ref. [216].

Abbreviation	*Full name / composition*
IPA	Isopropyl alcohol (2-Propanol)
PMMA	Polymethyl methacrylate
MIBK	Methyl isobutyl ketone
ZED-N50	n-Amyl acetate
ZDMAC	N,N-Dimethylacetamide
NMP	N-Methylpyrrolidone
ma-D 525	based on tetramethylammonium hydroxide
mr-Rem 400	based on N-Ethylpyrrolidone

Table A.1: List of abbreviations for chemical products.
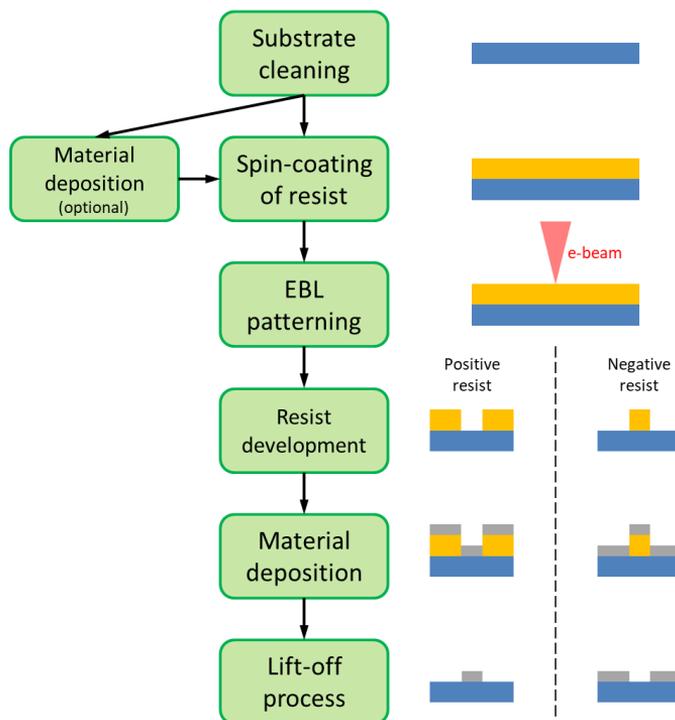
Figure A.1: Block diagram summarizing the nanofabrication fabrication workflow, starting from the bare substrate and arriving at the final sample.

A.1 Double-layer PMMA on silicon substrate

1. **Substrate cleaning**

    1.1 Ultrasonic bath in acetone for 5 min

    1.2 Ultrasonic bath in IPA for 5 min and dry

    1.3 Plasma ashing in oxygen atmosphere for 3 min

2. **Spin-coating of resist** (total estimated thickness of ≈ 150 nm)

    2.1 *PMMA 495K A2*: 60 s at 2000 rpm

    2.2 Hot plate baking for 5 min at 180 °C

    2.3 *PMMA 950K A2*: 60 s at 4000 rpm

    2.4 Hot plate baking for 5 min at 180 °C

3. **EBL patterning**

Accelerating voltage (kV)	Objective aperture (μm)	Base dose (μC $\cdot$ cm^{-2})
10	10	120

4. **Resist development**

    4.1 Dip in MIBK/IPA 1:3 for 40 s

    4.2 Dip in IPA for 20 s and dry

5. **Material deposition**

6. **Lift-off process**

    6.1 Dip in acetone (overnight if needed)

    6.2 Dip in IPA for washing and dry

A.2   ZEP on silicon substrate

1. **Substrate cleaning**

    1.1 Ultrasonic bath in acetone for 5 min

    1.2 Ultrasonic bath in IPA for 5 min and dry

    1.3 Plasma ashing in oxygen atmosphere for 3 min

2. **Spin-coating of resist** (total estimated thickness of $\approx$ 240 nm)

    2.1 *ZEP520A-7*: 60 s at 6000 rpm

    2.2 Hot plate baking for 5 min at 180 °C

3. **EBL patterning**

Accelerating voltage (kV)	Objective aperture (μm)	Base dose (μC $\cdot$ cm^{-2})
20	10	108

4. **Resist development**

    4.1 Dip in ZED-N50 for 30 s

    4.2 Dip in IPA for 30 s and dry

5. **Material deposition**

6. **Lift-off process**

   6.1 Dip in ZDMAC or NMP (overnight if needed)

   6.2 Dip in acetone for washing

   6.3 Dip in IPA for washing and dry

A.3   ZEP on glass substrate

1. **Substrate cleaning**

   1.1 Ultrasonic bath in acetone for 5 min

   1.2 Ultrasonic bath in IPA for 5 min and dry

   1.3 Plasma ashing in oxygen atmosphere for 3 min

2. **Material deposition**

   2.1 Deposit a thin titanium film ($\approx$ 4 nm)

3. **Spin-coating of resist** (total estimated thickness of $\approx$ 240 nm)

   3.1 *ZEP520A-7*: 60 s at 6000 rpm

   3.2 Remove part of the resist with acetone in order to create a conductive path to ground (not needed, but suggested)

   3.3 Hot plate baking for 5 min at 180 °C

4. **EBL patterning**

Accelerating voltage (kV)	Objective aperture (μm)	Base dose ($\mu C \cdot cm^{-2}$)
20	10	108

5. **Resist development**

   5.1 Dip in ZED-N50 for 30 s

   5.2 Dip in IPA for 30 s and dry

6. **Material deposition**

7. **Lift-off process**

   7.1 Dip in ZDMAC or NMP (overnight if needed)

   7.2 Dip in acetone for washing

   7.3 Dip in IPA for washing and dry
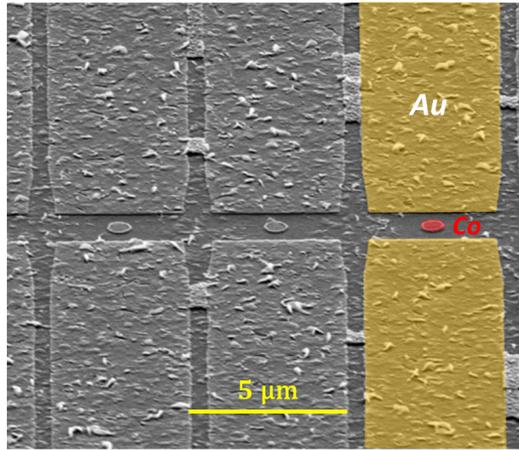
Figure A.2: SEM image of cobalt nanostructures (of 1 μm diameter) placed in the 2 μm wide gap of gold dipolar antennas (of 4 μm width).

A.4   Recipe for negative resist

Negative resists are extremely useful when the designed structures have to be obtained by etching, i.e. the removal of previously deposited material. The following recipe describes the fabrication of an actual sample, since the development of a general and reproducible recipe for negative EBL is still in progress. The chosen negative e-beam resist for this application has been the ma-N 2403 [217]. In this sample, circular cobalt nanostructures have been fabricated starting from a continuous cobalt film deposited on a glass substrate and, subsequently, gold dipolar antennas have been patterned around them. Figure A.2 shows a SEM image of the resulting device. The small residues visible on the image reflects the fact that the recipe is not fully optimized yet.

1. **Substrate cleaning**

   1.1 Ultrasonic bath in acetone for 5 min

   1.2 Ultrasonic bath in IPA for 5 min and dry

   1.3 Plasma ashing in oxygen atmosphere for 3 min

2. **Material deposition**

   2.1 Deposit a cobalt film (10 nm thick)

3. **Spin-coating of negative resist** (total estimated thickness of $\approx$ 320 nm)

   3.1 *ma-N 2403*: 60 s at 3000 rpm

    3.2 Remove part of the resist with acetone in order to create a conductive path to ground

    3.3 Hot plate baking for 60 s at 90 °C

4. **EBL patterning** for cobalt nanostructures and alignment markers

Accelerating voltage (kV)	Objective aperture (μm)	Dose ($\mu C \cdot cm^{-2}$)
20	10	25

5. **Negative resist development**

    5.1 Dip in ma-D 525 for 50 s

    5.2 Dip in distilled water for 30 s and dry

6. **Physical etching**

    6.1 Argon ion milling for 200 s at 15 rpm

Material	Ar flow (sccm)	Beam voltage / current (V / mA)	Acc. voltage (V)	Milling rate ($\text{Å} \cdot s^{-1}$)
Co	15	300 / 80	100	1

7. **Lift-off process**

    7.1 Dip in mr-Rem 400 (overnight)

    7.2 Ultrasonic bath in mr-Rem 400 for 2 min

    7.3 Dip in acetone for washing

    7.4 Dip in IPA for washing and dry

8. **Spin-coating of positive resist** (total estimated thickness of ≈ 240 nm)

    8.1 *ZEP520A-7*: 60 s at 6000 rpm

    8.2 Hot plate baking for 5 min at 180 °C

9. **Material deposition**

    9.1 Deposit a thin gold film (≈ 2.5 nm) in order to create a conductive path to ground

10. **EBL patterning** for gold antennas

Accelerating voltage (kV)	Objective aperture (μm)	Dose (μC · cm⁻2)
20	10	108

11. **Chemical etching** for removing gold

    11.1 Dip in gold etchant (nickel compatible) for 5 s

    11.2 Dip (sequentially) in two different beakers containing distilled water (few seconds each) and dry

12. **Positive resist development**

    12.1 Dip in ZED-N50 for 30 s

    12.2 Dip in IPA for 30 s and dry

13. **Material deposition**

    13.1 Deposit a thin titanium film ($\approx$ 2.5 nm) as an adhesion layer

    13.2 Deposit gold (150 nm thick)

14. **Lift-off process**

    14.1 Dip in ZDMAC or NMP (overnight if needed)

    14.2 Dip in acetone for washing

    14.3 Dip in IPA for washing and dry

Appendix B

Matrix Representation of Polarization

B.1   Jones calculus

An electromagnetic wave whose electric field vector variates temporally and spatially in a regular manner rather than with random oscillations in direction and amplitude is said to be a *polarized* wave [62, 218].

For a polarized plane harmonic wave with wavenumber k and angular frequency ω travelling along the z-axis, a general way of expressing the electric field vector $\mathbf{E}$ is, in terms of the unit vectors $\hat{\mathbf{x}}$ and $\hat{\mathbf{y}}$,

$$\mathbf{E} = \hat{\mathbf{x}}\mathrm{E}_x + \hat{\mathbf{y}}\mathrm{E}_y, \tag{B.1}$$

where

$$\mathrm{E}_x = \mathrm{E}_{0x}\mathrm{e}^{i(kz-\omega t+\phi_x)}, \tag{B.2a}$$

$$\mathrm{E}_y = \mathrm{E}_{0y}\mathrm{e}^{i(kz-\omega t+\phi_y)}. \tag{B.2b}$$

The parameters E_{0x} and E_{0y} are real quantities representing the projections of the electric field vector along the coordinate axes, whereas ϕ_x and ϕ_y represent the initial phases of the two components. Equation (B.1) can also be written as

$$\mathbf{E} = \left[\hat{\mathbf{x}}\mathrm{E}_{0x} + \hat{\mathbf{y}}\mathrm{E}_{0y}\mathrm{e}^{i(\phi_y-\phi_x)}\right]\mathrm{e}^{i(kz-\omega t+\phi_x)} = \tilde{\mathbf{E}}_{\mathbf{0}}\mathrm{e}^{i(kz-\omega t+\phi_x)}. \tag{B.3}$$

The bracketed quantity represents the complex vector amplitude $\tilde{\mathbf{E}}_{\mathbf{0}}$ for the po-

larized wave. Since the state of polarization is completely determined by the relative amplitude and phase between the components of the electric field vector, it can be described by $\tilde{\mathbf{E}}_0$, which can be expressed as a two-element matrix called *Jones vector*:

$$\tilde{\mathbf{E}}_0 \;=\; \begin{pmatrix} \tilde{E}_{0x} \\ \tilde{E}_{0y} \end{pmatrix} \;=\; \begin{pmatrix} E_{0x} \\ E_{0y}e^{i\delta} \end{pmatrix}, \tag{B.4}$$

where $\delta = \phi_y - \phi_x$ is the relative phase between the components. The normalized form of the Jones vector is obtained by dividing by the norm of the vector, namely $\left|\tilde{\mathbf{E}}_0\right| = \sqrt{E_{0x}^2 + E_{0y}^2}$. Any information on light intensity is lost by using normalized Jones vectors. In general, Eq. (B.4) represents an elliptically polarized wave: at a given position in space, the electric field vector describes an ellipse, whose major axis is inclined at an angle ϑ with respect to the x-axis given by

$$\tan 2\vartheta \;=\; \frac{2E_{0x}E_{0y}\cos\delta}{E_{0x}^2 \;-\; E_{0y}^2}. \tag{B.5}$$

When viewed against the direction of propagation, if $0 < \delta < \pi$ the electric field vector rotates counter-clockwise, whereas if $-\pi < \delta < 0$ the electric field vector rotates clockwise; these modes are called *left* elliptical polarization and *right* elliptical polarization, respectively.

Two special cases are of particular importance, namely when the polarization ellipse degenerates into a straight line or a circle. In the case of *linearly* polarized light ($\delta = 0, \pm\pi$), the electric field vector oscillates along a constant direction. The normalized Jones vector representing this state takes the form

$$\frac{1}{\sqrt{E_{0x}^2 + E_{0y}^2}} \begin{pmatrix} E_{0x} \\ E_{0y} \end{pmatrix} \;=\; \begin{pmatrix} \cos\vartheta \\ \sin\vartheta \end{pmatrix}, \tag{B.6}$$

where ϑ (given by $\tan\vartheta = E_{0y}/E_{0x}$) is the angle between the direction of polarization and the x-axis. When $E_{0x} = E_{0y}$ and $\delta = \pm\pi/2$, the light is said to be *circularly* polarized and the normalized Jones vectors are given by

$$\frac{1}{\sqrt{2}} \begin{pmatrix} 1 \\ i \end{pmatrix} \qquad left \text{ circularly polarized,} \tag{B.7a}$$

$$\frac{1}{\sqrt{2}} \begin{pmatrix} 1 \\ -i \end{pmatrix} \qquad right \text{ circularly polarized.} \tag{B.7b}$$

One of the application of the Jones notation is calculating the result of adding two or more waves with given polarization: the result is obtained simply by adding

the Jones vectors. Through this property, light of arbitrary polarization can be resolved into *orthogonal* components. Two waves whose states of polarization are represented by the complex vector amplitudes $\tilde{\mathbf{E}}_1$ and $\tilde{\mathbf{E}}_2$ are orthogonally polarized if

$$\tilde{\mathbf{E}}_1^\dagger \tilde{\mathbf{E}}_2 \;=\; 0, \tag{B.8}$$

where the dagger denotes the Hermitian conjugate. For linearly polarized light, orthogonality merely means that the electric field vectors are polarized at right angles to one another. In the case of circular polarization, it can be seen that right circular and left circular polarizations are mutually orthogonal states. Thus, resolution into linear components is written (for $A, B \in \mathbb{C}$)

$$\begin{pmatrix} A \\ B \end{pmatrix} \;=\; A \begin{pmatrix} 1 \\ 0 \end{pmatrix} \;+\; B \begin{pmatrix} 0 \\ 1 \end{pmatrix} \tag{B.9}$$

and into circular components is written

$$\begin{pmatrix} A \\ B \end{pmatrix} \;=\; \frac{1}{2} \left(A - iB \right) \begin{pmatrix} 1 \\ i \end{pmatrix} \;+\; \frac{1}{2} \left(A + iB \right) \begin{pmatrix} 1 \\ -i \end{pmatrix}. \tag{B.10}$$

Another use of the matrix notation is that of computing the effect of inserting a train of linear optical elements into a beam of light of given polarization. The optical elements are represented by $2{\times}2$ matrices called *Jones matrices*. If $\tilde{\mathbf{E}}_0$ is the Jones vector of the light incident on an optical train composed by n linear optical elements, the emerging light is characterized by a Jones vector $\tilde{\mathbf{E}}_0'$ given by

$$\tilde{\mathbf{E}}_0' \;=\; \mathfrak{J}_n \cdots \mathfrak{J}_2 \mathfrak{J}_1 \tilde{\mathbf{E}}_0, \tag{B.11}$$

where $\mathfrak{J}_j$ is the $2{\times}2$ Jones matrix of the j-th optical element.

The optical elements that are of interest in MOKE microscopy are the *linear polarizer* and the *linear retarder* [219]. A linear polarizer is a device which modifies any polarization state to the state of linear polarization. The transmitted wave is linearly polarized in the direction of the polarization axis of the polarizer. If ψ is the angle between the polarization axis and the x-axis, the Jones matrix $\mathfrak{J}_{LP}$ of a linear polarizer is expressed by

$$\mathfrak{J}_{LP}\left(\psi \right) \;=\; \begin{bmatrix} \cos^2 \psi & \cos \psi \sin \psi \\ \cos \psi \sin \psi & \sin^2 \psi \end{bmatrix}. \tag{B.12}$$

The action of a linear retarder is to introduce a phase shift ϕ between linearly polarized waves with orientations along two orthogonal directions determined by

the physical structure of the retarder and called fast and slow axes. If α represents the angle between the fast axis and the y-axis and the phase introduced on the fast axis advances the slow axis one by ϕ, the Jones matrix $\mathfrak{J}_{LR}$ of a linear retarder is

$$\mathfrak{J}_{LR}\left(\phi;\alpha\right) \;=\; e^{i\frac{\phi}{2}} \begin{bmatrix} \cos\left(\frac{\phi}{2}\right) - i\sin\left(\frac{\phi}{2}\right)\cos 2\alpha & -i\sin\left(\frac{\phi}{2}\right)\sin 2\alpha \\ -i\sin\left(\frac{\phi}{2}\right)\sin 2\alpha & \cos\left(\frac{\phi}{2}\right) + i\sin\left(\frac{\phi}{2}\right)\cos 2\alpha \end{bmatrix}.$$

Choosing $\alpha = 0$, a linear retarder with the fast axis parallel to the y-axis can be obtained, whose Jones matrix is given by

$$\mathfrak{J}_{LR}\left(\phi;0\right) \;=\; \begin{bmatrix} 1 & 0 \\ 0 & e^{i\phi} \end{bmatrix}, \tag{B.13}$$

whereas considering $\phi = \pm\pi/2$ a *quarter-wave plate* can be obtained, a device that allows to produce circularly polarized light starting from linearly polarized light. A phase shift of $\phi = \pm\pi$ determines a *half-wave plate*, an optical element that can change the polarization direction for a linearly polarized wave passing through it. Considering the normalized Jones vector expressed by (B.6) and characterizing an arbitrary linear polarization state, the effect of $\mathfrak{J}_{LR}\left(\pi;\alpha\right)$ on it is given by

$$\mathfrak{J}_{LR}\left(\pi;\alpha\right) \begin{pmatrix} \cos\vartheta \\ \sin\vartheta \end{pmatrix} \;=\; \begin{pmatrix} \cos\left(2\alpha - \vartheta\right) \\ \sin\left(2\alpha - \vartheta\right) \end{pmatrix}. \tag{B.14}$$

Since the angle between the initial and the final linear polarization states is $2\alpha - 2\vartheta$, the choice $\alpha - \vartheta = 45°$ determines a rotation of the polarization axis by $90°$.

B.2   Rotation and ellipticity

A general elliptical polarization state as expressed by Eq. (B.4) can also be described in terms of two angles related to the ellipse itself, as shown in Fig. B.1:

- the *rotation* is the angle ϑ between the major axis and the x-axis (see Eq. (B.5));

- the *ellipticity* is the angle ε whose tangent expresses the ratio between the minor and the major axis.

In order to show how to extract these parameters from magneto-optical measurements, let's express Eq. (B.4) in a slightly different way, having in mind that
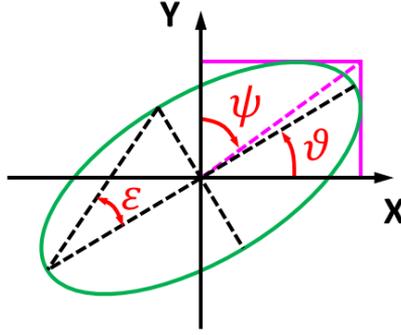
Figure B.1: Ellipse swept by the electric field vector at a given position in space in case of a general elliptical state of polarization. The angle ϑ represents the rotation of the ellipse, while the angle ε is its ellipticity.

a factor common to both the components of a Jones vector does not alter the polarization state and can be neglected:

$$
\begin{pmatrix} \mathrm{E}_{0x} \\ \mathrm{E}_{0y}\mathrm{e}^{i\delta} \end{pmatrix} \propto \begin{pmatrix} 1 \\ \dfrac{\mathrm{E}_{0y}}{\mathrm{E}_{0x}}\mathrm{e}^{i\delta} \end{pmatrix} \equiv \begin{pmatrix} 1 \\ x+iy \end{pmatrix} = \begin{pmatrix} 1 \\ \tan(z) \end{pmatrix} \propto \begin{pmatrix} \cos(z) \\ \sin(z) \end{pmatrix}, \quad \text{(B.15)}
$$

where z is a proper complex number ($z \in \mathbb{C}$). The equality in Eq. (B.15) states that, given an arbitrary complex number $x+iy$ ($x, y \in \mathbb{R}$), it is always possible to find $z \in \mathbb{C}$ such that $x+iy = \tan(z)$. This is true since the image of the complex tangent function is $\mathbb{C} \setminus \{\pm i\}$ and the two excluded values ($\pm i$) correspond to left and right circular polarization, respectively (which are trivial cases). According to the definition of complex sine and cosine functions, it can be seen that

$$
\begin{pmatrix} \cos(z) \\ \sin(z) \end{pmatrix} = \begin{bmatrix} \cos\left[\Re(z)\right] & -\sin\left[\Re(z)\right] \\ \sin\left[\Re(z)\right] & \cos\left[\Re(z)\right] \end{bmatrix} \begin{pmatrix} \cosh\left[\Im(z)\right] \\ i \ \sinh\left[\Im(z)\right] \end{pmatrix}, \quad \text{(B.16)}
$$

where the matrix corresponds to a 2-dimensional rotation matrix of angle $\Re(z)$ and the vector acted on by the matrix represents an ellipse aligned with the coordinate axes, highlighting the fact that

$$
\vartheta = \Re\left[\arctan(x+iy)\right], \quad \text{(B.17a)}
$$

$$
\tan(\varepsilon) = \tanh\{\Im\left[\arctan(x+iy)\right]\}. \quad \text{(B.17b)}
$$

When both rotation and ellipticity are small ($\vartheta, \varepsilon \ll 1$), as in the case of magneto-optical effects, $\arctan(x+iy)$ can be expanded in a Taylor series and the leading

terms give

$$\vartheta \; = \; \Re(z) \; \approx \; x, \tag{B.18a}$$

$$\varepsilon \; \approx \; \Im(z) \; \approx \; y. \tag{B.18b}$$

These results have been validated by means of the analytic formulas provided in Ref. [219] for the ellipsometric angles:

$$\vartheta \; = \; \frac{\pi}{2} \; - \; \frac{1}{2} \arctan\left(\tan 2\psi \cos\delta\right), \tag{B.19a}$$

$$\varepsilon \; = \; \frac{1}{2} \arcsin\left(\sin 2\psi \sin\delta\right), \tag{B.19b}$$

where $\tan\psi = \mathrm{E}_{0x}/\mathrm{E}_{0y}$ (see Fig. B.1).

Appendix C

Micromagnetics on a Regular Lattice

The LLG equation (1.48) is a partial differential equation relating time and spatial partial derivatives. The two most spread micromagnetic simulation softwares (*OOMMF* [179] and *mumax*³ [25]) solve it by means of the *finite difference method* (FDM), in which ratios between finite differences approximate derivatives [220]. The FDM needs the space to be discretized according to a regular lattice (i.e. to be *meshed*) in order to perform the above mentioned differences in a consistent way. Since all the terms composing the LLG equation involve the normalized magnetization $\mathbf{m}(\mathbf{r}) = \mathbf{M}(\mathbf{r})/\mathrm{M}_S$, particular care has to be taken when meshing magnetic bodies. The most usual choice is to consider cubic cells (or square-base prisms) where the side is shorter than the exchange length (see Eq. (1.43)) in order to consider an ensemble of uniformly magnetized entities. Hence, this condition allows substituting each cell with a macrospin $\mathbf{m}_i$ placed at the center of the corresponding cell. To work within this framework, all the micromagnetic energies in Eq. (1.31) have to be expressed in a discrete form, substituting integrals with sums. Since the discrete form of the magnetocrystalline anisotropy energy depends on the kind of anisotropy to be considered and it is not needed in this thesis, it will not be mentioned here.

C.1   Micromagnetic energies

Let us consider a magnetic structure meshed in N cells, each of which of height t and with a square base of side d, so corresponding to a volume $\mathcal{V} = d^2 t$.

The Zeeman energy E_Z is given by

$$E_Z \;=\; -\mu_0 \mathrm{M}_S \mathcal{V} \sum_{j=1}^{N} \mathbf{H}_j \cdot \mathbf{m}_j, \tag{C.1}$$

where M_S is the saturation magnetization and $\mathbf{H}_j$ is the external magnetic field applied to the j-th cell. The exchange energy E_{ex} is given by [25]

$$E_{ex} \;=\; \frac{A\mathcal{V}}{d^2} \sum_{j=1}^{N} \sum_{n}^{n.n.} \left(1 - \mathbf{m}_j \cdot \mathbf{m}_n\right), \tag{C.2}$$

where A is the exchange stiffness and $n.n.$ represents the nearest-neighbours to be considered in the sum (usually six, i.e. two for each Cartesian axis). The magnetostatic energy E_{ms} is given by

$$E_{ms} \;=\; \frac{\mu_0 \mathrm{M}_S^2 \mathcal{V}}{2} \sum_{i=1}^{N} \sum_{j=1}^{N} \mathbf{m}_i \cdot \mathfrak{N}_{ij} \cdot \mathbf{m}_j, \tag{C.3}$$

where $\mathfrak{N}_{ij}$ is a tensor expressing the demagnetizing effect of the j-th cell on the i-th cell. Considering that the interaction energy between magnetic moments is of the form (4.1), the tensor $\mathfrak{N}_{ij}$ is given by

$$\mathfrak{N}_{ij} = \begin{cases} \dfrac{3\mathcal{V}}{4\pi \mathrm{r}_{ij}^3} \begin{bmatrix} \dfrac{1}{3} - \left(\hat{\mathrm{r}}_{ij}^x\right)^2 & -\left(\hat{\mathrm{r}}_{ij}^x\right)\left(\hat{\mathrm{r}}_{ij}^y\right) & -\left(\hat{\mathrm{r}}_{ij}^x\right)\left(\hat{\mathrm{r}}_{ij}^z\right) \\ -\left(\hat{\mathrm{r}}_{ij}^y\right)\left(\hat{\mathrm{r}}_{ij}^x\right) & \dfrac{1}{3} - \left(\hat{\mathrm{r}}_{ij}^y\right)^2 & -\left(\hat{\mathrm{r}}_{ij}^y\right)\left(\hat{\mathrm{r}}_{ij}^z\right) \\ -\left(\hat{\mathrm{r}}_{ij}^z\right)\left(\hat{\mathrm{r}}_{ij}^x\right) & -\left(\hat{\mathrm{r}}_{ij}^z\right)\left(\hat{\mathrm{r}}_{ij}^y\right) & \dfrac{1}{3} - \left(\hat{\mathrm{r}}_{ij}^z\right)^2 \end{bmatrix} & \text{for } i \neq j \\[6pt] 2 \begin{bmatrix} \dfrac{1}{3} & 0 & 0 \\ 0 & \dfrac{1}{3} & 0 \\ 0 & 0 & \dfrac{1}{3} \end{bmatrix} & \text{for } i = j \end{cases} , \tag{C.4}$$

where $\mathbf{r}_{ij}$ is the distance between $\mathbf{m}_i$ and $\mathbf{m}_j$. However, this approach does not take into account the fact that the magnetostatic interaction acts between magnetized cells and not between macrospins. This limitation can be overcome by following the approach developed by Newell at al. [162], where the finite size of the cells is actually considered in the calculation of $\mathfrak{N}_{ij}$.
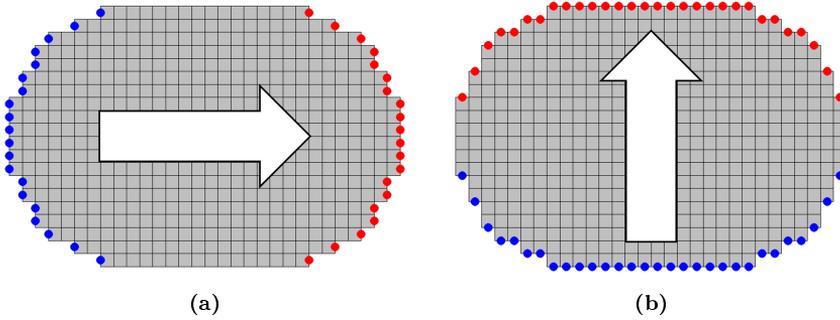
Figure C.1: (a) Net magnetic charge (positive in red and negative in blue) appearing at the opposite ends of a meshed nanostructure uniformly magnetized along its major axis. (b) Net magnetic charge (positive in red and negative in blue) appearing at the opposite ends of a meshed nanostructure uniformly magnetized along its minor axis.

C.2 Interaction energy in case of uniform magnetization

Equation (C.3) is quite general and it can also be used when the various $\mathbf{m}_j$ belong to different structures, in order to evaluate their interaction energy. In fact, the quantity $\mathfrak{N}_{ij} \cdot \mathrm{M}_S \mathbf{m}_j$ is the magnetic field produced by the magnetic moment $\mathrm{M}_S \mathbf{m}_j$ in the i-th site, and $\mu_0 \mathrm{M}_S^2 \mathcal{V} \mathbf{m}_i \cdot \mathfrak{N}_{ij} \cdot \mathbf{m}_j$ is the corresponding Zeeman energy. However, in case of uniformly magnetized bodies, an alternative and faster method can be envisaged. Figure C.1 shows two slices of a meshed magnetic nanostructure considered to be uniformly magnetized (either along its major axis or along its minor axis). According to Eq. (1.45a), the magnetic charge inside the volume is zero, but a net charge appears at the opposite nanostructure's ends. Each one of the border cells has a lateral surface (perpendicular to the depicted slices) of area td, where t is the height of the cell and d its side. Hence, a magnetic charge $(q_m)_j$ (represented by the filled dots in Fig. C.1) can be associated to the center of each j-th border cell surface:

$$(q_m)_j \;=\; td\mathrm{M}_S \hat{\mathbf{n}} \cdot \mathbf{m}_j \;=\; \pm td\mathrm{M}_S, \tag{C.5}$$

where where $\hat{\mathbf{n}}$ is the outward-pointing surface normal. Now, for obtaining the interaction energy E_{int} between multiple nanostructures, it is enough to evaluate the interaction energy between all the surface magnetic charges, instead of

considering the interaction energy between all the cells according to Eq. (C.3):

$$E_{int} \; = \; \frac{\mu_0}{8\pi} \sum_{i \neq j} \frac{(q_m)_i (q_m)_j}{\mathbf{r}_{ij}}, \tag{C.6}$$

where $\mathbf{r}_{ij}$ is the distance between the i-th and the j-th magnetic charges. For the geometrical arrangements (vertices) analyzed in this thesis, the energies so calculated differ by less than 0.01 % with respect to the same evaluations performed by *OOMMF* [179].

Appendix D

The Kinetic Monte Carlo Method

The *kinetic* (or *continuous-time*) *Monte Carlo* (kMC) method is a Monte Carlo algorithm allowing for the simulation of dynamical phenomena [29, 165–167]. Through this method, both the equilibrium expectation values and their time evolution during a thermalization process can be retrieved. Indeed, the kMC method provides a numerical solution to the *master equation*, which is a system of linear differential equations describing the evolution of the probabilities for Markov processes in systems that jump from one state to another in continuous time [29].

To clarify these concepts, we can consider a generic system characterized by two states (A, C) with energies E_A and E_C separated by two energy barriers E_B and E_D, as depicted in Fig. D.1a. In this case, the stochastic process of interest involves the transition between the A state and the C state, as indicated by the coloured arrows in Fig. D.1a. We are considering two energy barriers separating the equilibrium states in order to resemble what occurs in our DVA. For this system, the probabilities $P_A(t)$ and $P_C(t)$ of being in state A or C, respectively, are given by the following master equation:

$$\begin{cases} \dot{P}_A = -\nu_{CA}P_A + \nu_{AC}P_C \\ \dot{P}_C = \nu_{CA}P_A - \nu_{AC}P_C \end{cases} , \qquad (D.1)$$

where $\nu_{ji}dt$ represents the probability of having a transition $i \to j$ in the time interval $[t, t+dt)$. In order to combine the two transitions (i.e. from i to j through either the B state or the D state, with $i = A, C$ and $j = C, A$, respectively) into a

(a)   **(b)**
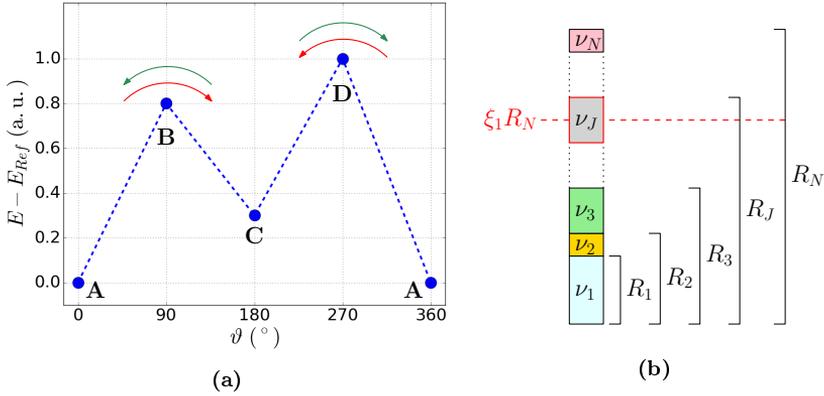
Figure D.1: (a) Generic energy landscape representing transitions between A and C states over the E_B and E_D energy barriers. The coloured arrows highlight the four possible transitions. (b) Schematic representation of the kMC algorithm steps 2 and 3. The key quantities here depicted are the sequences R_j ($j = 1, \ldots, N$) of the partial sums of the switching frequencies and the uniform random number $\xi_1 \in [0, 1)$.

unique switching frequency, we consider them as independent, parallel transition channels, hence summing their corresponding switching frequencies:

$$\nu_{ji} = \nu(i \to B \to j) + \nu(i \to D \to j). \tag{D.2}$$

The solution to the linear system (D.1) is given by Eq. (1.57):

$$P_A(t) = \frac{\nu_{AC}}{\nu_{MEq}} + \left[P_A(0) - \frac{\nu_{AC}}{\nu_{MEq}} \right] \exp\left(-\nu_{MEq} t\right), \tag{D.3}$$

where $\nu_{MEq} = \nu_{CA} + \nu_{AC}$ and $P_A(t) + P_C(t) = 1 \; \forall t$. So, the equilibrium probabilities can be obtained by setting $t \to \infty$:

$$\begin{cases} P_A(t \to \infty) = \dfrac{\nu_{AC}}{\nu_{MEq}} \\ P_C(t \to \infty) = \dfrac{\nu_{CA}}{\nu_{MEq}} \end{cases} . \tag{D.4}$$

Alternatively, the equilibrium probabilities can be retrieved by extracting the eigenvector corresponding to the zero eigenvalue of the coefficient matrix associated to Eq. (D.1), a useful method for more complicated situations. From Eq. (D.4), it is possible to see that a proper definition of the switching frequencies is mandatory in order to get the physically correct probabilities for the equilibrium state (i.e. the values predicted by equilibrium statistical mechanics). This condition is usually referred to as *detailed balance criterion* and expressed by setting

the time derivatives in Eq. (D.1) equal to zero [165]:

$$\nu_{CA} P_A \;=\; \nu_{AC} P_C. \tag{D.5}$$

In dealing with switching frequencies in form of the Néel–Arrhenius equation (1.56), the detailed balanced criterion is satisfied for the case depicted in Fig. D.1a, and the Boltzmann distribution is retrieved at equilibrium:

$$\begin{cases} \nu_{AC} \;=\; \nu_0 \left[\exp\left(-\dfrac{E_B}{k_B T} \right) \;+\; \exp\left(-\dfrac{E_D}{k_B T} \right) \right] \exp\left(\dfrac{E_C}{k_B T} \right) \\[4mm] \nu_{CA} \;=\; \nu_0 \left[\exp\left(-\dfrac{E_B}{k_B T} \right) \;+\; \exp\left(-\dfrac{E_D}{k_B T} \right) \right] \exp\left(\dfrac{E_A}{k_B T} \right) \end{cases}$$

$$\Downarrow$$

$$\begin{cases} P_A(t \to \infty) \;=\; \dfrac{\exp\left(-\dfrac{E_A}{k_B T} \right)}{\exp\left(-\dfrac{E_A}{k_B T} \right) \;+\; \exp\left(-\dfrac{E_C}{k_B T} \right)} \\[6mm] P_C(t \to \infty) \;=\; \dfrac{\exp\left(-\dfrac{E_C}{k_B T} \right)}{\exp\left(-\dfrac{E_A}{k_B T} \right) \;+\; \exp\left(-\dfrac{E_C}{k_B T} \right)} \end{cases} \tag{D.6}$$

where we made use of Eqs. (D.2) and (D.4).

All these considerations can be mode more general, in order to be extended to any kind of systems described by Markov processes [29, 165]. In particular, we can apply the master equation approach to square ASI systems, where a state consists in specifying the direction of the magnetization in *every* nanostructure composing the array. For a square system formed by $n \times n$ vertices, the number of involved nanostructures[1] N is given by $N = 2n(n + 1)$ and the number of states m is $m = 2^N$. This implies that the corresponding master equation would involve a huge number of terms, even for relatively small arrays ($n = 3 \Rightarrow m = 2^{24} \approx 16.8 \cdot 10^6$). Anyway, under the approximations characterizing the DVA, the Markov process consists in the single flip of a selected nanostructure and, since we are only considering interactions with respect to first and second nearest-neighbours, the switching frequencies are indeed representative of the transitions between states in extended square ASI systems. Regarding the assumption of dealing with single-flip events, we have seen that $\nu_{ji} dt$ represents the probability of having a transition $i \to j$ in the time interval $[t, t + dt)$. In case of independent events, the multiple-flip transitions would occur with a

---

[1]For square ASI systems only composed by full vertices (also on the array edges).

$\mathcal{O}(dt^2)$ probability, which can be neglected in the limit $dt \to 0$ performed for obtaining the master equation (D.1) [29]. However, we are neglecting any kind of statistical and physical correlations between transitions. Nonetheless, single-flip events allows satisfying another defining condition for the master equation approach, which is *ergodicity*: some of the switching frequencies of the above-described Markov process can be zero, but there must be at least one path (no matter how many events it involves) between any two states of the system [165].

The solution of the master equation for a system characterized by m states requires the solution of a system of $m-1$ independent linear differential equations, a task which can be computationally hard since the number of states for square ASI systems exponentially grows. The kMC method does provide a recipe for iteratively solving this kind of systems. Essentially, it belongs to the family of Monte Carlo methods, but the fact of producing (i.e. sampling) the states according to switching frequencies endowed with a physical meaning allows calculating proper time increments (in physical units). The kMC algorithm consists in the following steps [165, 166]:

1. initialize the square ASI system composed by N nanostructures. The j-th nanostructure is characterized by the switching frequency ν_j obtained in the DVA according to the configuration of the neighbouring nanostructures;

2. calculate the sequence R_j $(j = 1, \ldots, N)$ of the partial sums of the switching frequencies:

$$R_j \ = \ \sum_{i=1}^{j} \nu_i. \tag{D.7}$$

   Visually, R_j corresponds to the height of a stack of j blocks, whose length is proportional to the switching frequency they represent, as shown in Fig. D.1b;

3. select the J-th transition by generating a random number ξ_1 uniformly distributed in the $[0, 1)$ interval and using the following criterion:

$$R_{J-1} \ = \ \sum_{i=1}^{J-1} \nu_i \ < \ \xi_1 R_N \ \leq \ \sum_{i=1}^{J} \nu_i \ = \ R_J. \tag{D.8}$$

   Visually, this selection process corresponds to the choice of any transition with a probability proportional to the length of the relative block (see Fig. D.1b), which in turn is proportional to the switching frequency: the higher the switching frequency, the more probable the associated transition;

4. perform the transition by flipping the magnetization in the selected island (*rejection-free* algorithm) and generate a time step Δt for the occurred event according to

$$\Delta t \;=\; -\frac{\ln\left(\xi_2\right)}{R_N}, \tag{D.9}$$

where ξ_2 is a random number uniformly distributed in the $[0,1)$ interval. The time step Δt is then used to increment the total simulated time;

5. since a new state has been obtained, repeat steps 2 to 4 until needed (reached thermal equilibrium, relevant features discovered in the time evolution, ...).

Equation (D.9) can be justified by considering the single-flip events as a *Poisson process* [221] with rate R_N, a statement consistent both with a master equation approach [167] and with what happens in square ASI systems. In this case, the distribution of time intervals between events (Δt) is described by the *exponential distribution* [221], whose *probability distribution function* $f_{\Delta t}(t; \nu)$ and *cumulative distribution function* $F_{\Delta t}(t; \nu)$ are

$$f_{\Delta t}(t; \nu) \;=\; \nu \exp\left(-\nu t\right), \tag{D.10a}$$

$$F_{\Delta t}(t; \nu) \;=\; 1 \;-\; \exp\left(-\nu t\right), \tag{D.10b}$$

for $t \geq 0$. Hence, Eq. (D.9) corresponds to the random generation of a time interval according to the exponential distribution characterized by $\nu = R_N$.

Fou our purpose, the great advantage of the kMC algorithm resides in the fact that the geometrical arrangement of nanostrucures in a square ASI system is naturally taken into account, without the need of writing a master equation connecting all the states of the system. Moreover, in the DVA, the switching frequencies can be calculated and stored before running the kMC simulation (at any fixed temperature). Since each event only affects a limited number of switching frequencies (given the finite range of interaction in the DVA), not all the partial sums in Eq. (D.7) have to be recalculated every iteration. The Python code developed for performing the kMC simulations reported in Chap. 4 is available as a GitHub repository [222].

Appendix E

Supplementary Information for Section 3.3
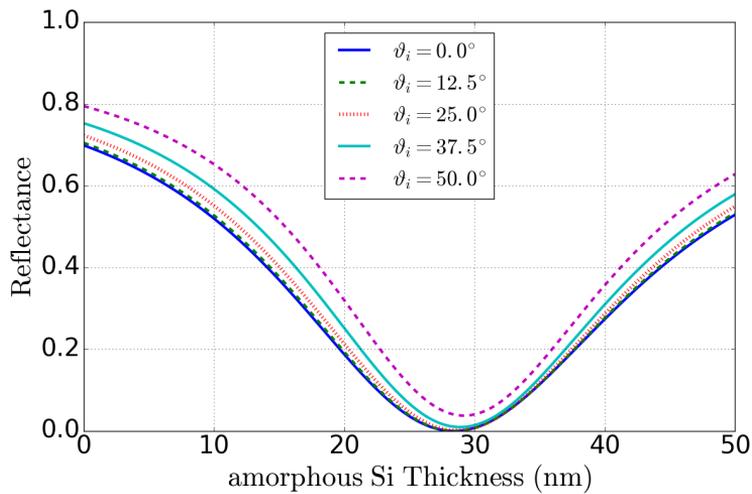
Figure E.1: Reflectance as a function of the amorphous Si (α-Si) thickness t for an Air|α-Si(t)|Au(20 nm)|Si(500 μm)|Air multilayer system. S-polarized light with a wavelength of 800 nm has been considered. Each curve corresponds to a different ϑ_i angle of incidence.
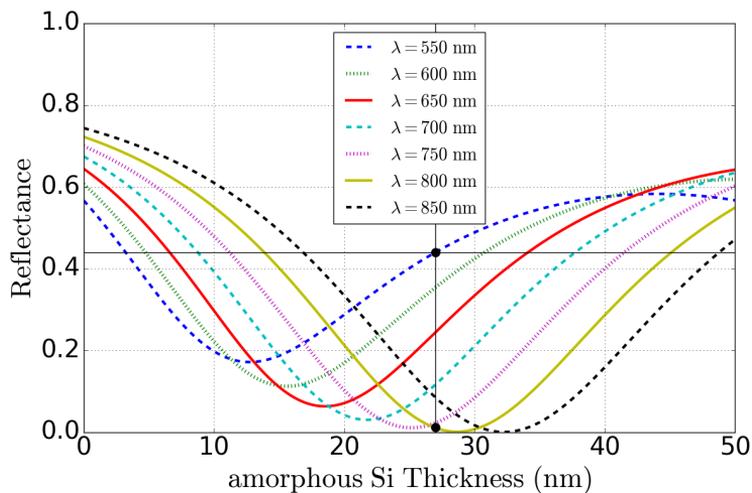
Figure E.2: Reflectance as a function of the amorphous Si (α-Si) thickness t for an Air$|\alpha$-Si$(t)|$Au$(20$ nm$)|$Si$(500$ μm$)|$Air multilayer system. S-polarized light at $25°$ of incidence has been considered. Each curve corresponds to a different λ wavelength of the impinging light, while the vertical black line corresponds to the deposited α-Si coating thickness (27 nm). The black-filled dots highlight the experimental working points. As shown by the horizontal black line, the 550 nm reflectance for a 27 nm thick α-Si coating is the same as the 800 nm reflectance for a 14 nm (or 45 nm) thick α-Si coating. This implies that using radiation of a different wavelength, having fixed the α-Si thickness, is equivalent to consider samples with different α-Si thickness.

Appendix F

Supplementary Information for Chapter 4
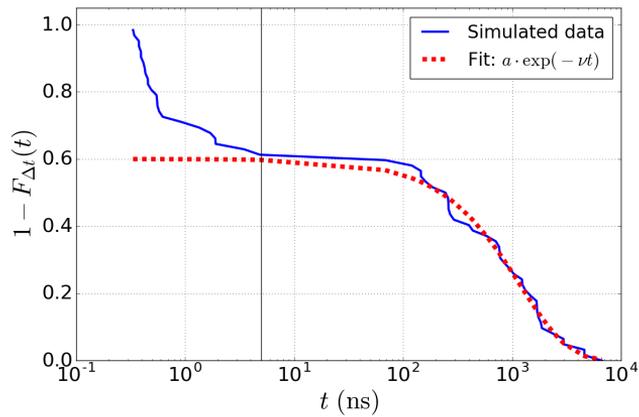
Figure F.1: Switching time cCDF at $T = 575$ K.
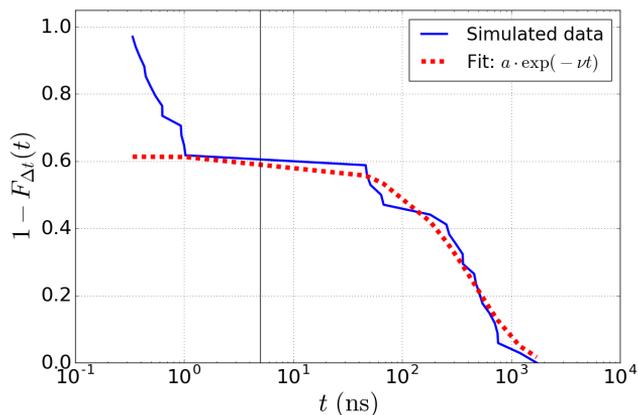
Figure F.2: Switching time cCDF at $T = 600$ K.
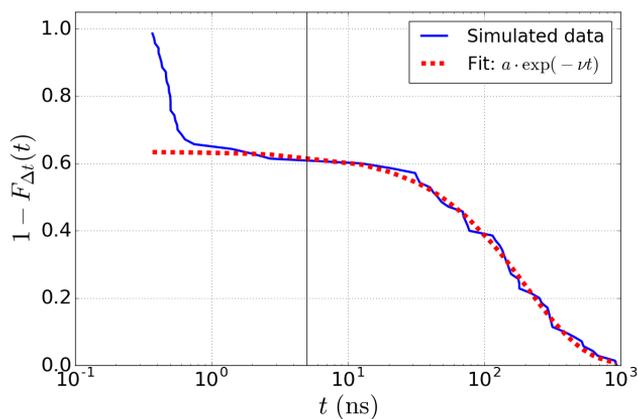
Figure F.3: Switching time cCDF at $T = 625$ K.
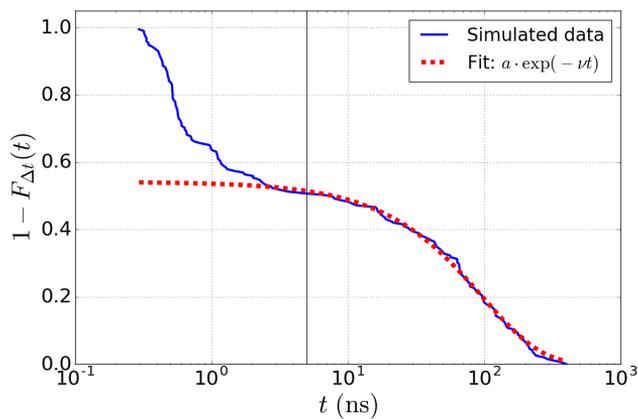
Figure F.4: Switching time cCDF at $T = 650$ K.
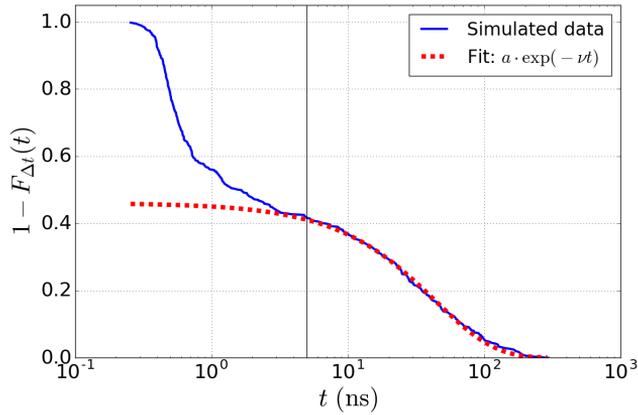
Figure F.5: Switching time cCDF at $T = 675$ K.
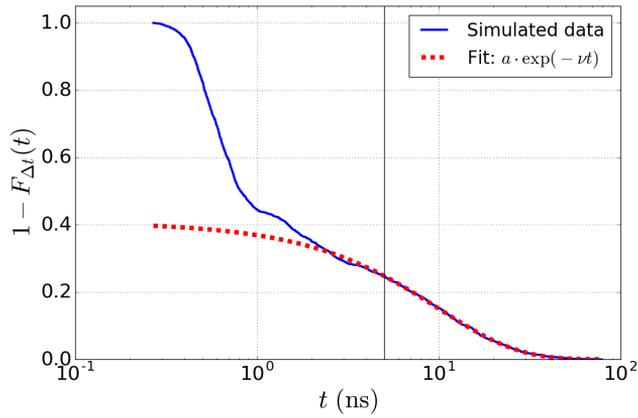
Figure F.6: Switching time cCDF at $T = 725$ K.
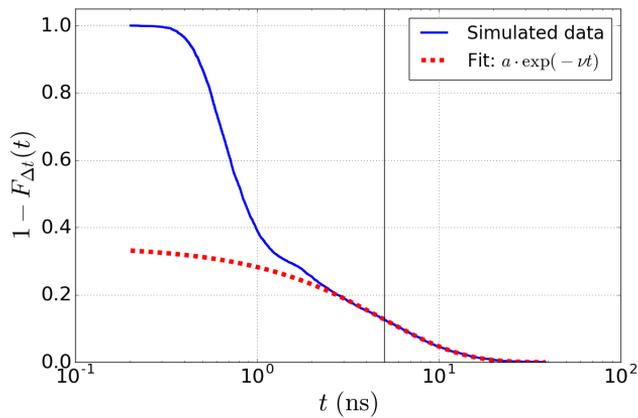
Figure F.7: Switching time cCDF at $T = 750$ K.

Appendix G

Supplementary Information for Chapter 5

Equations (5.7a) and (5.7b) can be written in terms of the beam intensity I_b instead of the beam power $\mathcal{P}$:

- **circular uniform beam**

$$I_b = \frac{4\mathcal{P}}{\pi D^2}, \tag{G.1a}$$

$$\Delta T_0 \approx \frac{\sigma_{abs} I_b}{4\pi \bar{\kappa} a} + \frac{\sigma_{abs} I_b D}{4\bar{\kappa} S}\left(1 - \frac{2\sqrt{S}}{D\sqrt{\pi}}\right); \tag{G.1b}$$

- **Gaussian beam** (with standard deviation σ_{I_b})

$$I_b(r) = \frac{4\mathcal{P}\ln(2)}{\pi H^2}\exp\left(-\frac{4r^2\ln(2)}{H^2}\right) \text{ where } H = 2\sqrt{2\ln(2)}\sigma_{I_b}, \tag{G.2a}$$

$$\Delta T_0 \approx \frac{\sigma_{abs} I_b(0)}{4\pi \bar{\kappa} a} + \frac{\sigma_{abs} I_b(0) H}{8\bar{\kappa} S}\sqrt{\frac{\pi}{\ln(2)}}\left(1 - \frac{4\sqrt{S\ln(2)}}{\pi H}\right). \tag{G.2b}$$

See Sec. 5.1 and Ref. [194] for the definition of the various parameters. Concerning I_b and H, the first term in Eq. (G.2b) (i.e. the self contribution) *only* depends on the beam intensity I_b, whereas the second term (i.e. the contribution of the surrounding structures) *also* depends on the beam FWHM H.

(a) Experimental $1 - T$ (b) Hysteresis loops
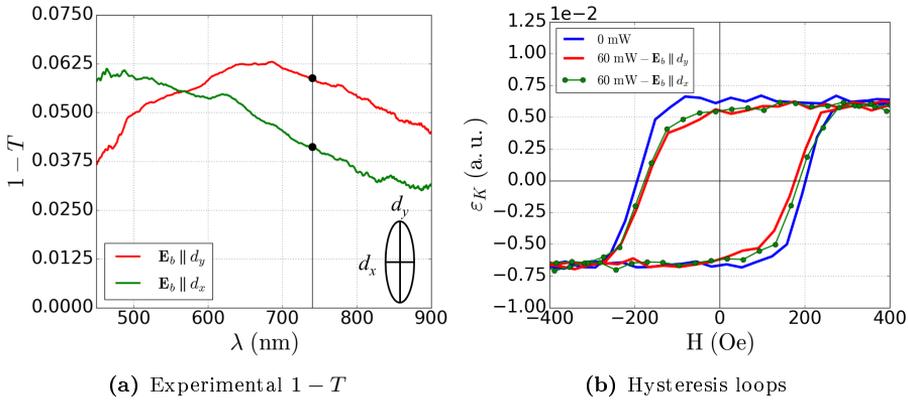
Figure G.1: A control array corresponding to array $B1 - 1.75$ has been fabricated by only depositing a 15 nm thick Permalloy film, so avoiding the gold layers below and above it. (a) Experimental extinction spectra $(1 - T)$ measured using linearly polarized light. The incident electric field $\mathbf{E}_b$ was parallel either to the major axis d_y or to the minor axis d_x of the nanostructures composing the array. The black vertical line corresponds to $\lambda = 740$ nm, the wavelength considered to be the best compromise between heating efficiency and selectivity. (b) Measured hysteresis loops along d_y while pumping with linearly polarized light at $\lambda = 740$ nm. The red and green hysteresis loops correspond to measurements performed at $\mathcal{P} = 60$ mW for $\mathbf{E}_b \parallel d_y$ and $\mathbf{E}_b \parallel d_x$, respectively. Both the reduced coercive field variation ($\Delta H_C < 25$ Oe) and the small difference between the $\mathbf{E}_b \parallel d_y$ and $\mathbf{E}_b \parallel d_x$ cases (≈ 10 Oe) confirm the loss of heating efficiency and selectivity.

(a) Probe spot   (b) Pump spot
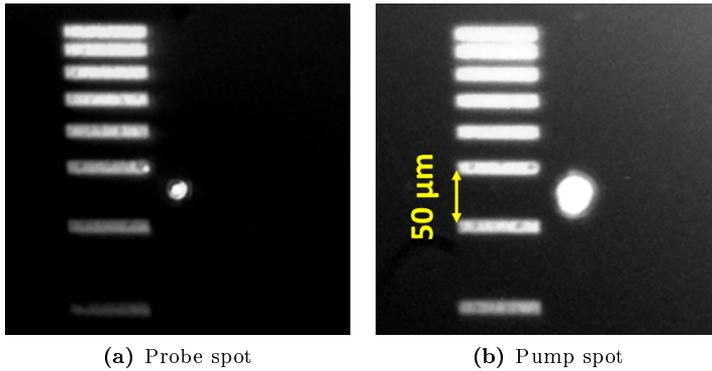
Figure G.2: (a) Image of the probe spot ($\lambda = 532$ nm). Its FWHM is 15 μm. (b) Image of the pump spot ($\lambda = 785$ nm). Its FWHM is 30 μm. The horizontal bars appearing in both the images have been fabricated on each sample in order to have a "visual" estimate of the spot size during the measurements.

List of Publications

1. H. Corte-León, L. A. Rodríguez, <u>M. Pancaldi</u>, D. Cox, E. Snoeck, V. Antonov, P. Vavassori, and O. Kazakova.
   Magnetic Force Microscopy Imaging Using Geometrically Constrained Nano-Domain Walls.
   arXiv:1804.04400v1 [physics.ins-det] (2018).

2. <u>M. Pancaldi</u>, R. Freeman, M. Hudl, M. C. Hoffmann, S. Urazhdin, P. Vavassori, and S. Bonetti.
   Anti-reflection coating design for metallic terahertz meta-materials.
   Opt. Express **26,** 2917 (2018). DOI: 10.1364/OE.26.002917. This entry corresponds to Ref. [108].

3. D. Polley, <u>M. Pancaldi</u>, M. Hudl, P. Vavassori, S. Urazhdin, and S. Bonetti.
   THz-driven demagnetization with perpendicular magnetic anisotropy: towards ultrafast ballistic switching.
   J. Phys. D: Appl. Phys. **51,** 084001 (2018). DOI: 10.1088/1361-6463/aaa863. This entry corresponds to Ref. [101].

4. L. Fallarino, B. J. Kirby, <u>M. Pancaldi</u>, P. Riego, A. L. Balk, C. W. Miller, P. Vavassori, and A. Berger.
   Magnetic properties of epitaxial CoCr films with depth-dependent exchange-coupling profiles.
   Phys. Rev. B **95,** 134445 (2017). DOI: 10.1103/PhysRevB.95.134445

5. M. Kozina, <u>M. Pancaldi</u>, C. Bernhard, T. van Driel, J. M. Glownia, P. Marsik, M. Radovic, C. A. F. Vaz, D. Zhu, S. Bonetti, U. Staub, and M. C. Hoffmann.
   Local terahertz field enhancement for time-resolved x-ray diffraction.
   Appl. Phys. Lett. **110,** 081106 (2017). DOI: 10.1063/1.4977088. This entry corresponds to Ref. [100].

6. B. Van de Wiele, S. Fin, M. Pancaldi, P. Vavassori, A. Sarella, and D. Bisero.
   Magnetization reversal in magnetic dot arrays: Nearest-neighbor interactions and global configurational anisotropy.
   J. Appl. Phys. **119,** 203901 (2016). DOI: 10.1063/1.4949554

7. N. Maccaferri, L. Bergamini, M. Pancaldi, M. K. Schmidt, M. Kataja, S. van Dijken, N. Zabala, J. Aizpurua, and P. Vavassori.
   Anisotropic Nanoantenna-Based Magnetoplasmonic Crystals for Highly Enhanced and Tunable Magneto-Optical Activity.
   Nano Lett. **16,** 2533 (2016). DOI: 10.1021/acs.nanolett.6b00084. This entry corresponds to Ref. [197].

8. E. Albisetti, D. Petti, M. Pancaldi, M. Madami, S. Tacchi, J. Curtis, W. P. King, A. Papp, G. Csaba, W. Porod, P. Vavassori, E. Riedo, and R. Bertacco.
   Nanopatterning reconfigurable magnetic landscapes via thermally assisted scanning probe lithography.
   Nat. Nanotech. **11,** 545 (2016). DOI: 10.1038/nnano.2016.25

9. P. Vavassori, M. Pancaldi, M. J. Perez-Roldan, A. Chuvilin, and A. Berger.
   Remote Magnetomechanical Nanoactuation.
   Small **12,** 1013 (2016). DOI: 10.1002/smll.201503351

10. L. Martini, M. Pancaldi, M. Madami, P. Vavassori, G. Gubbiotti, S. Tacchi, F. Hartmann, M. Emmerling, S. Höfling, L. Worschech, and G. Carlotti.
    Experimental and theoretical analysis of Landauer erasure in nanomagnetic switches of different sizes.
    Nano Energy **19,** 108 (2016). DOI: 10.1016/j.nanoen.2015.10.028

11. A. Berger, R. Alcaraz de la Osa, A. K. Suszka, M. Pancaldi, J. M. Saiz, F. Moreno, H. P. Oepen, and P. Vavassori.
    Enhanced Magneto-Optical Edge Excitation in Nanoscale Magnetic Disks.
    Phys. Rev. Lett. **115,** 187403 (2015). DOI: 10.1103/PhysRevLett.115.187403

12. A. Sarella, A. Torti, M. Donolato, M. Pancaldi, and P. Vavassori.
    Two-Dimensional Programmable Manipulation of Magnetic Nanoparticles on-Chip.
    Adv. Mater. **26,** 2384 (2014). DOI: 10.1002/adma.201304240

Acknowledgements

This thesis concludes the hard but gratifying work started on the 6th of February 2014. All the people I met during all this time (corresponding to 1594 days) helped me in going through my Ph.D. project.

First of all, I would like to thank Paolo for being my mentor. He constantly guided me, wisely relaxing his influence in a progressive way in order to facilitate my path towards an independent scientific thinking. Moreover, I would also like to thank Andreas for having well received me in the Nanomagnetism group. Both Paolo and Andreas managed to make their group a stimulating environment, both from a scientific point of view and in terms of personal relationships. Indeed, all the Nanomagnetism group members (past and present) had a fundamental role in the development of my Ph.D. project: César (our great technician), Ania, Juan, Olatz, Txema, Anandakumar, Jon Ander, Nicolò, Lorenzo, Patricia, Alberto, Adrián, Eva, Eleftheria, Mario, Andrea and Leonardo. In particular, Nicolò and Lorenzo (together with Luca, Álvaro, Guido and Raisa) represented the (first) pillar on top of which I built my stay in Donosti. Thanks to Ralph for his continuous and endless support on clean-room stuff. Regarding my four-month research stay at Stockholm University, I would like to acknowledge Stefano and Matthias for the great time I spent there and for what I could learn. Thanks also to all the people that contributed to the achievement of the results reported in Chaps. 4, 5 and 6: Jonathan, Sabri, Dieter, David and Pedro.

A relevant role has also been played by all the people I left behind when I moved to Donosti. I would like to acknowledge my family (Giancarlo, Nicoletta and Lorenzo) for pushing me to pursue my dreams without having to worry about anything else. Thanks to all my friends, since I lost contact with them, but I know they will always be there: Luca G., Damiano, Francesco, Daniele, Corrado, Michele, Filippo, Tullio, Dario, Luca P. and Jacopo. The last big "thank you" goes to Ilargi. Since we met, you became my second pillar, both reinforcing my stay in Donosti and making me a complete person. Eskerrik asko maitia!

Matteo

Donostia–San Sebastián,
18th of June 2018

Bibliography

[1] R. Skomski, *J. Phys.: Condens. Matter* **15,** R841 (2003).

[2] H. Dosch, *Appl. Surf. Sci.* **182,** 192 (2001).

[3] R. F. Wang et al., *Nature* **439,** 303 (2006).

[4] R. P. Feynman, *Caltech Engineering and Science* **23,** 22 (1960).

[5] J. D. Jackson, *Classical Electrodynamics* (John Wiley & Sons, 1998).

[6] M. Born and E. Wolf, *Principles of Optics* (Cambridge University Press, 1999).

[7] R. W. Boyd, *Nonlinear Optics* (Academic Press, 2008).

[8] G. Manfredi, *Eur. J. Phys.* **34,** 859 (2013).

[9] H. Goldstein, C. Poole, and J. Safko, *Classical Mechanics* (Addison Wesley, 2000).

[10] B. D. Cullity and C. D. Graham, *Introduction to Magnetic Materials* (John Wiley & Sons, 2009).

[11] J. M. D. Coey, *Magnetism and Magnetic Materials* (Cambridge University Press, 2010).

[12] A. Aharoni, *Introduction to the Theory of Ferromagnetism* (Oxford University Press, 2000).

[13] J. Kübler, *Theory of Itinerant Electron Magnetism* (Oxford University Press, 2009).

[14] B. H. Bransden and C. J. Joachain, *Physics of Atoms and Molecules* (Pearson Education, 2003).

[15] P. Weiss, *Compt. Rend.* **143,** 1136 (1906). P. Weiss, *J. de Phys.* **6,** 661 (1907).

[16] R. Skomski, *Simple Models of Magnetism* (Oxford University Press, 2008).

[17] S. Chikazumi, *Physics of Ferromagnetism* (Oxford University Press, 1997).

[18] W. F. Brown, *Micromagnetics* (John Wiley & Sons, 1963).

[19] G. Bertotti, *Hysteresis in Magnetism* (Academic Press, 1998).

[20] J. A. Osborn, *Phys. Rev.* **67,** 351 (1945).

[21] G. S. Abo et al., *IEEE Trans. Magn.* **49,** 4937 (2013).

[22] C. Kittel, *Rev. Mod. Phys.* **21,** 541 (1949).

[23] T. L. Gilbert, *IEEE Trans. Magn.* **40,** 3443 (2004).

[24] M. D'Aquino, *Nonlinear Magnetization Dynamics in Thin-fils and Nanoparticles* (Ph.D. Thesis, Università degli Studi di Napoli "Federico II", 2004). Available at `http://wpage.unina.it/mdaquino/index_file/phd_thesis.html`.

[25] A. Vansteenkiste et al., *AIP Adv.* **4,** 107133 (2014). `http://mumax.github.io/`.

[26] E. C. Stoner and E. P. Wohlfarth, *Phil. Trans. R. Soc. Lond. A* **240,** 599 (1948).

[27] S. Bedanta and W. Kleemann, *J. Phys. D: Appl. Phys.* **42,** 013001 (2009).

[28] W. F. Brown, *Phys. Rev.* **130,** 1677 (1963).

[29] R. Toral and P. Colet, *Stochastic Numerical Methods – An Introduction for Students and Scientists* (John Wiley & Sons, 2014).

[30] H.-B. Braun, *J. Appl. Phys.* **76,** 6310 (1994).

[31] D. Suess et al., *Phys. Rev. B* **84,** 224421 (2011).

[32] M. P. Sharrock, *IEEE Trans. Magn.* **26,** 193 (1990).

[33] A. Lyberatos, D. V. Berkov, and R. W. Chantrell, *J. Phys.: Condens. Matter* **5,** 8911 (1993).

[34] K. Y. Guslienko et al., *J. Magn. Magn. Mater.* **272-276,** 251 (2004).

[35] J. L. García-Palacios and F. J. Lázaro, *Phys. Rev. B* **58,** 14937 (1998).

[36] J. Leliaert et al., *AIP Adv.* **7,** 125010 (2017).

[37] W. Scholz, T. Schrefl, and J. Fidler, *J. Magn. Magn. Mater.* **233,** 296 (2001).

[38] Y. Nakatani et al., *J. Magn. Magn. Mater.* **168,** 347 (1997).

[39] O. Chubykalo-Fesenko et al., *Phys. Rev. B* **74,** 094436 (2006).

[40] G. Grinstein and R. H. Koch, *Phys. Rev. Lett.* **90,** 207201 (2003).

[41] M. Kirschner et al., *J. Appl. Phys.* **97,** 10E301 (2005).

[42] R. H. Victora and P.-W. Huang, *IEEE Trans. Magn.* **49,** 751 (2013).

[43] D. D. Stancil and A. Prabhakar, *Spin Waves – Theory and Applications* (Springer-Verlag, 2009).

[44] C. Herring and C. Kittel, *Phys. Rev.* **81,** 869 (1951).

[45] M. Grimsditch et al., *EPL* **54,** 813 (2001).

[46] M. Grimsditch et al., *Phys. Rev. B* **69,** 174428 (2004).

[47] C. Kittel, *Phys. Rev.* **73,** 155 (1948).

[48] S. A. Maier, *Plasmonics – Fundamentals and Applications* (Springer-Verlag, 2007).

[49] I. D. Mayergoyz, *Plasmon Resonances in Nanoparticles* (World Scientific, 2013).

[50] W. Yan, R. Faggiani, and P. Lalanne, *Phys. Rev. B* **97,** 205422 (2018).

[51] M. Fox, *Optical Properties of Solids* (Oxford University Press, 2010).

[52] N. Maccaferri, *Designer magneto-optics with plasmonic magnetic nanostructures* (Ph.D. Thesis, University of the Basque Country UPV/EHU, 2016). Available at `http://www.nanogune.eu/nanomagnetism/publications/p-1-phd-theses/`.

[53] N. W. Ashcroft and N. D. Mermin, *Solid State Physics* (Brooks/Cole, Cengage Learning, 1976).

[54] P. Biagioni, J.-S. Huang, and B. Hecht, *Rep. Prog. Phys.* **75,** 024402 (2012).

[55] T. J. Davis and D. E. Gómez, *Rev. Mod. Phys.* **89,** 011003 (2017).

[56] A. Moroz, *J. Opt. Soc. Am. B* **26,** 517 (2009).

[57] H. C. van de Hulst, *Light Scattering by Small Particles* (Dover Publications, 1981).

[58] P. B. Johnson and R. W. Christy, *Phys. Rev. B* **6,** 4370 (1972).

[59] G. Baffou, *Thermoplasmonics – Heating Metal Nanoparticles Using Light* (Cambridge University Press, 2018).

[60] M. Faraday, *Phil. Trans. R. Soc. Lond.* **136,** 1 (1846).

[61] J. Kerr, *Philos. Mag.* **3,** 321 (1877).

[62] G. R. Fowles, *Introduction to Modern Optics* (Dover Publications, 1989).

[63] M. J. Freiser, *IEEE Trans. Magn.* **4,** 152 (1968).

[64] Š. Višňovský, *Optics in Magnetic Multilayers and Nanostructures* (CRC Press, 2006).

[65] Š. Višňovský, *Czech. J. Phys. B* **36,** 1424 (1986).

[66] R. M. Osgood III, *Hysteresis Loops in Anisotropic Thin Films* (Ph.D. Thesis, Stanford University, 1996).

[67] Z. Q. Qiu and S. D. Bader, *Rev. Sci. Instrum.* **71,** 1243 (2000).

[68] H. R. Hulme, *Proc. Royal Soc. A* **135,** 237 (1932).

[69] P. N. Argyres, *Phys. Rev.* **97,** 334 (1955).

[70] H. S. Bennett and E. A. Stern, *Phys. Rev.* **137,** A448 (1965).

[71] S. Gasiorowicz, *Quantum Physics* (John Wiley & Sons, 2003).

[72] A. Hubert and R. Schäfer, *Magnetic Domains – The Analysis of Magnetic Microstructures* (Springer-Verlag, 1998).

[73] C. Liu and S. D. Bader, *J. Appl. Phys.* **67,** 5758 (1990).

[74] G. Metzger, P. Pluvinage, and R. Torguet, *Ann. Phys.* **13,** 5 (1965).

[75] Z. J. Yang and M. R. Scheinfein, *J. Appl. Phys.* **74,** 6810 (1993).

[76] C. Y. You and S. C. Shin, *Appl. Phys. Lett.* **69,** 1315 (1996).

[77] R. Atkinson and P. H. Lissberger, *Appl. Opt.* **31,** 6076 (1992).

[78] G. Neuber et al., *Appl. Phys. Lett.* **83,** 4509 (2003).

[79] J. Goldstein et al., *Scanning Electron Microscopy and X-Ray Microanalysis* (Springer, 2003).

[80] F. Rohrlich and B. C. Carlson, *Phys. Rev.* **93,** 38 (1954).

[81] CASINO v2.51 by D. Drouin et al., Université de Sherbrooke (Quebec, Canada), `http://www.gel.usherbrooke.ca/casino/index.html`.

[82] G. Owen, *Rep. Prog. Phys.* **48,** 795 (1985).

[83] PMMA positive e-beam resists by MicroChem, `http://microchem.com/Prod-PMMA.htm`.

[84] ZEP520A positive e-beam resist by ZEON, `http://www.zeon.co.jp/business_e/enterprise/imagelec/zep520A.html`.

[85] A. Berger and M. R. Pufall, *Appl. Phys. Lett.* **71,** 965 (1997). A. Berger and M. R. Pufall, *J. Appl. Phys.* **85,** 4583 (1999).

[86] P. Vavassori, *Appl. Phys. Lett.* **77,** 1605 (2000).

[87] E. Jiménez et al., *Rev. Sci. Instrum.* **85,** 053904 (2014).

[88] D. A. Allwood et al., *J. Phys. D: Appl. Phys.* **36,** 2175 (2003).

[89] M. C. Hoffmann and J. A. Fülöp, *J. Phys. D: Appl. Phys.* **44,** 083001 (2011).

[90] M. Liu et al., *Nature* **487,** 345 (2012).

[91] T. Kubacka et al., *Science* **343,** 1333 (2014).

[92] G. L. Dakovski et al., *Phys. Rev. B* **91,** 220506(R) (2015).

[93] S. Bonetti et al., *Phys. Rev. Lett.* **117,** 087205 (2016).

[94] F. Chen et al., *Phys. Rev. B* **94,** 180104(R) (2016).

[95] H.-T. Chen et al., *Nature* **444,** 597 (2006).

[96] L. Razzari et al., *Opt. Express* **19,** 26088 (2011).

[97] C. A. Werley et al., *Opt. Express* **20,** 8551 (2012).

[98] J. Zhang et al., *Appl. Phys. Lett.* **107,** 231101 (2015).

[99] M. Savoini et al., *Opt. Express* **24,** 4552 (2016).

[100] M. Kozina et al., *Appl. Phys. Lett.* **110,** 081106 (2017). This reference corresponds to entry n. 5 in the list of publications.

[101] D. Polley et al., *J. Phys. D: Appl. Phys.* **51,** 084001 (2018). This reference corresponds to entry n. 3 in the list of publications.

[102] K. Balasubramanian, A. S. Marathay, and H. A. Macleod, *Thin Solid Films* **164,** 391 (1988).

[103] R. Atkinson, I. W. Salter, and J. Xu, *J. Magn. Magn. Mater.* **102,** 357 (1991).

[104] N. Qureshi, H. Schmidt, and A. R. Hawkins, *Appl. Phys. Lett.* **85,** 431 (2004).

[105] N. Qureshi et al., *Nano Lett.* **5,** 1413 (2005).

[106] A. Barman et al., *Nano Lett.* **6,** 2939 (2006).

[107] S. Wang et al., *Appl. Phys. Lett.* **90,** 252504 (2007).

[108] M. Pancaldi et al., *Opt. Express* **26,** 2917 (2018). This reference corresponds to entry n. 2 in the list of publications.

[109] G. Hass, H. H. Schroeder, and A. F. Turner, *J. Opt. Soc. Am.* **46,** 31 (1956).

[110] S. Yoshida, *Thin Solid Films* **56,** 321 (1979).

[111] K. C. Park, *Appl. Opt.* **3,** 877 (1964).

[112] S. Adachi and H. Mori, *Phys. Rev. B* **62,** 10158 (2000).

[113] M. N. Polyanskiy, *Refractive index database*, `https://refractiveindex.info`.

[114] F. D. J. Brunner et al., *Opt. Express* **16,** 16496 (2008).

[115] COMSOL Multiphysics v. 5.0. `https://www.comsol.com`. COMSOL, AB, Stockholm, Sweden.

[116] H. T. Diep, *Frustrated Spin Systems* (World Scientific, 2013).

[117] C. Nisoli, R. Moessner, and P. Schiffer, *Rev. Mod. Phys.* **85,** 1473 (2013).

[118] J. Cumings et al., *New J. Phys.* **16,** 075016 (2014).

[119] G. H. Wannier, *Phys. Rev.* **79,** 357 (1950).

[120] J. Villain, *J. Phys. C: Solid State Phys.* **10,** 1717 (1977).

[121] C. Castelnovo, R. Moessner, and S. L. Sondhi, *Annu. Rev. Condens. Matter. Phys.* **3,** 35 (2012).

[122] C. Castelnovo, R. Moessner, and S. L. Sondhi, *Nature* **451,** 42 (2008).

[123] R. J. Baxter, *Exactly Solved Models in Statistical Mechanics* (Dover Publications, 2007).

[124] L. Pauling, *J. Am. Chem. Soc.* **57,** 2680 (1935).

[125] A. P. Ramirez et al., *Nature* **399,** 333 (1999).

[126] E. H. Lieb, *Phys. Rev.* **162,** 162 (1967).

[127] M. J. Harris et al., *Phys. Rev. Lett.* **79,** 2554 (1997).

[128] M. J. P. Gingras and B. C. den Hertog, *Can. J. Phys.* **79,** 1339 (2001).

[129] S. V. Isakov, R. Moessner, and S. L. Sondhi, *Phys. Rev. Lett.* **95,** 217201 (2005).

[130] F. Y. Wu, *Phys. Rev. Lett.* **22,** 1174 (1969).

[131] D. Levis, *Two-dimensional Spin Ice and the Sixteen-Vertex Model* (Ph.D. Thesis, Université "Pierre et Marie Curie" – Paris VI, 2012). Available at https://tel.archives-ouvertes.fr/tel-00763350/.

[132] L. Foini et al., *J. Stat. Mech.* **2013,** P02026 (2013).

[133] L. F. Cugliandolo, *J. Stat. Phys.* **167,** 499 (2017).

[134] C. Phatak et al., *Phys. Rev. B* **83,** 174431 (2011).

[135] A. Farhan et al., *Nat. Phys.* **9,** 375 (2013).

[136] A. Farhan et al., *Phys. Rev. Lett.* **111,** 057204 (2013).

[137] X. Ke et al., *Appl. Phys. Lett.* **93,** 252504 (2008).

[138] S. Ladak et al., *Nat. Phys.* **6,** 359 (2010).

[139] L. A. S. Mól, A. R. Pereira, and W. A. Moura-Melo, *Phys. Rev. B* **85,** 184410 (2012).

[140] X. Zhou et al., *Adv. Funct. Mater.* **26,** 1437 (2016).

[141] V. Brajuskovic et al., *Sci. Rep.* **6,** 34384 (2016).

[142] A. Farhan et al., *Nat. Commun.* **7,** 12635 (2016).

[143] A. Farhan et al., *Nat. Commun.* **8,** 995 (2017).

[144] S. Gliga et al., *Nat. Mater.* **16,** 1106 (2017).

[145] A. Farhan et al., *Phys. Rev. B* **89,** 214405 (2014).

[146] G. Möller and R. Moessner, *Phys. Rev. Lett.* **96,** 237202 (2006).

[147] G.-W. Chern, C. Reichhardt, and C. Nisoli, *Appl. Phys. Lett.* **104,** 013101 (2014).

[148] Y. Perrin, B. Canals, and N. Rougemaille, *Nature* **540,** 410 (2016).

[149] F. S. Nascimento et al., *New J. Phys.* **14,** 115019 (2012).

[150] L. A. Mól et al., *J. Appl. Phys.* **106,** 063913 (2009).

[151] M. J. Morrison, T. R. Nelson, and C. Nisoli, *New J. Phys.* **15,** 045009 (2013).

[152] I. Gilbert et al., *Nat. Phys.* **10,** 670 (2014).

[153] I. Gilbert et al., *Nat. Phys.* **12,** 162 (2016).

[154] R. F. Wang et al., *J. Appl. Phys.* **101,** 09J104 (2007).

[155] C. Nisoli et al., *Phys. Rev. Lett.* **98,** 217203 (2007).

[156] J. P. Morgan et al., *Nat. Phys.* **7,** 75 (2011).

[157] J. M. Porro et al., *New J. Phys.* **15,** 055012 (2013).

[158] J. P. Morgan et al., *Phys. Rev. B* **87,** 024405 (2013).

[159] A. J. Bray, *Adv. Phys.* **51,** 481 (2002).

[160] R. W. Balluffi, S. M. Allen, and W. C. Carter, *Kinetics of Materials* (John Wiley & Sons, 2005).

[161] S. Zhang et al., *Nature* **500,** 553 (2013).

[162] A. J. Newell, W. Williams, and D. J. Dunlop, *J. Geophys. Res.* **98,** 9551 (1993).

[163] D. Thonig et al., *J. Phys.: Condens. Matter* **26,** 266006 (2014).

[164] R. Macedo et al., under review in *Phys. Rev. Lett.* (2018).

[165] M. E. J. Newman and G. T. Barkema, *Monte Carlo Methods in Statistical Physics* (Oxford University Press, 1999).

[166] A. B. Bortz, M. H. Kalos, and J. L. Lebowitz, *J. Comput. Phys.* **17,** 10 (1975).

[167] K. A. Fichthorn and W. H. Weinberg, *J. Chem. Phys.* **95,** 1090 (1991).

[168] R. C. Silva et al., *New J. Phys.* **14,** 015008 (2012).

[169] Z. Budrikis et al., *New J. Phys.* **14,** 035014 (2012).

[170] D. Levis and L. F. Cugliandolo, *EPL* **97,** 30002 (2012).

[171] D. Levis et al., *Phys. Rev. Lett.* **110,** 207206 (2013).

[172] D. Levis and L. F. Cugliandolo, *Phys. Rev. B* **87,** 214302 (2013).

[173] R. P. Cowburn et al., *Phys. Rev. Lett.* **83,** 1042 (1999).

[174] N. A. Usov, C.-R. Chang, and Z.-H. Wei, *J. Appl. Phys.* **89,** 7591 (2001).

[175] P. Vavassori et al., *Phys. Rev. B* **69,** 214404 (2004).

[176] V. Kapaklis et al., *Nat. Nanotech.* **9,** 514 (2014).

[177] M. S. Andersson et al., *Sci. Rep.* **6,** 37097 (2016).

[178] S. A. Morley et al., *Phys. Rev. B* **95,** 104422 (2017).

[179] M. J. Donahue and D. G. Porter, *OOMMF User's Guide, Version 1.0.* Interagency Report **NISTIR 6376**, National Institute of Standards and Technology, Gaithersburg, MD (1999). `https://math.nist.gov/oommf/`.

[180] W. F. Brown, *J. Appl. Phys.* **30,** 130S (1959).

[181] *Non-linear least squares* algorithm from the *scipy.optimize* package, `https://docs.scipy.org/doc/scipy/reference/generated/scipy.optimize.curve_fit.html`.

[182] J. R. Taylor, *Introduzione all'Analisi degli Errori* (Zanichelli, 2000).

[183] W. T. Coffey and Y. P. Kalmykov, *J. Appl. Phys.* **112,** 121301 (2012).

[184] S. Y. Liashko, H. Jónsson, and V. M. Uzdin, *New J. Phys.* **19,** 113008 (2017).

[185] J. Stöhr and H. C. Siegmann, *Magnetism – From Fundamentals to Nanoscale Dynamics* (Springer-Verlag, 2006).

[186] Footnote 7 in K. Müller and L. D. Brown, *Theor. Chim. Acta* **53,** 75 (1979).

[187] W. E, W. Ren, and E. Vanden-Eijnden, *J. Chem. Phys.* **126,** 164103 (2007). The MATLAB code for calculating the string evolution on the Müller potential is available at `https://cims.nyu.edu/~eve2/string.htm`.

[188] W. E, W. Ren, and E. Vanden-Eijnden, *Phys. Rev. B* **66,** 052301 (2002).

[189] W. E, W. Ren, and E. Vanden-Eijnden, *J. Phys. Chem. B* **109,** 6688 (2005).

[190] R. Dittrich et al., *J. Magn. Magn. Mater.* **250,** L12 (2002).

[191] G. D. Chaves, *Numerical studies of transition states for magnetization reversal in ferromagnetic nanostructures* (Ph.D. Thesis, New York University, 2011). Available at `http://www.physics.nyu.edu/kentlab/papersandthesis.html#theses`.

[192] A. O. Govorov and H. H. Richardson, *Nano Today* **2,** 30 (2007).

[193] G. Baffou and R. Quidant, *Laser Photonics Rev.* **7,** 171 (2013).

[194] G. Baffou et al., *ACS Nano* **7,** 6478 (2013).

[195] G. Baffou, R. Quidant, and C. Girard, *Phys. Rev. B* **82,** 165424 (2010).

[196] G. Baffou, R. Quidant, and F. J. García de Abajo, *ACS Nano* **4,** 709 (2010).

[197] N. Maccaferri et al., *Nano Lett.* **16,** 2533 (2016). This reference corresponds to entry n. 7 in the list of publications.

[198] K. K. Tikuišis et al., *Mater. Des.* **114,** 31 (2017).

[199] M. Donolato et al., *Adv. Mater.* **22,** 2706 (2010).

[200] A. Imre et al., *Science* **311,** 205 (2006).

[201] J. M. Porro Azpiazu, *Exploiting magnetic dipolar interactions in artificially nanostructured systems* (Ph.D. Thesis, University of the Basque Country UPV/EHU, 2014). Available at `http://www.nanogune.eu/nanomagnetism/publications/p-1-phd-theses/`.

[202] J. M. Porro et al., *J. Appl. Phys.* **111,** 07B913 (2012).

[203] T. Verducci et al., *Appl. Phys. Lett.* **99,** 092501 (2011).

[204] M. Grimsditch and P. Vavassori, *J. Phys.: Condens. Matter* **16,** R275 (2004).

[205] G. Leaf et al., *Phys. Rev. Lett.* **96,** 017201 (2006).

[206] G. Gubbiotti et al., *Phys. Rev. B* **72,** 184419 (2005).

[207] M. Grimsditch et al., *Phys. Rev. B* **70,** 054409 (2004).

[208] R. Zivieri and G. Consolo, *Adv. Condens. Matter Phys.* **2012,** Article ID 765709 (2012).

[209] R. D. McMichael and M. D. Stiles, *J. Appl. Phys.* **97,** 10J901 (2005).

[210] F. Montoncello et al., *Phys. Rev. B* **76,** 024426 (2007).

[211] F. Montoncello et al., *Phys. Rev. B* **77,** 214402 (2008).

[212] M. Bailleul, D. Olligs, and C. Fermon, *Phys. Rev. Lett.* **91,** 137204 (2003).

[213] B. B. Maranville et al., *J. Appl. Phys.* **99,** 08C703 (2006).

[214] R. D. McMichael and B. B. Maranville, *Phys. Rev. B* **74,** 024424 (2006).

[215] G. Gubbiotti et al., *J. Appl. Phys.* **99,** 08C701 (2006).

[216] M. Ohring, *Material Science of Thin Films* (Academic Press, 2002).

[217] ma-N 2400 series of negative e-beam resists by Micro Resist Technology, `http://microresist.de/en/products/negative-photoresists/e-beam-deep-uv-lithography/ma-n-2400-mr-ebl-6000-series`.

[218] F. L. Pedrotti and L. S. Pedrotti, *Introduction to Optics* (Prentice–Hall International, 1993).

[219] H. G. Tompkins and E. A. Irene, *Handbook of Ellipsometry* (William Andrew Publishing, 2005).

[220] W. H. Press et al., *Numerical Recipes – The Art of Scientific Computing* (Cambridge University Press, 2007).

[221] E. Çinlar, *Introduction to Stochastic Processes* (Dover Publications, 2013).

[222] `https://github.com/matteopanca/kmc_asi`.

Index